P-ISSN 2525-2461 • E-ISSN 2615-9937

Vietnam Journal of Science, Technology and Engineering

JUNE 2021 • VOLUME 63 NUMBER 2

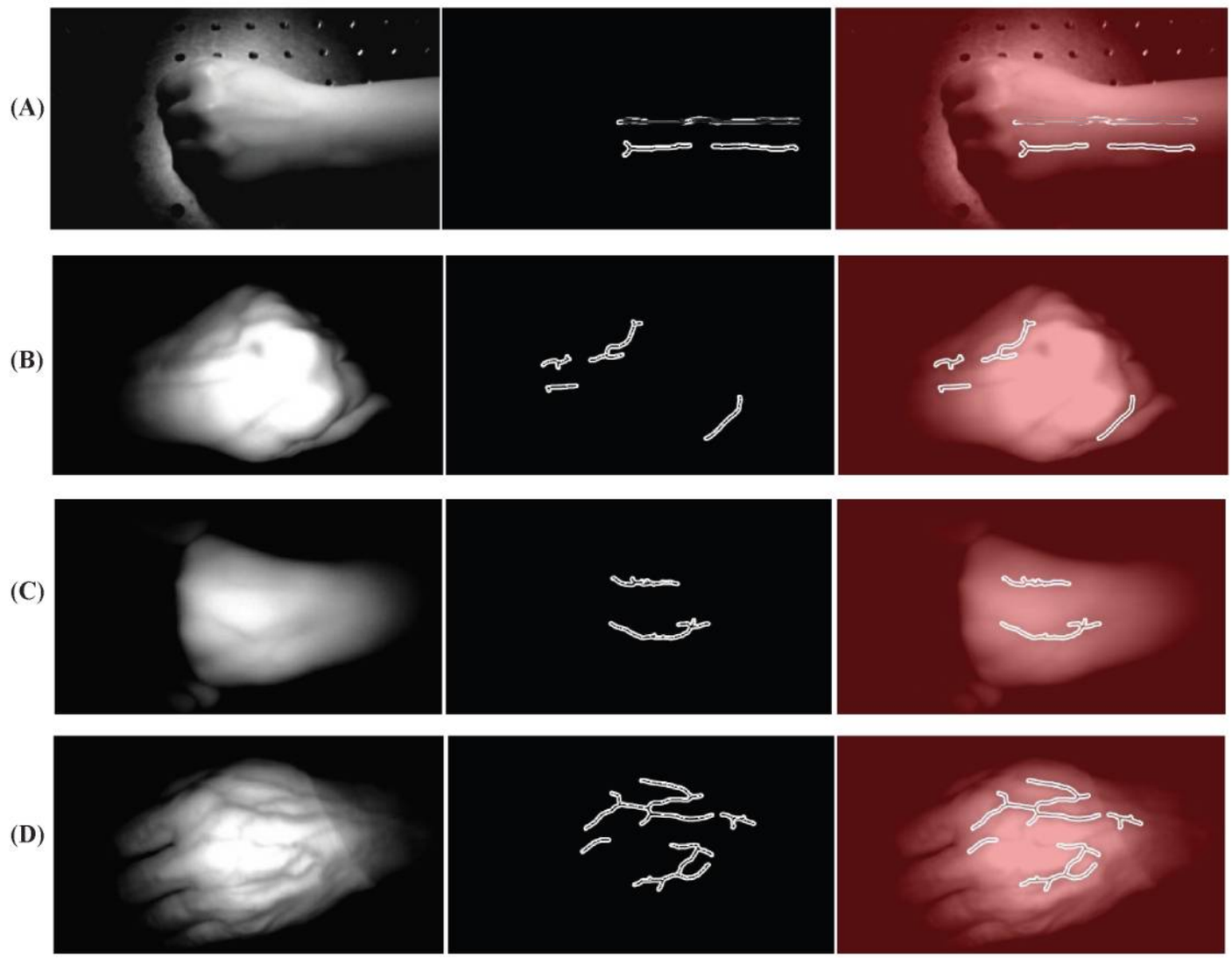

AN EFFECTIVE METHOD FOR DETECTING DORSAL HAND VEINS UTILISING NEAR-INFRARED IMAGING TECHNOLOGY

VIETNAM JOURNAL OF SCIENCE, TECHNOLOGY AND ENGINEERING * JUNE 2021 * VOLUME 63 NUMBER 2
vietnamscience.vn or vietnamscience.vjst.vn

Vietnam Journal of Science, Technology and Engineering (VJSTE) **is a quarterly double-blind peer-reviewed academic journal. VJSTE publishes research articles and review articles in all areas of science, technology and engineering with the focus on the physical sciences, life sciences and environmental sciences including the following topics:**

- **Physical Sciences**
- **Agriculture**
- **Medicine**
- **Pharmacology**
- **Biology**
- **Biotechnology**
- **Biomedical Applications**
- **Ecology**
- **Climatology**
- **Environmental Science.**

CLASSIFICATION SCHEME

1. **Mathematics and Computer Science**
   - **1.1. Mathematics**
   - **1.2. Computer Science**
   - **1.3. Computational Science**
2. **Physical Sciences**
   - **2.1. Physics**
   - **2.2. Chemistry**
   - **2.3. Engineering**
3. **Life Sciences**
   - **3.1. Agriculture**
   - **3.2. Medicine**
   - **3.3. Pharmacology**
   - **3.4. Biology**
   - **3.5. Biotechnology**
   - **3.6. Biomedical Applications**
4. **Earth Sciences**
   - **4.1. Geography**
   - **4.2. Geology**
   - **4.3. Geophysics**
   - **4.4. Oceanography**
5. **Environmental Sciences**
   - **5.1. Ecology**
   - **5.2. Climatology**
   - **5.3. Environmental Science**

CONTENTS

JUNE 2021 • VOLUME 63 NUMBER 2

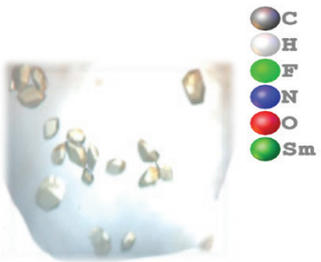

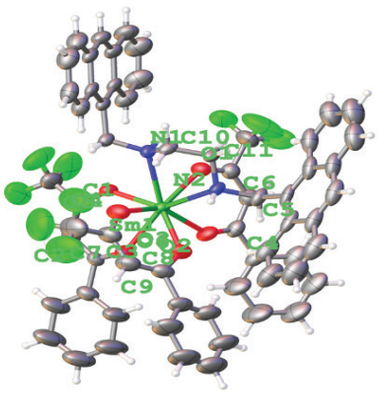

PHYSICAL SCIENCES

LIFE SCIENCES

CONTENTS

JUNE 2021 • VOLUME 63 NUMBER 2

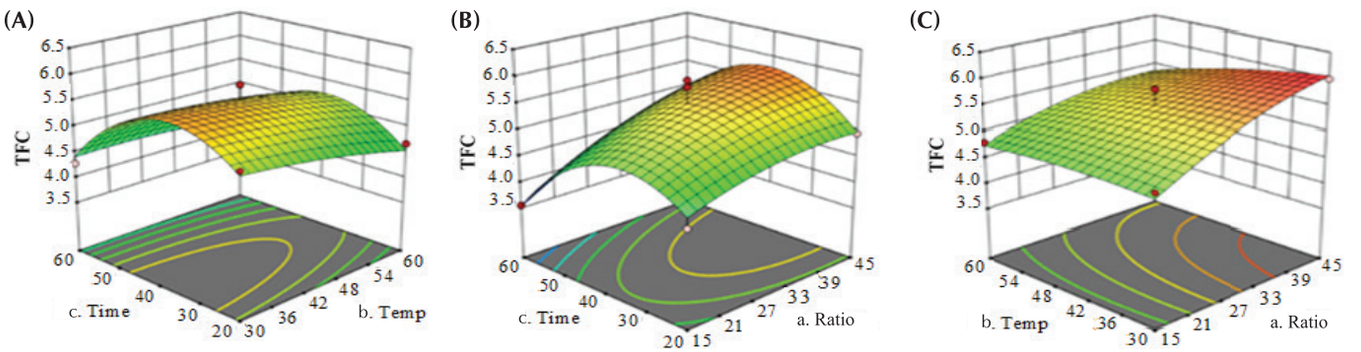

ENVIRONMENTAL SCIENCES

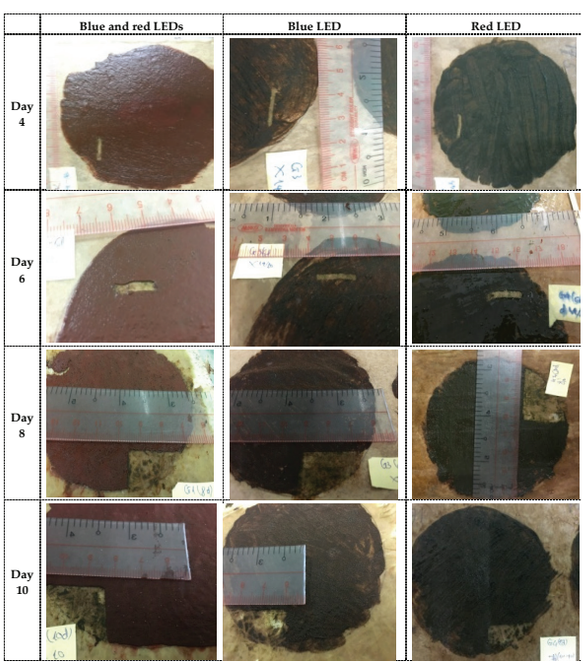

DOI: 10.31276/VJSTE.63(2).03-06

Flavone glycosides from *Uraria crinita*

Tran Duc Dai[1], Dao Duc Thien[2], Nguyen Thanh Tam[2, 3*]

[1]*Tan Trao University, Km 6, Trung Mon Commune, Yen Son District, Tuyen Quang Province, Vietnam*
[2]*Institute of Chemistry, Vietnam Academy of Science and Technology, 18 Hoang Quoc Viet Street, Nghia Do Ward, Cau Giay District, Hanoi, Vietnam*
[3]*Graduate University of Science and Technology, Vietnam Academy of Science and Technology, 18 Hoang Quoc Viet Street, Nghia Do Ward, Cau Giay District, Hanoi, Vietnam*

Received 4 January 2021; revised 13 March 2021; accepted 25 March 2021

Abstract:

A common edible herb found in all regions of Vietnam is Uraria crinita (L.) DC. (Leguminosae). It has been used as a vegetable or in folk medicine to treat lung disorders, sprains, bruises, diarrhea, and rheumatism. Pharmacological studies have shown that U. crinita possesses a range of medicinal qualities, including as antioxidant, anti-inflammatory, and osteogenic activity, as well as the ability to lessen ulcers brought on by stress. Numerous substances, including flavonoids, triterpenes, megastigmanes, and nucleosides, have been identified as this plant's active ingredients. Four flavone glycosides including apigenin 7-*O*- *β*-glucoside (1), chrysoeriol 7-*O*-*β*-glucoside (2), rhoifolin (3), and 3'-methoxyapiin (4) were isolated from the n-butanol extract of the whole plant *Uraria crinita* collected in the Phu Tho province, Vietnam. Their structures were elucidated by 1D- and 2D-NMR spectra and compared with those reported in the literature. The structures of compounds 1-4 were determined by spectroscopic methods and comparison with published data. Compounds 1-3 were obtained from the genus *Uraria* for the first time. This is the first report of these compounds from the genus *Uraria*.

Keywords: **apigenin 7-*O*-*β*-glucoside, chrysoeriol 7-*O*-*β*-glucoside, flavone glycosides, rhoifolin, *Uraria crinita*.**

Classification number: **2.2**

1. Introduction

Uraria crinita (L.) DC. (Leguminosae) is an edible herb that is widely distributed across all regions of Vietnam. It has been consumed as a vegetable or used in folk medicine for the treatment of rheumatism, diarrhoea, sprains, injuries, and lung diseases [1]. Pharmacological investigations have demonstrated that *U. crinita* has various therapeutic properties including antioxidant, anti-inflammatory, and osteogenic activities as well as reduce stress-induced ulcers [2, 3]. Several compounds including flavonoids, triterpenes, megastigmanes, and nucleosides have been reported to be active components in this plant [3-6]. Our previous studies on *U. crinita* has led us to isolate four new phenolics, (3*S*)-5,7-dihydroxy-2′,3′,4′-trimethoxy-6,5′-diprenylisoflavanone, 3,5,7,2',4'-pentahydroxyisoflavanone, 3,4-dimethoxyphenyl 1-*O*-(6′-*O*-acetyl)-*β*-D-glucopyranoside, and 3,4,5-trimethoxyphenyl 1-*O*-(6′-*O*-acetyl)-*β*-D-glucopyranoside, along with eleven known compounds [7, 8]. Here, we report the isolation and structural determination of four flavone glycosides **1-4** from the n-butanol extract of the whole plant *U. crinita*.

2. Materials and methods

2.1. General experimental procedures

Nuclear magnetic resonance (NMR) spectra were taken on a Bruker Avance III 500 spectrometer (Bruker, Fällanden, Switzerland) and electrospray ionisation mass spectrometry (ESI-MS) was conducted on an Agilent LC-MSD-Trap-SL spectrometer (Varian, USA). Infrared (IR) spectra were performed on Perkin Elmer Spectrum Two IR spectrometer (Perkin Elmer, Waltham, MA, USA). Column chromatography was carried out on silica gel 60 (0.040-0.063 mm, Merck, Darmstadt, Germany), Sephadex LH-20 (Amersham Pharmacia Biotech, Tokyo, Japan), and Rp-18 (30-50 µm, Fuji Silysia Chemical Ltd, Aichi, Japan). Thin layer chromatography was performed on silica gel 60F254 (0.25 mm, Merck, Darmstadt, Germany). The spots on the plates were observed under UV light and by spraying with a solution of vanillin/sulfuric acid and 5 min of heating.

2.2. Plant material

The whole plant *U. crinita* was collected in the Phu Tho province, Vietnam, in May 2019. The botanical identification

*Corresponding author: Email: nttam76@yahoo.com

was made by D.H. Thu, Institute of Ecology and Biological Resources, Vietnam Academy of Science and Technology (VAST). A voucher specimen (UC05/2019) was deposited at the Laboratory of Natural Products Research, Institute of Chemistry, VAST, Hanoi, Vietnam.

2.3. Extraction and isolation

The dried whole plant *U. crinita* (12 kg) was ground and extraction was performed three times with methanol-water (95:5, v/v) at room temperature. The extracted solution was concentrated under reduced pressure in a rotary evaporator at 45°C to remove the methanol. The obtained crude extract was suspended in water and successively partitioned with n-hexane, ethyl acetate, and n-butanol, respectively. The organic solvents were evaporated to yield extracts of 138.6, 81.2, and 117.3 g, respectively.

The n-butanol extract (115 g) was subjected to silica gel chromatography eluted with a CH_2Cl_2-MeOH-H_2O system (from 10:0:0 to 7:3:1, v/v) to give 10 fractions. Fraction 3 was repeatedly chromatographed on a silica gel column (CH_2Cl_2-MeOH-H_2O, 4:1:0.1, v/v) and then on a Sephadex LH-20 column (MeOH) to give compounds **1** (6 mg) and **2** (4 mg). Fraction 6 was purified on a silica gel column (CH_2Cl_2-MeOH-H_2O, 3:1:0.1, v/v) and then on an Rp-18 column (MeOH-H_2O, 2.5:2, v/v) to yield compound **3** (7 mg). Fraction 7 was measured using silica gel chromatography, eluted with CH_2Cl_2-MeOH-H_2O (3:1:0.1, v/v), and then on Sephadex LH-20 column (MeOH) to give compound **4** (4 mg).

Apigenin 7-*O*-*β*-glucoside (1):

Yellow solid. ^{1}H-NMR (500 MHz, DMSO-d_6): δ_H 12.96 (1H, s, 5-OH), 7.96 (2H, d, *J*=9.0 Hz, H-2′, H-6′), 6.94 (2H, d, *J*=9.0 Hz, H-3′, H-5′), 6.86 (1H, s, H-3), 6.83 (1H, d, *J*=1.5 Hz, H-8), 6.45 (1H, d, *J*=1.5 Hz, H-6), 5.39 (1H, br s, OH), 5.12 (1H, br s, OH), 5.06 (1H, d, *J*=7.0 Hz, H-1″), 5.06 (1H, br s, OH), 4.61 (1H, m, OH), 3.72 (1H, d, *J*=10.5 Hz, H-6a″), 3.49-3.17 (5H, m, H-2″-H-6b″). ^{13}C-NMR (125 MHz, CD_3OD): δ_C 182.03 (C-4), 164.25 (C-2), 162.96 (C-7), 161.35 (C-4′), 161.08 (C-5), 156.90 (C-9), 128.59 (C-2′, C-6′), 120.99 (C-1′), 115.98 (C-3′, C-5′), 105.33 (C-10), 103.11 (C-3), 99.88 (C-1″), 99.49 (C-6), 94.88 (C-8), 77.15 (C-5″), 76.44 (C-3″), 73.10 (C-2″), 69.58 (C-4″), 60.60 (C-6″). ESI-MS *m/z* 433.3 $[M + H]^+$, $C_{21}H_{20}O_{10}$. IR (KBr) ν_{max}: 3390 (O-H), 2923 (C-H), 1635 (C=O), 1600, 1510, 1462 (C=C), 1205, 1143 (C-O) cm^{-1}.

Chrysoeriol 7-*O*-*β*-glucoside (2):

Yellow solid. ^{1}H-NMR (500 MHz, DMSO-d_6): δ_H 12.96 (1H, s, 5-OH), 7.60 (1H, dd, *J*=8.5, 1.5 Hz, H-6′), 7.59 (1H, d, *J*=1.5 Hz, H-2′), 6.98 (1H, s, H-3), 6.95 (1H, d, *J*=8.5 Hz, H-5′), 6.86 (1H, d, *J*=2.0 Hz, H-8), 6.45 (1H, d, *J*=2.0 Hz, H-6), 5.39 (1H, br s, OH), 5.12 (1H, br s, OH), 5.06 (1H, d, *J*=7.0 Hz, H-1″), 5.06 (1H, br s, OH), 4.61 (1H, m, OH), 3.89 (3H, s, 3′-OCH_3), 3.72 (1H, d, *J*=10.5 Hz, H-6a″), 3.49-3.17 (5H, m, H-2″-H-6b″). ^{13}C-NMR (125 MHz, CD_3OD): δ_C 182.03 (C-4), 164.14 (C-2), 162.96 (C-7), 161.08 (C-5), 156.90 (C-9), 150.93 (C-4′), 148.04 (C-3′), 121.31 (C-1′), 120.49 (C-6′), 115.76 (C-5′), 110.30 (C-2′), 105.33 (C-10), 103.43 (C-3), 99.99 (C-1″), 99.49 (C-6), 95.01 (C-8), 77.23 (C-5″), 76.44 (C-3″), 73.10 (C-2″), 69.58 (C-4″), 60.60 (C-6″), 55.96 (3′-OCH_3). ESI-MS *m/z* 463.4 $[M + H]^+$, $C_{22}H_{22}O_{11}$. IR (KBr) ν_{max}: 3405 (O-H), 2906 (C-H), 1648 (C=O), 1612, 1506, 1453 (C=C), 1185, 1126, 1087 (C-O) cm^{-1}.

Rhoifolin (3):

White solid. ^{1}H-NMR (500 MHz, CD_3OD): δ_H 7.90 (2H, d, *J*=9.0 Hz, H-2′, H-6′), 6.96 (2H, d, *J*=9.0 Hz, H-3′, H-5′), 6.81 (1H, d, *J* = 2.0 Hz, H-8), 6.68 (1H, s, H-3), 6.48 (1H, d, *J*=2.0 Hz, H-6), 5.31 (1H, d, *J*=2.0 Hz, H-1‴), 5.22 (1H, d, *J*=8.0 Hz, H-1″), 3.97-3.41 (C<u>H</u>-OH, C<u>H$_2$</u>-OH sugar), 1.35 (1H, d, *J*=6.0 Hz, H-6‴). ^{13}C-NMR (125 MHz, CD_3OD): δ_C 184.06 (C-4), 166.82 (C-2), 164.43 (C-7), 162.96 (C-4′, C-5), 159.01 (C-9), 129.65 (C-2′, C-6′), 123.07 (C-1′), 117.08 (C-3′, C-5′), 107.14 (C-10), 104.15 (C-3), 102.54 (C-1‴), 101.08 (C-6), 99.94 (C-1″), 95.95 (C-8), 79.11 (C-2″), 79.02 (C-5″), 78.36 (C-3″), 73.96 (C-4‴), 72.22 (C-4″, C-3‴), 71.41 (C-2‴), 70.02 (C-5‴), 62.44 (C-6″), 18.23 (C-6‴). ESI-MS *m/z* 579.2 $[M + H]^+$, $C_{27}H_{30}O_{14}$. IR (KBr) ν_{max}: 3458 (O-H), 2908 (C-H), 1653(C=O), 1600, 1452 (C=C), 1210, 1148 (C-O) cm^{-1}.

3′-Methoxyapiin (4):

Yellow solid. ^{1}H-NMR (500 MHz, CD_3OD): δ_H 7.56 (1H, d, *J*=8.5 Hz, H-6′), 7.52 (1H, s, H-2′), 6.95 (1H, d, *J*=8.5, H-5′), 6.83 (1H, brs, H-8), 6.69 (1H, H-3), 6.48 (1H, d, *J*=1.5 Hz, H-6), 5.48 (1H, d, *J*=1.5 Hz, H-1‴), 5.17 (1H, d, *J*=7.5 Hz, H-1″), 4.07-3.41 (C<u>H</u>-OH, C<u>H$_2$</u>-OH sugar). ^{13}C-NMR (125 MHz, CD_3OD): δ_C 184.05 (C-4), 166.67 (C-2), 164.66 (C-7), 162.91 (C-5), 158.98 (C-9), 152.36 (C-4′), 149.55 (C-3′), 123.51 (C-1′), 122.00 (C-6′), 116.83 (C-5′), 110.94 (C-1‴), 110.83 (C-2′), 107.11 (C-10), 104.50 (C-3), 101.07 (C-6), 100.29 (C-1″), 96.11 (C-8), 80.71 (C-3‴), 78.82 (C-2″), 78.46 (C-3″), 78.36 (C-5″), 78.19 (C-2‴), 75.45 (C-4‴), 71.34 (C-4″), 65.91 (C-5‴), 62.49 (C-6″), 56.75 (O<u>CH$_3$</u>). ESI-MS *m/z* 595.4 $[M + H]^+$, $C_{27}H_{30}O_{15}$. IR (KBr) ν_{max}: 3445 (O-H), 2895 (C-H), 1640 (C=O), 1585, 1426 (C=C), 1175, 1050 (C-O) cm^{-1}.

3. Results and discussion

Compound **1** was assigned to have a molecular formula of $C_{21}H_{20}O_{10}$ by a combination of its NMR data and ESI-MS *pseudo*-molecular ion peak at *m*/z 433.3 $[M+H]^+$. The

presence of intramolecularly hydrogen-bonded proton signal [δ_H 12.96 (1H, s)] suggested that this hydroxyl group was at C-5. The ^{1}H-NMR spectrum showed signals due to a *para*-disubstituted B-ring [δ_H 7.96 (2H, d, *J*=9.0 Hz, H-2′, H-6′), 6.94 (2H, d, *J*=9.0 Hz, H-3′, H-5′)], a *meta*-disubstituted A-ring [δ_H 6.83 (1H, d, *J*=1.5 Hz, H-8), 6.45 (1H, d, *J*=1.5 Hz, H-6)], and a one-proton singlet of the C-ring [δ_H 6.86 (1H, s, H-3)] on the flavone skeleton. In addition, signals of a glucopyranosyl unit [δ_H 5.06 (1H, d, *J*=7.0 Hz, H-1″), and 3.72-3.17 (6H, m, H-2″, H-3″, H-4″, H-5″, H-6″)] were also observed. The large coupling constant (*J*=7.0 Hz) of the anomeric proton indicated the *β*-configuration of the glucopyranosyl moiety [9]. The ^{13}C-NMR and heteronuclear single quantum coherence (HSQC) spectra revealed 15 carbon signals due to a flavone skeleton comprising one carbonyl carbon, seven sp^2 methine, and seven sp^2 quaternary carbons; in addition to six carbon signals due to a glucopyranosyl moiety. The heteronuclear multiple bond correlation (HMBC) from the anomeric proton H-1″ (δ_H 5.06) and two protons H-6 (δ_H 6.45) and H-8 (δ_H 6.83) to the carbon of A-ring at δ_C 162.96 confirmed that the glucosyl unit was at C-7. From the above spectral data, the structure of **1** was determined to be apigenin 7-*O*-*β*-glucoside. The ^{13}C-NMR data of **1** were in good agreement with those of apigenin 7-*O*-*β*-glucoside in the literature [10].

Compound **2** was isolated as a yellow solid. Its molecular formula was established as $C_{22}H_{22}O_{11}$ on the basis of an ion peak $[M + H]^+$ at *m/z* 463.4 in ESI-MS. ^{1}H- and ^{13}C-NMR spectral data of compound **2** were similar with those of **1** except for the presence of three aromatic protons of an ABX spin system of ring B at δ_H 7.60 (1H, dd, *J*=8.5, 1.5 Hz, H-6′), 7.59 (1H, d, *J*=1.5 Hz, H-2′), and 6.95 (1H, d, *J*=8.5 Hz, H-5′); and an additional methoxyl group at δ_H 3.89 (3H, s). The position of the methoxyl group was at C-3′ based on the nuclear Overhauser effect spectroscopy (NOESY) correlations of H-2′ (δ_H 7.59) with 3′-OCH$_3$ (δ_H 3.89) and the HMBC correlations between the protons of 3′-OCH$_3$ (δ_H 3.89), H-2′ (δ_H 7.59), H-6′ (δ_H 7.60), and carbon C-3′ (δ_C 148.04). Moreover, the carbon chemical shifts of C-1′-C-6′ in **2** were very similar to those reported for chrysoeriol [11]. On the basis of the above evidence, the structure of **2** was elucidated to be chrysoeriol 7-*O*-*β*-glucoside [12].

The ^{13}C-NMR and HSQC spectra of **3** confirmed the presence of 27 carbons that were attributed to 15 carbons of a flavone skeleton and 12 carbons of two sugar residues. The ^{1}H-NMR spectrum showed resonance for two *meta*-coupled aromatic protons at δ_H 6.81 (1H, d, *J*=2.0 Hz, H-8) and 6.48 (1H, d, *J*=2.0 Hz, H-6); four *ortho*-coupled aromatic protons of an AA′BB′ spin system at δ_H 7.90 (2H, d, *J*=9.0 Hz, H-2′, H-6′) and 6.96 (2H, d, *J*=9.0 Hz, H-3′, H-5′); and a one-proton singlet at δ_H 6.68 (1H, s, H-3). Thus, the flavonoid moiety of **3** was determined as apigenin. In addition, a series of sugar signals at *δ* 3.97-3.41, along with two signals at δ_H 5.31 (1H, d, *J*=2.0 Hz, H-1‴) and 5.22 (1H, d, *J*=8.0 Hz, H-1″) corresponding to anomeric protons of two sugar residues, were also observed in the ^{1}H-NMR spectrum. The coupling constants (*J*=8.0 Hz and 2.0 Hz) of the anomeric protons indicated the *β*- and *α*-configurations for glucopyranosyl and rhamnopyranosyl, respectively [9, 13]. The HMBC correlation from the anomeric proton H-1″ of glucose to C-7 (δ_C 164.43), H-1‴ (δ_H 5.31) with the carbon C-2″ (δ_C 79.11), and H-2″ (δ_H 3.74) with the carbon C-1‴ (δ_C 102.54) indicated 7-*O*-glycosidation and the interglycosidic linkage in **3** as -*O*-*α*-rhamnopyranosyl(1→2)-*O*-*β*-glucopyranoside. On the basis of the above evidence, the structure of **3** was assigned to be rhoifolin [14].

Compound **4** was obtained as a yellow solid. Its molecular formula was established as $C_{27}H_{30}O_{15}$ on the basis of an ion peak $[M+H]^+$ at *m/z* 595.4 in ESI-MS. The ^{1}H- and ^{13}C-NMR spectra of **4** were similar to those of **2** except for the appearance of an additional *α*-arabinofuranosyl moiety [δ_H 5.48 (1H, d, *J*=1.5 Hz, H-1‴); δ_C 110.94 (C-1‴), 80.71 (C-3‴), 78.19 (C-2‴), 75.45 (C-4‴), 65.91 (C-5‴)]. The *α*-arabinofuranosyl moiety was attached to C-2″ of glucopyranosyl based on the HMBC correlations between the anomeric proton H-1‴ (δ_H 5.48) and carbon C-2″ (δ_C 78.82) and between proton H-2″ (δ_H 3.69) and carbon C-1‴ (δ_C 110.94). Based on the evidence above and in comparison with those reported in the literature [15], compound **4** was determined to be 3′-methoxyapiin (Fig. 1).

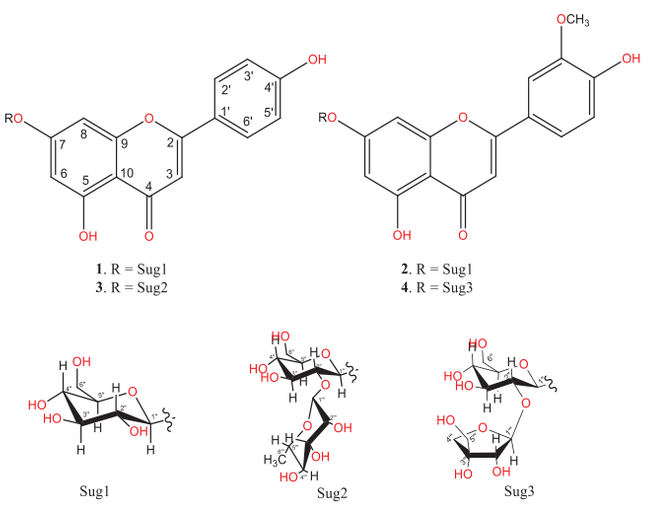

Fig. 1. Structure of compounds 1-4.

4. Conclusions

From the n-butanol extract of the whole plant *U. crinita*, using column chromatography, four flavone glycosides including apigenin 7-*O*-β-glucoside (**1**), chrysoeriol 7-*O*-β-glucoside (**2**), rhoifolin (**3**), and 3′-methoxyapiin (**4**) were isolated. The structures of compounds **1-4** were determined by spectroscopic methods and comparison with published data. This is the first report of these compounds from the genus *Uraria*.

CRediT author statement

Tran Duc Dai: Conceptualisation, Methodology, Software, Resources, Writing - Review and Editing; Dao Duc Thien: Data curation, Software, Writing - Original draft preparation; Nguyen Thanh Tam: Supervision, Software, Validation.

ACKNOWLEDGEMENTS

This work was financially supported by the National Foundation for Science & Technology Development (NAFOSTED) of Vietnam (code: 104.01-2016.41). The authors are grateful to Assoc. Prof. Do Huu Thu, Institute of Ecology and Biological Resources, Vietnam Academy of Science and Technology for identification of plant samples.

COMPETING INTERESTS

The authors declare that there is no conflict of interest regarding the publication of this article.

REFERENCES

[1] P.H. Ho (2000), *An Illustrated Flora of Vietnam*, Youth Publishing House, Ho Chi Minh City, **1**, pp.930-933, (in Vietnamese).

[2] G.C. Yen, H.H. Lai, H.H. Chou (2001), "Nitric oxidescavenging and antioxidant effects of *Uraria crinita* root", *Food Chemistry*, **74(4)**, pp.471-478, DOI: 10.1016/S0308-8146(01)00165-0.

[3] Y.W. Mao, R.D. Lin, H.C. Hung, et al. (2014), "Stimulation of osteogenic activity in human osteoblast cells by edible *Uraria crinita*", *Journal of Agricultural and Food Chemistry*, **62(24)**, pp.5581-5588, DOI: 10.1021/jf5012177.

[4] N. Morita, M. Arisawa, M. Nagase, et al. (1977), "Studies on the constituents of Formosan Leguminosae. II. The constituents in the leaves of *Uraria crinita* Desv.", *Journal of The Pharmaceutical Society Japan*, **97(6)**, pp.701-703, DOI: 10.1248/yakushi1947.97.6_701.

[5] Y. Wang, X. Zhang, L. Gong, et al. (2009), "Studies on chemical constituents in roots of *Uraria crinita*", *Chinese Pharmaceutical Journal*, **44**, pp.1217-1220.

[6] M. Okawa, R. Akahoshi, K. Kawasaki, et al. (2019), "Two new triterpene glycosides in the roots of *Uraria crinita*", *Chemical and Pharmaceutical Bulletin*, **67(2)**, pp.159-162, DOI: 10.1248/cpb.c18-00753.

[7] D.D. Thien, T.T. Thuy, N.T.H. Anh, et al. (2019), "A new isoflavanone from *Uraria crinita*", *Natural Product Reseach*, **35(13)**, pp.2211-2217, DOI: 10.1080/14786419.2019.1667352.

[8] D.D. Thien, B.H. Tai, T.D. Dai, et al. (2020), "New phenolics from *Uraria crinita* (L.) DC.", *Natural Product Reseach*, **36(13)**, pp.3381-3388, DOI: 10.1080/14786419.2020.1860973.

[9] S.K. Hyun, S.S. Kang, K.H. Son, et al. (2005), "Biflavone glucosides from *Ginkgo biloba* yellow leaves", *Chemical and Pharmaceutical Bulletin*, **53(3)**, pp.1200-1201, DOI: 10.1248/cpb.53.1200.

[10] P.M. Giang, P.T. Son (2004), "Apigenin 7-*O*-*β*-glucoside from the leaves of *Acanthus integrifolius* T. Anders., Acanthaceae", *Vietnam Journal of Chemistry*, **42(4)**, pp.496-498.

[11] H. Wagner, V. M. Chari (1976), "^{13}C-NMR-spektren naturlich vorkommender flavonoide", *Tetrahedron Letters*, **17(21)**, pp.1799-1802, DOI: 10.1016/S0040-4039(00)93787-0.

[12] C.M.N. Ngaffo, R.S.V Tchangna, A.T. Mbaveng, et al. (2020), "Botanicals from the leaves of *Acacia sieberiana* had better cytotoxic effects than isolated phytochemicals towards MDR cancer cells lines", *Heliyon*, **6(11)**, DOI: 10.1016/j.heliyon.2020.e05412.

[13] A.L. Piccinelli, A. Veneziano, S. Passi, et al. (2007), "Flavonol glycosides from whole cottonseed byproduct", *Food Chemistry*, **100(1)**, pp.344-349, DOI: 10.1016/j.foodchem.2005.09.053.

[14] E.J. Lee, J.S. Kim, H.P Kim, et al. (2010), "Phenolic constituents from the flower buds of *Lonicera japonica* and their 5-lipoxygenase inhibitory activities", *Food Chemistry*, **120(1)**, pp.134-139, DOI: 10.1016/j.foodchem.2009.09.088.

[15] V.K. Thu, N.T.K. Thoa, P.V. Kiem (2016), "Flavonoid glycosides from *Viscum album*", *Vietnam Journal of Chemistry*, **54(4)**, pp.443-447, DOI: 10.15625/0866-7144.2016-00344.

DOI: 10.31276/VJSTE.63(2).07-12

Investigation of the removal of Ni(II) from aqueous solution using pomelo fruit peel

Van Phuc Dinh*

Duy Tan University, 254 Nguyen Van Linh Street, Thac Gian Ward, Thanh Khe District, Da Nang City, Vietnam

Received 8 September 2020; revised 28 November 2020; accepted 4 December 2020

Abstract:

The growth of numerous industries has helped many developing nations' economies significantly in recent years. However, the governments of these nations face serious environmental issues, particularly those involving the polluting of industrial zones' effluent with heavy hazardous metals. Pomelo fruit peel, an organic waste, was utilised as a biosorbent to remove Ni(II) from aqueous solutions. Some major factors influencing Ni(II) uptake such as pH, adsorption time, and initial Ni(II) concentration were examined. Several isotherm and kinetic models including the Langmuir, Freundlich, Sips, pseudo-first-order, pseudo-second- order, and intra-diffusion models were fit to the experimental data. The Ni(II) adsorption onto pomelo fruit peel was investigated. Kinetic studies showed that the Ni(II) uptake was controlled by various mechanisms. Results showed that the Ni(II) uptake obtained an equilibrium at pH=6 after 80 min at 303 K. The Sips isotherm model described the Ni(II) adsorption better than other models and the monoadsorption capacity calculated from the Langmuir model was 9.67 mg/g. The adsorption of Ni(II) followed pseudo-second-order kinetic models with three stages.

Keywords: **biosorption, isotherm models, Ni(II), pomelo fruit peel.**

Classification number: **2.2**

1. Introduction

In recent years, the expansion of many industries has promote a huge increase in the economy of a large number of developing countries. However, the governments in these countries are faced with significant environmental problems especially those related to heavy toxic metal pollution in the effluent of industrial zones. Ni(II) is one such heavy toxic metal, which has existed in the wastewater of many factories such as electroplating, mineral processing, batteries manufacturing, and so on [1, 2]. As claimed by the World Health Organization (WHO), the limit of Ni(II) concentration in water is 0.005 kg/m^3 [2]. Hence, various physicochemical methods have been applied to eliminate Ni(II) from aqueous solutions including adsorption [1-4], precipitation [5, 6], ion-exchange [7, 8] and so on. Among them, adsorption is a promising method since it is simple, low-cost, and easily reused [9, 10].

The use of agricultural waste as biosorbents has attracted many scientists because they are abundantly available, environmentally friendly, and low cost. There are many biosorbents used to remove Ni(II) from aqueous solutions including *Sophora japonica* pod powder [11], *Sargassum* sp. [12], activated banana peel [13], modified plantain peel [14], and Citrus reticulata (fruit peel of orange) [15]. However, the utilisation of pomelo fruit peel (Citrus grandis) as a biosorbent to remove Ni(II) from aqueous solutions has been limited. In previous reports, the pomelo fruit peel was used to adsorb methylene blue [16], Cr(III) [16], Pb(II) [17], and Cd(II) [17]. The obtained results indicated that the pomelo fruit peel is a potential biosorbent to uptake heavy toxic metals and organic molecules from aqueous solutions. Therefore, in this work, the study is extended to Ni(II) adsorption onto the pomelo fruit peel. The $pH_{solution}$, adsorption time, and initial Ni(II) concentration, all of which affect the Ni(II) adsorption, are examined. Some common isotherm and kinetic models are fit to the experimental data to understand the nature of the uptake.

2. Materials and methods

2.1. Preparation of biosorbent

The biosorbent was prepared identical to the author's previous studies [17]. Herein, the pomelo fruit peel was washed by deionised water several times after collection from the Vinh Cuu district, Dong Nai province, Vietnam. The material was then dried in an oven at 80^{o}C within 24 h, prior to cutting into small pieces about 0.5-1 mm in size. Finally, the biosorbent was stored in the oven.

*Email: dinhvanphuc@duytan.edu.vn

2.2. Chemicals

The Ni (II) ion was used as an adsorbate, which was prepared by dissolving a Ni(II) standard (1000 mg/l) in deionised (DI) water. The pH adjustment of the investigated solution was carried by using HNO_3 and NaOH with different concentrations. All experimental chemicals used in this work were from Merck (Germany) and were in the analytical reagent grade.

2.3. Instruments

The pH meter (Martini instruments, Mi-15, Romania), with buffer solution values of 4.01±0.01, 7.01±0.01, and 10.01±0.01, was used to determine the $pH_{solution}$ values. The material's morphology was examined by ultrahigh resolution SEM (S-4800), whereas the bonding in the materials' structure was found out by Fourier-transform infrared (FT-IR) spectroscopy that was conducted on a Tensor 27 (Bruker, Germany).

In order to determine the Ni(II) concentration before and after the uptake, an atomic absorption spectrophotometer (Shimadzu AA-7000, Japan) was used.

2.4. Batch adsorption study

The Ni(II) batch adsorption onto the pomelo fruit peel was carried on IKA magnetic stirrers with a RT 10 P heater. Herein, 0.1 g of the synthesised material was placed into 100 ml flasks together with 50 ml of Ni(II) aqueous solution. These flasks were stirred at a constant rate of 150 rpm. The factors affecting the uptake including pH (2-6), adsorption time (10-240 min), and Ni(II) initial concentration (5-50 mg/l) were examined.

The percentage of the Ni(II) uptake (% removal) and adsorption capacity, Q_e, (mg/g) were determined based on the following equations:

$$\% \text{ Removal} = \frac{(C_o - C_e)}{C_o}.100\% \quad (1)$$

$$Q_e = \frac{(C_o - C_e).V}{m} \quad (2)$$

where the Ni(II) concentration in the aqueous solution before and after the adsorption are symbolised C_o (mg/l) and C_e (mg/l), respectively, V is the volume (l) of metal solution, and m is the mass (g) of the material used.

2.5. Adsorption isotherm and kinetic models

In this report, some common adsorption isotherm and kinetic models are fit to the experimental data [17, 18]. These models are given in Table 1.

Table 1. Some common nonlinear isotherm and kinetic models.

Models	Nonlinear forms	Nomenclature
Isotherm models		
Langmuir	$Q_e = \frac{Q_m.K_L.C_e}{1+K_L.C_e}$	Q_e (mg/g): amount of adsorbate in the adsorbent at equilibrium. Q_m (mg/g): maximum monolayer adsorption capacity. K_L (l/mg): Langmuir isotherm constant. K_F [(mg/g).(l/mg)$^{1/n}$]: Freundlich isotherm constant. *n:* heterogeneity factor. Q_s (l/g): Sips isotherm model constant. α_s (l/mg): Sips isotherm model constant. β_s: Sips isotherm model exponent.
Freundlich	$Q_e = K_F.C_e^{1/n}$	
Sips	$Q_e = \frac{Q_s.C_e^{\beta_s}}{1+\alpha_s.C_e^{\beta_s}}$	
Kinetic models		
Pseudo-first-order	$Q_t = Q_e\left(1-e^{-k_1 t}\right)$	Q_t (mg/g): adsorption capacity at time *t*. Q_e (mg/g): adsorption capacity at the equilibrium. k_1 (min^{-1}): pseudo-first-order model constant. k_2 (g.mg^{-1}.min^{-1}): pseudo-second-order model constant. k_d: intra-diffusion models constant.
Pseudo-second-order	$Q_t = \frac{Q_e^2.k_2.t}{1+k_2.Q_e.t}$	
Intra-diffusion	$Q_t = k_d t^{1/2} + C$	

3. Results and discussion

3.1. Characterisations of the biosorbent

SEM - EDX analyses: Figs. 1A and 1B show SEM images of pomelo fruit peel at 1.00k and 10.0k magnifications. As seen in these images, the adsorbent surface is very rough, porous, and heterogeneous. These properties are favourable for the heavy metal ion adsorption. The elemental composition of this material was determined by energy-dispersive X-ray spectroscopy (EDX), which is presented in Fig. 1C. The results confirm that the weight percentages of carbon and oxygen were 47.41 and 52.59%, respectively.

Point of zero charge (pH_{PZC}): pH_{PZC} is the pH value of the solution when the material's surface charge is neutral. Indeed, if $pH_{solution}$ is less than pH_{PZC}, the material surface is positively charged. In contrast, the material's surface charge is negative when $pH_{solution} > pH_{PZC}$. Fig. 1D presents the pH_{PZC} of the pomelo fruit peel in this study, which was determined to be 4.6.

FT-IR spectrum: Fig. 2 depicts the vibrations of characteristic groups in the pomelo fruit peel. As seen in this figure, the vibrations of the O-H groups of pectin, cellulose, and lignin are recorded at 3246 cm^{-1}, while the vibrations of the C-H bonds in the CH_2 and CH_3 groups are assigned to wavenumbers 2924 cm^{-1} and 2851 cm^{-1}, respectively. The wavenumbers 1747 cm^{-1} and 1643 cm^{-1} are related to the C=O groups [19]. Finally, the wavenumbers 1107 cm^{-1} and 1026 cm^{-1} confirm the C-O group's stretching vibrations in the lignin structure of pomelo fruit peel [16].

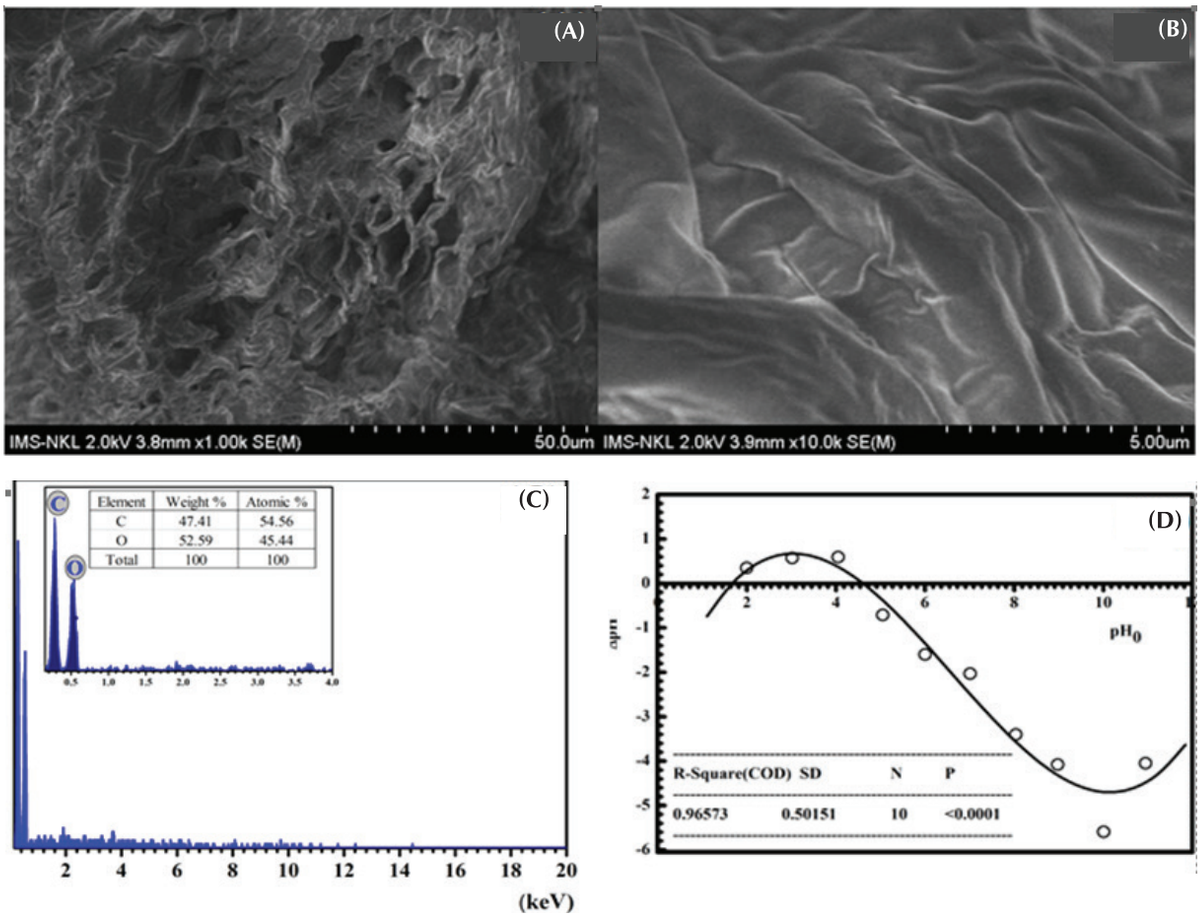

Fig. 1. (A, B) SEM images at different magnifications, (C) the EDX spectrum, and (D) pH_{PZC} of the pomelo fruit peel.

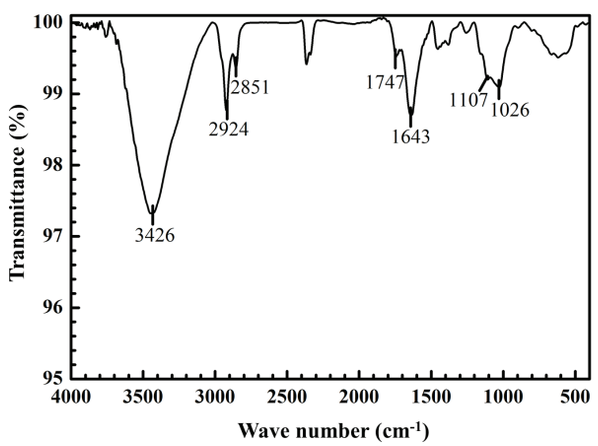

Fig. 2. FT-IR spectrum of pomelo fruit peel.

3.2. Factors affecting the removal of Ni(II)

$pH_{solution}$: $pH_{solution}$ directly affects the removal of Ni(II) due to its effects on the formation of different complexes of Ni(II) and the surface charge of materials. Fig. 3A indicates that the uptake of Ni(II) rises rapidly when $pH_{solution}$ is increased from 2 to 4. In the next stage, there is a slight increase in the adsorption prior to obtaining the maximum at pH=6. The increase in $pH_{solution}$ from 2 to 6 leads to a change in material surface charge from positive to negative. At $pH_{solution}$>pH_{PZC}=4.6, the material's surface charge is negative, which leads to a rise in Ni(II) adsorption due to the electrostatic attraction between Ni(II) cations and the negatively-charged material surface [20, 21]. However, the author observed that nickel (II) hydroxide can be formed at $pH_{solution}$>6. Therefore, pH=6 is chosen for further experiments.

The adsorption time: The influence of the adsorption time on the Ni(II) biosorption by pomelo fruit peel is indicated in Fig. 3B. The uptake rate of Ni(II) significantly increases prior to reaching equilibrium at 80 min and then remained stable. Therefore, the optimal adsorption time was determined to be 80 min.

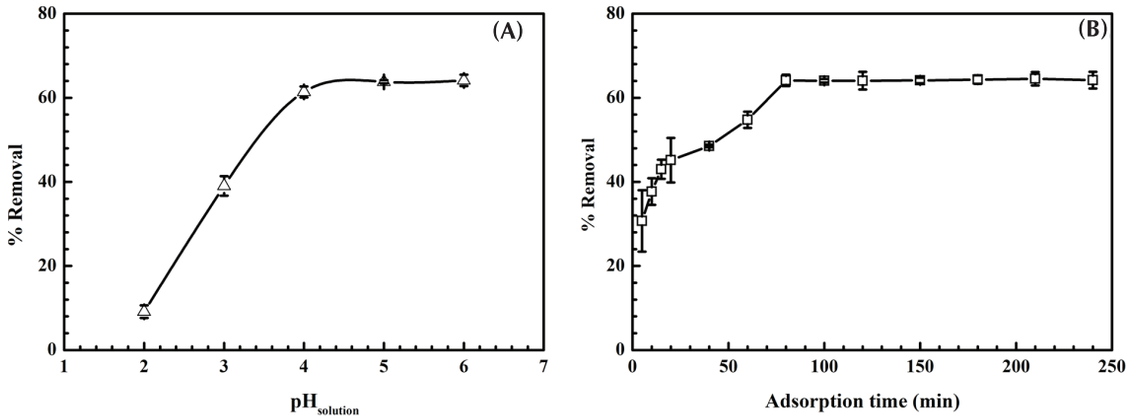

Fig. 3. Plots of the effects of (A) $pH_{solution}$ and (B) adsorption time on Ni(II) adsorption.

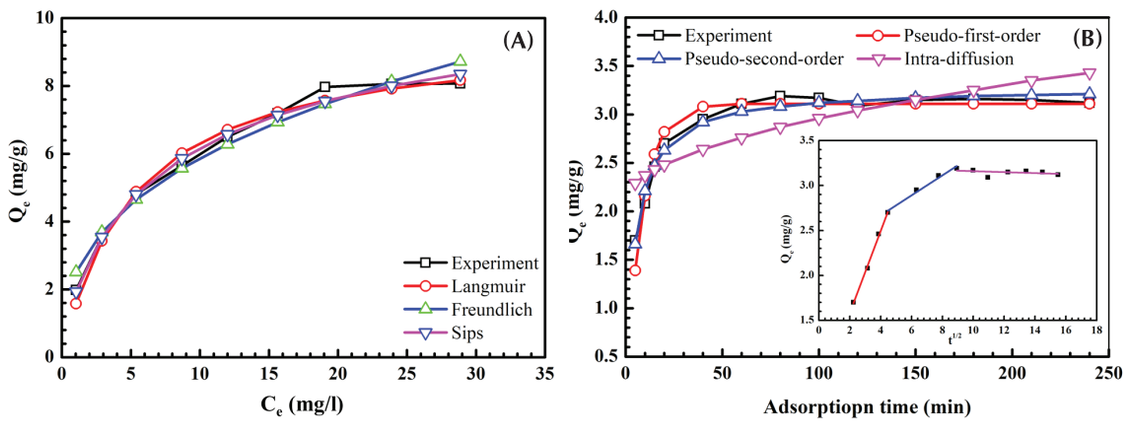

Fig. 4. Plots of (A) isotherm models and (B) kinetic models of the Ni(II) adsorption onto pomelo fruit peel.

3.3. Isotherm studies

The plots of several common isotherm models including Langmuir, Freundlich, and the Sips models are presented in Fig. 4A. The nonlinear isotherm parameters of these models are listed in Table 2. According to calculated RMSE and χ^2 values, the experimental data had a better fit with the Sips model than the others as determined by the smallest RMSE and χ^2 values. The main reason is that the Langmuir and Freundlich models are constrained by the adsorbates' concentration, while the Sips model combines these models and overcomes this problem [18]. Furthermore, the Langmuir maximum monolayer adsorption capacity was 9.67 mg/g, which is higher than other biosorbents such as hazelnut shell, fly ash, rice husk, banana peel, and doum palm (Hyphaene thebaica L.) (Table 3). The n value (n=2.67) evaluated from the Freundlich model ranges from 1 to 10 and indicates how favourable conditions are for adsorption [18, 22]. However, the Ni(II) adsorption capacity is lower than Pb(II), Cd(II), and Cr(III) when the same pomelo fruit peel is used [16, 17]. This shows that the pomelo fruit peel is a potential material for removing heavy metals from aqueous solutions.

Table 2. Parameters of nonlinear isotherm models at temperature of 303 K.

Isotherm models	Parameters	
Langmuir	K_L (l/mg)	0.1891
	Q_m (mg/g)	9.67
	RMSE	0.2625
	R^2	0.9854
	χ^2	0.1413
Freundlich	n	2.67
	K_F [(mg/g).(l/mg)$^{1/n}$]	2.48
	RMSE	0.3752
	R^2	0.9701
	χ^2	0.2519
Sips	Q_s (l/g)	2.25
	α_s (l/mg)	0.1938
	β_s	0.7667
	RMSE	0.1975
	R^2	0.9917
	χ^2	0.0428

Table 3. Maximum adsorption capacities of several biosorbents for the Ni(II) uptake from aqueous solutions [23-27].

Biosorbents	Adsorptive condition	Adsorption capacity (mg/g)	References
Doum palm (Hyphaene thebaica L.)	pH=7.00, t=120 min	3.24	[1]
Banana peel	pH=6.89, t=24 h	6.88	[23]
Rice husk	pH=6.00, t=120 min	8.86	[24]
Fly ash	pH=8.00, t=60 min	0.03	[25]
Hazelnut shell	pH=7.00, t=180 min	7.18	[26]
Cone biomass of Thuja orientalis	pH=4.00, t=7 min	12.42	[27]
Brown algae *Sargassum* sp.	pH=6.00, t=90 min	50.97	[12]
Pomelo fruit peel	pH=6.00, t=80 min	9.67	This study

3.4. Kinetic studies

Figure 4B and Table 4 present the plots of the kinetic models and non-linear parameters, respectively. Clearly, the pseudo-second-model fit to the experimental data is better than the pseudo-first-order model owing to the small RMSE and χ^2 values. However, both models cannot describe the mass transfer of cations onto the material's surface. The intra-diffusion model is therefore applied to determine the Ni(II) adsorption kinetic onto pomelo fruit peel. As seen from the plot of Q_e versus $t^{1/2}$ in Fig. 4B, the removal of Ni(II) includes three stages. Firstly, Ni(II) cations are steeply transferred from the solution to the material's surface within about 20 min. In the next stage, the Ni(II) uptake more gradually occurs from 20 to 80 min, prior to obtaining the equilibrium in the last stage. From the nonzero C value calculated from the intra-diffusion model, the Ni(II) uptake follows not only the intra-diffusion process but also two or more different mechanisms [28, 29].

Table 4. Parameters of nonlinear kinetic models at 303 K.

Kinetic models	Parameters	
	C_o (mg/l)	10
	$Q_{e\,(exp)}$ (mg/g)	3.2
Pseudo-first-order model	$Q_{e\,(cal)}$ (mg/g)	3.11
	k_1(min^{-1})	0.1190
	RMSE	0.1185
	R^2	0.9395
	χ^2	0.0831
Pseudo-second-order model	$Q_{e\,(cal)}$ (mg/g)	3.27
	k_2 (g.mg^{-1}.min^{-1})	0.0633
	RMSE	0.0678
	R^2	0.9802
	χ^2	0.0208
Intra-diffusion model	k_d	0.0865
	C	2.0945
	RMSE	0.2858
	R^2	0.6480
	χ^2	0.4217

Conclusions

The Ni(II) adsorption onto pomelo fruit peel was investigated. The results showed that the Ni(II) uptake reached equilibrium at pH=6.00 after 80 min at 303 K. Kinetic studies showed that the Ni(II) uptake was controlled by various mechanisms. The Langmuir maximum adsorption capacity was 9.67 mg/g, which was higher than some other biosorbents. Therefore, pomelo fruit peel can be used as a promising, eco-friendly, and low-cost material to eliminate Ni(II) from the effluent.

ACKNOWLEDGEMENTS

This research is funded by Vietnam National Foundation for Science and Technology Development (NAFOSTED) under grant number 103.02-2018.368.

COMPETING INTERESTS

The author declares that there is no conflict of interest regarding the publication of this article.

REFERENCES

[1] M.E. Sadaawy, O. Abdelwahab (2014), "Adsorptive removal of nickel from aqueous solutions by activated carbons from doum seed *(Hyphaenethebaica)* coat", *Alexandria Engineering Journal*, **53(2)**, pp.399-408, DOI: 10.1016/j.aej.2014.03.014.

[2] H. Pahlavanzadeh, M. Motamedi (2020), "Adsorption of nickel, Ni(II), in aqueous solution by modified zeolite as a cationexchange adsorbent", *Journal of Chemical and Engineering Data*, **65(1)**, pp.185-197, DOI: 10.1021/acs.jced.9b00868.

[3] S. Ghrab, S. Mefteh, M. Medhioub, et al. (2018), "Adsorption of nickel(II) and chromium(III) from aqueous phases on raw smectite: Kinetic and thermodynamic studies", *Arabian Journal of Geosciences*, **11**, DOI: 10.1007/s12517-018-3749-2.

[4] K. Kadirvelu, K. Thamaraiselvi, C. Namasivayam (2001), "Adsorption of nickel(II) from aqueous solution onto activated carbon prepared from coirpith", *Separation and Purification Technology*, **24(3)**, pp.497-505, DOI: 10.1016/S1383-5866(01)00149-6.

[5] S. Janyasuthiwong, E.R. Rene, G. Esposito, et al. (2015), "Effect of pH on Cu, Ni and Zn removal by biogenic sulfide precipitation in an inversed fluidized bed bioreactor", *Hydrometallurgy*, **158**, pp.94-100, DOI: 10.1016/j.hydromet.2015.10.009.

[6] J. Esalah, M.M. Husein (2008), "Removal of heavy metals from aqueous solutions by precipitation-filtration using novel organophosphorus ligands", *Separation Science and Technology*, **43(13)**, pp.3461-3475, DOI: 10.1080/01496390802219661.

[7] N.H. Shaidan, U. Eldemerdash, S. Awad (2012), "Removal of Ni(II) ions from aqueous solutions using fixed-bed ion exchange column technique", *Journal of the Taiwan Institute of Chemical Engineers*, **43(1)**, pp.40-45, DOI: 10.1016/j.jtice.2011.06.006.

[8] N.K. Amin, O. Abdelwahab, E.S.Z. El-Ashtoukhy (2015), "Removal of Cu(II) and Ni(II) by ion exchange resin in packed rotating cylinder", *Desalination and Water Treatment*, **55(1)**, pp.199-209, DOI: 10.1080/19443994.2014.913208.

[9] V.P. Dinh, M.D. Nguyen, Q.H. Nguyen, et al. (2020a), "Chitosan-MnO_2 nanocomposite for effective removal of Cr(VI) from aqueous solution", *Chemosphere*, **257**, DOI: 10.1016/j.chemosphere.2020.127147.

[10] E.N. Zare, M.M. Lakouraj, A. Ramezani (2015), "Effective adsorption of heavy metal cations by superparamagnetic poly (aniline-co-m-phenylenediamine)@Fe_3O_4 nanocomposite", *Advances in Polymer Technology*, **34(3)**, DOI: 10.1002/adv.21501.

[11] M.W. Amer, R.A. Ahmad, A.M. Awwad (2015), "Biosorption of Cu(II), Ni(II), Zn(II) and Pb(II) ions from aqueous solution by Sophora japonica pods powder", *International Journal of Industrial Chemistry*, **6(1)**, pp.67-75, DOI: 10.1007/s40090-014-0030-8.

[12] C.E.R. Barquilha, E.S. Cossich, C.R.G. Tavares , et al. (2019), "Biosorption of nickel(II) and copper(II) ions by *Sargassum* sp. in nature and alginate extraction products", *Bioresource Technology Reports*, **5**, pp.43-50, DOI: 10.1016/j.biteb.2018.11.011.

[13] Z. Liu, Y. Liu, L. Chen, et al. (2014), "Performance study of heavy metal ion adsorption onto microwave-activated banana peel", *Desalination and Water Treatment*, **52(37-39)**, pp.7117-7124, DOI: 10.1080/19443994.2013.841108.

[14] Z.N. Garba, N.I. Ugbaga, A.K. Abdullahi (2016), "Evaluation of optimum adsorption conditions for Ni(II) and Cd(II) removal from aqueous solution by modified plantain peels (MPP)", *Beni-Suef University Journal of Basic and Applied Sciences*, **5(2)**, pp.170-179, DOI: 10.1016/j.bjbas.2016.03.001.

[15] M. Ajmal, R.A. Rao, R. Ahmad, et al. (2000), "Adsorption studies on Citrus reticulata (fruit peel of orange): Removal and recovery of Ni(II) from electroplating wastewater", *Journal of Hazardous Materials*, **79(1)**, pp.117-131, DOI: 10.1016/s0304-3894(00)00234-x.

[16] V.P. Dinh, T.D.T. Huynh, H.M. Le, et al. (2019), "Insight into the adsorption mechanisms of methylene blue and chromium(III) from aqueous solution onto pomelo fruit peel", *RSC Advances*, **9(44)**, pp.25847-25860, DOI: 10.1039/c9ra04296b.

[17] V.P. Dinh, T.D. Xuan, N.Q. Hung, et al. (2020b), "Primary biosorption mechanism of lead (II) and cadmium (II) cations from aqueous solution by pomelo (*Citrus maxima*) fruit peels", *Environmental Science and Pollution Research*, **28(45)**, pp.63504-63515, DOI: 10.1007/s11356-020-10176-6.

[18] K.Y. Foo, B.H. Hameed (2010), "Insights into the modeling of adsorption isotherm systems", *Chemical Engineering Journal*, **156(1)**, pp.2-10, DOI: 10.1016/j.cej.2009.09.013.

[19] M.T. Mostaedi, M. Asadollahzadeh, A. Hemmati, et al. (2013), "Equilibrium, kinetic, and thermodynamic studies for biosorption of cadmium and nickel on grapefruit peel", *Journal of The Taiwan Institute of Chemical Engineers*, **44(2)**, pp.295-302, DOI: 10.1016/j.jtice.2012.11.001.

[20] A.M.C. Pena, J.G. Ibanez, R.V. Medrano (2012), "Determination of the point of zero charge for electrocoagulation precipitates from an iron anode", *Int. J. Electrochem. Sci.*, **7(7)**, pp.6142-6153, DOI: 10.1016/S1452-3981(23)19469-7.

[21] M. Singh, D.N. Thanh, P. Ulbrich, et al. (2010), "Synthesis, characterization and study of arsenate adsorption from aqueous solution by α-and δ-phase manganese dioxide nanoadsorbents", *Journal of Solid State Chemistry*, **183(12)**, pp.2979-2986, DOI: 10.1016/j.jssc.2010.09.023.

[22] H. Liu, F. Zhang, Z. Peng (2019), "Adsorption mechanism of Cr(VI) onto GO/PAMAMs composites", *Scientific Reports*, **9(1)**, DOI: 10.1038/s41598-019-40344-9.

[23] G. Annadurai, R.S. Juang, D.J. Lee (2003), "Adsorption of heavy metals from water using banana and orange peels", *Water Science and Technology*, **47(1)**, pp.185-190.

[24] M. Bansal, D. Singh, V.K. Garg, et al. (2009), "Use of agricultural waste for the removal of nickel ions from aqueous solutions: Equilibrium and kinetics studies", *International Journal of Civil and Environmental Engineering*, **3(3)**, pp.174-180.

[25] M. Rao, A.V. Parwate, A.G. Bhole (2002), "Removal of Cr^{6+} and Ni^{2+} from aqueous solution using bagasse and fly ash", *Waste Management*, **22(7)**, pp.821-830, DOI: 10.1016/s0956-053x(02)00011-9.

[26] E. Demirbaş, M. Kobya, S. Öncel, et al. (2002), "Removal of Ni(II) from aqueous solution by adsorption onto hazelnut shell activated carbon: Equilibrium studies", *Bioresource Technology*, **84(3)**, pp.291-293, DOI: 10.1016/S0960-8524(02)00052-4.

[27] E. Malkoc (2006), "Ni(II) removal from aqueous solutions using cone biomass of *Thuja orientalis*", *Journal of Hazardous Materials*, **137(2)**, pp.899-908, DOI: 10.1016/j.jhazmat.2006.03.004.

[28] S. Vasiliu, I. Bunia, S. Racovita, et al. (2011), "Adsorption of cefotaxime sodium salt on polymer coated ion exchange resin microparticles: Kinetics, equilibrium and thermodynamic studies", *Carbohyd. Polym.*, **85(2)**, pp.376-387, DOI: 10.1016/j.carbpol.2011.02.039.

[29] V.P. Dinh, N.C. Le, L.A. Tuyen, et al. (2018), "Insight into adsorption mechanism of lead(II) from aqueous solution by chitosan loaded MnO_2 nanoparticles", *Materials Chemistry and Physics*, **207**, pp.294-302, DOI: 10.1016/j.matchemphys.2017.12.071.

DOI: 10.31276/VJSTE.63(2).13-19

Synthesis and elaboration of modified comb type (maleic anhydride-α-tetradecene) copolymers for cold flow improvers of biodiesel

Mai Thi Tuyet Phan*, Boi Van Luu, Lan Ngoc Pham

University of Science, Vietnam National - University, Hanoi, 334 Nguyen Trai, Thanh Xuan Trung Ward, Thanh Xuan District, Hanoi, Vietnam

Received 12 November 2020; revised 12 March 2021; accepted 30 March 2021

Abstract:

The maleic anhydride-α-tetradecene copolymer (OMAC) with an approximate relative maleic anhydride to α-tetradecene composition ratio of 1:1.2 was synthesized by free radical copolymerization. The copolymers were modified by the esterification reaction between the anhydride groups and the OH- group of hexadecanol. Comb-type (-maleic acid cetyl ester-co-α-tetradecene-) copolymers (MCEC) with various ratios of alkyl group/carboxyl group (*r*) were investigated. Upon cooling, the MCEC changed the crystallization state of the wax crystals, and reduced the pour point of the biodiesel, which was observed by pour point and dynamic viscosity testing. The MCEC efficiency that improved the cold flow properties of the biodiesel was found to be correlated to *r*. MCEC with *r*=2.76 was found to be the most effective in improving the flow ability of the palm oil biodiesel. Our study demonstrates the ability of MCEC3 at 1000 ppm concentration to reduce the pour point of palm oil biodiesel to 10.5°C and the dynamic viscosity up to 1.04 mPa.s. A correlation was found between the number and the length of the pendant alkyl groups of additives and the compositions of the fatty acid methyl ester of the biodiesel.

Keywords: **biodiesel, cold flow property, comb type copolymer, flow-ability, wax crystals.**

Classification number: **2.2**

1. Introduction

Today, humans face an impending energy crisis as fossil fuel resources are being depleted and the environment is becoming seriously polluted. People are seeking solutions to overcome these problems by using new energy sources such as wind power, solar energy, biomass, etc. Biodiesel is a fuel produced from animal fats or vegetable oils. It can not only replace fossil energy but also contribute to the treatment of environmental pollution. It is well known that most of biodiesel fuel properties are equivalent to those of diesel, except for the ability to flow at low temperatures. So far, improving the flow ability of biodiesel remains a major challenge for use in diesel engines. To avoid a negative impact on edible oils in the food sector, countries around the world, including Vietnam, have developed a strategy to use non-edible oils, including waste oil and fats, as raw materials for producing biodiesel. Depending on the choice of vegetable oil as a starting material, the pour point (PP) of biodiesel ranges between 15-40°C, which is much higher than that of petro-diesel. In the cold season, viscosity of biodiesel increases and crystals appear due to the presence of saturated fatty acid chains. These solid crystals clog fuel lines and filters, which then obstructs the engine's operation. Indeed, there have been many approaches to overcome this significant problem, for example, the use of additives [1-7], blends of biodiesel with petro-diesel [8-11], anti-frost compounds [12-14], and esters with side chains [15-17]. Among those approaches, the use of additives that have economic advantages and convenience are the most appropriate [18]. These additives are known as cold flow improver (CFI), which include PP depressants (PPDs), surfactants [19, 20], and diluents [21, 22]. The CFIs are added to biodiesel in order to change the crystallization state of the wax to prevent the network structure from forming and therefore lower the pour point and viscosity of the biodiesel fuels. As a result, the working temperature range of biodiesel is extended. Although some additives are reported to be available for biodiesel, employing them to improve the flowability of biodiesel at low temperatures remains a challenge and more research is needed.

*Corresponding author: Email: maimophong@gmail.com

A number of studies have reported that many commercial petro-diesel cold flow improver additives also greatly reduced PP and the cold filter plugging point of biodiesel. The majority of diesel CFIs are poly (vinyl acetate) copolymers, poly (olefin) copolymers, alkyl methacrylate copolymers, and poly (maleic anhydrite) copolymers [2-5]. These CFIs have a common chemical structure that consists of a hydrocarbon chain capable of co-crystallizing with the hydrocarbon chains of fatty acids of biodiesel and thus affects the nucleation and growth of wax crystals [23, 24]. Cold flow properties of biodiesel generally depend on the fatty acid compositions. So, it becomes essential to design copolymeric CFIs with a special structure that would be suitable for a specific biodiesel [25]. It is known that copolymers with the comb shape structure exhibit a good flow improver for fuels in general. However, the synthesis of copolymers with a comb shape structure that consists of long and short branch chains in a regular arrangement is still a challenge for researchers [2, 3, 15, 23, 26]. It is well known in polymer chemistry that the generation of copolymers with a regular alternative structure requires the use of the pairs of monomers containing a small copolymerization constants (~0). Maleic anhydride (MA) is a unique and interesting monomer, which has almost no affinity to homopolymerization but easily forms copolymers [2, 23]. Thus, MA and an olefin as copolymers are a reasonable choice to form the desired alternative structure. In our previous reports, comb-shaped poly(maleic anhydride-co-α-olefin) (OMAC) [27, 28] and poly(maleic acid alkyl ester-co-vinylacetate) esters (MAVA) [29] were used to improve the cold flowing ability of palm oil biodiesel. The results proved that copolymers having comb-shape structures, with long and short side alkyl chains arranged alternatively to one another, determined the activity of the additives [27]. So, to design the comb-shape copolymer additives, the number and length of their branch alkyl chains for a specific biodiesel should be adjusted. In our present work, comb-type copolymers poly (maleic anhydride-co-α-tetradecene) esterified by the long alkyl chain alcohol with various ratios of alkyl group/carboxyl group were synthesized. This study assessed the effect of different proportions of alkyl/carboxyl group ratio and alkyl side chain length on cold flow improvement on wax crystallization and biodiesel flow ability by pour point testing and dynamic viscosity measurements. Moreover, the palm oil biodiesel (PB), the waste oil biodiesel (WB), and the animal fat biodiesel (AFB) were used to test the pour point reducing ability of the synthesized CFIs.

2. Experimental

2.1. Materials

Benzoyl peroxide and p-toluene sulfonic acid were purchased from Merck, Co., Ltd and 1-tetradecence was purchased from Kasei Kogyo. Maleic anhydride and 1-Hexadecanol were purchased from Wako, Japan. Palm oil biodiesel was produced from the palm oil in Viet Nam. Waste cooking oil biodiesel and animal fat biodiesels were produced in Japan. Other chemicals like ethanol, toluene, and methanol were supplied from Merck Co., Ltd and used without further purification. Table 1 presents the results of composition and distribution of the fatty acid methyl esters (FAMEs) of different biodiesels analysed by gas chromatography-mass spectroscopy (GC-MS) on an Agilent 6890N.

Table 1. GC-MS analysis of biodiesel from PB, AFB, and WB.

Name of FAME, corresponding acid	Mass percent (%)		
	PB	*AFB*	*WB*
Methyl hexadecanoate, C16:0	44.23	26.68	5,7
Methyl octadecanoate, C18:0	3.63	23.42	2,7
Methyl oleate, C18:1	41.06	33.94	53.8
Methyl linoleate, C18:2	8.36	6.33	23.5
Methyl linolenoate, C18:3	0.12	1.72	11.8
Other	2.64		

2.2. Preparation methods

2.2.1. Synthesis of MCAC copolymer

MCEC copolymers were synthesized by radical polymerization in two steps (Scheme 1). In the first step, maleic anhydride and α-tetradecene were copolymerized in toluene at 110°C for 8 h with benzoyl peroxide as an initiator under nitrogen gas atmosphere, to get the OMAC.

MCEC copolymers were synthesized by a two-step polymerization reaction (Scheme 1). In the first step, maleic anhydride reacted with α-tetradecene in toluene at 110°C for 8 hours, in a nitrogen atmosphere. Benzoyl peroxide served as an initiator. The product in the first step was OMAC.

In the second step, 1-hexadecanol was fed into the reactor with the copolymer OMAC at 120°C for 8 h. The crude product of MCEC was isolated from the reaction mixture by precipitating with methanol, was then washed thoroughly with warm water, and finally dried in a vacuum

oven at 60°C to reach a constant weight. By changing the feeding ratios of maleic anhydride/cetyl alcohol (1:1.0, 1:1.5, 1:2.0, 1:2.5 and 1:3.0), several MCECs were obtained and named MCEC1, MCEC2, MCEC3, MCEC4 and MCEC5, respectively.

Step-1:

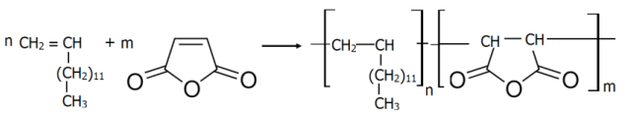

Step-2:

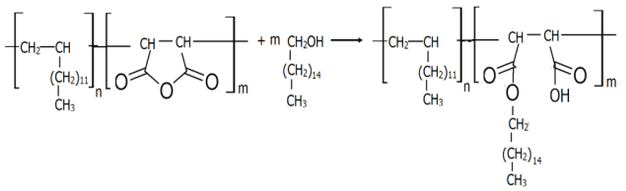

Scheme 1. Synthesis routine for the preparation of MCEC.

2.2. Methods of analysis

- Fourier transform infrared (FT-IR) spectra were recorded on a Perkin Elmer GX spectrophotometer using samples prepared as pressed KBr discs. All spectra were scanned 4 times at a resolution of 2 cm^{-1} from 400 to 4000 cm^{-1}.

- ^{1}H-NMR spectra were recorded on a JNM-ECX400 (Japan) spectrometer operating at 400 MHz and a Bruker Advance III spectrometer operating at 500 MHz (Faculty of Chemistry, HUS, Vietnam) at ambient temperature using $CDCl_3$ as the solvent.

- Gas chromatography mass spectroscopy (GC-MS) was used to determine the FAME content. The gas chromatograph (Agilent 6890 N) was equipped with a direct capillary column DB-5ms (film thickness of 30 m×0.25 mm×0.25 µm). The column temperature was initially kept at 60°C and then increased with speed of 4°C/min to 200°C, then held at this temperature for 2 min, followed by an increase to 280°C, and a hold at this temperature for 2 min. The temperature of the injector was set to 300°C. Helium was used as the carrier gas at a constant flow rate of 1 ml/min. Electron ionization (EI) mass spectra were recorded at 70 eV ionization voltage in the range of m/z 40-550 in full scan mode. The ion source and the transfer line temperatures were set to 200°C and 250°C, respectively. Measurements of the pour points of biodiesel were conducted in accordance with ASTM D97 [30].

- The viscosimetric molecular weight was determined by the measurement of the viscosity of the polymer solutions at 25°C in toluene and using the Mark - Houwink - Sakurada equation:

$$\mathrm{Log}[\eta]=\log K+\alpha.\log M \quad (1)$$

where [η] is the intrinsic viscosity, M is the molecular weight, and K and α are constants that depend on polymer, solvent, and temperature (in our case $K=1.52.10^{-4}$ and $\alpha=0.71$ [6]).

- The dynamic viscosity of the control and PPD-treated biodiesels were measured on a viscometer of the falling ball type (Gilmont, Thermo Scientific) using an isothermal bath at 40°C. The dynamic viscosity determinations were performed in accordance with ASTM D445-97 [25].

3. Results and discussion

3.1. Synthesis and characterization of MCEC

The chemical structures of the OMAC and MCEC4 copolymers were confirmed by the FTIR spectra shown in Fig. 1.

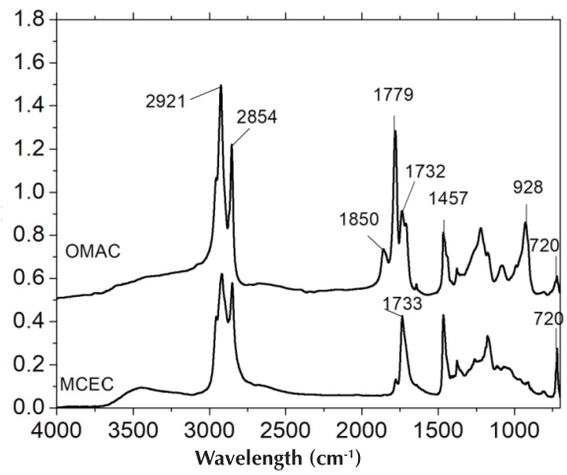

Fig. 1. FTIR spectra of synthesized OMAC and MCEC4.

It is clearly seen that the stretching vibration of C-H (in CH_3 and CH_2) absorbs strongly at 2921 cm^{-1} and 2854 cm^{-1} and the stretching vibration of C-H appears at 1457 cm^{-1}. The strong absorption band of the scissoring vibration of the $(CH_2)_n$ alkyl chains of α-tetradecene appears at 720 cm^{-1}. The carbonyl group C=O of the anhydride was demonstrated by strong bands at 1779 cm^{-1} and 1732 cm^{-1}, and a weak band at 1850 cm^{-1} characteristic for the MA ring. In addition, the absorption peak of the characteristic C=C group at 1630-

1642 cm^{-1} [8] of the monomers disappeared completely, which indicates the polymerization reaction was thoroughly completed.

The chemical structure of the OMAC was also confirmed by the ^{1}H-NMR spectrum shown in Fig. 2.

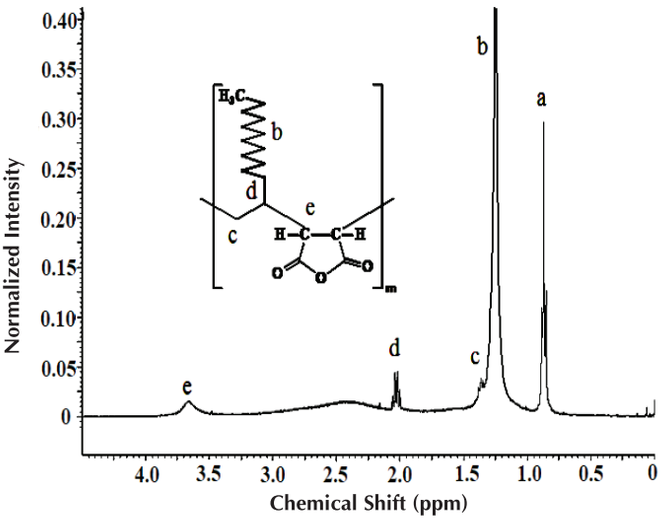

Fig. 2. ^{1}H-NMR spectra of synthesized OMAC.

It can be seen from Fig. 2 that the -CH_3 exhibited the chemical shift at 0.88 ppm (peak a), and the -$(CH_2)_n$- displayed a chemical shift at 1.25 ppm (peak b), while the hydrogen peak of the methylene groups of the MA showed the chemical shift at 3.6 ppm (peak e) [15]. Thus, the presence of all the structural groups in the OMAC and MCEC copolymers was confirmed by FTIR and ^{1}H-NMR spectra. The FTIR in combination with ^{1}H-NMR are commonly used to confirm the structure of the polymer compounds [15, 18].

Based on the peak intensity of -CH in maleic anhydride and of -CH_2- in the α-tetradecene, it is possible to determine the percentage of MA residue in a polymer unit. Using this method, the obtained polymer had an MA to α-tetradecene composition relative ratio of 1:1.2.

The obtained OMAC was esterified by cetyl alcohol with varying feeding ratios of MA:alcohol (1:1.0, 1:1.5, 1:2.0, 1:2.5, 1:3.0) and the resulting copolymers were named MCEC1, MCEC2, MCEC3, MCEC4, and MCEC5, respectively. The structures of all modified copolymers were confirmed by the FTIR spectra. The FTIR spectrum of MCEC4 is shown in Fig. 3. By analysing the significant signals in the FTIR spectra we can see the intensities of the CH_3 and CH_2 bands increase with the increase of the number of cetyl alkyl that are attracted to the main chain of the copolymer. It can be clearly seen that the intensities of the characteristic C=O stretching peaks of the MA at 1857 cm^{-1} and 1778 cm^{-1} decrease and that of the characteristic C=O adsorption peaks of alkyl ester at 1733 cm^{-1} increase**.** The decreasing C=O bands of MA (1857 cm^{-1} and 1778 cm^{-1}) in the OMAC confirmed the formation of the MCEC.

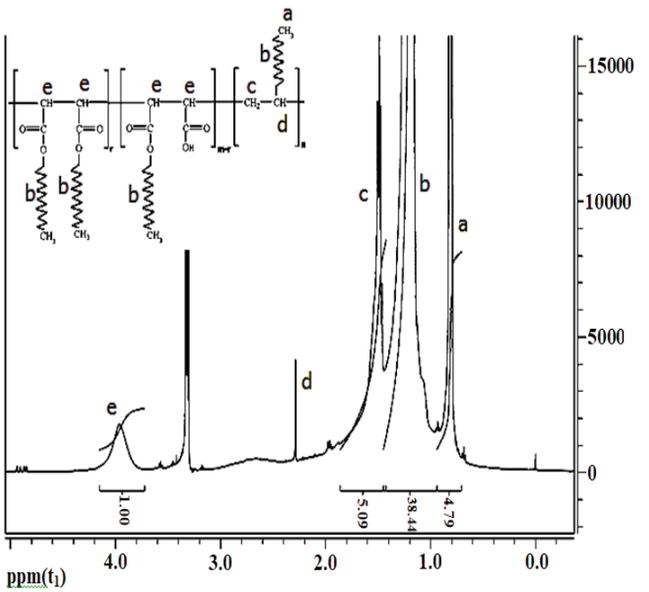

Fig. 3. ^{1}H-NMR spectra of MCEC4.

The esterification ratio (f) is defined as the molar amount of the alkyl-alcohols for one mole of the maleic anhydride group in a polymer (0<f< 2), which is estimated from the integrated area of the H_a and H_e peaks (H_a, H_e are protons at positions a and e, respectively, in Fig. 3).

From the relation $\frac{A_{He}}{A_{Ha}} = \frac{2}{3x1.2+3xf}$, the esterification ratio (f) can be given as follows:

$$f = \frac{2A_{Ha}}{3A_{He}} - 1.2 \quad (2)$$

In this equation, A_{Ha} and A_{He} are the integrated area of protons H_a and H_e, respectively and r is defined as the ratio of total alkyl groups (C-16 and C-14) to carbonyl group (-COOH) and is calculated by using the following equation:

$$r = \frac{f+1.2}{2-f} \quad (3)$$

The viscosimetric method was used to determine the molecular weight of the MCEC copolymers. The values of *f*, *r,* and molecular weight (M_W) of all samples are presented in Table 2.

Table 2. Values of f, r and M_w of OMAC samples.

Sample	Molar ratio of MA-Cetyl	f	r	M_w
OMAC		-	-	11700
MCEC1	1:1.0	0.92	1.98	19900
MCEC2	1:1.5	0.97	2.12	20500
MCEC3	1:2.0	1.04	2.34	21050
MCEC4	1:2.5	1.15	2.76	21900
MCEC5	1:3.0	1.46	3.35	24400

From Table 2, it can be seen that the values of *f*, *r*, and M_w increase with the increase of molar ratio of MA-Cetyl. These results prove that when the MA-Cetyl ratio rises, the number of alkyl pendant chains attached to the OMAC copolymer increases.

3.2. Effect of MCECs on the improvement of palm oil biodiesel cold flow

The efficiency of the cold flow improvement of MCECs on palm oil biodiesel was investigated by PP and dynamic viscosity measurements. The results are presented in Table 3. From this table, all the MCECs exhibit a positive effect on the reduction of the PP of palm oil biodiesel. The PP of the biodiesel decreases with increase in *r* and at *r*=2.76 the most effective improvement of the biodiesel flow ability is reached. However, we also can see that PP increases as *r* further increases to 3.35. This indicates that the MCEC5 had a value of *r* that was too high and not reducing the pour point. This feature can be explained as follows: it is known that the most beneficial profile structure of additives for reducing PP are alkyl groups C14 and C16 alternatively grafted to the polymer backbone. Too many alkyl groups will disrupt their alternative attachment and cause their reducing ability to trap the biodiesel's long alkyl chains that create favourable conditions for self-crystallization.

Table 3. PP and dynamic viscosity (μ) values of PB and MCECs treated PB at 1000 ppm.

Sample	PP (°C)	μ, 40°C, mPa.s	
		Average	*Std.dev*
PB	15.0	4.10	0.04
PB+ MCEC1	7.0	3.39	0.04
PB+ MCEC2	6.5	3.30	0.06
PB+ MCEC3	5.8	3.19	0.04
PB+ MCEC4	4.5	3.06	0.03
PB+ MCEC5	5.5	3.15	0.04

The dynamic viscosity values in Table 3 show that the trend in viscosity variation looks similar to that of PP. A high reduction in viscosity was observed upon increase in *r* from 1.98 to 2.76 while insignificant decrease was observed when *r* was further raised to 3.35. Thus, there is a correlation between the influence of additives on the PP and viscosity of biodiesel. The additives that promote the reduction of PP also produce the highest viscosity reduction. This is clearly related to the additive's ability to provide the formation of small waxy crystals dispersed in the fuel environment [9]. The assembly between the carboxyl and alkyl groups of MCECs with the methyl ester group appears to stabilize the biodiesel under the steric effects of the number of alkyl groups of MCEC polymers, thereby improving the flow-ability of the biodiesel gels formed upon cooling [18]. So, the balance between the alky groups of the additive and the methyl ester groups of the biodiesel is an important factor.

One of the goals of this study was to clarify the effect of additive loading on the ability to reduce PP of biodiesel. Here, different concentrations of MCEC4 (500, 1000, 2000 and 3000 ppm) were taken. The results are presented in Fig. 4.

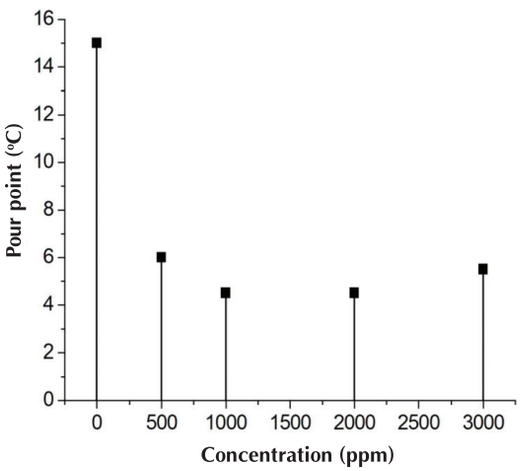

Fig. 4. The change in activity of the MCEC4 additive with different concentrations.

It can be seen that ΔT increases with increasing additive concentration whereas an optimum additive concentration of 1000 ppm was found. If the concentration is lower than the optimum value, it may be difficult for the additive to completely co-crystallize with the FAMEs and the cold flow performance of the biodiesel does not further improve. On the other hand, if the copolymer additive concentration is higher than the optimum value, the additive molecules could form small wax crystals to prevent them from co-crystallization with the FAMEs and then the higher concentrations would not be economical. Therefore, at the 1000 ppm concentration, the additive shows a better ability to lower PP of the palm oil biodiesel.

At present, there are different commercial additives available for biodiesel and blends with diesel, but for the additives to be effective a much higher concentration is needed than the one used in this work [7, 15, 19, 26, 31]. Moreover, the performance of the additives compared to the biodiesel control was often negligible. When using poly (dodecyl acrylate-co-tetradecyl methacrylate) as an improver for the palm oil biodiesel, Oliveira [18] reported that PP dropped from 14.7°C to 13°C at 1000 ppm concentration. Here, better PP reductions were found in the control palm biodiesel.

3.3. Effect of additive' side chain length on the cold flow-ability of biodiesel

Although biodiesel has a potential for environmental emission reduction, it also has a high PP and a high viscosity compared to conventional diesel fuel [7]. The correlation between the FAMEs composition and the number of alkyl pendant chains of MCECs on the activity of the additive was investigated at 1000 ppm concentration. The results of these tests are shown in Table 4.

Table 4. Results of the test on activity of MCEC for different biodiesels and some methyl ester of fatty acids.

Sample	PP, °C (1000 ppm)	
	No additives	*MCEC-C16*
PB*	15.0	**4.5**
AFB**	22.0	18.0
WB**	-10.0	-15.0
Methyl hexadecanoate** (C16:0)	30.0	**25.0**
Methyl octadecanoate** (C18:0)	40.0	36.0
Methyl oleate** (C18:1)	-3.0	-12.0

(*): biodiesel was supplied from Vietnam.
(**): biodiesels and methyl ester of fatty acids were supplied from Japan.

The data in Tables 1 and 4 show that biodiesel with a lot of methyl esters of saturated fatty acids has a high PP value. On the other hand, it is seen that at the same additive concentration, the effectiveness of the MCEC on the PB was better than that of AFB and WB. As seen above in Table 4, PP has the dominate amount of C16 alkyl chains compared to WB and AFB. This means there is a greater similarity between alkyl chain length in PB and the additive.

The effect of the additive side chain length on the cold flow ability of biodiesel was also investigated by viscosity measurements. The dynamic viscosities of all samples are presented in Fig. 5.

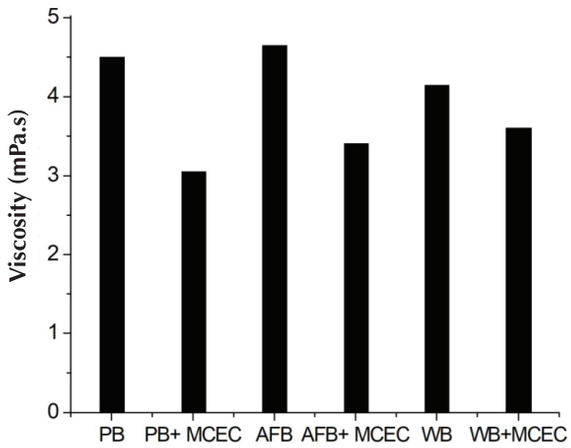

Fig. 5. The viscosity of neat and MCEC treated biodiesels.

This figure shows that biodiesel with higher percentages of saturated fatty esters has a higher dynamic viscosity, which is in agreement with results of other authors [11,17, 32]. Some researchers have pointed out the effect of unsaturated levels on cold flow properties. They showed that the higher the unsaturated level, the better the cold flow performance [9]. It was observed that the effectiveness of the MCEC in the dynamic viscosity of the PB was also significantly better than that of AFB and WB. This, in turn, explains the higher efficiency of the MCEC as a flow improver for the PB as the one most suitable between the alkyl saturated chain length of the FAMEs and the alkyl side chain length of the additive. The trend in viscosity variation looks similar to that of PP.

4. Conclusions

Comb-type MCEC copolymers with various ratios of alkyl group:carboxyl group (r) were synthesized by the esterification of OMAC with alkyl alcohols. The structure and molecular weight of the obtained copolymers were characterized by FTIR, ^{1}H-NMR, and the viscosimetric method. The results showed that with r=2.76, the additive MCEC appears to be the most effective in improving the flow ability of the palm oil biodiesel. In addition, by using MCEC4 of 1000 ppm concentration, the PP of the palm oil biodiesel could be reduced up to 10.5°C and the viscosity up to 1.04 mPa.s. The results also indicated that similarity between the alkyl length in both additives and biodiesel is important for improving the flow ability of biodiesel upon cooling.

CRediT author statement

Mai Thi Tuyet Phan, Boi Van Luu, Lan Ngoc Pham: Conceptualisation, Methodology, Software, Resources, Writing - Review and Editing, Validation.

ACKNOWLEDGEMENTS

This work was supported by Vietnam National University - Ha Noi under the QG.14.18 project.

COMPETING INTERESTS

The authors declare that there are no conflicts of interest regarding the publication of this paper.

REFERENCES

[1] L. Cao, J. Wang, K. Liu, et al. (2014), "Ethyl acetoacetate: A potential biobased diluents for improving the cold flow properties of biodiesel from waste cooking oil", *Applied Energy*, **114**, pp.18-21, DOI: 10.1016/j.apenergy.2013.09.050.

[2] L. Cao, J. Wang, C. Liu, et al. (2014), "Ethyelene vinyl acetate copolymer: A bio-based cold flow improver for waste cooking oil derived biodiesel fuel", *Applied Energy*, **132**, pp.163-167, DOI: 10.1016/j.apenergy.2014.06.085.

[3] J. Wang, L. Cao, S. Han (2014), "Effect of polymeric cold flow improvers on flow properties of biodiesel from waste cooking oil", *Fuel*, **117(Part A)**, pp.876-881, DOI: 10.1016/j.fuel.2013.10.006.

[4] S. Giraldo, L. Rios, N. Suarez (2013), "Comparison of glycerol ketals, glycerol acetates and branched alcohol-derived fatty esters as cold-flow improvers for palm biodiesel", *Fuel*, **108**, pp.709-714, DOI: 10.1016/j.fuel.2013.02.039.

[5] R.O. Dunn, M.W. Shockley, M.O. Bagby (1996), "Improving the low-temperature properties of alternative diesel fuels: Vegetable oil- derived methyl esters", *Journal of The American Oil Chemical s Society*, **73(12)**, pp.1719-1728, DOI: 10.1007/BF02517978.

[6] M.A. Masuelli (2014), "Mark-Houwink paramaters for aqueous-souluble polymers and biopolymer at various temperatures", *Journal of Polymer and Biopolymer Physics Chemical*, **2(2)**, pp.37-43, DOI: 10.12691/jpbpc-2-2-2.

[7] P. Lv, Y.F. Cheng, Z.H. Yuan, et al. (2013), "Improving the low temperature flow properties of palm oil biodiesel: Addition of cold flow improver", *Fuel Processing Technology*, **110**, pp.61-64, DOI: 10.1016/j.fuproc.2012.12.014.

[8] A.F. Fernando, S.M. Aline, R.S.O. Angelo, et al. (2018), "Bio-based comb-like copolymers derived from alkyl 10-undecenoates and maleic anhydride", *Journal of Polymer Science, Part A: Polymer Chemical*, **56(10)**, pp.1039-1045, DOI: 10.1002/pola.28978.

[9] B. Yao, L. Wang, F. Yang, et al. (2017), "Effect of vinylacetate moiety molar fraction on the performance of poly (octadecyl acrylate-vinyl acetate) pour point depressants: Expriments and mesoscopic dynamics simulation", *Energy & Fuels*, **31(1)**, pp.448-457, DOI: 10.1021/acs.energyfuels.6b02688.

[10] A. Sarin, R. Arora, N.P. Singh, et al. (2009), "Effect of blends of Palm-Jatropha-Pongamia biodiesels on cloud point and pour point", *Energy*, **34(11)**, pp.2016-2021, DOI: 10.1016/j.energy.2009.08.017.

[11] A.S. Silitonga, H.H. Masjuki, T.M.I. Mahlia, et al. (2013), "Overview properties of biodiesel diesel blends from edible and non-edible feedstock", *Renewable and Sustainable Energy Reviews*, **22**, pp.346-360, DOI: 10.1016/j.rser.2013.01.055.

[12] G.M. Chupka, L. Fouts, J.A. Lennon, et al. (2014), "Saturated monoglyceride effects on low-temperature performance of biodiesel blends", *Fuel Processing Technology*, **118**, pp.302-309, DOI: 10.1016/j.fuproc.2013.10.002.

[13] A. Prez, A. Casas, C.M. Fernandez, et al. (2010), "Winterization of peanut biodiesel to improve the cold flow properties", *Bioresource Technology*, **101(19)**, pp.7375-7381, DOI: 10.1016/j.biortech.2010.04.063.

[14] T.H. Doğan, H. Temur (2013), "Effect of fractional winterization of beef tallow biodiesel on the cold flow properties and viscosity", *Fuel*, **108**, pp.793-796, DOI: 10.1016/j.fuel.2013.02.028.

[15] P.V. Bhale, N.V Deshpande, S.B. Thombre (2009), "Improving the low temperature properties of biodiesel fuel", *Renewable Energy*, **34(3)**, pp.794-800, DOI: 10.1016/j.renene.2008.04.037.

[16] E.C. Zuleta, L.A. Rios, P.N. Benjumea (2012), "Oxidative stability and cold flow behavior of palm, sacha-inchi, jatropha and castor oil biodiesel blends", *Fuel Processing Technology*, **102**, pp.96-101, DOI: 10.1016/j.fuproc.2012.04.018.

[17] L.Y. Chen, Y.H. Chen, Y.S. Hung, et al. (2013), "Fuel properities and combustion characteristics of jatropha oil biodieseldiesel blends", *Journal of the Taiwan Institute of Chemical Engineers*, **44(2)**, pp.214-220, DOI: 10.1016/j.jtice.2012.09.011.

[18] M. Ramalho, J.R. Carvalho, A.R. Albuquerque, et al. (2012), "Low temperature behavior of poultry fatbiodiesel: Diesel blends", *Fuel*, **93**, pp.601-605, DOI: 10.1016/j.fuel.2011.10.051.

[19] R.A. El-Ghazawy, A.M. Atta, K.I. Kabela (2014), "Modified maleic anhydride-co-octadecene copolymers as flow improver for waxy Egyptian crude oil", *Journal of Petroleum Science and Engineering*, **122**, pp.411-441, DOI: 10.1016/j.petrol.2014.07.040.

[20] X. Jun, X. Shili, Q. Hauiqin, et al. (2013), "Effect of polar/nonpolar groups in comb-type copolymers on cold flowability and paraffin crystallization of waxy oils", *Fuel*, **103**, pp.600-605, DOI: 10.1016/j.fuel.2012.06.027.

[21] S.F. Cheng, C.L. Yung, L.D. Noor, et al. (2006), "Crystallisation and melting behavior of methyl esters of palm oil", *American Journal of Applied Sciences*, **3(5)**, pp.1859-1863.

[22] ASTM International (2012), *ASTM D97-17b Standard Test Method for Pour Point of Petroleum Products*.

[23] S.P. Srivastava, R.S. Tandon, P.S. Verma, et al. (1995), "Phase transitions in middle-distillate waxes: Effect of pour point depressant additives", *Fuel*, **74(6)**, pp.928-931, DOI: 10.1016/0016-2361(95)00007-R.

[24] A.E. Kuzmić, M. Radošević, G. Bogdanić, et al. (2008), "Studies on the influence of long chain acrylic ester copolymer with polar monomers as crude oil flow improver additives", *Fuel*, **87**, pp.2943-2950, DOI: 10.1016/j.fuel.2008.04.006.

[25] H.P. Soni, D.P. Bharambe (2006), "Synthesis and evaluation of polymeric additives as flow improvesr for Indian crude oil", *Iranian Polymer Journal*, **15(12)**, pp.943-954.

[26] C.H. Sern, C.Y. May, Z. Zakaria, et al. (2007), "The effect of polymers and surfactants on the pour point of palm oil products", *European Journal of Lipid Science and Technology*, **108**, pp.709-714, DOI: 10.1002/ejlt.200600242.

[27] T.C. Ming, N. Ramli, O.T. Lye, et al. (2005), "Strategies for decreasing the pour point and cloud point of palm oil products", *European Journal of Lipid Science and Technology*, **107(7-8)**, pp.505-512, DOI: 10.1002/ejlt.200400944.

[28] P. Verma, M.P. Sharma, G. Dwivedi (2016), "Evaluation and enhancement of cold flow properties of palm oil and its biodiesel", *Energy Reports*, **2**, pp.8-13, DOI: 10.1016/j.egyr.2015.12.001.

[29] L. Xiang, X. Yuan, X. Guangwen, et al. (2016), "Effect of methyl acetoacetate as a potential cold flow improver for biodiesel", *Energy Soucers, Part A: Recovery, Utilization, and Environmental Effects*, **39(1)**, pp.97-102, DOI: 10.1080/15567036.2016.1200164.

[30] ASTM International (2012), *ASTM D445-97 Standard Test Method for Kinematic Viscosity of Stransparent and Opaque Liquid*.

[31] T.T.H. Tran, T.T.M. Phan, V.B. Luu, et al. (2018), "Synthesis and modification of maleic anhydride-vinyl acetate copolymer by a long alkyl chain alcohol for cold flow impovers of biodiesel", *Vietnam Journal of Sicence, Technology and Engineering*, **60(3)**, pp.3-8, DOI: 10.31276/VJSTE.60(3).03.

[32] T.T.M. Phan, T.T.H. Tran, V.B. Luu, et al. (2017), "Synthesis and characterization of comb-shape (maleic acid alkyl ester-vinyl acetate) copolymers for cold flow improvers of biodiesel", *6th Asian Symposium on Advanced Materials*, pp.728-733.

DOI: 10.31276/VJSTE.63(2).20-24

Structure and luminescent property of a Sm^{3+} complex containing benzoyltrifluoroacetone and 1,2-bis[(anthracen-9-ylmethyl)amino]ethane ligands

Thi Hien Dinh[1*], Minh Hai Nguyen[2]

[1]*Faculty of Chemistry, Hanoi National University of Education, 136 Xuan Thuy Street, Dich Vong Hau Ward, Cau Giay District, Hanoi, Vietnam*
[2]*Faculty of Chemistry, University of Science, Vietnam National University - Hanoi, 334 Nguyen Trai, Thanh Xuan Trung Ward, Thanh Xuan District, Hanoi, Vietnam*

Received 1 April 2021; revised 14 May 2021; accepted 31 May 2021

Abstract:

One of the rare earth coordination compounds that has been studied the most in-depth is -diketonate complexes. This is mostly because they can be rapidly synthesized, are sold commercially, and have a wide range of uses, including photoluminescence and magnetism. The narrow and strong emission of rare earth ions with P-diketonates makes them applicable in optical and electroluminescent devices as well as in luminescence sensors for cations and anions. The synthesis, structure, and luminescent properties of a samarium(III) complex (A2) containing benzoyltrifluoroacetone (HTFPB) and 1,2-bis[(anthracen-9-ylmethyl) amino]ethane (BAAE2) ligands are herein reported. The structure of A2 has been elucidated by infrared spectroscopy and single crystal X-ray diffraction. X-ray crystallographic analysis demonstrated that A2 has a mononuclear structure with a formula of $Sm(TFPB)_3(BAAE2)$ in which Sm^{3+} ion is coordinated to six O-atoms from three TFPB ligands and two N-atoms from one ancillary ligand (BAAE2). The substantial absorptions generated by the -diketonate and anthracenyl fragments are confirmed by UV-Vis measurements. The data show that A2 strongly absorbs in the region of 220-400 nm. Nonetheless, A2 gives poor emission due to a quenching effect of the anthracenyl moiety.

Keywords: **anthracene, β-diketone, rare earth complex.**

Classification number: **2.2**

1. Introduction

β-diketonate complexes are among the most thoroughly explored rare earth coordination compounds. This is mainly due to the fact that they are easily synthesized, readily available from commercial sources, and are utilized in many applications ranging from magnetism to photoluminescence [1, 2]. The narrow and strong emission of rare earth ions with β-diketonates makes them applicable in optical and electroluminescent devices as well as in luminescence sensors for cations and anions. However, due to "Laporte-forbidden" f-f transitions, emissions from the direct excitation of lanthanide ions are infeasible [3]. Benzoyltrifluoroacetone (HTFPB) is a commercially available and efficient sensitizer that is able to transfer excited energy to rare earth ions. Due to the suitable triplet energy level of TFPB, a so-called "antenna effect" is produced that turns on lanthanide emissions. Typically, the synthesis of lanthanide β-diketonates in the first step involves two water molecules in the coordination sphere of the central metal ion. Subsequent displacement of the coordinated water by ancillary chelating ligands with various electronic structures may lead to a fine tuning of lanthanide-centered emissions [4-6]. It has been well documented that bispyridine, phenanthroline, and many pyridine-based ligands are able to turn on the emission of the central metal ion due to additional sensitizer effects [7, 8]. In this study, 1,2-bis[(anthracen-9-ylmethyl)amino]ethane (BAAE2), a ligand with a low-lying triplet state, has been utilized to construct a tris β-diketonate complex [9-12]. BAAE2 is a potentially good bidentate ligand as the trivalent rare-earth ions are Lewis acids that preferentially form complexes with nitrogen donor bases. In the following discussions, the main attention will be focused on the syntheses, structures, and luminescent properties of Sm^{3+} complexes containing TFPB and BAAE2 ligands.

2. Experimental

2.1. Synthesis of ligands and complexes

2.1.1. Synthesis of BAAE2 ligand

Step 1: Synthesis of BAAE1 [13]

BAAE1 was synthesized via a condensation reaction between ethylenediamine and anthracene-9-carcbadehyde, which is depicted in Scheme 1.

*Corresponding author: Email: dth0104@gmail.com

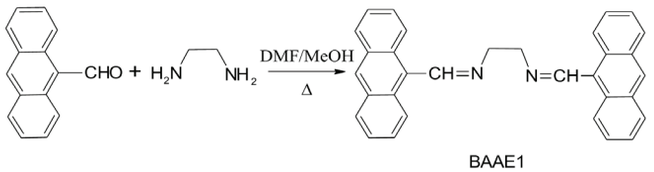

Scheme 1.

A solution of anthracene-9-caboxaldehyde (0.400 g; 1.94 mmol) in 12 ml DMF/CH_3OH (v/v, 1:5) was added to ethylenediamine (0.067ml, 0.97 mmol) in methanol and the mixture was refluxed for 4 h with constant stirring. After the solution had cooled to room temperature, a yellow precipitate was formed and collected by vacuum filtration. The product was washed by a few drops of DMF, a large amount of methanol, and air-dried. The yield was 0.364 g (86%).

Step 2: Synthesis of BAAE2 ligand [13]

The synthetic procedure of ligand BAAE2 was based on a reaction reducing ligand BAAE1 by $NaBH_4$ in methanol as described in Scheme 2.

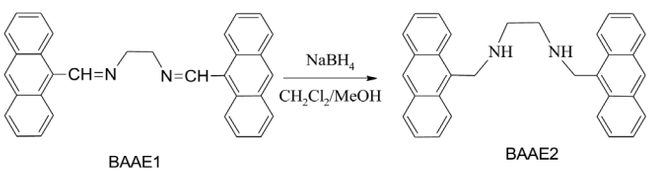

Scheme 2.

BAAE1 (0.396 g, 0.907 mmol) was dissolved in a mixture of CH_2Cl_2 (30 ml) and CH_3OH (15 ml) to obtain a yellow solution. A solution of $NaBH_4$ (0.527 g, 13.9 mmol) in methanol (3 ml) was added under stirring to the mixture. The solution was stirred overnight at room temperature to give a yellow solid. The product was washed several times with distilled water, finally with diethyl ether, and air-dried. The yield was 0.320 g (80%).

2.1.2. Synthesis of the complexes

Synthesis of $Sm(TFPB)_3(H_2O)_2$ complex (**A1**)

Sm_2O_3 (0.070 g, 0.2 mmol) was dissolved in HCl at 50°C, then distilled water was added and heated at 100°C to form $SmCl_3$. A solution of NaOH (0.048 g, 1.2 mmol) and HTFPB (0.259 g, 1.2 mmol) in MeOH (15 ml) was added dropwise under stirring to a solution of $SmCl_3$ in MeOH (15 ml). The mixture was stirred at room temperature until a white solid completely formed. The product was washed by a large amount of CCl_4 and air-dried. The yield was 88%.

Synthesis of $Sm(TFPB)_3BAAE2$ complex (**A2**)

A2 was achieved by reacting **A1** with BAAE2 ligand in chloroform-methanol solvent mixture (Scheme 3).

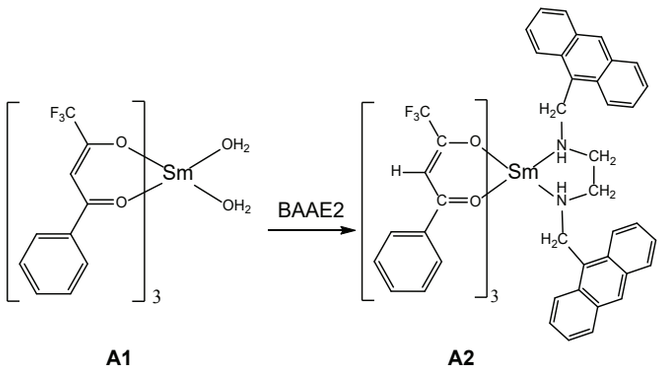

Scheme 3.

A solution of BAAE2 (0.397 g, 1 mmol) in $CHCl_3$ (15 ml) was added dropwise under stirring to a solution of **A1** (0.831 g, 1 mmol) in MeOH (15 ml). The mixture was stirred at room temperature for about 1 h until a yellowish precipitate formed. The solvent was removed in vacuum and the resulting solid was then washed with n-hexane. After drying under vacuum, a pale-yellow powder was obtained. The product was crystallized in EtOH/CH_2Cl_2 (v/v, 1:1) and the yield was 74%.

2.2. Measurements

The IR spectra of A2 was measured with a FT-IR 8700 infrared spectrophotometer (4000-400 cm^{-1}) in KBr pellets at Institute of Chemistry, Vietnam Academy of Science and Technology, Hanoi, Vietnam.

Single crystal X-ray diffraction data of the complex **A2** was collected on the X-ray diffractometer (Bruker D8 Quest) at 298 K at the Faculty of Chemistry, University of Science, Vietnam National University - Hanoi, Vietnam. Structure solution and refinement were performed with OLEX2 programs.

Absorption spectra of the ligands and the complexes were measured in dichloromethane at room temperature on Cary 5000 UV/Vis spectrometer at Faculty of Environmental Chemistry, Hanoi National University of Education. Emission spectra of the complexes were measured on Hitachi Fluorescence Spectrophotometer F-7000.

3. Results and discussion

3.1. Infrared spectroscopy

The infrared spectrum of the complex $Sm(TFPB)_3BAAE2$ (**A2**) is shown in Fig. 1. Typical absorption bands of the complexes and ligand are shown in Table 1.

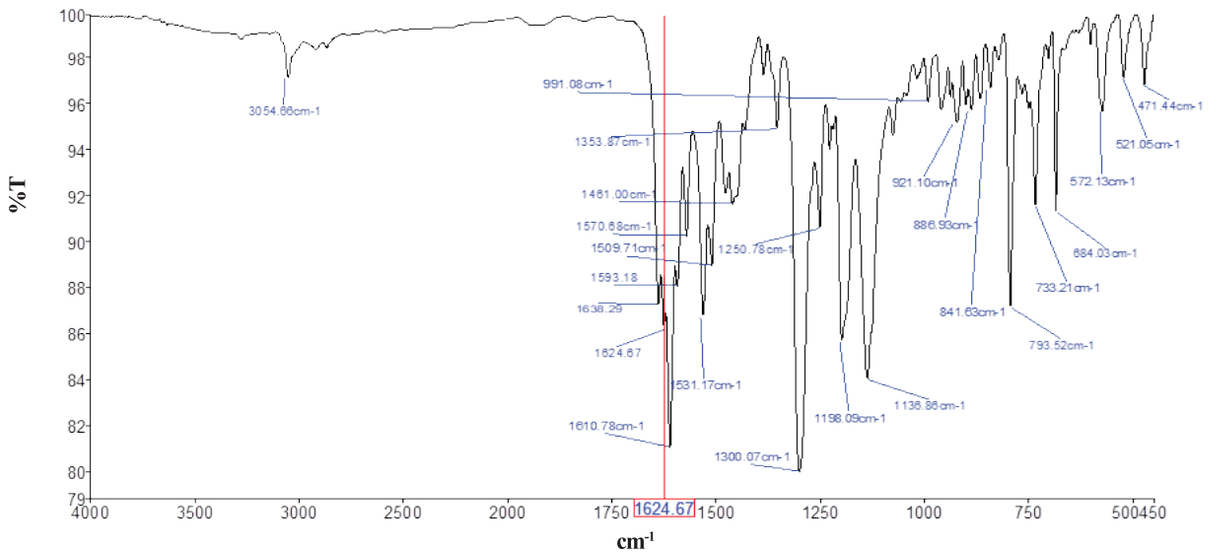

Fig. 1. The infrared spectrum of A2.

Table 1. Typical absorption bands of the complexes and ligand (cm^{-1}).

Compounds	ν_{O-H}	$\nu_{C-Caroma}$	ν_{C-F}	$\nu_{C=O}$	ν_{C-N}	ν_{Sm-O}
HTFPB	3450	3030	1191	1600	-	-
BAAE2	-	3040	-	-	1100	-
A1	3300	3035	1170	1608	-	557
A2	-	3054	1295	1609	991	562

The IR spectrum of **A1** exhibits the typical broad absorption in the region 3000-3500 cm^{-1}, which proposes the presence of water molecules coordinated to the central ion Sm^{3+}. In contrast, the absence of the broad bands in the region of 3000-3500 cm^{-1} for **A2** suggests that water molecules in **A1** have been displaced by the nitrogen donor of BAAE2 ligand. The respective ν_{C-F} vibration of **A2** is found at 1295 cm^{-1} that, compared to the starting material, is shifted to a somewhat higher frequency. The absorption at 1600 cm^{-1}, which is typical for C=O sketch in the HTFPB ligand, is red-shifted to 1609 cm^{-1} in **A2** [2]. In addition, the absorption band responsible for ν_{Sm-N} at 506 cm^{-1} in **A2** confirms the complexation of Sm^{3+} ions with BAAE2 ligands through nitrogen atoms. The change in absorption frequency of $\nu_{C=O}$ compared with free ligands and the emergence of ν_{Sm-N} absorption in the low frequency prove that HTFPB and BAAE2 ligands are present in the coordination sphere of Sm^{3+}.

3.2. Single crystal X-ray diffraction

The structure of **A2** was determined by single crystal X-ray diffraction (Fig. 2). Selected bond lengths and angles are provided in Table 2. Crystal data and data collection parameters for the complex are given in Table 3.

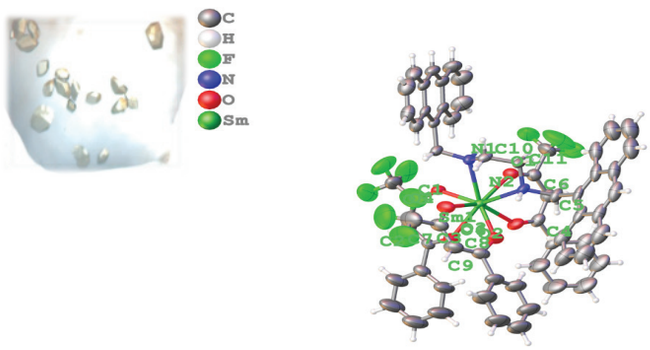

Fig. 2. Molecular structure of A2.

The structure of the complex reveals a coordination number of eight in the central metal ion in which Sm^{3+} is bonded to six oxygen atoms from three TFPB and two nitrogen atoms from the BAAE2 ligand. The bond lengths of Sm1-O are 2.355-2.418 Å. The bond lengths of Sm^{3+} with two nitrogen atoms of BAAE2 are 2.599-2.658 Å. The O-Sm1-O bond angles are nearly the same and in the range of 69.58-70.7°, which is longer than that of N-Sm1-N (67.26°). The C-N bond lengths (1.465-1.491 Å) in the complex were found to be longer than a C-N single bond (1.472 Å). This confirms the delocalization of π electrons in the chelate ring upon complexation of BAAE2. The C-C bond length in the diketonate of C2 is 1.359-1.430 Å, which is shorter than the C-C bond length (1.54 Å) but longer than that of C=C (1.34 Å). Similarly, the C-O bond length in the diketone of **A2** is 1.247-1.268 Å and it is also shorter than the bond length of C-O but longer than that of C=O. This confirms the delocalization of π electrons in the β-diketonate upon complexation between Sm^{3+} and TFPB ligands. The coordination of Sm^{3+} with BAAE2 ligands through two nitrogen atoms forms a five-membered chelate ring.

Table 2. Selected bond lengths and angles for A2.

Bond lengths/Å			
Sm1-O1	2.418(5)	O6-C14	1.249(8)
Sm1-O2	2.355(5)	N1-C1	1.491(9)
Sm1-O3	2.370(5)	N1-C2	1.465(9)
Sm1-O4	2.368(5)	N2-C3	1.486(7)
Sm1-O5	2.374(5)	N2-C4	1.478(8)
Sm1-O6	2.357(5)	N2-C5	1.480(8)
Sm1-N1	2.599(6)	C2-C3	1.351(12)
Sm1-N2	2.658(6)	C6-C7	1.394(12)
O1-C6	1.259(9)	C7-C8	1.373(12)
O2-C8	1.273(9)	C9-C10	1.418(11)
O3-C9	1.258(9)	C10-C11	1.365(10)
O4-C11	1.247(7)	C12-C13	1.496(10)
O5-C12	1.268(7)	C13-C14	1.412(10)
Bond angles/°			
O1-Sm1-O2	69.58(18)		
O3-Sm1-O4	70.7(2)		
O5-Sm1-O6	70.34(17)		
N1-Sm1-N2	67.26(17)		
C1-N1-C2	112.6(5)		
N1-C2-C3	110.4(5)		
C2-C3-N2	111.9(5)		
C3-N2-C4	109.4(5)		
C4-N2-C5	107.5(5)		
C5-N2-C3	108.9(5)		

Table 3. Crystal data and structure refinement for A2.

Formula	**$C_{50}H_{50}N_6O_6F_9Sm$**
M_w/g.mol^{-1}	1046.12
Crystal system	monoclinic
a/Å	10.7101(10)
b/Å	23.075(2)
c/Å	23.458(2)
α/°	90
β/°	102.355(3)
γ/°	90
Volume/Å^3	5663.0(9)
Space group	$P2_1/c$
Z	4
ρ_{calc}g/cm^3	1.227
μ/mm^{-1}	1.107
Reflections collected	33163
Independent reflections	10312 [R_{int}=0.1464, R_{sigma}=0.1418]
Data/restraints/parameters	10312/741/721
R1/wR2 [I≥2σ (I)]	R_1=0.0641, wR_2=0.1364
GOF	0.996

3.3. UV-Vis absorption spectroscopy

To determine the photophysical properties of the compounds, we measured absorption spectra of ligands and Sm^{3+} complexes in the region of 200-800 nm in a CH_2Cl_2 solvent. The absorption spectra of **A1**, **A2**, HTFPB, and BAAE2 are displayed in Fig. 3.

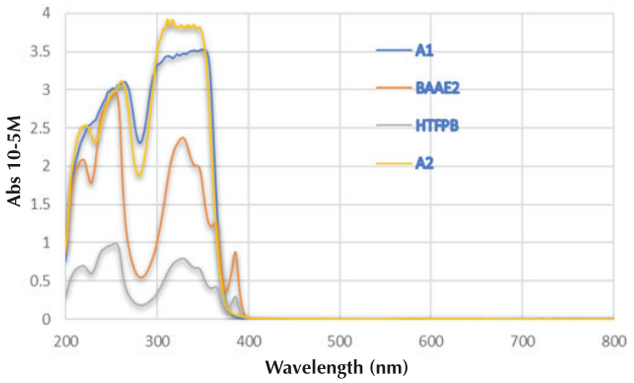

Fig. 3. Absorption spectra of A1, A2, HTFPB, and BAAE2 in CH_2Cl_2 at room temperature.

The spectra highlight strong absorptions in the region of 220-400 nm for the HTFPB and BAAE2 ligands as well as the **A1** and **A2** complexes. The broad bands observed at 327 and 328 nm are assigned to singlet-singlet π-π* transition in β-diketonate moiety [14]. These absorption bands are shifted slightly to the longer wavelength region compared with that of free HTFPB (325 nm), which hints at the perturbation of Sm^{3+} upon complexation [7]. The bands at a lower wavelength around 260 nm are anthracene-based π-π* electronic transitions. The auxiliary ligand BAAE2 is also absorbed at ultraviolet wavelengths. The lanthanide f-f transitions are not allowed, which makes absorption due to Sm^{3+} ions imperceptible in the spectra of **A1** and **A2**.

3.4. Photoluminescence spectroscopy

The photoluminescence spectra of **A1** and **A2** were studied using an excitation wavelength of 365 nm. The emission spectra are shown in the Fig. 4. Despite the quenching effect of O-H stretches, **A1** gives a strong orange color and narrow band emission. This might be due to the very efficient sensitization of TFPB to Sm^{3+}. Meanwhile, **A2** is much less emissive than **A1** but gives the same pattern of emission bands. We assume that the low-lying triplet energy level of the anthracenyl core in BAAE2 leads to intramolecular energy transfer from excited Sm^{3+}. The emission lines at 565, 603, 651, and 710 nm are assigned to the $^4G_{5/2} \rightarrow 6F_J$ (J=1/2-9/2) transitions of Sm^{3+}. The strongest emission band centered at 651 nm stems from the $^4G_{5/2} \rightarrow {}^6F_{7/2}$ transition.

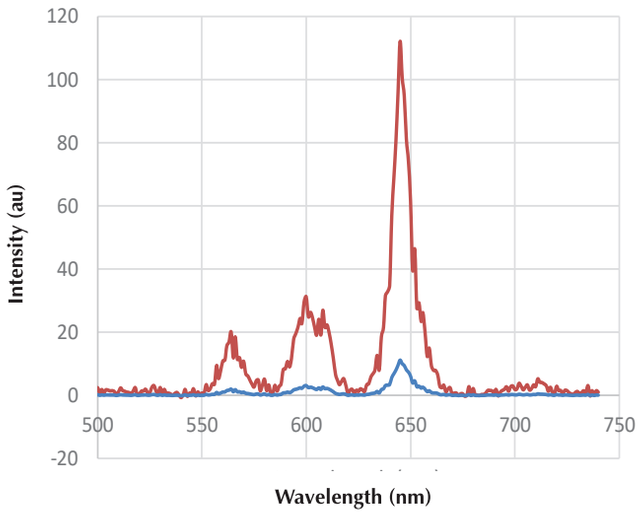

Fig. 4. PL spectra of A1 (a red line), A2 (a blue line) complexes.

4. Conclusions

Samarium (III) complexes containing TFPB and BAAE2 ligands were synthesized. The structure of **A2** was definitively determined by X-ray diffraction and revealed a five-membered chelate ring of BAAE2 with Sm^{3+} ions. The results also described that Sm^{3+} in **A2** adopts a coordination number of eight as it is bonded to six oxygen atoms from three TFPB ligands and two nitrogen atoms of BAAE2. UV-Vis results confirm the strong absorptions produced by the β-diketonate and anthracenyl fragments. The **A1** and **A2** complexes both display Sm^{3+}-centered orange emissions in which that of **A2** is much weaker due to triplet-triplet energy transfer arising from the anthracenyl ring of BAAE2. Attempts to disrupt the aromaticity of the anthracenyl ring in order to switch on Sm^{3+} emissions in **A2** are presently being made in our laboratory.

CRediT author statement

Thi Hien Dinh, Minh Hai Nguyen: Conceptualisation, Methodology, Software, Resources, Writing - Review and Editing, Validation.

ACKNOWLEDGEMENTS

This work was completed with financial support from the Ministry of Education and Training of Vietnam, under the project B2018-SPH-49.

COMPETING INTERESTS

The authors declare that there is no conflict of interest regarding the publication of this article.

REFERENCES

[1] B. Song, G. Wang, M. Tan, et al. (2006), "A europium(III) complex as an efficient singlet oxygen luminescence probe", *J. Am. Chem. Soc.*, **128(4)**, pp.13442-13450, DOI: 10.1021/ja062990f.

[2] Y. Wang, H. Wang, X. Zhao, et al. (2017), "A β-diketonate-europium(iii) complex-based fluorescent probe for highly sensitive time-gated luminescence detection of copper and sulfide ions in living cells", *New J. Chem.*, **41(13)**, pp.5981-5987, DOI: 10.1039/C7NJ00802C.

[3] M. Hatanaka, S. Yabushita (2009), "Theoretical study on the f-f transition intensities of lanthanide trihalide systems", *J. Phys. Chem. A*, **113(45)**, pp.12615-12625, DOI: 10.1021/jp9049507.

[4] Y.W. Yip, H. Wen, W.T. Wong, et al. (2012), "Increased antenna effect of the lanthanide complexes by control of a number of terdentate n-donor pyridine ligands", *Inorg. Chem.*, **51(13)**, pp.7013-7015, DOI: 10.1021/ic300916e.

[5] E.G. Moore, A.P.S. Samuel, K.N. Raymond (2009), "From antenna to assay: Lessons learned in lanthanide luminescence", *Acc. Chem. Res.*, **42(4)**, pp.542-552, DOI: 10.1021/ar800211j.

[6] H.Q. Yin, X.Y Wang, X.B. Yin (2019), "Rotation restricted emission and antenna effect in single metal-organic frameworks", *J. Am. Chem. Soc.*, **141(38)**, pp.15166-15173, DOI: 10.1021/jacs.9b06755.

[7] T.N. Trieu, T.H. Dinh, H.H. Nguyen, et al. (2015), "Novel lanthanide(iii) ternary complexes with naphthoyltrifluoroacetone: A synthetic and spectroscopic study", *Z. Anorg. Allg. Chem.*, **641(11)**, pp.1934-1940, DOI: 10.1002/zaac.201500158.

[8] Y. Ni, J. Tao, J. Jin, et al. (2014), "An investigation of the effect of ligands on thermal stability of luminescent samarium complexes", *J. Alloys Compd.*, **612**, pp.349-354, DOI: 10.1016/j.jallcom.2014.05.211.

[9] J. Sun, B. Song, Z. Ye, et al. (2015), "Mitochondria targetable time-gated luminescence probe for singlet oxygen based on a P-diketonate-europium complex", *Inorg. Chem.,* **54**, pp.1166011668.

[10] J. Wu, Y. Xing, H. Wang, et al. (2017), "Design of a β-diketonate-Eu^{3+} complex-based time-gated luminescence probe for visualizing mitochondrial singlet oxygen", *New J. Chem.*, **41(24)**, pp.15187-15194, DOI: 10.1039/C7NJ03696E.

[11] H. Ma, X. Wang, B. Song, et al. (2018), "Extending the excitation wavelength from UV to visible light for a europium complex-based mitochondria targetable luminescent probe for singlet oxygen", *Dalton Trans.*, **47(37)**, pp.12852-12857, DOI: 10.1039/C8DT02829J.

[12] S.N.A. Jenie, S.M. Hickey, Z. Du, et al. (2017), "A europium-based 'off-on' colourimetric detector of singlet oxygen", *Inorg. Chim. Acta*, **462**, pp.236-240, DOI: 10.1016/j.ica.2017.03.043.

[13] G.Q. Zhang, G.Q. Yang, L.Y. Yang, et al. (2005), "Synthesis, characterization and photophysical properties of novel dinuclear silver(I) and mononuclear palladium(II) complexes with 1,2-bis[(anthracen-9-ylmethyl)amino]ethane", *Eur. J. Inorg. Chem.*, **2005(10)**, pp.1919-1926, DOI: 10.1002/ejic.200400926.

[14] K. Lunstroot, P. Nockemann, K.V. Hecke, et al. (2009), "Visible and near-infrared emission by samarium(III)-containing ionic liquid mixtures", *Inorg. Chem.*, **48(7)**, pp.3018-3026, DOI: 10.1021/ic8020782.

DOI: 10.31276/VJSTE.63(2).25-31

A simple approach for air-gap permeance calculations in double excitation synchronous motor modelling with reluctance network

Trung-Kien Hoang[1*], L. Vido[2], Dinh-Quang Nguyen[3]

[1]Graduate University of Science and Technology, Vietnam Academy of Science and Technology, 18 Hoang Quoc Viet Street, Nghia Do Ward, Cau Giay District, Hanoi, Vietnam
[2]SATIE, Cergy - Pontoise University, Cergy City, France
[3]Institute of Energy Science, Vietnam Academy of Science and Technology, 18 Hoang Quoc Viet Street, Nghia Do Ward, Cau Giay District, Hanoi, Vietnam

Received 3 July 2020; revised 14 October 2020; accepted 28 October 2020

Abstract:

This article proposes an easy-to-use approximation for air-gap permeance calculations in a reluctance network. An extension of the overlap area between the stator and its corresponding rotor tooth to a position where the permeance becomes zero is also proposed. The advantage of this method is the simplification of conventional complex reluctance calculations while maintaining high accuracy. The proposed approach is applied to a double excitation synchronous motor, which usually requires a 3D simulation tool for the calculations. The validation of the accuracy of the proposed method on the flux linkage, back EMF, and electromagnetic torque are accomplished by comparison with those obtained from a conventional method and experimental data. This method used in this paper is less time consuming and has a lower complexity in building RN model, which makes the proposed approach quite adaptive to the design phase when a lot of geometry variants must be realised and examined, for example, during the optimisation process. The results of the comparison recommend the use of the proposed method for different electrical motor geometries.

Keywords: **double excitation, reluctance network, 3D simulation.**

Classification number: **2.3**

1. Introduction

A double excitation synchronous motor (DESM) combines permanent magnets and excitation windings to form the double excitation principle. The advantages of permanent magnets and windings is that they satisfy the requirements of railway traction applications that require a wide range of motor operations. Several papers have been published that focus on DESM [1-4].

The finite element method (FEM) is a traditional tool that is capable of highly accurate results. However, FEM is time consuming and, further, 3D FEM makes the optimisation design stage of a motor impossible. As an alternative, the reluctance network (RN) method provides fast, ready-to-analyse results while good accuracy is still maintained. This method transforms the motor into a magnetic circuit represented by nodes, reluctances, and magneto-motive forces (MMF). The RN method is widely employed in electric motor analysis [5-8].

One of the key components of the RN model is the air-gap permeance, which varies according to the relative position between the rotor and stator [9]. In order to calculate air-gap permeance, flux paths through the air-gap are often structurally approximated [10-13]. In the simplest approach, the air-gap flux is bounded by an overlapped area between the stator and rotor teeth. In V. Ostovic (1989) [10] research a permeance evolution law is defined to connect a stator tooth to a rotor tooth. The Schwarz-Christoffel transformation was used to calculate the air-gap permeance for a simple 2D air-gap configuration such as that of transformer cores [11]. Z. Zhu, et al. (2005) [12] research the air-gap permeance is well approximated considering every possible flux path between the stator and rotor teeth. In this paper, the authors propose to calculate the air-gap permeance by extending the overlapped area between the stator and its corresponding rotor tooth to the position where the permeance becomes zero. To examine the validity of the proposed approach, the results are compared with the ones obtained by the method and experimental measurements.

[*]Corresponding author: Email: hoang-trung.kien@usth.edu.vn

2. Reluctance network method with DESM

2.1. DESM model configuration

The studied model of the DESM is displayed in Fig. 1 [3].

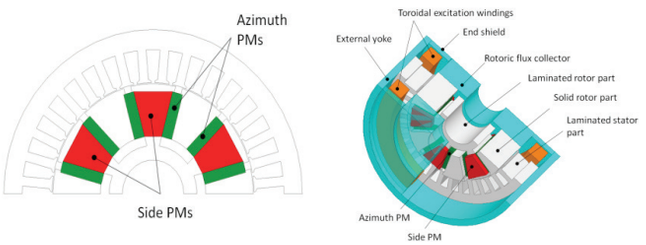

(A) (B)

Fig. 1. The DESM model (A) the arrangement of permanent magnets (PMs) in a 2D and (B) a 3D view.

In the configuration of Fig. 1 (phase windings are not shown for clarity), two toroidal excitation windings are placed in the stator. Ferrite permanent magnets (PMs) are placed in the rotor to increase the air-gap flux density under the flux focusing principle. The stator has a conventional laminated core while both solid and laminated cores are used in the rotor due to the presence of 3D flux paths.

2.2. RN method

In this article, the flux tube method is employed. This is the most popular implementation of the RN method, which was proposed by V. Ostovic (1989) [10]. Each part of the machine is represented by the reluctance limited by a flux tube. Inside the tube, the flux is assumed to be constant. A basic expression for the reluctance of the flux tube can be given by Eq. 1 [2]:

$$R = \frac{l}{\mu_r \mu_0 S} \tag{1}$$

where l is the length, S is the cross section of the flux tube, μ_r is the relative permeability of the tube's material, and μ_0 is the absolute permeability of the air. For the air and PMs, μ_r equals unity and for the core, μ_r is computed based on the nonlinear magnetization curve of the core material.

A permanent magnet can be modelled by a reluctance connected in series with an equivalent MMF as in Eq. 2:

$$M_{PM} = \frac{B_r}{\mu_r \mu_0} h_m \tag{2}$$

where h_m and B_r are the magnet thickness and remanence, respectively.

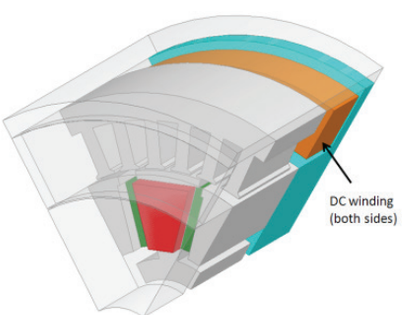

(A)

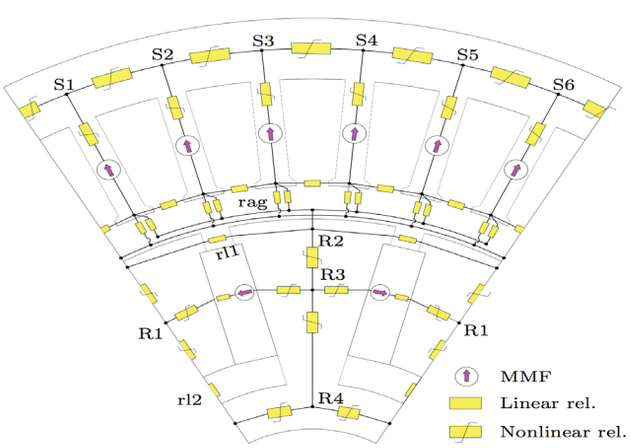

(B)

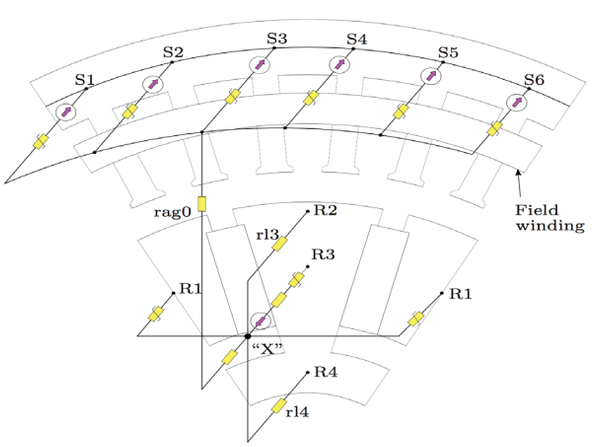

(C)

Fig. 2. The RN model of the studied DESM (A) one pole pair for modelling, (B) first part of the RN, and (C) second part of the RN (in the axial direction).

Figure 2 presents the reluctance model, which is defined for one pole pair. The air-gap length is exaggerated to be large for ease of observation.

The reluctance model is comprised of two parts. The first part, presented in Fig. 2B, consists of the stator, rotor, phase windings, and azimuth magnets. The second part, with one of its two identical sides shown in Fig. 2C, is composed of the external yoke, rotoric flux collectors, excitation windings, side magnets, and end shields. The purpose of the second part is to conduct the flux along the third dimension. This flux begins at the stator, goes through the air-gap reluctance (Fig. 2B) and then passes through the side PMs, rotoric collector, outer air- gap reluctance (Fig. 2C), and the end shield before returning to the stator. In Fig. 2B, the phase MMFs are put in the stator teeth and the net MMF is given by Eq. 3:

$$M_{phase} = (I_1 - I_2)N_c \tag{3}$$

where N_c is the number of turns in the phase winding, and I_1 and I_2 are the phase currents flowing through the winding placed in the slot.

In this model, two reluctances are used to connect a stator tooth to two rotor poles. The flux is assumed to be perpendicular to the stator and rotor tooth surfaces. In this sense, the tangential component of the air-gap flux density is neglected. In the simplest manner, the air-gap flux path is confined to the overlapped area between the rotor pole and stator tooth. Improved approximations to mitigate the fringing effect will be discussed in next section.

3. Air-gap permeance calculations

3.1. Air-gap permeance with detailed flux fringing path

In comparison to the permeances of the ferromagnetic regions and permanent magnets, the permeances of the air-gap region are more complicated because of their flux fringing paths as displayed in Fig. 3. To simplify the complex flux paths, Z. Zhu, et al. (2005) [12] assume an equipotential on the stator and rotor surface flux paths that are perpendicular to the tooth surfaces.

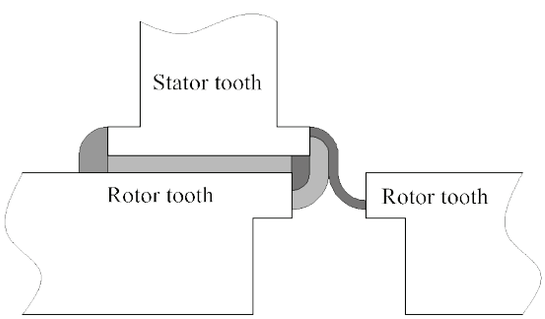

Fig. 3. Fringing effect illustration in the air-gap region.

Figure 4 shows several typical flux paths and permeance calculations in the air-gap. Given a motor geometry, all possible flux paths can be approximated according to the above assumptions.

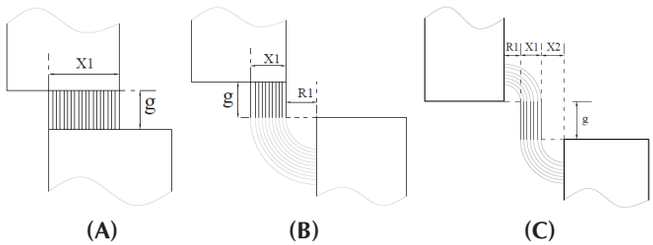

Fig. 4. Typical air-gap permeance.

The permeance for the air-gap in Figs. 4A, 4B, and 4C can be calculated from Eqs. 4-6, respectively [12]:

$$P = \frac{\mu_0 L_a X_1}{g} \tag{4}$$

$$P = \frac{2\mu_0 L_a}{\pi} \ln\left(1 + \frac{\pi X_1}{\pi X_1 + 2g}\right) \tag{5}$$

$$P = \frac{\mu_0 L_a}{\pi} \ln\left(1 + \frac{2\pi X_1}{\pi(R_1 + R_2 + 2g)}\right) \tag{6}$$

where L_a is axial length of the teeth, other variables are shown in Fig. 4.

This approach considers every flux fringing path in detail; however, the difficulty is that every combination of relative positions between the stator and rotor teeth must be considered. For example, the prototype of the DESM in the present work has 17 relative positions to be analysed and each position includes several functions to determine the permeances of different flux paths. The air-gap permeance between the stator and rotor teeth as function of the stator tooth position is shown in Fig. 5.

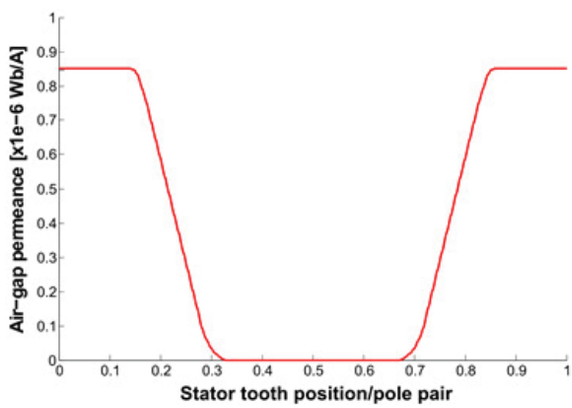

Fig. 5. Air-gap permeance as function of the stator tooth position.

3.2. Simple approximation method

In response to the time-consuming nature of considering every possible flux path presented in the air-gap permeance approximation above, this paper proposes an approach to further simplify the calculations. The overall strategy is to define a new approach that simplifies the process while keeping the air-gap permeance closely matched to the one obtained by the traditional approach. The permeance curve shown in Fig. 5 consists of three different types: the maximum permeance, zero permeance, and the transition between those two values. The approach proposed in this article determines the positions in which the air-gap permeances are maximum and minimum (zero). A linear transition from maximum to zero is proposed. This is based on the fact that the transition displayed in Fig. 5 is mostly linear.

The air-gap permeance is a maximum value when the overlapped area is maximized as shown in Fig. 6. The approach Z. Zhu, et al. (2005) [12] presents three different flux paths, however, in this work, these three flux paths are replaced by one equivalent path. The overlapped area will, therefore, be extended to create the same permeance as calculated Z. Zhu, et al. (2005) [12]. In the proposed method, the overlapped area will be extended by 0.41 mm to each side of the stator tooth, which is approximately equivalent to 80% of the air-gap length (g=0.5 mm). In a general case, the extended area is suggested to be between 0.8 to 1.0 times the air-gap length. The air-gap permeance remains constant until the right edge of stator tooth reaches the right side of rotor tooth as illustrated in Fig. 6C.

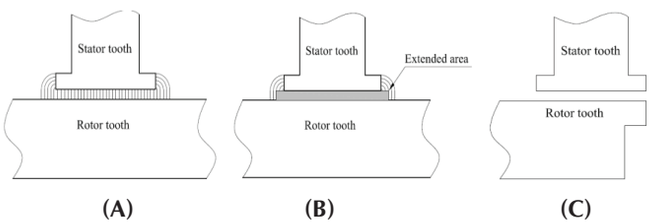

Fig. 6. Replacement of flux fringing paths by extending the overlapped area (A) the flux fringing path under consideration, (B) the overlapped area extension, and (C) the end position for the maximum air-gap permeance area.

One can assume that the starting point for the zero-permeance area (shown in Fig. 7) is the same as the one in the above method. The permeance comparison for this case is shown in Fig. 8. As can be seen from Fig. 8, there is a significant difference between the two air-gap permeances.

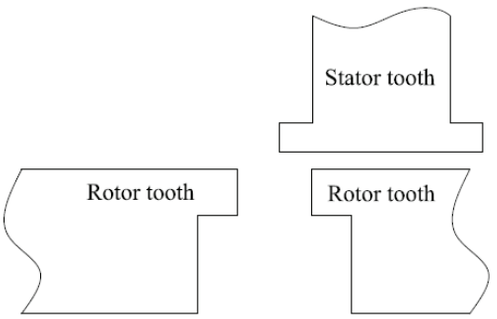

Fig. 7. Position where the air-gap permeance between the stator tooth and the left rotor tooth becomes zero.

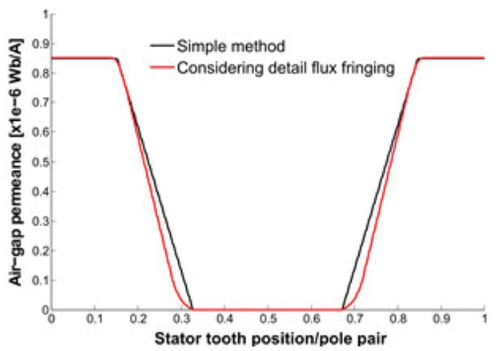

Fig. 8. Air-gap permeance comparison between the two approaches (with the same zero-permeance area).

In order to deal with the error, we suppose a starting point for the zero-permeance area that is earlier than that of the method considering detailed flux fringing paths. In this article, the starting point is assumed to be in the middle of the right edge of the rotor tooth at the point where the permeance considering the fringing path becomes zero. A comparison of the air-gap permeance, accounting for this difference, is displayed in Fig. 9. As seen in Fig. 9, there is a smooth transformation from maximum to zero permeance for the method considering every flux fringing path.

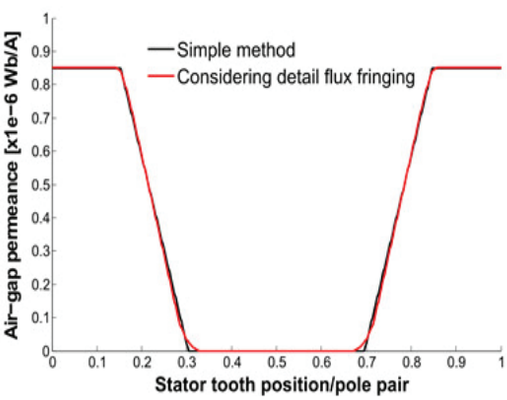

Fig. 9. Air-gap permeance comparison between two approaches (the starting point of zero-permeance area is shifted to the left).

By this simplification, the determination of the air-gap permeance at various rotor angle becomes straightforward. Only five critical positions, corresponding to five different waveforms, need to be determined as seen in Fig. 9. Compared to the 17 positions that must be determined in the previous method, this new method greatly reduces the complexity of the permeance function determination.

4. Comparison between two methods and with experiments

4.1. RN nonlinear equation solving

The system of equations for flux calculations is given by Eq. 7:

$$[P]\times[U]=[\Phi] \tag{7}$$

where *[P]*, *[U],* and *[ϕ]* are the permeance, magnetic scalar potential, and equivalent flux source matrices, respectively. At each rotor position, the fixed-point method is employed to solve Eq. 7. The new permeability update is expressed by Eq. 8, which was first developed and used by J.C. Wilson (1969) [14]:

$$\mu^{n+1}=\alpha\left(\mu_p^{n+1}-\mu^n\right)+\mu^n \tag{8}$$

where μ^n is the permeability obtained from the n^{th} iteration, μ_p^{n+1} is the provisional permeability computed during the $(n+1)^{th}$ iteration, and α is the relaxation factor. In this paper, α is chosen to be 0.5. The algorithm is explained in Fig. 10. In this algorithm, the maximum number of iterations can be set to avoid infinite loops.

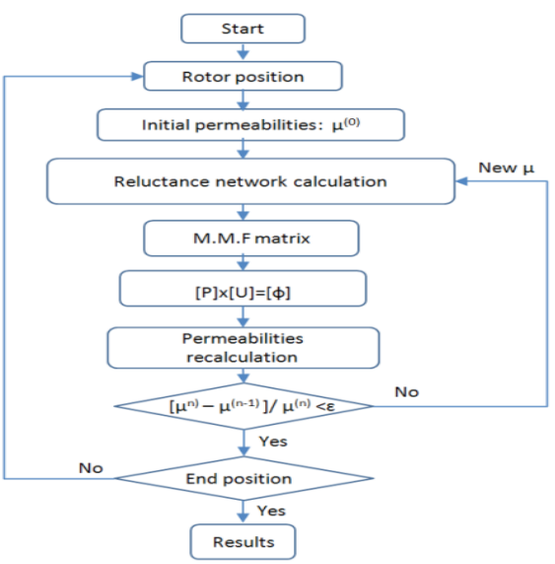

Fig. 10. Algorithm diagram for nonlinear equation solving.

In Fig. 10, the permeability recalculations are based on the B-H curve of the core material. J. Cale, et al. (2006) [15] research, the permeability is presented as a function of the flux density. This approximation function is advantageous because of the quick computation time and high accuracy due to smooth interpolation when compared to using a look-up table of the original magnetization curve. This permeability fitting function is given by Eq. 9 and is shown in Fig. 11:

$$\mu_B(B)=\mu_0\frac{\frac{1}{K}\sum_{k=1}^{K}\left(\left|\frac{B}{m_k}\right|^{n_k}+a_k^{n_k}\right)^{\frac{1}{n_k}}}{\frac{1}{K}\sum_{k=1}^{K}\left(\left|\frac{B}{m_k}\right|^{n_k}+a_k^{n_k}\right)^{\frac{1}{n_k}}-1} \tag{9}$$

where μ_B is the permeability, which is flux density dependent, K is the approximation order, and a_k, m_k, and n_k are the fitting coefficients. The coefficient b_k is defined such that $a_k=b_k/(b_k-1)$. The values of the coefficients are shown in Table 1. According to Eq. 9, when the flux density increases toward infinity, the permeability approaches the permeability of the air, μ_0.

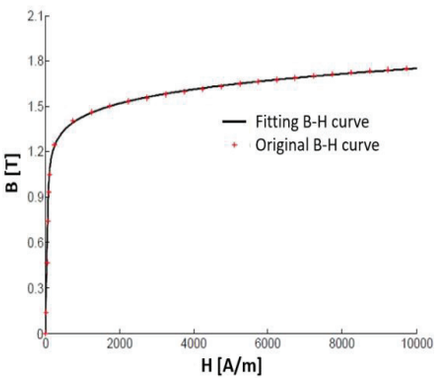

Fig. 11. Magnetization curve of the core material.

Table 1. Fitting coefficients for permeability function.

k	1	2	3	4	5
b_k	1e10	3e6	694	723	111
n_k	6.7	11.8	7.1	12.6	40.0
m_k	19.9	1.9	50.0	21.5	17.6

4.2. Result comparisons

The simulations are implemented by MATLAB and done for one pole pair, which is a 60 mechanical degree consisting of 60 points. The computation time is about one second, which is extremely advantageous thanks to the use of the RN method. By the use of the DC excitation windings, the air-gap flux can be easily increased or decreased by controlling the excitation current (I_{dc}). The motor's prototype is displayed in Fig. 12 for the comparison analysis with the RN.

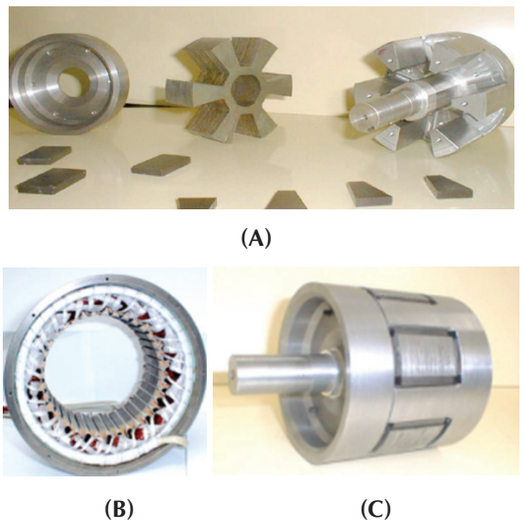

Fig. 12. DESM prototype (A) disassembled rotor, (B) stator, and (C) assembled rotor.

Flux linkage and back EMF: The flux linkage, Ψ, can be computed directly by solving Eq. 7 where the phase back EMFs are found from the derivatives of the phase flux linkage in Eq. 10:

$$e = -\frac{d\psi}{dt} \tag{10}$$

The experimental flux is derived from an integral of the measured winding's voltage. The principle of the DC excitation current supply is shown in Fig. 13 where the excitation winding is represented by the inductance L. With this control circuit, the current excitation direction can be reversed. Fig. 14 compares the flux linkages and back EMFs at a speed of 170 rpm and under a no-load condition. The flux weakening is also tested by injecting a negative DC excitation current of amplitude -3 A. As can be seen from Fig. 14, a good accordance is achieved and there is almost no difference reported in the flux linkage comparisons. However, there is a little difference between the waveforms of the back EMF, which is due to the smoother wave form that leads to a smoother waveform of the back EMF when taking the first derivative. Both methods agree well with the experimental results.

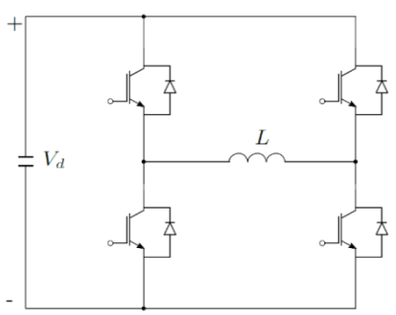

Fig. 13. DC power supply circuit for the excitation windings.

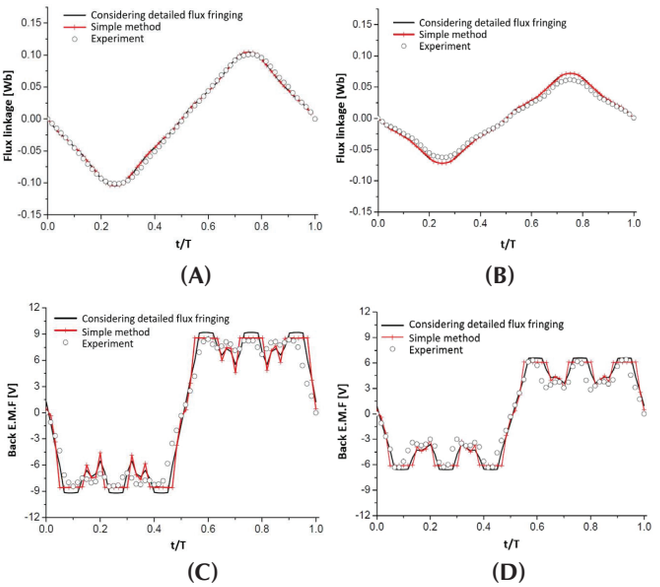

Fig. 14. Comparisons under a no-load condition at 170 rpm (A) flux linkage at I_{dc}=0 A, (B) flux linkage at I_{dc}=-3 A, (C) EMF at I_{dc}=0 A, and (D) EMF at I_{dc}=-3 A.

Electromagnetic torque calculation: In this paper, the electromagnetic torque is calculated by using the virtual work principle, which is based on the derivative of the magnetic co-energy, W_{co}, with respect to the rotor's angular position, θ, while keeping the phase current constant as in Eq. 11:

$$T_e = \left.\frac{\Delta W_o}{\Delta\theta}\right|_{i=const} \tag{11}$$

The torque comparisons are displayed in Fig. 15 for a range of phase current from zero to the rated value (10 A) and the excitation windings are not excited. The phase shift angle between the EMF and phase current is null. As seen in Fig. 15, a good accordance is reported. In Fig. 16, the torque comparison between the proposed concepts, the RN method considering detailed flux paths, and 3D FEM is presented. In this comparison, an air-gap flux enhancement by a positive excitation current of 3 A is examined. As seen in Fig. 16, the proposed concept agrees well with the two other methods.

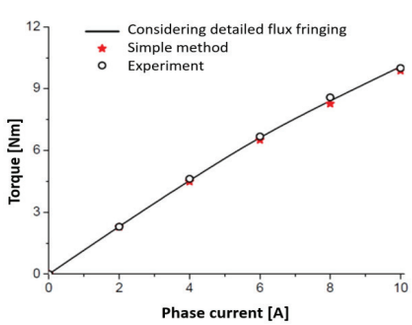

Fig. 15. Torque comparison for various phase currents (I_{dc}=0 A).

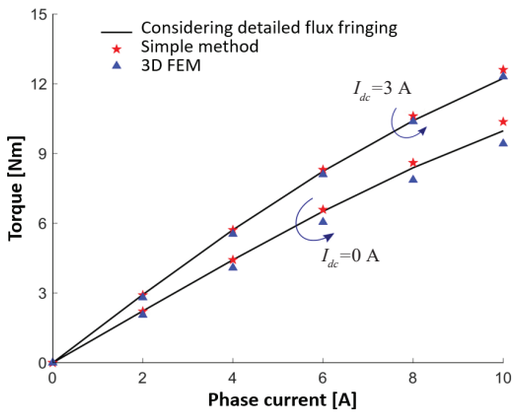

Fig. 16. Torque comparison between RN method and 3D FEM.

5. Conclusions

This paper has proposed a simple approach for air-gap permeance calculations. The proposed method's convenience and efficiency was shown by comparisons with other methods and measurement. This method is suggested for other machine types with different teeth structures. This method is less time consuming and has a lower complexity in building RN model, which makes the proposed approach quite adaptive to the design phase when a lot of geometry variants must be realised and examined, for example, during the optimisation process.

CRediT author statement

Trung-Kien Hoang, L. Vido, Dinh-Quang Nguyen: Conceptualisation, Methodology, Software, Resources, Writing - Review and Editing, Validation.

ACKNOWLEDGEMENTS

This research is funded by Graduate University of Science and Technology under grant number GUST.STS. DT2019-KHVL02. The authors gratefully acknowledge University of Science and Technology of Hanoi for supporting this research.

COMPETING INTERESTS

The authors declare that there is no conflict of interest regarding the publication of this article.

REFERENCES

[1] Y. Amara, L. Vido, M. Gabsi, et al. (2009), "Hybrid excitation synchronous machines: Energy-efficient solution for vehicles propulsion", *IEEE Transactions on Vehicular Technology*, **58(5)**, pp.2137-2149, DOI: 10.1109/TVT.2008.2009306.

[2] C. Ilie, M. Mihaiescu, I. Chirita, et al. (2019), "Synchronous electric generator with double excitation", *11th International Symposium on Advanced Topics in Electrical Engineering (ATEE)*, pp.1-4, DOI: 10.1109/ATEE.2019.8724866.

[3] L. Vido, M. Gabsi, M. Lecrivain, et al. (2005), "Homopolar and bipolar hybrid excitation synchronous machines", *IEEE International Conference on Electric Machines and Drives*, pp.1212-1218, DOI: 10.1109/IEMDC.2005.195876.

[4] B. Nedjar, S. Hlioui, Y. Amara, et al. (2011), "A new parallel double excitation synchronous machine", *IEEE Transactions on Magnetics*, **47(9)**, pp.2252-2260, DOI: 10.1109/TMAG.2011.2134864.

[5] Y. Hane, K. Nakamura (2018), "Reluctance network model of permanent magnet synchronous motor considering magnetic hysteresis behaviour", *IEEE International Magnetics Conference (INTERMAG)*, Singapore, pp.1-5, DOI: 10.1109/INTMAG.2018.850811.

[6] N. Ullah, F. Khan, W. Ullah, et al. (2018), "Magnetic equivalent circuit models using global reluctance networks methodology for design of permanent magnet flux switching machine", *15th International Bhurban Conference on Applied Sciences and Technology (IBCAST),* Islamabad, pp.397-404, DOI: 10.1109/IBCAST.2018.8312255.

[7] K. Nakamura, O. Ichinokura (2008), "Dynamic simulation of Pm motor drive system based on reluctance network analysis", *13th International Power Electronics and Motion Control Conference*, pp.758-762, DOI: 10.1109/EPEPEMC.2008.4635358.

[8] N. Bracikowski, M. Hecquet, P. Brochet, et al. (2012), "Multiphysics modeling of a permanent magnet synchronous machine by using lumped models", *IEEE Transactions on Industrial Electronics*, **59(6)**, pp.2426-2437, DOI: 10.1109/TIE.2011.2169640.

[9] J.M. Williams (2004), *Modelling and Analysis of Electric Machines with Asymmetric Rotor Poles Using a Reluctances Based, Magnetic Equivalent Circuit*, Doctoral Dissertation, University of Missouri-Rolla, 202pp.

[10] V. Ostovic (1989), *Dynamics of Saturated Machines,* Springer-Verlag New York, 445pp.

[11] A. Balakrishnan, W. Joines, T. Wilson (1997), "Air-gap reluctance and inductance calculations for magnetic circuits using a Schwarz-Christoffel transformation", *IEEE Transactions on Industrial Electronics*, **12(4)**, pp.654-663, DOI: 10.1109/63.602560.

[12] Z. Zhu, Y. Pang, D. Howe, et al. (2005), "Analysis of electromagnetic performance of fluxswitching permanent-magnet machines by nonlinear adaptive lumped parameter magnetic circuit model", *IEEE Transactions on Magnetics*, **41(11)**, pp.4277-4287, DOI: 10.1109/TMAG.2005.854441.

[13] C. Stuebig, B. Ponick (2008), "Determination of air-gap permeances of hybrid stepping motors for calculation of motor behaviour", *18th International Conference on Electrical Machines*, pp.1-5, DOI: 10.1109/ICELMACH.2008.4800016.

[14] J.C. Wilson (1969), *Theory of The Solid Rotor Induction Machine*, Doctoral Dissertation, University of Colorado, 396pp.

[15] J. Cale, S. Sudhoff, J. Turner (2006), "An improved magnetic characterisation method for highly permeable materials", *IEEE Transactions on Magnetics*, **42(8)**, pp.1974-1981, DOI: 10.1109/TMAG.2006.876087.

DOI: 10.31276/VJSTE.63(2).32-38

An effective method for detecting dorsal hand veins utilising near-infrared imaging technology

Hai Thanh Le[1*], Hien Thi-Thu Pham[2]

[1]Faculty of Mechanical Engineering, University of Technology, Vietnam National University - Ho Chi Minh City, 268 Ly Thuong Kiet Street, Ward 14, District 10, Ho Chi Minh City, Vietnam

[2]Department of Biomedical Engineering, International University, Vietnam National University - Ho Chi Minh City, 268 Ly Thuong Kiet Street, Ward 14, District 10, Ho Chi Minh City, Vietnam

Received 23 April 2019; revised 14 June 2019; accepted 26 June 2019

Abstract:

Intravenous access for blood collection and other related therapies is one of the most frequently practiced procedures in the modern medical system. The procedure requires complex training and experience, as it might cause dangerous nerve damage and subcutaneous bleeding. This paper proposes a dorsal hand vein detection method utilising the near-infrared (NIR) imaging device to segment and visualise the subcutaneous vein patterns on the skin directly. Applying NIR light has received substantial attention because of its non-invasive and revealing substantially more information than the visible one. The proposed method is divided into the low- and high-level processes. The captured image is smoothed and enhanced to make the vein patterns clearer in the low-level process. The pre-processed image is then segmented step by step to extract the vein features and eliminate the pseudo-vein regions precisely. Lastly, the detected veins are thinned to reduce the thickness and projected back onto the acquired image in the high-level process. The proposed method performs effectively in detecting the clear dorsal hand veins through the experiment with a processing time of 0.61s for the high-resolution image.

Keywords: **adaptive thresholding, feature extraction, image processing, near-infrared, vein detection.**

Classification number: **2.3**

1. Introduction

Venipuncture is an invasive procedure to obtain intravenous access for blood collection and other intravenous therapies. One of the most frequently practiced procedures in modern medicine, over one billion cases are performed annually by 90% of hospitals worldwide [1]. It causes mild pain, and subsequent nerve damage and subcutaneous bleeding are not uncommon. Extreme internal bleeding, trauma, and chronic pain such as complex regional pain syndrome resulting from damage to the peripheral and central nervous system have been reported across decades [2-4]. Venipuncture is difficult even for experienced medical practitioners as a result of many factors such as the size and depth of a patient's vein, non-uniform fat distribution. or skin color. Clinical studies have indicated that 25 to 50% of patients necessitate multiple attempts to obtain peripheral venous access [5].

Several imaging modalities have recently been proposed to improve the success rate of the procedure attempt, including transillumination, ultrasound, and NIR imaging devices. Transillumination is a technique in which light is focused through tissues. The method is limited to infants and small children because the light intensity decreases by absorption in thicker, denser tissues and cannot penetrate through the hand or wrist area [6]. Ultrasound utilises high-frequency acoustic waves to image vessels and tissues, but its probe requires haptic control and occupies the attention of one hand; the procedure itself requires skills and experience to attempt placing the needle precisely in a three-dimensional structure with only its two-dimensional projection to work on [7]. The NIR light vein-viewing device has the advantages of offering a quick, cost-effective solution to intravenous access in critically ill children [8].

Applications of NIR imaging technique in vein detection have not been exhaustively explored relative to those of other imaging techniques. This non-invasive imaging technique can rapidly deliver high-end results at a low

[*]Corresponding author: Email: lthai@hcmut.edu.vn

cost. T.D. Pham, et al. (2015) [9] developed a device using six NIR light-emitting diodes (LEDs) and a webcam to construct a finger-vein database. This database provided training data sets to distinguish real fingers from fake fingers. They also incorporated in their image recognition algorithm a convolutional neural network for vein feature extraction, principal component analysis for dimensionality reduction, and a support vector machine for classification [10]. H. Li, et al. (2015) [11] developed a method to extract the dorsal hand vein by first registering the region of interest on the back of the hand and then detecting the veins with a thickness of one pixel through normalisation, morphological operators, and refinement. Additionally, S. Crisan, et al. (2018) [12] presented a system to detect the liveness of the hand vein by embedding the temperature, pressure, and humidity sensors in the developed biometric module. However, the accuracy of this system could depend on the calibration step of the sensors.

The previous study proposed an imaging system which consists of a computer with MATLAB and Simulink software, a Raspberry Pi 2 (a credit card-sized single-board computer), a NIR light source and camera, a visible light filter, and a Pico projector [13]. The imaging system will examine the area of interest by flooding it with NIR light of 940 nm wavelength. The reflected light passes through the plastic filter to remove visible light before being captured by the camera board and converted into digital signals. This system can quickly capture and process a high-resolution image of a hand but has yet to mark the position of vein patterns on the original image. This study is intended to improve upon the previous result by changing the programming language from MATLAB to Python to reduce processing time, modifying and integrating some techniques to extract vein patterns and project them back onto the original image.

2. Materials and methods

The NIR imaging system has been used to collect a dataset of dorsal left- and right-hand 1280×720-pixel images from 12 males and 10 females between the ages of 9 and 66 years (with an average age of 28.1 years). These images are twice the size of the previous ones we used [13]. Figs. 1 and 2 depict the dorsal right-hand of female and male subjects.

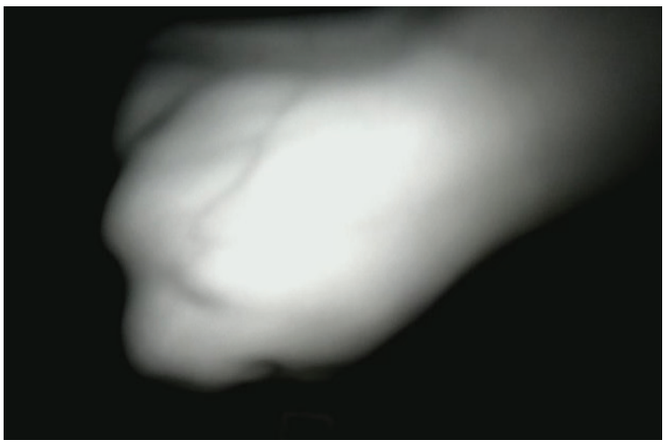

Fig. 1. Dorsal hand of female of 40 years.

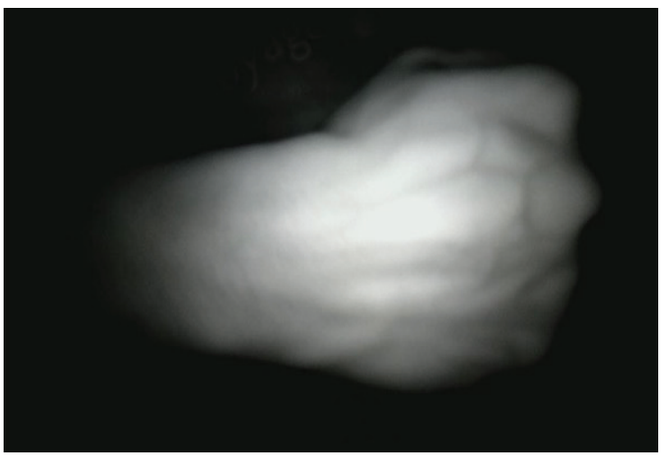

Fig. 2. Dorsal hand of male of 21 years.

Figure 3 illustrates the 10-step procedure of the proposed method. This method is divided into two types of computerising processes: low- and high-level. The low-level process involves basic image pre-processing to smoothen the image and enhance contrast. High-level processing involves partitioning an image into regions or objects (segmentation), removing objects that are not the cephalic veins, also called pseudo-vein objects (simplification), and vein refinement. Low-level processing involves pre-processing an image for effective vein extraction by the high-level process. Image pre-processing improves the quality of images captured under poor lighting conditions so that cephalic veins can be easily segmented in the next step. The high-level process segmented and simplified the image to extract branching patterns, edges of vessel walls, and other characteristics of the veins.

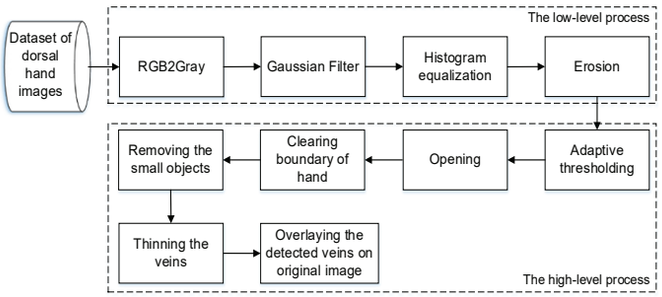

Fig. 3. The 10-step procedure of the proposed method.

2.1. Low-level process

A Gaussian filter is applied after the colour-to-grayscale conversion step. This filter attenuates the high-frequency noise of glare and non-uniform brightness resulting from the close proximity of the light source to the region of interest and the device's variable positioning. This filter blurs an image based on a weighted average of each pixel's neighbourhood; therefore, it can preserve edges better than the median filter used in the previous study. The histogram equalisation was maintained to keep the local contrast consistent. Because hemoglobin in the blood has higher absorption coefficient around NIR frequencies than collagen or melanin, vein patterns would appear darker, whereas skin would appear lighter; therefore, a morphological erosion operator was used to thicken the veins by adding more pixels to dark regions. Figs. 4B, 4C, 4D illustrate the result of the three above steps applied to the grayscale image in Fig. 4A. These pre-processing steps rendered cephalic veins clearly visible and easy to identify and segment in the subsequent step.

2.2. High-level process

Segmentation is the most crucial step in this process to extract the characteristics of the vein, create patterns, and clear the other remaining objects. The adaptive thresholding technique for segmentation is suitable where illumination change affects the image and vein size is minor relative to the skin area and image background. D. Bradley, et al. (2011) [14] developed an adaptive thresholding method to set a pixel to black or white based on the average of its neighbourhood in the $s \times s$ window. This study has optimised the sensitivity and computational intensiveness of D. Bradley's method by reducing the threshold value from 15 to 4% and the neighbourhood size s by half. The value of the current pixel can be completely calculated by T(x,y), as given in Equation 1.

$$T(x,y) = \begin{cases} 0 & if\left(f(x,y)\text{x}N_{sxs}\right) > sumA\text{x}(100\text{x}t)/100 \\ 1 & otherwise \end{cases} \quad (1)$$

where $T(x,y)$ is the binary image, $f(x,y)$ is the preprocessed image, $N_{s\times s}$ is number of pixels in the $s \times s$ window, and $sumA$ is the sum of intensity of all pixels in the $s \times s$ window.

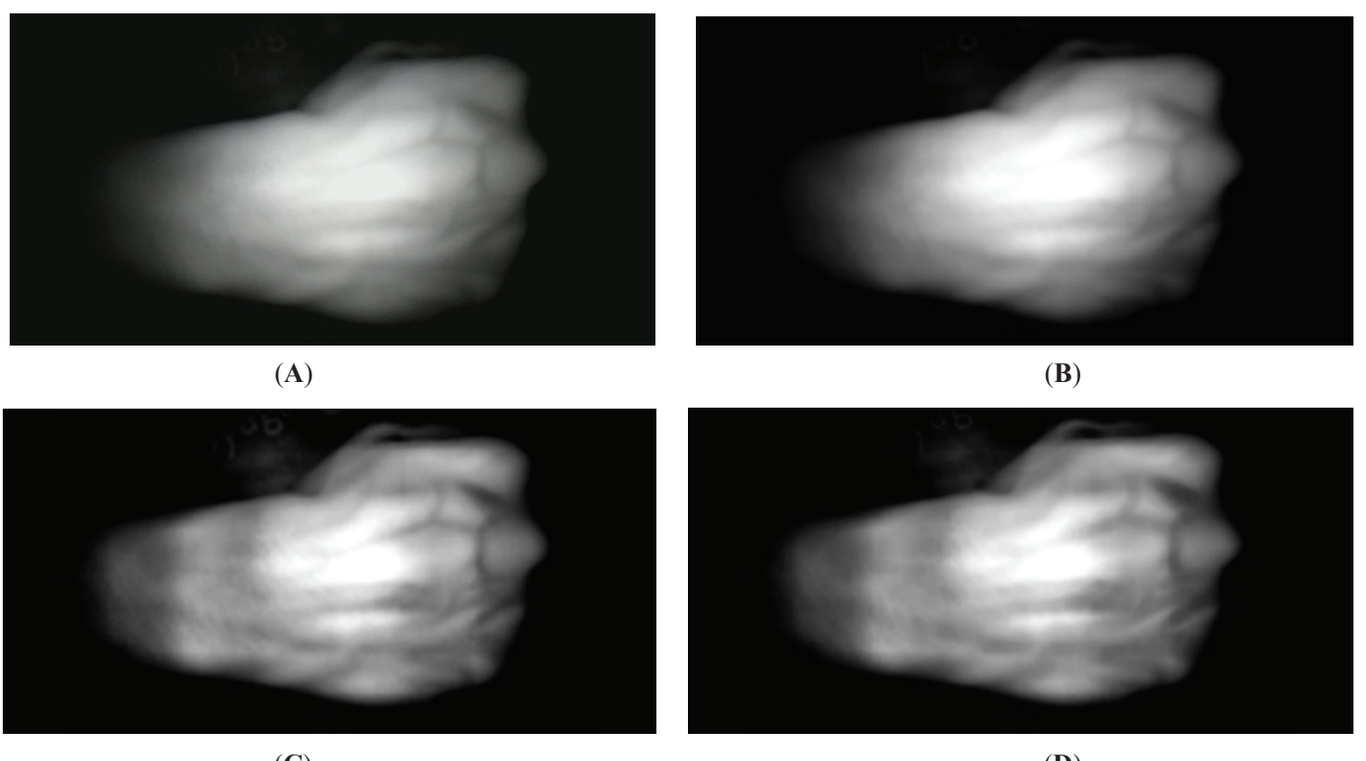

(A) **(B)**

(C) **(D)**

Fig. 4. Result images in low-level process. (**A, B**) Grayscale image is applied Gaussian filter with σ=2.5; (**C**) Histogram equalisation; (**D**) Erosion operator with the structure element size 7×7.

The vein patterns were then determined, the other objects were removed during post-processing. Objects' boundaries were curved from smoothening with circular structuring element. This operator removed some of the small objects inside and separated them from the border (Fig. 5). The clear_border function was used to remove any object that touches the border within a 0÷50 pixels range (Fig. 6) [15]. Any object less than 100 pixels in length was eliminated based on the characteristics of the vein patterns in the dataset (Fig. 7). The erosion step during pre-processing can alter the thickness of the detected veins; therefore, a thinning algorithm and morphological dilation operator is applied for better depiction of vein thickness. Fig. 8 illustrates the thinned line and boundary of the dilated veins. Finally, these veins were projected back onto the original image (Fig. 9).

Fig. 5. Opening image.
The circular structuring element has a diameter of nine pixels. The input image is Fig. 4B.

Fig. 6. Cleared border image.

Fig. 7. Image of removed short objects in horizontal axis.

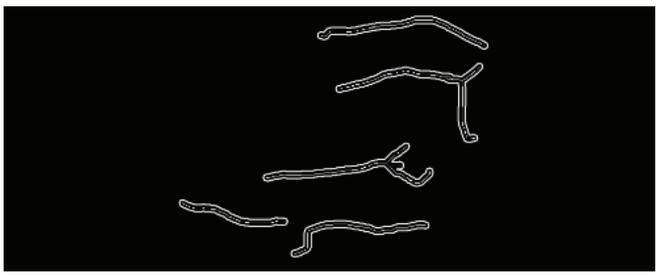

Fig. 8. Thinned and bounded vein image.
After applying the thinning technique, the dilation operator is used with the circular structuring element of five pixels. The input image is Fig. 7.

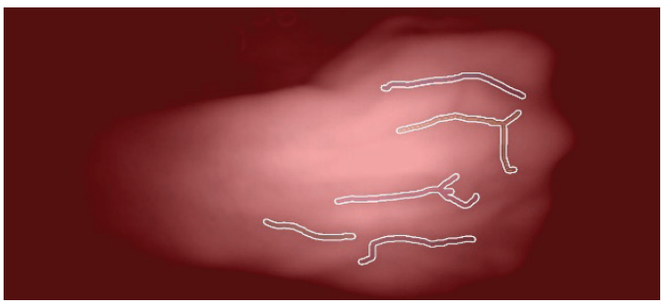

Fig. 9. Coloured veins on the original image.
The segmented vein patterns (colors) overlaid on Fig. 4A.

3. Results and discussion

It was proven that the adaptive thresholding algorithm with modified parameters could better segment the veins. Fig. 10 illustrates the results of the original adaptive thresholding and the modified technique. The processing time of the modified algorithm in Cython was 0.025s, approximately 37% faster than the threshold_local algorithm in scikit-image library, suitable for any real-time application [15, 16]. The proposed method was written with Python and scikit-image library and processed the high-resolution image with the computational time of 0.61s. Figs. 11 and 12 illustrate vein segmentation results of the left- and right-hand of female and male from the dataset, respectively. For a simpler and more straightforward method, the performance was comparable to H. Li, et al.'s (2015) [11] approach, and even the detected veins were more apparent when projected back onto the original image.

Since no skill was required to operate the NIR imaging system, the captured image could impose some problems, as suggested in Figs. 11 and 12. Nonetheless, the segmentation results clearly indicated the effectiveness and stability of the proposed method. Any exception to this high performance, which prevents the extraction of the vein patterns, may be the result of the over-illumination of an area in some images (Figs. 11B and 12B), or inadequate contrast and an object's size disproportion during the adaptive thresholding step (Fig. 12C). Some pseudo-vein patterns can be detected as large dark regions (Figs. 11B, 11D, 12A, 12D), or sometimes the vein is close to the dark region, and a longer vein is therefore segmented (Figs. 11C and 12C).

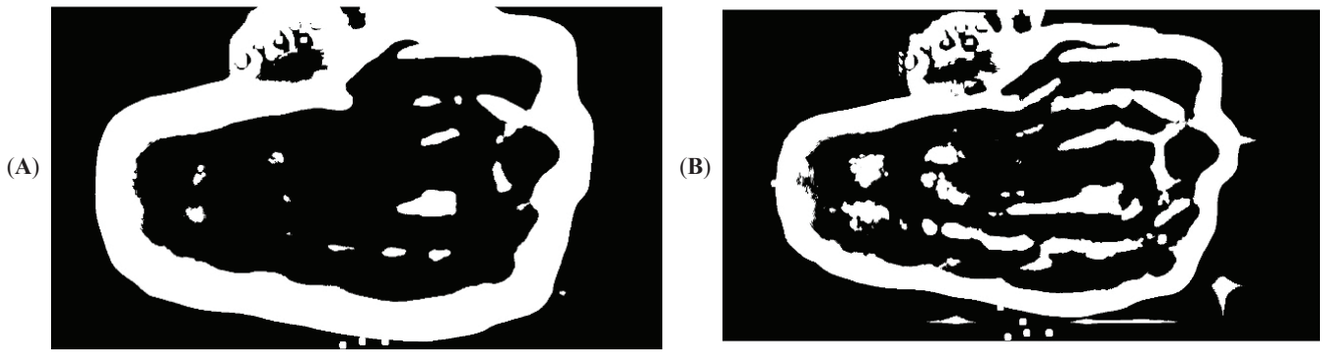

Fig. 10. Comparison of the result of the adaptive thresholding of Bradley, et al. (2011) [14] **and our modified technique.** (**A**) The original technique of Bradley, et al. (2011) has the kernel size of s=1/8th of image width and t=15%; (**B**) The modified technique has the kernel size of s=1/16th of image width and t=4%. The input image is Fig. 4D.

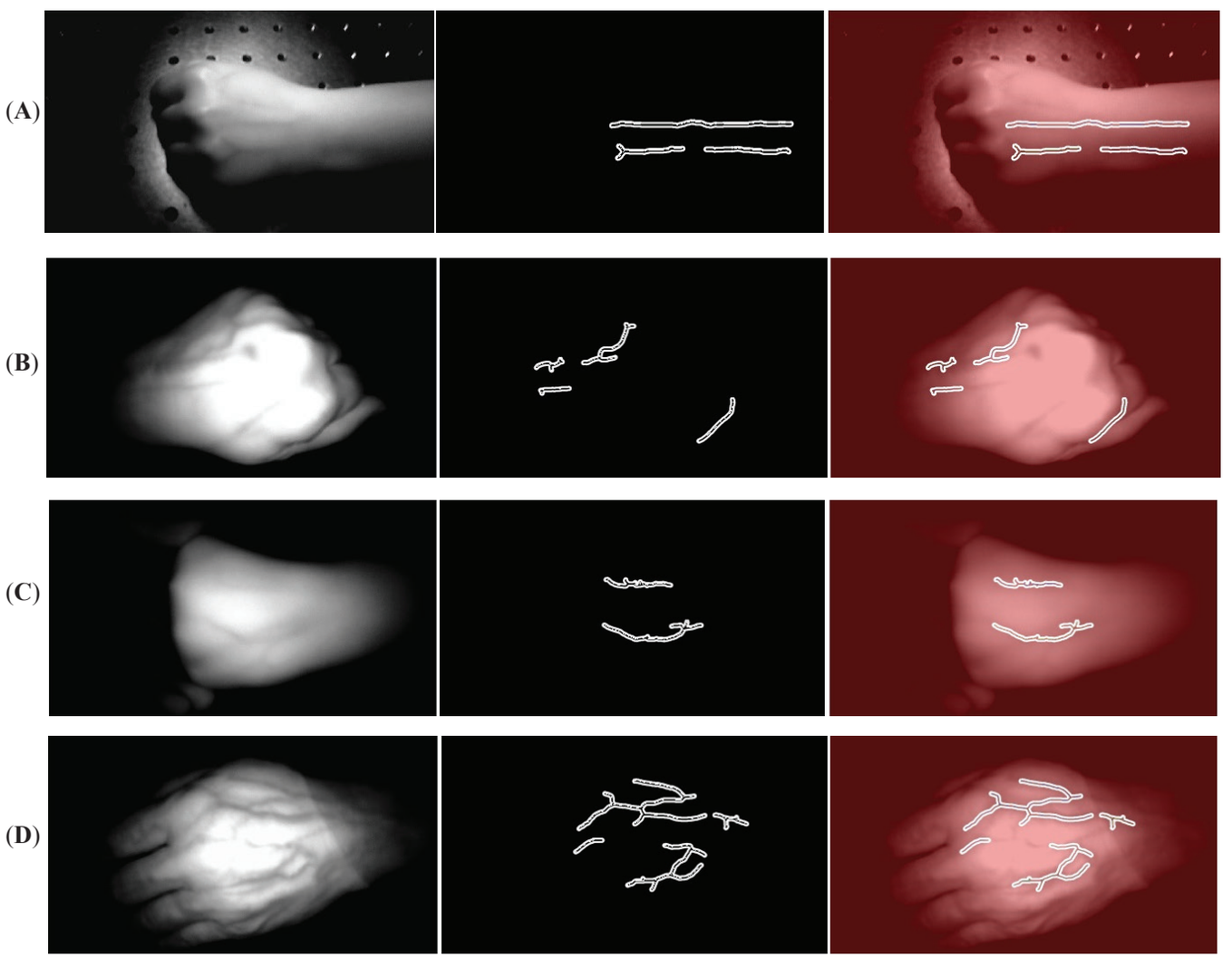

Fig. 11. Vein segmentation results of left-hand of females and males. (**A-D**) The images are the hands of females who are 23 and 56 years of age and males 9 and 66 years of age. The first column displays the original (grayscale) image, and the second contains the thinned and bounded vein patterns after removing the small objects. The last column shows the detected vein overlaid on the dorsal hand image from the first column.

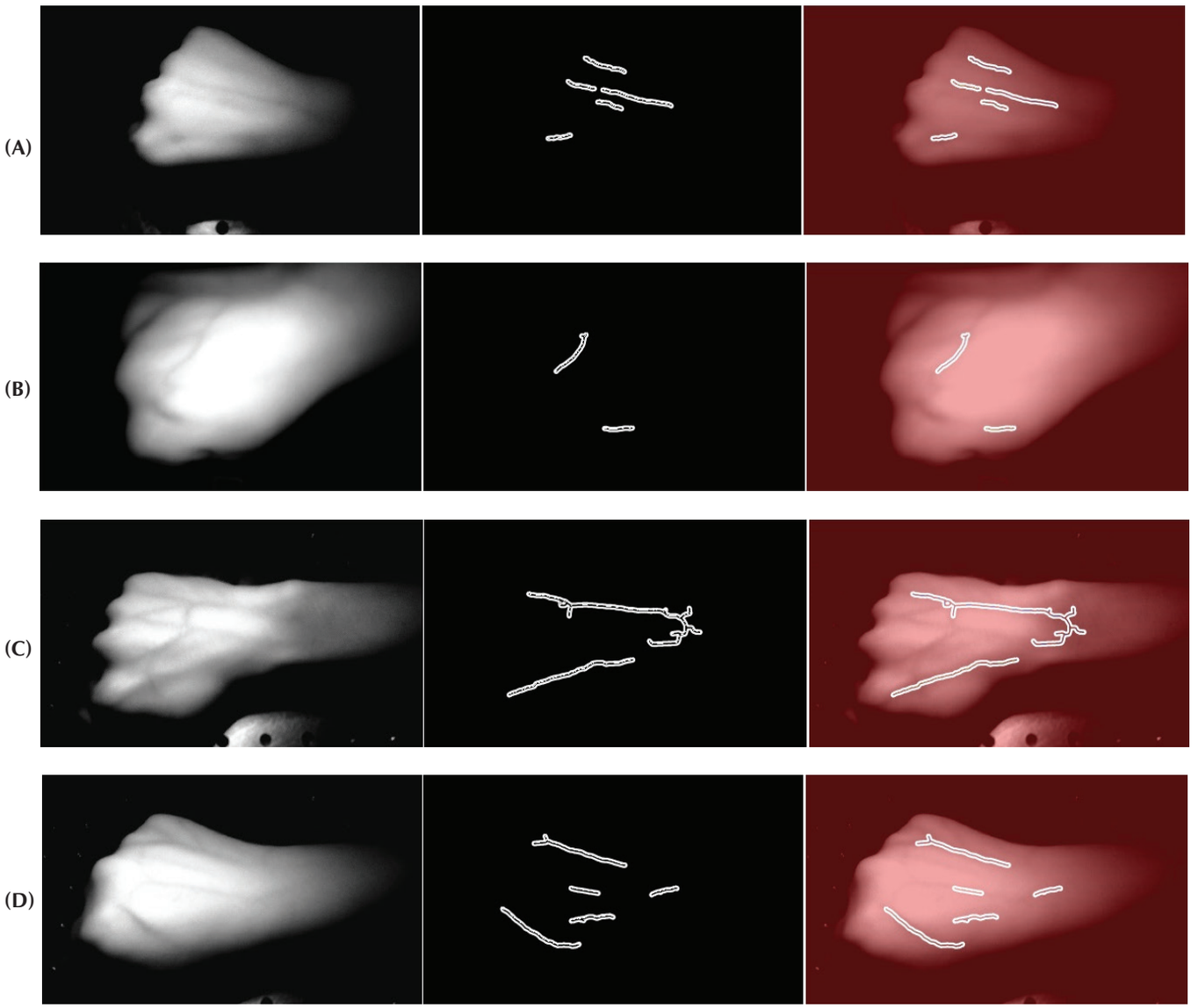

Fig. 12. Vein segmentation results of right-hand of females and males. (A-D) The images are the hands of females 23 and 40 years of age and males 22 and 35 years of age. The order of images is similar to Fig. 11.

3. Conclusions

This work has optimised the vein detection method and projection in 10 steps categorised under low- and high-level processes. The low-level process filters out the noise, enhances the contrast, and enlarges the dark regions to improve the image quality. A modified fast adaptive thresholding algorithm segmented the objects in the high-level process; a clear and refined vein pattern was extracted and projected back onto the original image. This method allows for the visualisation of precise, high-resolution vein patterns with a faster, simpler algorithm. This method can potentially assist and increase the success rate of venepuncture by visualising and locating vein patterns.

CRediT author statement

Hai Thanh Le, Hien Thi-Thu Pham: Conceptualisation, Methodology, Software, Resources, Writing - Review and Editing, Validation.

COMPETING INTERESTS

The authors declare that there is no conflict of interest regarding the publication of this article.

REFERENCES

[1] O.G. Helen, W.G Gary (2005), "Phlebotomy puncture juncture: Preventing phlebotomy errors - Potential for harming your patients", *Lab Medicine*, **36(7)**, pp.430-433, DOI: 10.1309/EXTW9LBM0CD7P9EV.

[2] S.H. Horowitz (1994), "Peripheral nerve injury and causalgia secondary to routine venepuncture", *Neurology*, **44(5)**, pp.962-964, DOI: 10.1212/wnl.44.5.962.

[3] B. Newman (2001), "Venipuncture nerve injuries after wholeblood donation", *Transfusion*, **41(4)**, pp.571-572, DOI: 10.1046/j.1537-2995.2001.41040571.x.

[4] B.H. Newman, D.A. Waxman (1996), "Blood donation-related neurologic needle injury: Evaluation of 2 years' worth of data from a large blood center", *Transfusion*, **36(3)**, pp.213-215, DOI: 10.1046/j.1537-2995.1996.36396182137.x.

[5] R.A. Lininger (2003), "Pediatric peripheral i.v. insertion success rates", *Journal of Pediatric Nursing*, **29(5)**, pp.351-354.

[6] D.B. Shurtleff (1964), "Transillumination of skull in infants and children", *The American Journal of Diseases of Children*, **107**, pp.14-24, DOI: 10.1001/archpedi.1964.02080060016003.

[7] No authors listed (2013), "AIUM practice guideline for the use of ultrasound to guide vascular access procedures", *Journal of Ultrasound in Medicine*, **32(1)**, pp.191-215, DOI: 10.1002/jum.14954.

[8] C.Y. Sun, K.C. Lee, I.H. Lin, et al. (2013), "Near-infrared light device can improve intravenous cannulation in critically ill children", *Pediatrics and Neonatology*, **54(3)**, pp.194-197, DOI: 10.1016/j.pedneo.2012.12.012.

[9] T.D. Pham, Y.H. Park, D.T. Nguyen, et al. (2015), "Nonintrusive finger-vein recognition system using NIR image sensor and accuracy analyses according to various factors", *Sensors*, **15(7)**, pp.16866-16894, DOI: 10.3390/s150716866.

[10] D.T. Nguyen, H.S. Yoon, T.D. Pham, et al. (2017), "Spoof detection for finger-vein recognition system using NIR camera", *Sensors*, **17(10)**, DOI: 10.3390/s17102261.

[11] H. Li, Q. Zhang, C. Li (2015), "An effective hand vein feature extraction method", *Technology and Health Care*, **23(2)**, pp.S343-S353, DOI: 10.3233/THC-150971.

[12] S. Crisan, B. Tebrean, T.E. Crisan (2018), "Multimodal liveness detection system for hand vein biometrics", *2018 Proceedings IEEE Int. Sym. on Med. Measurements and Apps. (MeMeA)*, pp.1-6, DOI: 10.1109/MeMeA.2018.8438734.

[13] H.D.K. Nguyen, L.T.A. Nguyen, T.T.H. Pham (2017), "Constructing real time vein imaging device utilizing near infrared technology and embedded system", *The 6th International Conference on The Development of Biomedical Engineering in Vietnam (BME6)*, **63**, pp.559-562, DOI: 10.1007/978-981-10-4361-1_95.

[14] D. Bradley, G. Roth (2011), "Adaptive thresholding using the integral image", *Journal of Graphics Tools*, **12(2)**, pp.13-21, DOI: 10.1080/2151237X.2007.10129236.

[15] S. Walt, J.L. Schönberger, J.N. Iglesias, et al. (2014), "Scikit-image: Image processing in Python", *Peer J.*, **19(2)**, DOI: 10.7717/peerj.453.

[16] S. Behnel, R. Bradshaw, C. Citro, et al. (2011), "Cython: The best of both worlds", *Jounal of Computing in Science & Engineering*, **13(2)**, pp.31-39, DOI: 10.1109/MCSE.2010.118.

DOI: 10.31276/VJSTE.63(2).39-44

Optimum sizing of members of truss structures using direct design and a self-adaptive mutation differential evolution

Manh-Hung Ha*, Hoang-Anh Pham

Faculty of Building and Industrial Construction, National University of Civil Engineering, 55 Giai Phong Street, Dong Tam Ward, Hai Ba Trung District, Hanoi, Vietnam

Received 16 April 2020; revised 30 June 2020; accepted 15 July 2020

Abstract:

Direct design using nonlinear inelastic analysis has been recently enabled for structural design as this approach can directly predict the behaviour of a structure as a whole, which eliminates capacity checks for individual structural members. However, the use of direct design is often accompanied by excessive computational efforts, especially for complicated structural design problems such as optimization or reliability analysis. In this study, we introduce an efficient method for the sizing optimization of truss structures employing nonlinear inelastic analysis for the direct design of structures. The objective function is the total weight of the structure while the strength and serviceability constraints are evaluated with nonlinear inelastic analysis. To save computational cost, an improved differential evolution (DE) algorithm is employed. Compared to the conventional DE algorithm, the proposed method has two major improvements: (1) a self-adaptive mutation strategy based on the *p-best* method to enhance the balance between global and local searches and (2) use of the multi-comparison technique (MCT) to reduce redundant structural analyses. The numerical results of a 72-bar truss case study demonstrate that the performance of the proposed method has significant advantages over the traditional DE method.

Keywords: **differential evolution, direct design, nonlinear inelastic analysis, optimization, truss.**

Classification number: **2.3**

1. Introduction

Conventional approaches such as allowable stress design (ASD), load and resistance factor design (LRFD), and the direct design paradigm are presented in Fig. 1. In these conventional techniques, a two-step member-based method is used where elastic analysis is first employed to calculate the forces acting on the structural members and then the strength equations provided from the design codes are applied to the strength checks of each member. Within these methods, strength and stability interactions between the whole structure and its elements are not considered. Further, the compatibility between structural members and the whole system is not guaranteed and therefore cannot ensure that all members will maintain their design loads under the geometric configuration of the structure. In contrast, direct design using nonlinear inelastic analysis allows the direct capture of both material nonlinear and geometric inelastic behaviours of the structure [1-5]. Thereby, the capacity check for individual structural elements, which is a requirement of the old paradigms, is eliminated. However, compared to the old paradigms, direct design requires excessive computation effort especially for complicated structural design problems such as optimization or reliability analysis [6-18].

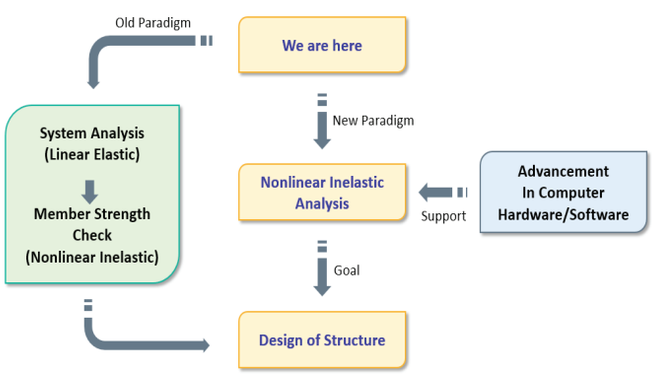

Fig. 1. Structural design concept [1].

*Corresponding author: Email: hunghm@nuce.edu.vn

Sizing optimization of truss structures has been favoured recently as it leads to a substantial reduction in cost. In sizing optimization, the cross-sectional areas of the members are optimized such that the total weight of the structure is minimized while all design requirements are guaranteed. The sizing optimization of truss structures is often considered as a discrete engineering optimization problem, where the design variables (member cross-sectional areas) can take only discrete values. To evaluate the constraints that are related to the strength and the serviceability of the truss structure during the optimization procedure, direct design using nonlinear inelastic analysis has been preferred by many researchers because this approach can capture the nonlinear behaviours of the structure and yield more realistic and lighter optimum results [7, 9, 10, 12]. The aforementioned issues imply that a sizing optimization of truss structures using nonlinear inelastic analysis is highly nonlinear, non-convex, and multimodal. To solve this optimization problem, preference is given to meta-heuristic optimization algorithms, which implement searching techniques of a stochastic nature to select potential solutions in a given search space [7, 9, 10, 12]. However, the use of meta-heuristic optimization algorithms necessitates one to conduct a large number of structural analyses that render the optimization process very computationally demanding.

In this study, an efficient method for sizing optimization of steel trusses using nonlinear inelastic analysis is introduced. The objective function is the structural total weight. Nonlinear inelastic analysis is used to calculate the constraint functions regarding strength and serviceability. To reduce the computation efforts of the optimization process, a DE algorithm is employed with two major improvements as follows: (1) a self-adaptive mutation strategy that uses the *p-best* method to enhance the balance between global and local searches and (2) the MCT to reduce redundant structural analyses. A 72 bar-space truss is then studied to demonstrate the efficiency of the proposed method.

2. Formulation of sizing truss optimization problem

The objective function of the optimization is the total weight of a truss structure and the design variables are cross-sectional areas of the truss elements. The design constraints include strength and serviceability constraints. The problem is typically formulated as follows:

$$\begin{aligned} &\textbf{Minimize} && W(\mathbf{Y}) = \sum_{i=1}^{nm} \rho_i A_i L_i \\ &\textbf{Subjected to} && 1 - \frac{R_j}{S_j} \le 0 \quad j = 1,..,nstr \\ & && \frac{|d_{k,l}|}{|d_{k,l}^u|} - 1 \le 0 \;\; k = 1,..,nser;\; l = 1,..,nn \\ & && A_i \subset \mathbf{S}_i \end{aligned} \tag{1}$$

where ρ_i, A_i, and L_i are the material density, cross-sectional area, and length of the i^{th} element, respectively, S_i is the list of cross-sectional areas used for the i^{th} element, $\mathrm{Y}=(A_1, A_2, ..., A_n)$ is the vector of design variables, R_i and S_j are the load-carrying capacity of the structure and the factored loading with the j^{th} strength load combination, respectively, $d_{k,l}$ and $d_{k,l}^u$ are the displacement of the node l and its allowable value with the k^{th} serviceability load combination, respectively, *nm* and *nn* are the numbers of truss elements and nodes, respectively, and *nstr* and *nser* are the numbers of strength and serviceability load combinations considered, respectively. In Eq. (1), $\frac{R_j}{S_j}$ can be designated as the ultimate load factor of the truss with the j^{th} strength load combination and is directly determined by using nonlinear inelastic analysis. The nodal displacements $d_{k,l}$ are also calculated by performing nonlinear elastic analysis. In this study, the practical advanced analysis program (PAAP) [2], which is efficient software for nonlinear inelastic analysis of steel structures like trusses and frames, is used to calculate the structural ultimate load factor and nodal displacements. A detailed implementation of PAAP for truss structures can be found in Refs [2, 19].

The objective function in Eq. (1) is transformed into unconstrained one as:

$$W_{uncstr}(\mathbf{Y}) = \left(1 + \sum_{j=1}^{nstr} \alpha_{str,j} \beta_{1,j} + \sum_{k=1}^{nser} \alpha_{disp,k} \beta_{2,k}\right) \times \left(\sum_{i=1}^{nm} \rho_i A_i L_i\right) \tag{2}$$

where

$$\begin{aligned} \beta_{1,j} &= \max\left(1 - \frac{R_j}{S_j}, 0\right); j = 1,..,nstr \\ \beta_{2,k} &= \sum_{l=1}^{nn} \max\left(\frac{|d_{k,l}|}{|d_{k,l}^u|} - 1, 0\right); k = 1,..,nser \end{aligned} \tag{3}$$

in which $\alpha_{str,j}$ and $\alpha_{disp,k}$ are the penalty factors corresponding to the strength load combination j^{th} and serviceability load combination k^{th}, respectively.

3. Self-adaptive mutation differential evolution

The DE algorithm was developed by R. Storn, et al. (1997) [20] and has been considered as one of the most efficient methods. "DE/rand/1" and "DE/best/1", two popular mutation strategies in DE, have opposite ways to balance the global and local searches of the optimization process. In "DE/rand/1", the generation of the trial individual is based on an individual selected at random, so this strategy is good for global exploration and maintenance of the diversity of the population, but it has a low converge rate. On the contrary, in "DE/best/1" the trial individual is created using the current best individual of the population; hence, this strategy is effective in local search and increases

the convergence speed but can easily get trapped into locally optimum results. Obviously, to balance the global and local searches of the optimization process a combination of both the above mutation strategies is an ideal approach. Particularly, at the early stage of the optimization process the population diverges making 'DE/rand/1' preferable, while "DE/best/1" is favoured at the late stage of the optimization process when the population starts to converge. In light of this, a mutation strategy developed using the *p-best* method is employed in this study. In this method, the trial individual is created by using a random member of the *p%* best individuals of the current population. The *p* value is calculated using a self-adaptive equation as follows:

$$p = \frac{1}{NP} + \left(1 - \frac{1}{NP}\right) \times \frac{DI_{(t)}}{DI_{(0)}} \tag{4}$$

where

$$DI_{(t)} = \frac{1}{NP}\sum_{j=1}^{NP}\sqrt{\sum_{i=1}^{D}\left(\frac{x_{j,i} - \frac{1}{NP}\sum_{j=1}^{NP} x_{j,i}}{x_i^{UB} - x_i^{LB}}\right)^2} \tag{5}$$

where D and NP are the number of design variables and individuals, respectively; $x_{j,i}$ is the i^{th} design variable of the j^{th} individual; x_i^{LB} and x_i^{UB} are the lower- and upper-bounds of $x_{j,i}$, respectively; and $DI_{(t)}$ is a diversity index of the population at the t^{th} generation. As presented in Eq. (5), $DI_{(t)}$ represents the individual distribution around the centre of the current population. From Eq. (4), the value of p is dependent on $DI_{(t)}$. Therefore, if $DI_{(t)}$ is large, which means that the individuals are still highly dispersed, a large p value is used and vice versa.

On the other hand, the strength and serviceability constraints are evaluated through the use of nonlinear analysis. The total structural analyses required are equal to the product of the total strength and serviceability load combinations under consideration, the population size, and the number of generations. For example, with 3 strength load combinations, 1 serviceability load combination, 20 individuals in the population, and 400 generations, the number of structural analyses is 32,000. Due to this fact, the optimization process takes an excessive amount of computational time. Note that, in the selection operator of the DE method, the trial individual will replace the target individual in the population if its objective function is smaller than that of the target individuals, otherwise it is neglected. Therefore, to reduce computation costs, the strength and serviceability constraints are evaluated step-by-step. After each step, the corresponding cumulative value of the trial individual's objective function is determined. Afterward, the program checks if it is higher than the target individual's objective function. If so, the trial individual is immediately ignored without evaluation of the remaining constraints. This method is so-called the multi-comparison technique (MCT) [9]. Further details of this method can be found in V.H. Truong, et al. (2018a) [9] research. Besides, the discrete variables are solved by rounding the continuous variables to the nearest value of the discrete variables.

4. Case study

In this section, a 72-bar truss, presented in Fig. 2, is optimized to show the efficiency of the proposed optimization method. The material properties are as follows: an elastic modulus of 68.95 (GPa), a yield strength of 172.375 (MPa), and a density of 2,767.99 (kg/m^3). The applied loads are a dead load (DL) of 100 kN, live load (LL) of 100 kN, and wind load (W) of 100 kN, which are applied to the structure as point loads as presented in Fig. 2. The cross-sectional areas of all 72 elements are classified into 16 design groups as presented in Table 1. A discrete list of the cross-sectional areas of the truss element including 42 values is also shown in Table 1. Three strength and one serviceability load combinations are considered such as (1.4DL), (1.2DL+1.6LL), (1.2 DL+0.5 LL+1.7W), and (1.0DL+0.5LL+0.7W), respectively. The drift constraint for the serviceability load combination is equal to *h/400* where *h* is the story height.

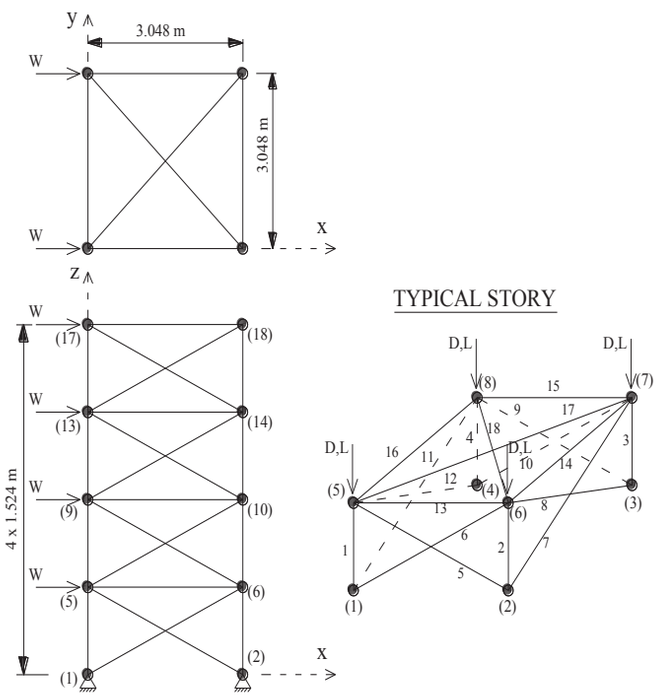

Fig. 2. 72-bar truss.

Table 1. Information of design groups of spatial 72-bar truss.

Element group number	Content
1	Element 1 to 4
2	Element 5 to 12
3	Element 13 to 16
4	Element 17 to 18
5	Element 19 to 22
6	Element 23 to 30
7	Element 31 to 34
8	Element 35 to 36
9	Element 37 to 40
10	Element 41 to 48
11	Element 49 to 52
12	Element 53 to 54
13	Element 55 to 58
14	Element 59 to 66
15	Element 67 to 70
16	Element 71 to 72
List for cross-sectional areas (in^2)	1.62, 1.80, 1.99, 2.13, 2.38, 2.62, 2.63, 2.88, 2.93, 3.09, 3.13, 3.38, 3.47, 3.55, 3.63, 3.84, 3.87, 3.88, 4.18, 4.22, 4.49, 4.59, 4.80, 4.97, 5.12, 5.74, 7.22, 7.97, 11.5, 13.5, 13.9, 14.2, 15.5, 16.0, 16.9, 18.8, 19.9, 22.0, 22.9, 26.5, 30.0, 33.5

The traditional DE method with the two mutation operators 'DE/rand/1' and 'DE/best/1' is used for comparison with the proposed method. To save computation time, the MCT method is implemented into the traditional DE method. The parameters used for all considered methods are NP=20; D=16; maximum value of generations =400; scale factor F=0.7; and crossover factor CR=0.6. The termination of the optimization process is defined as (1) the number of generations reaches 400 or (2) the difference between the worst and the best individuals of the population is smaller than 0.0001.

Table 2 presents the optimization results where each method is performed 10 times. All methods yield the same best optimum design with a total weight of 1,200.1 (kg). However, the proposed method has a greater stability than the other methods because it produces the lowest values of the unfavourable weight, the average weight, and standard deviation (std) of the optimum weights. The performance of the "DE/best/1" method is the worst with the highest value of the worst weight. This implies that this method was trapped in a local optimum. Regarding the "DE/rand/1" method, its performance converged more slowly than other methods as it required an average of 395 generations. Therefore, the optimum results of the "DE/rand/1" method are worse than the proposed method. Furthermore, Table 1 indicates that the proposed method requires only an average of 9,369 structural analyses for 227 generations. This means that it saves about 48.4% required structural analyses compared to using the traditional DE method (without using MCT). Also, Figs. 3A and 3B present the histories of the best and average scores during the optimization procedure, respectively. The proposed method converges more slowly than "DE/best/1" but more quickly than "DE/rand/1".

Table 2. Optimization results of spatial 72-bar truss.

Element group number	Proposed method (mm^2)	DE/best/1 (mm^2)	DE/rand/1 (mm^2)
1	9,999.980	9,999.980	9,999.980
2	2,238.705	2,238.705	2,238.705
3	1,045.159	1,045.159	1,045.159
4	1,045.159	1,045.159	1,045.159
5	7,419.340	7,419.340	7,419.340
6	2,290.318	2,290.318	2,290.318
7	1,045.159	1,045.159	1,045.159
8	1,045.159	1,045.159	1,045.159
9	3,703.218	3,703.218	3,703.218
10	1,690.319	1,690.319	1,690.319
11	1,045.159	1,045.159	1,045.159
12	1,045.159	1,045.159	1,045.159
13	1,045.159	1,045.159	1,045.159
14	1,535.481	1,535.481	1,535.481
15	1,045.159	1,045.159	1,045.159
16	1,045.159	1,045.159	1,045.159
Best weight (kg)	1,200.100	1,200.100	1,200.100
Worst weight (kg)	1,210.800	1,276.700	1,230.800
Average weight (kg)	1,203.782	1,212.638	1,207.927
Std. weight (kg)	4.292	20.572	9.969
Average objective function evaluations	9,369	9,720	12,844
Average number of generations	227	220	395

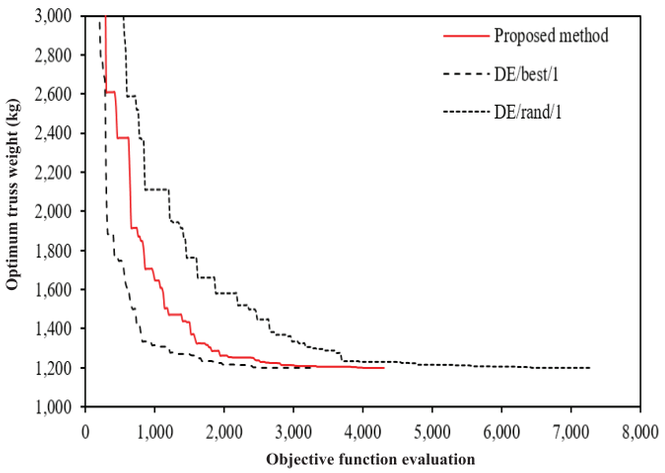

(A)

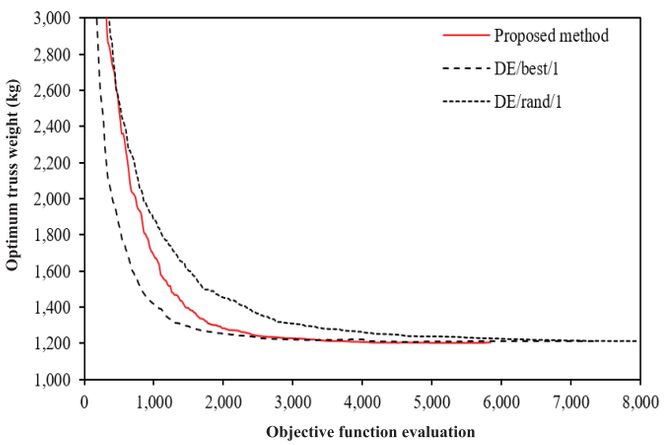

(B)

Fig. 3. Convergence histories of 72-bar truss. (A) The best optimum designs; **(B)** The average optimum designs.

5. Conclusions

An efficient method for the sizing optimization of truss structures was successfully developed. Direct design using nonlinear inelastic analysis was applied to the evaluation of constraints related to strength and serviceability. An improved differential evolution algorithm was developed using a self-adaptive mutation strategy to enhance the balance between global and local searches along with a multi-comparison technique to reduce redundant structural analyses. The traditional DE method with the two popular mutation operators "DE/best/1" and "DE/rand/1" were used to demonstrate the accuracy and efficiency of the proposed optimization method. The numerical results of a 72 bar-space truss prove that the proposed method's performance was better than that of the traditional DE method.

CRediT author statement

Manh-Hung Ha, Hoang-Anh Pham: Conceptualisation, Methodology, Software, Resources, Writing - Review and Editing, Validation.

ACKNOWLEDGEMENTS

This research is funded by Vietnam National Foundation for Science and Technology Development (NAFOSTED) under grant number 107.01-2018.327.

COMPETING INTERESTS

The authors declare that there is no conflict of interest regarding the publication of this article.

REFERENCES

[1] S.E. Kim, M.H. Park, S.H. Choi (2001), "Practical advanced analysis and design of three-dimensional truss bridges", *J. Constr. Steel Res.*, **57(8)**, pp.907-923, DOI: 10.1016/S0143-974X(01)00015-3.

[2] H.T. Thai, S.E. Kim (2011), "Practical advanced analysis software for nonlinear inelastic dynamic analysis of space steel structures", *J. Constr. Steel Res.*, **67(3)**, pp.453-461, DOI: 10.1016/j.jcsr.2010.09.009.

[3] V.H. Truong, G. Papazafeiropoulos, V.T. Pham, et al. (2019), "Effect of multiple longitudinal stiffeners on ultimate strength of steel plate girders", *Structures*, **22**, pp.366-382, DOI: 10.1016/j.istruc.2019.09.002.

[4] Q.V. Vu, V.H. Truong, G. Papazafeiropoulos, et al. (2019), "Bend-buckling strength of steel plates with multiple longitudinal stiffeners", *Journal of Constructional Steel Research*, **158**, pp.41-52, DOI: 10.1016/j.jcsr.2019.03.006.

[5] V.H. Truong, Q.V. Vu, H.T. Thai, et al. (2020), "A robust method for safety evaluation of steel trusses using Gradient Tree Boosting algorithm", *Advances in Engineering Software*, **147**, DOI: 10.1016/j.advengsoft.2020.102825.

[6] M.H. Ha, Q.A. Vu, V.H. Truong (2018), "Optimum design of stay cables of steel cable-stayed bridges using nonlinear inelastic analysis and genetic algorithm", *Structures*, **16**, pp.288-302, DOI: 10.1016/j.istruc.2018.10.007.

[7] V.-H. Truong, S.E. Kim (2017a), "An efficient method for reliability-based design optimization of nonlinear inelastic steel space frames", *Struct. Multidisc. Optim.*, **56(2)**, pp.331-351, DOI: 10.1007/s00158-017-1667-7.

[8] V.H. Truong, S.E. Kim (2017b), "An efficient method of system reliability analysis of steel cable-stayed bridges", *Advances in Engineering Software*, **114**, pp.295-311, DOI: 10.1016/j.advengsoft.2017.07.011.

[9] V.H. Truong, S.E. Kim (2018a), "A robust method for optimization of semi-rigid steel frames subject to seismic loading", *Journal of Constructional Steel Research*, **145C**, pp.184-195, DOI: 10.1016/j.jcsr.2018.02.025.

[10] M.H. Ha, Q.V. Vu, V.H. Truong (2020), "Optimisation of nonlinear inelastic steel frames considering panel zones", *Advances in Engineering Software*, **142**, DOI: 10.1016/j.advengsoft.2020.102771.

[11] S.E. Kim, V.H. Truong (2020), "Reliability evaluation of semi-rigid steel frames using advanced analysis", *Journal of Structural Engineering*, **146(5)**, DOI: 10.1061/(ASCE)ST.1943-541X.0002616.

[12] V.H. Truong, M.H. Ha, P.H. Anh, et al. (2020), "Optimisation of steel moment frames with panel-zone design using an adaptive differential evolution", *Journal of Science and Technology in Civil Engineering (STCE)-NUCE*, **14(2)**, pp.65-75, DOI: 10.31814/stce.nuce2020-14(2)-06.

[13] V.H. Truong, Q.V. Vu, V.T. Dinh (2019), "A deep learningbased procedure for estimation of ultimate load carrying of steel trusses using advanced analysis", *Journal of Science and Technology in Civil Engineering (STCE)-NUCE*, **13(3)**, pp.113-123, DOI: 10.31814/stce.nuce2019-13(3)-11.

[14] P.C. Nguyen, S.E. Kim (2017), "Investigating effects of various base restraints on the nonlinear inelastic static and seismic responses of steel frames", *International Journal of Non-Linear Mechanics*, **89**, pp.151-167, DOI: 10.1016/j.ijnonlinmec.2016.12.011

[15] P.C. Nguyen, S.E. Kim (2018), "A new improved fiber plastic hinge method accounting for lateral-torsional buckling of 3D steel frames", *Thin-Walled Struct.*, **127**, pp.666-675, DOI: 10.1016/j.tws.2017.12.031.

[16] T.N. Nguyen, S.K. Shukla, D.D.C. Nguyen, et al. (2019), "A new discrete method for solution to consolidation problem of ground with vertical drains subjected to surcharge and vacuum loadings", *Engineering Computations*, **37(4)**, pp.1213-1236, DOI: 10.1108/EC-01-2019-0035.

[17] P.C. Nguyen, S.E. Kim (2014), "Distributed plasticity approach for time-history analysis of steel frames including nonlinear connections", *Journal of Constructional Steel Research*, **100**, pp.36-49, DOI: 10.1016/j.jcsr.2014.04.012.

[18] P.C. Nguyen, S.E. Kim (2016), "Advanced analysis for planar steel frames with semi-rigid connections using plastic-zone method", *Steel and Composite Structures*, **21(5)**, pp.1121-1144, DOI: 10.12989/scs.2016.21.5.1121.

[19] V.H. Truong, S.E. Kim (2018b), "Reliability-based design optimization of nonlinear inelastic trusses using improved differential evolution algorithm", *Advances in Engineering Software*, **121**, pp.59-74, DOI: 10.1016/j.advengsoft.2018.03.006.

[20] R. Storn, K. Price (1997), "Differential evolution-a simple and efficient heuristic for global optimization over continuous spaces", *J. Glob. Optimiz.*, **11(4)**, pp.341-359, DOI: 10.1023/A:1008202821328.

DOI: 10.31276/VJSTE.63(2).45-51

The combination of microbiological, biochemical, and quality index methods in quality evaluation of Pacific white shrimps *(Litopenaeus vannamei)* preserved at 0°C

Nhat Tam Le [1*], Nguyen Que Anh Huynh[1], Nhu Khue Doan[1], Thuy Xuan Uyen Phan[1], Ba Thanh Nguyen[1], Sao Mai Dam[1], Thi Van Thi Tran[2], Le Phuong Lien Nguyen[3], Van Hai Chu[4], Huynh Anh Vu Truong[4]

[1]Institute of Biotechnology and Food Technology, Industrial University of Ho Chi Minh City, 12 Nguyen Van Bao Street, Ward 4, Go Vap District, Ho Chi Minh City, Vietnam
[2]Hue University of Science, Hue University, 77 Nguyen Hue Street, Phu Nhuan District, Hue City, Thua Thien Hue Province, Vietnam
[3]Department of Refrigeration and Livestock Product Technology, Szent Istvan University, 43-45 Ménesi Street, Budapest, Hungary
[4]Center of Analytical Services and Experimentation Ho Chi Minh City, 2 Nguyen Van Thu Street, Da Kao Ward, Distrist 1, Ho Chi Minh City, Vietnam

Received 28 May 2020; revised 14 August 2020; accepted 21 August 2020

Abstract:

In this study, the sensory, microbiological, and biochemical qualities were used to examine the quality of Pacific white shrimps (*Litopenaeus vannamei*) preserved at 0°C during a 10-day period. The sensory quality was evaluated by a quality index (QI) that resulted from a quality index method (QIM) scheme. Meanwhile, the total viable count (TVC) and K-value were used to assess the microbiological and biochemical qualities of the shrimp. On day 9, the results from TVC and QIM have shown that the shrimp showed signs of spoilage, corresponding to a log CFU/g of 6.4 and a QI of 21.37, which is unacceptable to consumers. The QI increased linearly with storage days therefore the remaining shelf-life of the shrimp was estimated from a linear regression equation. In particular, this study found a linear relationship between QI, K-value, and hypoxanthine content. Furthermore, hypoxanthine itself could be considered as an independent quality index like the K-index. In conclusion, the quality of Pacific white shrimp was categorized into four different classes: excellent, good, acceptable, and moderately acceptable, based on its sensory and biochemical quality indicators.

Keywords: **hypoxanthine, K-value, Pacific white shrimp, QIM.**

Classification number: **3.1**

1. Introduction

Shrimp are an important source of seafood with considerable nutrition and economic value in many countries around the world [1]. In Vietnam, Pacific white shrimp (*Litopenaeus vannamei*) have achieved a high export turnover rate in the seafood industry in recent years. However, the method used to assess the quality of shrimp in particular, and seafood in general, is not consistent with the current methods in other parts of the world. The quality of post-harvest shrimp decreases with storage time due to the impact of three main factors, which include the activity of endogenous enzymes, microorganisms, and chemical reactions. These activities alter the sensory state, chemical composition, as well as the total amount of aerobic microorganisms in shrimp [2, 3]. Therefore, methods that assess sensory, chemical, microbiological, and physical qualities are established based on these impact factors [2]. The organoleptic quality assessment method is based on variations of sensory properties including the color, smell, taste, and texture. The intensity rating method is considered the most popular at present, followed by the Torry scheme, quantitative descriptive analysis (QDA), and QIM, to name a few. Among those, QIM is predicted by Hyldig as the potential method for quality assessment in the European Community. QIM was developed by the Tasmanian Food Research Unit in Australia [4] and is continually being developed. QIM possesses many advantages such as short training time, short evaluation time, and high reliability in assessing the freshness of seafood preserved in ice [5]. The difference between QIM and other methods is that QIM is built to evaluate the sensory changes of specific species. QIM focuses on the correlation between the quality index

*Corresponding author: Email: lenhattam@iuh.edu.vn

and the storage time expressed via a linear regression equation. Thus, QIM allows an estimation of the remaining shelf-life of seafood. So far, QIM-Eurofish has developed 28 QIM schemes mainly for fish, shrimp, and squid species. However, the QIM scheme for Pacific white shrimp has not yet been developed [6]. In Vietnam, shrimp quality is assessed according to TCVN 3276-89 [7]. This standard is generally applied to all shrimp species and is not an intensity rating method, however, it is a semi-quantitative assessment that describes changes in the properties of shrimp. Therefore, quality results from TCVN 3276-89 do not resemble those obtained by the rating method used in importing countries. This leads to disputes over quality and financial losses for exporting enterprises. After shrimp die, the process of self-decomposition takes place immediately, which is followed by the process of decomposition [8]. This autolysis is caused by endogenous enzymes in the shrimp and results in the release of nucleotides and its derivatives. In 1959, Saito and his colleagues introduced the "K-value", which is calculated based on nucleotides and their derivatives. The "K-value" has been formulated as an index of freshness in seafood [9]. Unlike quality indicators such as TVB-N, TMA-N, or histamine that are suitable for assessing quality during the decomposition stage, the K-value tends to linearly correlate with storage time [10-15]. This allows researchers to develop a regression equation between the QI and K-value.

Therefore, this study aims to develop a complete quality assessment process including the analytical methods measuring the microbiological, biochemical, and sensory changes. The expected findings include the quality classification of Pacific white shrimp based on the QI and K-value as well as the linear regression equations between the quality indicators investigated.

2. Materials and methods

2.1. Shrimp collection and storage

Healthy Pacific white shrimp were purchased from the Binh Dien market in Ho Chi Minh city. The shrimp samples were then washed with filtered water and packaged in polyethylene zipper bags (26.8×27.9 cm) (Alcoa Products Inc., VA, USA). These sample bags were placed directly in a polystyrene container containing shaved ice with a ratio of 1 shrimp to 2 shaved ices (w/w) and were delivered to the testing facility within 2 hours. At the testing facility, the sample bags were preserved at 0°C in a refrigerator for research purposes.

2.2. Reagents

Reagents including Adenosine-5'-triphosphate (PubChem CID: 5957), Adenosine-5'-diphosphate (PubChem CID: 6022), Adenosine-5'-monophosphate (PubChem CID: 6083), Inosinmonophosphate (PubChem CID: 8582), Inosine (PubChem CID: 6021), and hypoxanthine (PubChem CID: 790) were purchased from Sigma - Aldrich (Merck KGaA, Germany). Other reagents such as methanol (PubChem CID: 887), ethanol (PubChem CID: 702), and HPLC-grade water were bought from Merck Vietnam Ltd. Co.

2.3. Determination of TVC

TVC was measured according to M.J. Leboffe, et al. (2015) [16]. In brief, 10 g of peeled shrimp were minced and mixed with 90 ml of 0.9% NaCl solution and then centrifuged at 3000 rpm at 30°C for 5 min. The pour-plate method using plate count agar was applied to determine the total plate counts. The extract from the samples were inoculated on agar plates and incubated at 30°C for 48 h before the colonies were counted. The experiments were repeated three times and the TVC values were expressed as log CFU/g (colony forming units).

2.4. Development of QIM scheme

The QIM scheme was developed based on three main steps according to D.C. Bernardi, et al. (2013) [17], N.T. Le, et al. (2017) [18], which include: (1) identification of quality attributes, (2) main sensory evaluation, and (3) quantification of the developed (sensory) QI, as mentioned below.

Step 1 (preliminary program): Three sensory experts observed all the changes in quality attributes (e.g. shape, odor, texture, eyes, shell color, and formation of black spots on the abdomen, body, tail). The terms were noted from direct observation [18-20]. The CATA (check all that apply) method was applied to select the most suitable descriptive terms from the preliminary terminology. Each attribute was then given a score from 0 to 3, with a low score suggesting a high quality level.

Step 2 (main program development and panel training): The shrimp samples were evaluated daily for ten consecutive days at 0°C. The start of day 0 was determined to be right after the shrimp arrived at the testing facility. The examination of the shrimp at different time points was conducted by six sensory panelists for one month. The panelists evaluated the samples and recorded the results without knowing the storage time. This process ensured accuracy, reliability, and minimized bias in data.

Step 3 (quantification of the recorded sensory QI): This step primarily involved quantification of the data collected from the QIM scheme. The regression equation between the days in storage and QI was developed to compare the projected shelf life with actual shelf life of shrimps. The data collected from ten different samples corresponded to each of the 10-day storage periods.

2.5. ATP, related compounds, and K-value

Nucleotides and related compounds including ATP, ADP, AMP, IMP, inosine, and hypoxanthine were measured by high-performance liquid chromatography with a diode array detector (HPLC-DAD). In this method, nucleotides and related compounds were extracted with 0.6 M perchloride acid and detected by the 2018 Cosmosil application [21] and M.V. Nogues, et al. (1997) [22]. In summary, 3±0.01 g of shrimp meat was blended with 10 ml of 0.6 M perchloride acid for 10 min by vortex. The mixture was then centrifuged at 3000 rpm for 10 min to collect the supernatant. This process was repeated three times. The extract was neutralized to pH 7.0 using 1 M KOH filtered through Whatman Grade 1 filter paper (Sigma-Aldrich, Germany) and diluted to 50 ml by volume. One milliliter of the diluted extract was uploaded into an SPE C18 column (Agilent Technologies, USA) and eluted with a 0.05 M K_2HPO_4 buffer to harvest 10 ml. Then, 50 µl of the harvested extract was injected into the column for the analysis of nucleotides and related compounds by HPLC. HPLC analyses were performed using an Agilent 1260 apparatus (Agilent Technologies, USA) equipped with diode array detector (Agilent 1260 detector), 5C18-PAQ column (size 5 µm, length 250 mm - 4.6 mm I.D) (Nacalai Tesque, Japan) at 30°C. The mobile phase of 0.05 M K_2HPO_3 was controlled at a flow rate of 1 ml/min. Nucleotides and related compounds were detected at a wavelength of 260 nm.

The K-value was calculated as the percent ratio of inosine (HxR) and hypoxanthine (Hx) to the sum of ATP and degradation products as shown below.

*K-value*s(%)=100(inosine+hypoxanthine)/(ATP+ADP+AMP+IMP+inosine+hypoxanthine).

2.6. Data analysis

All experiments were conducted in triplicate. The obtained data were preprocessed with Microsoft Excel (version 2010) and analyzed using Statgraphics centurion software. A linear regression model was fit to the data. The significance level was at $p<0.05$.

3. Results and discussion

3.1. The change in TVC

The initial number of microorganisms in shrimp was mainly from the breeding environment [23]. The shrimp samples, after being washed with clean water, were stored at 0°C and the TVC with a log CFU/g value of 4.7 was recorded on day 1. The TVC values for the following days 2, 3, and 4 did not change significantly with 4.78, 4.89, and 5.01 (log CFU/g), respectively. However, starting from day 5, significant changes were observed ($p<0.05$). The TVC value was 5.55 on day 5, 5.78 on day 6, 5.77 on day 7, 5.89 on day 8, 6.4 on day 9, and 6.4 on day 10. The TVC values increased rapidly after day 4 for 10 days and exceeded 6 log CFU/g on day 9. The value of 6 log CFU/g is regarded as the limit allowed by the International Commission on Microbiological Specifications for Foods (ICMSF) for frozen shrimp. Thus, the shelf life of shrimps was set at day 8. Two recent studies by R.P. Naik, et al. (2014) [23], C.O.R. Okpala, et al. (2014) [24] on black tiger and white shrimp samples have also shown that the shelf life are 8 days and 7 days, respectively. This difference in shelf life may be from different species, seasons, harvest techniques, age, and physiological conditions [2]. Microbiological changes in shrimp are closely related to sensory and biochemical changes. In the autolytic stage, as mentioned above, the main cause is due to the endogenous enzymes. Some components that are quickly metabolized during this period are ATP, glycogen that produces sweet IMP, and hypoxanthine derivatives that produce a bitter taste [2]. A decrease in pH, which is caused by lactic acid produced from glycogen digestion, facilitates the hydrolysis of the proteins of acidic enzymes. The hydrolysis of proteins forms basic substances such as TVB and biological amines [25]. This leads to the decomposition of proteins and lipids. This is the source of the unique flavors such as alcohols and aldehydes, especially aldehydes that have double bonds in the third position [26, 27]. Biochemical changes also strongly occur during the decomposition stage. TMA compounds have a fishy smell, which are formed by the reduction of TMAO and NH_3 resulting from the metabolism of amine acids by enzyme deaminases.

3.2. Development of QIM scheme for the quality evaluation of Pacific white shrimps

Changes in sensory qualities such as color, odor, and texture of head and tail were noted with preliminary descriptive terms. The CATA method was applied to select and arrange the terms in descending quality order as described in Table 1 [28].

Table 1. QIM scheme for Pacific white shrimp (*Litopenaeus vannamei*).

Characters		Description	Score
Odor	Meat	Fresh ocean smell	0
		Lightly fishy smell, smell of seashells	1
		Neutral or slightly trimethylamine (TMA)	2
		Strong trimethylamine (TMA)	3
Color	Head	Gray, gray - green, no spot	0
		Gray, gray - green, light yellow	1
		Light black, scattered black spots	2
		Black, large black spots	3
	Body	Shiny, gray, yellow, spotless	0
		Gray, green, some spots	1
		Gray, slightly pink, scattered spots	2
		Yellow, pink. Large black spots on the body and legs	3
	Tail	Gray, purple, spotless	0
		Gray, green, some spots	1
		Green, pink, large black spots	2
		Black	3
	Meat	Pearl color, translucent	0
		Translucent, silver-ish or gray-ish	1
		Milky white	2
		Milky white, pink, yellow	3
Texture	Shell	Hard, elastic	0
		Hard, slight elastic	1
		Slightly soft	2
		Soft	3
	Appearance	Head and body are intact. The head is tightly attached to the body. The tail is attached to the body	0
		Head is loose but body is still intact, and the tail is attached to the body	1
		Head is loosely attached to body; and flesh is loosely attached to shell	2
		Head is very loose, may not attached to the body; flesh is easily separated from shell	3
	Meat	Firm, springy, elastic	0
		Slightly less firm, less springy	1
		Soft, sticky, slightly elastic	2
		Soft, deformed	3

Other shrimp samples with different storage times were evaluated by the trained panel for ten consecutive days. Changes in sensory attributes, corresponding QI, and quality class from day 0 to day 10 are presented in Table 2.

Table 2. Sensory changes, QI, and Pacific white shrimp quality classifications during storage at 0°C.

Days	Descriptions	QI	Class
1	Shrimp has fresh ocean smell, blueish-gray head. Roes begin to turn yellow. The head has no black spots. Head is intact and tightly attached to the body Body is shiny gray and intact. The back is yellow. Body has no black spots Tail is gray, a bit purple at the top end and has no black spots. Tail is attached to the body Shell is hard and tough Meat is translucent, firm and elastic	1.32	Excellent
2	Shrimp has fresh ocean smell. Head is blueish-gray. Roes are light yellow. Head has no black spots. Head is intact and tightly attached to the body Body is shiny gray and intact. The back is yellow. Body has no black spots Tail is gray, a bit purple at the tip of the tail, and has no black spots. Tail is attached to the body Shell is less tough Meat is translucent, firm and elastic	2.90	
3	Seashell smell, lightly fishy. Roes are yellow Head is blueish-gray, lightly loose from the body, and has some black spots Body is shiny, gray, and green, has no spots Body is intact Tail is gray and blue and has some black spots Tail is attached to the body Shell is less tough and less hard Meat is translucent and grayish. Meat is less firm	5.60	Good
4	Seashell and fishy smell. Roes are yellow Head is blueish-gray. Black spots appear on the swimming legs. Head is intact Body is shiny, gray, and green. The body has black spots. Body is intact Tail is gray and blue, has some black spots. Tail is attached to the body Meat is translucent, silver gray. Meat is less firm Shell is less tough	8.87	
5	Seashell and fishy smell. Roes are yellow. Head is gray. Black spots appear on the swimming legs. Head is loose from the body Body is gray, and green. The body has black spots. Body is intact but lightly stretched Tail is gray and blue, has black spots. Tail is attached to the body Meat is milky white and lightly soft Shell is less tough	10.53	Moderately acceptable
6	Fishy smell. Roes are light orange. Head is pinkish gray. Black spots on swimming legs Head is loose from the body Body is gray; light pink on the back. The body has black spots. Body is intact but lightly stretched Tail is blue and has dark spots. Tail is attached to the body Crispy shell Meat is silver gray and lightly soft	14.12	

7	Fishy, ammonia smell Roes are light orange. Head is pinkish gray Black spots on swimming legs and head. Head is loose from the body Body is gray and pink. The body has large black spots. Body is stretchy Tail is blue, pink and has dark spots. Tail is attached to the body Crispy shell Meat is milky gray and soft.	16.93	Just acceptable
8	Fishy, slightly trimethylamine odor Roes are orange and broken. Head is pinkish gray. The head has large black spots. Head is loose from the body Body is gray and pink. The body has large black spots. Body is stretchy Tail is blue, pink at the tip of the tail. Tail is attached to the body Crispy shell Meat is milky gray and soft, not elastic, sticky	18.50	
9	Fishy, trimethylamine odor Head is orange, and black. Large black spots Head is loose from the body. Roes are broken Body is yellow, pink. Body has large black spots Black spots appear on the abdomen. Body is stretchy Tail is black. Tail is attached to the body Soft shell Meat is milky white, yellow, pink. Meat is sticky	21.37	Rejected
10	Strong trimethylamine smell (rotten smell) Head is orange, black. Large black spots. Head is loose from the body. Roes are broken Body is yellow, pink. Body has large black spots. Black spots are on the abdomen and legs. Body is stretchy Black tail. Tail is attached to the body Soft shell Meat is milky white, yellow, pink. Meat is sticky	22.77	

The changes in the sensory quality of Pacific white shrimp were divided into five stages corresponding to five storage periods: from day 1 to day 2; from day 3 to day 4; from day 5 to day 6; from day 7 to day 8; and from day 9 to day 10. In stage 1 (from day 1 to day 2), the shrimp underwent a period of stiffness and there were almost no changes in color, texture, and odor. The QI scores of day 1 to 2 went from 1.32 to 2.9, respectively. In stage 2 (from day 3 to day 4), the sensory characteristics of the shrimp were similar to those on days 1 and 2, however, the color of head and tail began to change and therefore the QI scores were 5.60 and 8.87, respectively. In stage 3, (from day 5 to day 6), the shrimp shell lost its glossiness and became slightly opaque. At this point, the shrimp were still quite fresh, milky white, and slightly soft, but they had lost their elasticity and had a few black spots on the head and tail. Thus, the QI scores were between 10.53 and 14.12. In stage 4 (from day 7 to day 8), the color of the head and tail changed considerably compared to the initial samples. The head and tail were slightly black and the head was attached to the loose body. The shrimp had a reddish body with a moderate density of black spots and opaque shell. The meat was not attached to the skin. It was slightly pink, soft, and had slightly sour smell, which acquired QI scores of 16.93 and 18.50, respectively. In stage 5 (from day 9 to day 10), the head was almost detached from the body, the shrimp had a foul and sour smell, soft meat, a lot of black spots, and no legs. The QI scores during this stage were 21.37 and 22.77, respectively. A linear relationship between storage days and QI score was found by a simple linear regression equation: QI=2.4×day-0.79 (R^2=0.990). The shelf life of Pacific white shrimp at 0°C was projected to 8 days corresponding to QI of 18.5. N.T. Le, et al. (2017), C.O.R. Okpala, et al. (2014), N.P. Nirmal, et al. (2009), and A. Hanpongkittikun, et al. (1995) [18, 24, 29, 30] also obtained a shelf-life for black tiger and white shrimp ranging between 7 and 8 days. In reference to previously published studies, we categorize the quality of Pacific white shrimp into 4 classes: Excellent (QI from 0-2.9), Good (QI 2.9-8.87), Moderately Acceptable (QI 8.87-14.12), and Just Acceptable (QI 14.12-18.50). The established QIM scheme was validated by comparison between its projected shelf-life and the actual shelf-life of the shrimp samples. Ten shrimp samples with different storage times were randomly selected and subjected to the QI evaluation. The QI score for each sample was the average score given by the sensory panel. The estimated shelf life was calculated using the linear regression equation (QI=2.41×day-0.79; R^2=0.990). The results in Table 3 show that the actual shelf life was not significantly different from the estimated shelf life ($p<0.05$). Table 3 describes the data from the 10 experimental samples.

Table 3. Validation of the QIM scheme with the projected and the actual shelf life.

Samples	QI	Equivalent number of storage days in ice	Projected shelf life according to QIM scheme	Actual shelf life (n=3)
1	1.14	0.8	7.2	7.07±0.06
2	2.82	1.5	6.5	6.5±0.10
3	4.27	2.1	5.9	5.97±0.12
4	6.43	3.0	5.0	5.03±0.12
5	10.04	4.5	3.5	3.57±0.15
6	13.17	5.8	2.2	2.23±0.15
7	2.58	1.4	6.6	6.50±0.10
8	12.93	5.7	2.3	2.23±0.12
9	6.92	3.2	4.8	4.97±0.15
10	9.80	4.4	3.6	3.50±0.10

Table 3 shows that the remaining shelf-life of the samples were nearly equal to the shelf-life calculated from the linear regression equation between QI and storage days. This validated the efficiency of the QIM scheme for Pacific white shrimp and proved that this scheme can be used to evaluate the quality and the classification of shrimp quality as shown in Table 2.

3.3. The change in K-value

Shrimp undergo the autolysis process quickly after harvest. ATP is one of the first metabolites in fisheries after death. The changes in nucleotide and related compounds are presented in Fig. 1. From this figure, the changes of ATP, ADP, AMP, IMP, and inosine became quickly prone due to the endogenous enzymes possess in fish and shellfish. In contrast, the transformation from hypoxanthine to uric acid occurred slowly. Therefore, the amount of hypoxanthine increased with the storage time. Fig. 1 depicts the ATP content and its derivatives resulting from the ATP autolytic process. The ATP components and their derivatives are expressed in µM/g. The contents of ATP, ADP, AMP, IMP, HxR, and Hx measured on day 1 were 0.4, 1.07, 7.03, 0.4, 0.44, and 0.59 µM/g, respectively. This proved that the metabolism from ATP to AMP occurred quickly at the beginning. The amount of ATP and ADP from the 3rd day onward had very low values in the remaining days. The amount of AMP decreased rapidly until day 4 (4.12 µM/g), meanwhile, the amount of IMP, Hx, and HxR increased gradually to 1.24, 1.09 , and 0.84 µM/g, respectively, on day 4. However, there were differences in these components in the following days: the amount of AMP decreased steadily; IMP increased until day 6 then decreased slightly to day 10; HxR almost did not change; while Hx increased gradually over the storage time. Thus, among the components considered, the Hx value increased linearly with the storage time and the linear regression equation between Hx and the storage day was Hx=0.177×day+0.33 (R^2=0.974). The K-value calculated from the equation increased with time of storage. The linear regression equation between the K-value and storage day was K-value=3.05×day+1.8 (R^2=0.992) (Fig. 2). Studies [10-15, 31] also show that the K-value and hypoxanthine amount increase linearly with storage time. This suggests that it is possible to use the amount of hypoxanthine to assess the quality change of Pacific white shrimps preserved at 0°C using the linear regression procedure between the K-value and hypoxanthine presented above.

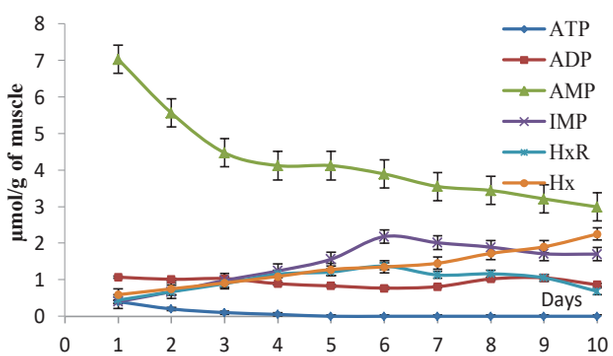

Fig. 1. Changes in nucleotide content and the composition of derivatives during 10-day storage. Adenosine triphosphate - ATP; Adenosine diphosphate - ADT; Adenosine monophosphate - AMP; Inosine monophosphate - IMP; Xanthine - HxR; Hypoxanthine - Hx.

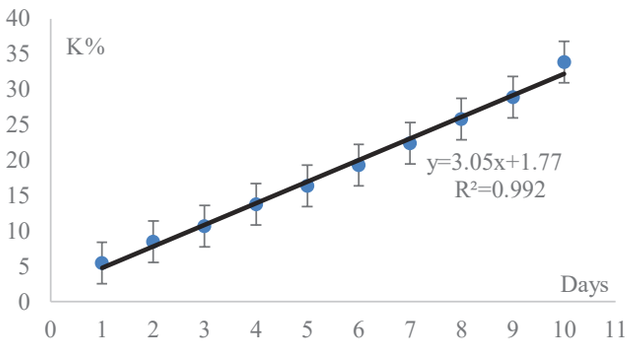

Fig. 2. Changes of K-value during 10-day storage.

3.4. Correlation between the quality indices and classification of shrimp quality

The results showed that the QI, K-value, and hypoxanthine correlated linearly with storage time. Therefore, these quality indicators correlate linearly with each other. The linear regression equation between the indicators are as follows: QI=0.79K-9.49 (R^2=0.956); QI=13.54Hx-7.44 (R^2=0.979); Hx=0.06K-0.13 (R^2=0.950). Table 4 presents the results of a combined quality classification of Pacific white shrimp between the QIM and chemical indicators including K-value and hypoxanthine.

Table 4. Quality classification of Pacific white shrimps based on QI, K-value, and hypoxanthine.

Quality class	QI	K-value	Hypoxanthine (Hx)
Excellent	0≤QI≤2.9	0≤K≤18.36	0≤Hx≤0.75
Good	2.9<QI≤8.87	18.36<K≤24.30	0.75<Hx≤1.09
Acceptable	8.87<QI≤14.12	24.30<K≤29.34	1.09<Hx≤1.35
Moderately acceptable	14.12<QI≤18.5	29.34<K≤ 34.11	1.35<Hx≤1.72

4. Conclusions

A QIM scheme has been developed for Pacific white shrimp (*Litopenaeus vannamei*) stored at 0°C. The scheme employs the descriptive terms for quality changes in sensory attributes in accordance with the quality requirements required by QIM (from 0 to 3). The quality of the shrimp was categorized into four classes, including Excellent, Good, Acceptable, and Moderately Acceptable, which are based on the QI score. The QIM scheme for Pacific white shrimp was validated for its accuracy and efficiency. This scheme can be combined with the K-value or hypoxanthine value for the quality assessment of Pacific white shrimp.

CRediT author statement

Nhat Tam Le, Nguyen Que Anh Huynh, Nhu Khue Doan: Conceptualisation, Methodology, Software, Resources, Writing - Review and Editing; Thuy Xuan Uyen Phan,

Ba Thanh Nguyen, Sao Mai Dam, Thi Van Thi Tran: Data curation, Software, Writing - Original draft preparation; Le Phuong Lien Nguyen, Van Hai Chu, Huynh Anh Vu Truong: Supervision, Software, Validation.

COMPETING INTERESTS

The authors declare that there is no conflict of interest regarding the publication of this article.

REFERENCES

[1] M. Li, W. Wang, W. Fang, et al. (2013), "Inhibitory effects of chitosan coating combined with organic acids on Listeria monocytogenes in refrigerated ready-to-eat shrimps", *Journal of Food Protection*, **76(8)**, pp.1377-1383, DOI: 10.4315/0362-028X.JFP-12-516.

[2] L.M. Nollet, F. Toldrá (Eds.) (2009), *Handbook of Seafood and Seafood Products Analysis*, CRC Press, 928pp.

[3] I.N.A. Ashie, J.P. Smith, B.K. Simpson, et al. (1996), "Spoilage and shelflife extension of fresh fish and shellfish", *Critical Reviews in Food Science & Nutrition*, **36(1-2)**, pp.87-121, DOI: 10.1080/10408399609527720.

[4] G. Hyldig, D.M.G. Petersen (2004), "Quality index method-an objective tool for determination of sensory quality", *Journal of Aquatic Food Product Technology*, **13(4)**, pp.71-80, DOI: 10.1300/J030v13n04_06.

[5] D. Nielsen (2005), "Quality index method provides objective seafood assessment", *Glob. Sea. Allian.*, https://www.globalseafood.org/advocate/quality-index-method-provides-objective-seafood-assessment/, accessed 17 February 2020.

[6] EUROFISH, QIM (2012), *How Fresh is Your Fish.*

[7] The General Department of Standards, Metrology, and Quality (1989), *TCVN 3726-1989: Fresh Shrimps for Food Processing* (in Vietnamese).

[8] H.H. Huss (Ed.) (1995), *Quality and Quality Changes in Fresh Fish*, Food and Agriculture Organization of the United Nations, Danish, 348pp.

[9] T. Saito, K. Arai, M. Matsuyoshi (1959), "A new method for estimating the freshness of fish", *B. Jpn. Soc. Sci. Fish*, **24(9)**, pp.749-750, DOI: 10.2331/suisan.24.749.

[10] K.I. Sallam (2007), "Chemical, sensory and shelf life evaluation of sliced salmon treated with salts of organic acids", *Food Chemistry*, **101(2)**, pp.592-600, DOI: 10.1016/j.foodchem.2006.02.019.

[11] F.A. Bakar, A.B. Salleh, C.N.A. Razak, et al. (2008), "Biochemical changes of fresh and preserved freshwater prawns (*Macrobrachium rosenbergii*) during storage", *Int. Food Res. J.*, **15(2)**, pp.181-191.

[12] M.H.U. Montoya, A.G.V. Villalba, R.P. Aguilar, et al. (2010), "Changes in quality parameters of Monterey sardine *(Sardinops sagax caerulea*) muscle during the canning process", *Food Chemistry*, **122(3)**, pp.482-487, DOI: 10.1016/j.foodchem.2009.05.071.

[13] R.K. Kalleda, I.Y. Han, J.E. Toler, et al. (2013), "Shelf life extension of shrimp (white) using modified atmosphere packaging", *Polish Journal of Food and Nutrition Sciences*, **63(2)**, pp.87-94, DOI: 10.2478/v10222-012-0071-7.

[14] D.F.C. Rodriguez, V.M.O. Higuera, E.M. Rios, et al. (2015), "Biochemical, physical, chemical, and microbiological assessment of blue shrimp (*Litopenaeus stylirostris*) stored in ice", *Journal of Aquatic Food Product Technology*, **24(3)**, pp.259-269, DOI: 10.1080/10498850.2013.771390.

[15] Y.R. Huang, M.F.J. Zelaya, C.Y Shiau (2016), "Changes in biochemical compositions and quality of white shrimp (*Litopenaeus vannamei*) during storage", *Journal of Aquatic Food Product Technology*, **25(1)**, pp.35-45, DOI: 10.1080/10498850.2013.824944.

[16] M.J. Leboffe, B.E. Pierce (2015), *Microbiology: Laboratory Theory and Application*, Morton Publishing Company, 888pp.

[17] D.C. Bernardi, E.T. Marsico, M.Q.D. Freitas (2013), "Quality index method (QIM) to assess the freshness and shelf life of fish", *Brazilian Archives of Biology and Technology*, **56(4)**, pp.587-598, DOI: 10.1590/S1516-89132013000400009.

[18] N.T. Le, N.K. Doan, T.N. Ba, et al. (2017), "Towards improved quality benchmarking and shelf life evaluation of black tiger shrimp (*Penaeus monodon*)", *Food Chemistry*, **235**, pp.220-226, DOI: 10.1016/j. foodchem.2017.05.055.

[19] G. Hyldig, G.D.M.G. Petersen (2005), "Quality index method-an objective tool for determination of sensory quality*"*, *Journal of Aquatic Food Product Technology*, **13(4)**, pp.71-80, DOI: 10.1300/J030v13n04_06.

[20] K. Azam, S.N. Alam, S.S. Naher (2010), "Quality assessment of farmed black tiger shrimp (*Penaeus monodon*) in supply chain: Organoleptic evaluation", *Journal of Food Processing and Preservation*, **34**, pp.164-175, DOI: 10.1111/j.1745-4549.2008.00331.x.

[21] Nacalai Tesque (2018), *Cosmosil Application*, https://www.nacalai.co.jp/cosmosil/data/csmosrchpng.cfm?sFile=AP-1485&columnID=011&lc=E&pg=Application, accessed 17 February 2020.

[22] M.V. Nogues, A.M. Font, M.V. Carou (1997), "Biogenic amines as hygienic quality indicators of tuna. Relationships with microbial counts, ATP-related compounds, volatile amines, and organoleptic changes", *Journal of Agricultural and Food Chemistry*, **45(6)**, pp.2036-2041, DOI: 10.1021/jf9609111.

[23] R.P. Naik, B.B. Nayak, M.K. Chouksey, et al. (2014), "Microbiological and biochemical changes during ice storage of farmed black tiger shrimp (*Penaeus monodon*)", *Bionano Frontier*, **7(2)**, pp.249-253.

[24] C.O.R. Okpala, W.S. Choo, G.A. Dykes (2014), "Quality and shelf life assessment of Pacific white shrimp (*Litopenaeus vannamei*) freshly harvested and stored on ice", *LWT-Food Science and Technology*, **55(1)**, pp.110-116, DOI: 10.1016/j.lwt.2013.07.020.

[25] A. Bevilacqua, M.R. Corbo, M. Sinigaglia (2016), *The Microbiological Quality of Food: Foodborne Spoilers*, Woodhead Publishing, 310pp.

[26] E.N. Frankel (1983), "Volatile lipid oxidation products", *Progress in Lipid Research*, **22(1)**, pp.1-33, DOI: 10.1016/0163-7827(83)90002-4.

[27] D.B. Josephson, R.C. Lindsay, D.A. Stuiber (1984), "Biogenesis of lipidderived volatile aroma compounds in the emerald shiner (*Notropis atherinoides*)", *Journal of Agricultural and Food Chemistry*, **32(6)**, pp.1347-1352, DOI: 10.1021/jf00126a032.

[28] G. Ares, S. Jaeger (2015), "Check-all-that-apply (CATA) questions with consumers in practice: experimental considerations and impact on outcome", *Rapid Sensory Profiling Techniques*, pp.227-245, DOI: 10.1533/9781782422587.2.227.

[29] N.P. Nirmal, S. Benjakul (2009), "Effect of ferulic acid on inhibition of polyphenoloxidase and quality changes of Pacific white shrimp (*Litopenaeus vannamei*) during iced storage", *Food Chemistry*, **116(1)**, pp.323-331, DOI: 10.1016/j.foodchem.2009.02.054.

[30] A. Hanpongkittikun, S. Siripongvutikorn, D.L. Cohen (1995), "Black tiger shrimp (*Penaeus monodon*) quality changes during iced storage", *ASEAN Food Journal*, **10**, pp.125-130.

[31] N.R. Jones, J. Murray (1962), "Degradation of adenine-and hypoxanthinenucleotide in the muscle of chill-stored trawled cod (*gadus callarias*)", *Journal of The Science of Food and Agriculture*, **13(9)**, pp.475-480, DOI: 10.1002/jsfa.2740130905.

DOI: 10.31276/VJSTE.63(2).52-57

Extraction of flavonoids in pomelo peels using Box-Behnken response surface design and their biological activities

Truong Ngoc Quynh Phuong[1, 2], Pham Van Hung[1, 2], Nguyen Thi Lan Phi[2, 3*]

[1]*Department of Food Technology, International University, Vietnam National University - Ho Chi Minh City, Quarter 6, Linh Trung Ward, Thu Duc City, Ho Chi Minh City, Vietnam*

[2]*Vietnam National University - Ho Chi Minh City, Quarter 6, Linh Trung Ward, Thu Duc City, Ho Chi Minh City, Vietnam*

[3]*Department of Food Technology, University of Technology, Vietnam National University - Ho Chi Minh City, 268 Ly Thuong Kiet Street, Ward 14, District 10 Ho Chi Minh City, Vietnam*

Received 9 January 2020; revised 20 March 2020; accepted 6 April 2020

Abstract:

The objectives of this study were to optimize the extraction conditions of flavonoids from the pomelo peel using the Box-Behnken response surface methodology and to investigate the chemical composition and biological activities of the extracts from three different pomelo species under optimized extraction conditions. Three extraction condition factors of were varied, including the solid-solvent ratio (1/15-1/45 g/ml), temperature (30-60°C), and time (20-60 min), which affected the efficiency of the total flavonoid content (TFC). The high R^2 coefficient of 0.93 indicated that the experimental data obtained in this study fit well to a second-order polynomial using multiple regression analysis. The maximum TFC extracted from the pomelo peel was 6.0 mg/g (dried basis, db), which was obtained using Derringer's desired function methodology under the following optimum conditions: a solid-solvent ratio of 1/44 g/ml, temperature of 30.7°C, and time of 34.6 min. The results also indicated that the Tan Trieu pomelo peel had the highest TFC and naringin concentration followed by the Nam Roi and Duong Hong pomelo peels, whereas the Nam Roi pomelo peel had a higher hesperidin concentration than the others. The extracts of the pomelo peels exhibited strong antioxidant activities with low IC_{50} values. However, these extracts showed only a slight effect on cancer cells, including lung cancer and breast cancer, when tested at 100 µg/ml.

Keywords: **antioxidant, Box-Behnken design, extraction, flavonoids, pomelo.**

Classification number: **3.1**

1. Introduction

Pomelo (*Citrus grandis*), a member of the citrus family, is grown in many eastern countries including India, Vietnam, and Thailand. Pomelos have been used as fresh fruit or for juice processing with good quality and low price. However, after processing, their peel is a primary by-product that contributes to environmental pollution. Therefore, it is necessary to take full advantage of technology to develop other kinds of products from the peels [1]. In recent years, pomelo has attracted more attention from scientists because of their nutritional and antioxidant properties. In addition, pomelo peels and seeds were found to contain two natural compounds such as flavonoids and limonoids, respectively, which play an important role in living systems. Significantly, flavonoids have a wide range of biological effects, such as chelation of metal catalysts, inhibition of key enzymes in mitochondrial respiration, protection from heart disease, and anti-inflammatory, anticancer, and antimicrobial activities [1, 2]. In the pomelo peels, flavonoids are present in three classes including flavanone, flavone, and flavanol compounds, in which flavanone is considered as the most abundant flavonoid in the pomelo peel (up to 80%). Naringin has been reported to be a predominant flavanone in the peel and edible portions of many varieties of pomelos [3-5], while a small concentration of hesperidin in a pomelo peel was also found [5, 6]. The naringin, hesperidin, and neohesperidin contents were found to be much higher in the peels than in the juice [5]. Naringin has the ability to prevent cancer by carcinogenesis suppression and induction of cell apoptosis, whereas neohesperidin contributes to the bitter taste in grapefruit and pomelo, and has the power to stimulate the immune system [2, 6-8]. Therefore, it is necessary to extract these flavonoids from the peels of the pomelo for food and pharmaceutical application.

*Corresponding author: Email: lanphi@hcmut.edu.vn

Various methods have been applied to extract flavonoid compounds of plants based on the manipulation of the physical properties of solvents to reduce surface tension, increase the solute's solubility, promote the higher diffusion rate, and change in solvent polarity. Solid-liquid extraction or the solvent extraction method, one of the most widely used extraction methods, has been used to extract one or more solutes from a solid matrix by a liquid solvent and has widely applied in food industry to recover various products including sugars, teas, coffees, vegetable oils, and functional compounds. The yield of the solutes is also influenced by numerous factors including the preparation of the solid, diffusion rate, temperature, and solvent choices [9]. Several extraction methods have been reported for the extraction of flavonoids from pomelo peels such as conventional extraction, enzyme-assisted extraction, ultrasound-assisted extraction, microwave-assisted extraction, supercritical CO_2 extraction, and pressurized fluid extraction [10-13]. To the best of our knowledge, there is no report on the optimization of extraction conditions to obtain maximum TFC from pomelo peels. Therefore, the objectives of this study is to optimize extraction conditions such as solid-solvent ratio, extraction temperature, and extraction time to get the highest flavonoid from the pomelo's peel based on Box-Behnken response surface design and to determine the chemical composition and biological properties of the extracts from the Tan Trieu, Duong Hong, and Nam Roi pomelo varieties.

2. Materials and methods

2.1. Plant materials

Tan Trieu, Duong Hong, and Nam Roi pomelo (*Citrus grandis* Osbeck) varieties grown at different locations of Vietnam were used in this study. The pomelo fruits were carefully washed to remove soil particles and dust. Peels were taken out from the pulp and then cut into small pieces. Then, the peel pieces were dried using a freeze-drying machine and ground into fine powder. The pomelo peel powder, with a moisture content of 12-14%, was stored in a desiccator prior to the experiment.

2.2. Extraction method

The dried peel powder (1 g) was accurately weighed and mixed with ethanol under predetermined extraction conditions based on the Box-Behnken response surface design as described in the experimental design section below and in Table 1. After shaking the sample in a water bath for a certain temperature and time, the samples were centrifuged for 15 min at 4°C. The supernatant was kept while the residue was repeatedly extracted 3 times. Then, the supernatants were combined, evaporated, and diluted with methanol to yield 20 ml of crude extract before storing for analysis.

Table 1. The coded level of variables chosen for the experiments.

Variable	Coded	Range and level		
		-1	*0*	*+1*
Solid-solvent ratio (w/v)	X_1	1/15	1/30	1/45
Incubation Temperature (°C)	X_3	30	45	60
Incubation time (h)	X_4	30	45	60

2.3. Experimental design

The total flavonoids of the pomelo peels were extracted with a solvent of 75% ethanol and optimized using the Box-Behnken design with three variables including solid-solvent ratio (1/15, 1/30 and 1/45), temperature (30, 45 and 60°C) and time (30, 45 and 60 min). The scientific basis behind the chosen testing levels was determined by screening experiments using the one-factor optimization method at which the total flavonoids were the highest (the details of these experiments are not shown in this paper).

Each independent variable was coded at three levels of -1, 0, and +1 (Table 1). The experimental design consisted of a total of 17 experiments with five centre points as shown in Table 2.

Table 2. Total flavonoids content of pomelo peel extracted using Box-Behnken design.

Trial no.	Solid-solvent ratio (w/v)	Temperature (°C)	Time (min)	TFC (mg/g)
1	1/15	45	20	4.31
2	1/30	45	40	5.81
3	1/30	60	60	4.15
4	1/30	45	40	5.17
5	1/30	30	60	4.28
6	1/45	30	40	6.00
7	1/15	45	60	3.55
8	1/45	60	40	5.26
9	1/45	45	20	4.94
10	1/30	30	20	5.21
11	1/15	60	40	4.81
12	1/30	45	40	5.81
13	1/45	45	60	5.11
14	1/30	60	20	4.67
15	1/30	45	40	5.42
16	1/15	30	40	4.94
17	1/30	45	40	5.32

2.4. Determination of total flavonoids content

The TFC was determined using the colorimetric method previously described by P.V. Hung, et al. (2008) [14] with a minor modification. The extract (0.5 ml) was mixed with 1.5 ml of 95% ethanol, 0.1 ml of 10% aluminium chloride solution, and 0.1 ml of 1 M potassium acetate. Then, distilled water was added to adjust the volume to 10 ml. The tubes were thoroughly mixed and stood at ambient temperature in the dark for 30 min. The absorbance was measured at 415 nm against the reagent blank using a spectrophotometer (Genesys 10S UV-Vis, USA). Rutin was used as the standard and the TFC was expressed as micrograms rutin equivalent (RE) per gram of sample.

2.5. HPLC analysis

Flavonoids in the citrus peels were analysed using high performance liquid chromatography (HPLC) according to the method of I.A. Ribeiro and M.H.L Ribeiro (2008) [15]. In detail, the extracts obtained at optimal extraction conditions were diluted with 20 ml of 0.02 M sodium acetate buffer (pH=4) and methanol (1:1). Then, the solutions were filtered through a 0.45 µm membrane filter before injection into the HPLC system. The mobile phase, including acetonitrile (solvent A) and distilled water (solvent B), was used. The gradient elution was conducted as starting at 23% A in 8 min, 23-65% A in 7 min, 65-70% A in 5 min, 70% A - 23% A in 1 min, and completing the gradient at 23% A in 1 min. The elution was monitored at a flow rate of 1 ml/min and UV wavelength of 280 nm. Naringin (Product #N1376, Sigma), hesperidin (product #H5254), and HPLC grade acetonitrile (product #1000302500) and methanol (product #1060182500, Merck) were used in this study.

2.6. DPPH radical scavenging assay

The antioxidant activity of the extracts was determined according to the method of P.V. Hung, et al. (2008) [14]. The final concentration of the DPPH solution was 0.075 mM. A mixture of 3.9 ml of DPPH solution and 0.1 ml of the extract was mixed and kept in the dark at ambient temperature for 30 min. Then, the absorbance of the mixture was read at 515 nm. Methanol (0.1 ml) was used to replace the extract to mix with the DPPH solution and counted as the blank sample. The scavenging of DPPH was calculated according to the following equation:

$$\% \text{ DPPH scavenging} = \{[Abs_{(t=0)} - Abs_{(t=30)}]/Abs_{(t=0)}\} \times 100$$

where $Abs(t_0)$ is the absorbance of the DPPH radical and methanol solution at t=0 min and $Abs(t_{30})$ is absorbance of the DPPH radical and the extracts at t=30 min.

The results were reported as a half maximal inhibitory concentration (IC_{50}) value. A lower IC_{50} value represents stronger DPPH scavenging capacity. The IC_{50} value was determined from linear regression analysis using Microsoft Excel with data analysis add-in.

2.6. Cytotoxic activity on cancer cells

The colorimetric cytotoxicity assay reported by P. Skehan, et al. (1990) [16] was used to investigate the effects of the extracts on the survival of cancer cells including Hep-G2 (human hepatocellular carcinoma), LU-1 (human lung adenocarcinoma), and MCF-7 (human breast adenocarcinoma). By using SRB (sulforhodamine B) as a basic colorimetric method, the cytotoxicity of the compounds was investigated. These cancer cells were maintained in E'MEM (Dulbecco's Modified Eagle Medium) with the addition of L-glutamine, sodium pyruvate, $NaHCO_3$, PSF (penicillin-streptomycin sulfate-fungizone), NAA (non-essential amino acids), and 10% BCS (bovine calf serum) before storage at 37°C in a 5% CO_2 incubator. A plate (96-well) was used to grow cells at 10^4 cells/well for Hep-G2 and MCF-7, and 7.5×10^3 cells/well for LU-1 in the growth medium. After 24 h of growth, these cells were incubated in the presence of the extracts with different concentrations in 48 h. Then, the total protein was maintained by using trichloroacetic acid (Sigma) 50% and dyed by SRB 0.2%. The standard was measured by ellipticine, vinblastine, or taxol dissolving DMSO. The result was read by an ELISA at 495-515 nm. The percentage of cell survival is determined by:

$$\% \text{ cell survival} = (Abs_{sample} - Abs_{control})/(Abs_{DMSO} - Abs_{control})$$

2.7. Statistical analysis

The data were analysed for multiple regression analysis and analysis of variance (ANOVA) to fit the mathematical modelling using Design Expert software (Version 11, Stat-Ease Inc., USA). After fitting the data to the models, the response surface and 3D contour were plotted and investigated.

3. Results and discussion

3.1. Box-Behnken design analysis

The statistically designed experiments under different extraction conditions were carried out to investigate the combined effect of independent variables (solid-solvent ratio, extraction temperature and extraction time) on the

extraction yield of the TFC and the results are shown in Table 2. The results indicated that the TFC of the extracts from the pomelo peel varied with different extraction conditions. Table 3 showed the fitting of four high degree polynomial models (linear, interactive (2FI), quadratic, and cubic models) with the experimental data. The quadratic model had a maximum adjusted R^2 with low p-value. Therefore, this model was the most suitable for the designed experiments. The experimental data was analysed by ANOVA and the results in Table 4 indicated that the model was significant because the p-value of the model was less than 0.05. Moreover, the F-value was 0.6093 meaning that the lack of fit of the model was not significant as compared to pure error and the designed model was good.

Table 3. Sequential model fitting for the response.

Source	Sequential p-value	Lack of fit p-value	Adjusted R^2	
Linear	0.095199	0.067263	0.232767	
2FI	0.820918	0.041751	0.086334	
Quadratic	0.001709	0.64349	0.831442	Suggested
Cubic	0.64349		0.797545	Aliased

Table 4. Analysis of variance (ANOVA) for Box-Behnken model.

Source	Sum of squares	Degree of freedom	Mean square	F-value	P-value
Model	6.22	9	0.6908	9.77	0.0033
Lack-of-fit	0.1552	3	0.0517	0.6093	0.6435
Pure error	0.3397	4	0.0849		
Corrected total	6.71	16			
R^2	0.9263				
adj R^2	0.8314				
C.V%	6.71%				

3.2. Fitting of second order polynomial equation

The relationship between the three factors with the response is given by the following equation in terms of coded factors:

$$TFC\ (mg/g)=5.51+0.4625X_1-0.1925X_2-0.2550X_3-0.1525X_1X_2+0.2325X_1X_3+0.1025X_2X_3-0.1768X_1^2-0.0768X_2^2-0.8517X_3^2$$

where X_1 is the solid-solvent ratio, X_2 is the extraction temperature, and X_3 is the extraction time.

The results indicated that the TFC of the extracts from the pomelo peels were not only dependent on all factors (X_1, X_2, and X_3), but also dependent on the relationship between the two independent factors (X_1X_2, X_1X_3, and X_2X_3).

3.3. Effect of independent variables on the TFC

Three factors including the solid-solvent ratio, extraction temperature, and time at three different levels were used to investigate the influence of the independent variables in the TFC. The 3D response surface and contour plots were developed from the model by maintaining two factors as constant while varying the third to illustrate the optimum conditions (Fig. 1).

Effect of solid-solvent ratio: Figs. 1B and 1C showed that the TFC increased with increasing solid-solvent ratio from 1:15 to 1:44 (g/ml). The difference in concentration between the cell tissue of the pomelo peel and the solvent improved the efficiency of extraction because of an increased mass transfer rate. The liquid circulation and turbulence produced by cavitation increased the contact surface between the solvent and target compounds by permitting greater penetration of solvent into the sample matrix [17].

Effect of extraction temperature: The effects of extraction temperature on the TFC under the Box-Behnken design can be observed in Figs. 1A and 1C. The results indicated that temperature did not affect TFC at solid-solvent ratio of 1:15 g/ml while it did affect the TFC at higher solid-solvent ratios. As a result, the TFC reached its highest level when the temperature was 30°C and the solid-solvent ratio was

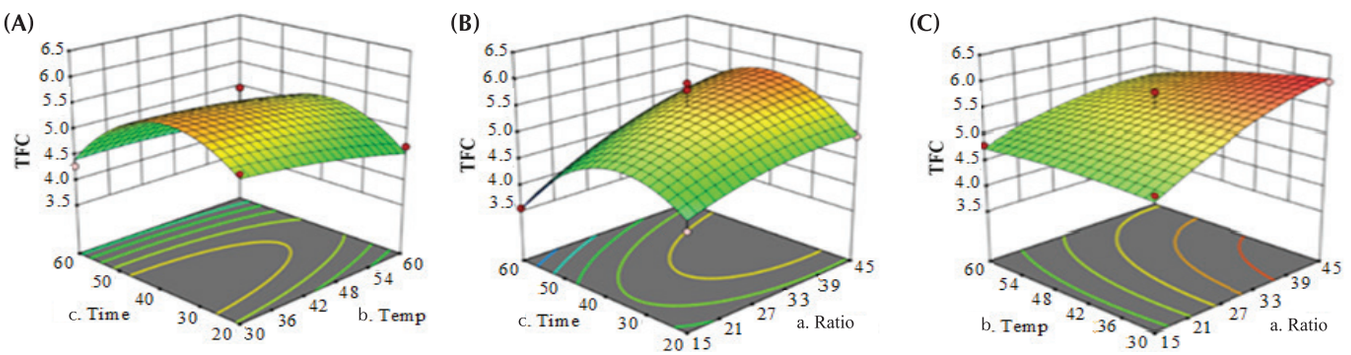

Fig. 1. Response surface plots representing the effect of extraction conditions on the TFC. (A) The solid-solvent ratio; **(B)** Extraction temperature; **(C)** Time at three different levels.

1:44 g/ml. As a result, the 30°C temperature was the ideal temperature for extraction of TFC from the pomelo peels in this study.

Effect of extraction time: The effects of extraction time on the TFC under the Box-Behnken design are shown in Figs. 1A and 1B. The TFC increased with increasing extraction time from 20 to 45 min. At a higher solid-solvent ratio, the TFC reduced upon lengthening the extraction time. The highest TFC of the pomelo peels was obtained with an extraction time of 34.6 min. Further increasing extraction time could cause the loss of solvent by vaporization.

3.4. Optimization and verification of model

The extraction conditions were optimized to get the maximum extractive TFC by employing Derringer's desired function methodology. From the model, the highest TFC was predicted to be 6.0 mg/g under the following optimized conditions: the solid-solvent ratio of 1/44 g/ml, extraction temperature of 30.7°C, and extraction time of 34.6 min.

For confirmation, triplicate extractions of TFC from pomelo peels were carried out under the optimum conditions stated above. The average TFC was 6.0±0.1 mg/g peels, which is not significantly different from the predicted results of the model. Thus, the model obtained in this study was significant. The TFC of the pomelo peels extracted under the optimal conditions in this study was significantly higher than that obtained by the conventional enzyme and ultrasound-assisted extraction methods reported by P.V. Hung, et al. (2020) [18].

3.5. Flavonoid concentration in pomelo's peels

The TFCs of the peel extracts from different pomelo varieties are given in Table 5. The TFC varied among the different varieties of pomelo ($p<0.05$), which ranged from 4.3±0.1 to 6.0±0.1 mg/g peels. The lowest TFC was presented in the Duong Hong pomelo peels (4.3±0.1 mg/g peels), whereas the highest TFC was 6.0±0.1 mg/g peels from the Tan Trieu pomelo peels. The difference in the TFC among the different pomelo varieties might be due their chemical composition, maturity at harvest, soil and water qualities, and the condition of the post-harvest method [19].

Table 5. Total flavonoid, naringin and hesperidin concentrations of pomelo peels' extracts under optimized condition (mg/g).

Sample	Concentration (mg/g, db)		
	Total flavonoids	*Naringin*	*Hesperidin*
Tan Trieu pomelo	6.0±0.1[b]	2.2±0.2[c]	0.36±0.1[b]
Duong Hong pomelo	4.3±0.1[a]	1.6±0.1[b]	0.18±0.2[a]
Nam Roi pomelo	4.5±0.1[a]	0.2±0.2[a]	0.69±0.3[c]

[a, b, c]: different letters in the same column are significantly different ($p<0.05$).

In the present study, the concentration of two flavonoids in pomelo peels including naringin and hesperidin was identified using the HPLC and are given in Table 5. The naringin concentration in the Tan Trieu pomelo was the highest (2.2±0.2 mg/g peels) followed by the Duong Hong pomelo peel (1.6±0.1 mg/g peel) and the Nam Roi pomelo peel (0.2±0.2 mg/g peel). The highest hesperidin concentration was 0.69±0.3 mg/g found in the Nam Roi pomelo peel, followed by the Tan Trieu and Duong Hong pomelo peels. The results found in this study were consistent with the results reported by G.H. Xu, et al. (2008) [20], which stated that the hesperidin concentration in the pomelo peels was 1.77 mg/g DW under the same extraction conditions. However, hesperidin could not be found in several of the pomelo types from China. It has been shown that flavonoids are not equally distributed among the different types and parts of the citrus fruit. H.D. Jang, et al. (2010) [21] reported that the essential oil of the Buntan peel contained a higher TFC than those from the extracts of fruit pulp with different solvents. The greatest TFC among the different parts of the fruits ranked as follows: peel>pulp>juice [3].

3.6. DPPH radical scavenging activities of pomelo peel extracts

The antioxidant capacities of the pomelo peel extracts measured by the DPPH scavenging activity and expressed as IC_{50} values are given in Table 6. The IC_{50} value was calculated as the amount of extract required to inhibit 50% of the DPPH radical. The lower the IC_{50} value is, the higher the antioxidant activity of the extract. The IC_{50} values of the citrus peel extracts ranged from 1.08 to 4.51 µg/ml, which is significantly higher than that of the Trolox (0.65±0.04 µg/ml). These results indicate that the Tan Trieu pomelo peel extract exhibited the highest antioxidant activity (IC_{50}=1.08±0.04 µg/ml), followed by the Nam Roi pomelo peel extract (IC_{50}=3.09±0.01 µg/ml) and Duong Hong pomelo peel extract (IC_{50}=4.51±0.03 µg/ml). Previous studies [22] revealed that the IC_{50} of ethanolic extracts from the peels of *C. hystrix* from Boyolali - Central Java, Indonesia were 16.7 µg/ml. The present study [23] also indicated that the peels of the pomelo varieties in Vietnam had a higher antioxidant capacity than other locations.

Table 6. DPPH radical scavenging (IC_{50} value) of pomelo peels' extracts.

Sample	IC_{50} value (µg/ml)
Trolox	0.65±0.04[a]
Tan Trieu pomelo	1.08±0.04[b]
Duong Hong pomelo	4.51±0.03[d]
Nam Roi pomelo	3.09±0.01[c]

[a, b, c]: different letters in the same column are significantly different ($p<0.05$).

3.7. Cytotoxic activity on cancer cells of peel's extracts

Table 7. Anticancer activity of pomelo peels' extracts.

Sample	Initial concentration (µg/ml)	CS value (%)		
		Hep-G2	*LU-1*	*MCF-7*
Standard (+)	5	4.34±0.42[a]	1.13±0.44[a]	2.53±0.06[a]
Tan Trieu	100	98.94±0.95[b]	99.24±1.06[c]	80.44±1.92[c]
Duong Hong	100	97.42±1.13[b]	83.77±1.51[b]	99.54±0.62[d]
Nam Roi	100	99.04±0.79[b]	85.42±0.52[b]	77.11±2.06[b]

[a, b, c]: different letters in the same column are significantly different ($p<0.05$).

The anticancer activities of the pomelo peel extracts are shown in Table 7. The results indicate that the pomelo peels did not affect Hep-G2 (human hepatocellular carcinoma). The percentage of dead cells after treatment was 1.06% (Tan Trieu pomelo peel extract), 2.58% (Duong Hong pomelo peel extract), and 0.96% (Nam Roi pomelo peel extract). The Tan Trieu pomelo peel extract also had no effect on Lung cancer cells (LU-1), in which 99.24% of the cancer cells survived. The Duong Hong and Nam Roi pomelo peel extracts slightly affected the LU-1 cells with a total percentage of dead cancer cells being 16.23% and 14.58%, respectively. In addition, the highest percentage dead of breast cancer cells (MCF-7) was 22.89% when treated with the Nam Roi pomelo peel extract, followed by the Tan Trieu pomelo peel extract (19.56%) and Duong Hong pomelo peel extract (0.46%). The previous study [24] also reported that the essential oils of lemon and grapefruit peels exhibited a weak cytotoxicity toward human prostate (PC-3), lung (A549), and breast (MCF-7) tumour cell lines.

4. Conclusions

The TFC of pomelo peel extracts were successfully maximized using the Box-Behnken design and response surface analysis. The results indicated that the solid-solvent ratio, extraction temperature, and extraction time were the most important factors that affect TFC values. After analysis, the quadratic models within the studied experimental range of the various process variables were used to maximize the TFC. As a result, the optimized TFC of the pomelo peel was 6.0 mg/g peels under the optimized extraction conditions, just as predicted. All pomelo peel extracts possessed strong antioxidant activities with a low IC_{50}. However, the pomelo peel extracts showed weak or moderate anticancer activities when treated with 100 µg/ml of the extract.

CRediT author statement

Truong Ngoc Quynh Phuong, Pham Van Hung, Nguyen Thi Lan Phi: Conceptualisation, Methodology, Software, Resources, Writing - Review and Editing, Validation.

ACKNOWLEDGEMENTS

This research is funded by Vietnam National Foundation for Science and Technology Development (NAFOSTED) under grant number 106-NN.02-2016.72.

COMPETING INTERESTS

The authors declare that there is no conflict of interest regarding the publication of this article.

REFERENCES

[1] J.B. Harborne, C. William (2000), "Advances in flavonoids research since 1992", *Photochem.*, **55(6)**, pp.481-504, DOI: 10.1016/s0031-9422(00)00235-1.

[2] M.K.N. Chidambara, J. Kim, A. Vikram, et al. (2012), "Differential inhibition of human colon cancer cells by structurally similar flavonoids of citrus", *Food Chem.*, **132(1)**, pp.27-34, DOI: 10.1016/j.foodchem.2011.10.014.

[3] Y. Nogata, K. Sakamoto, H. Shiratsuchi, et al. (2006), "Flavonoid composition of fruit tissues of citrus species", *Biosci. Biotechnol. Biochem.*, **70(1)**, pp.178-192, DOI: 10.1271/bbb.70.178.

[4] M. Zhang, H. Nan, Y. Wang, et al. (2011), "The flavonoid composition of flavedo and juice from the pummelo cultivar (*Citrus grandis* L. Osbeck) and the grapefruit cultivar (*Citrus paradisi*) from China", *Food Chem.*, **129(4)**, pp.1530-1536, DOI: 10.3390/molecules191117314.

[5] Y.C. Wang, Y.C. Chuang, Y.H. Ku (2007), "Quantitation of bioactive compounds in citrus fruits cultivated in Taiwan", *Food Chem.*, **102(4)**, pp.1163-1171, DOI: 10.1016/j.foodchem.2006.06.057.

[6] M.A. Alam, N. Subhan, M.M. Rahman, et al. (2014), "Effect of citrus flavonoids, naringin and naringenin, on metabolic syndrome and their mechanisms of action", *Adv. Nutr.*, **5(4)**, pp.404-417, DOI: 10.3945/an.113.005603.

[7] O.B. Garcia, J. Castillo (2008), "Update on uses and properties of citrus flavonoids: New findings in anticancer, cardiovascular, and anti-inflammatory activity", *J. Agric. Food Chem.*, **56(15)**, pp.6185-6205, DOI: 10.1021/jf8006568.

[8] I. Erlund (2004), "Review of the flavonoids, quercetin, hesperidin, and naringenin. Dietary sources, bioactivities, bioavailability, and epidemiology", *Nutr. Res.*, **24(10)**, pp.851-874, DOI: 10.1016/j.nutres.2004.07.005.

[9] D.V. Dandekar, G.K. Jayaprakasha, B.S. Patil (2008), "Hydrotropic extraction of bioactive limonin from sour orange (*Citrus aurantium* L.) seeds", *Food Chem.*, **109(3)**, pp.515-520, DOI: 10.1016/j.foodchem.2007.12.071.

[10] S.M. Jeong, S.Y. Kim, D.R. Kim, et al. (2004), "Effect of heat treatment on the antioxidant activity of extracts", *J. Agric. Food Chem.*, **52(11)**, pp.3389-3393, DOI: 10.1021/jf049899k.

[11] Y.Q. Ma, J.C. Chen, D.H. Liu, et al. (2009), "Simultaneous extraction of phenolic compounds of citrus peel extracts: effect of ultrasound", *Ultrason. Sonochem.*, **16(1)**, pp.57-62, DOI: 10.1016/j.ultsonch.2008.04.012.

[12] E.M.G. Castello, A.D.R. Lopez, L. Mayor, et al. (2015), "Optimization of conventional and ultrasound assisted extraction of flavonoids from grapefruit (*Citrus paradisi* L.) solid wastes", *LWT-Food Sci. Technol.*, **64(2)**, pp.1114-1122, DOI: 10.1016/j.lwt.2015.07.024.

[13] N. M'hiri, I. Ioannou, M. Ghoul, et al. (2014), "Extraction methods of citrus peel phenolic compounds", *Food Rev. Int.*, **30(4)**, pp.265-290, DOI: 10.1080/87559129.2014.924139.

[14] P.V. Hung, N. Morita (2008), "Distribution of phenolic compounds in the graded flours milled from whole buckwheat grains and their antioxidant capacity", *Food Chem.*, **109(2)**, pp.325-331.

[15] I.A. Ribeiro, M.H.L. Ribeiro (2008), "Naringin and naringenin determination and control in grapefruit juice by a validated HPLC method", *Food Control,* **19(4)**, pp.432-438, DOI: 10.1016/j.foodchem.2007.12.060.

[16] P. Skehan, R. Storeng, D. Scudiero, et al. (1990), "New colorimetric cytotoxiCityassay for anticancerdrug screening", *J. Natl. Cancer Inst.*, **82(13)**, pp.1107-1112, DOI: 10.1093/jnci/82.13.1107.

[17] M. Romdhane, C. Gourdon (2002), "Investigation in solid-liquid extraction: Influence of ultrasound", *Chem. Eng. J.*, **87(1)**, pp.11-19, DOI: 10.1016/S1385-8947(01)00206-6.

[18] P.V. Hung, N.H.Y. Nhi, L.Y. Ting, et al. (2020), "Chemical composition and biological activities of extracts from pomelo peel by-products under enzyme and ultrasound-assisted extractions", *J. Chem.*, **2020**, DOI: 10.1155/2020/1043251.

[19] C. Shahzad (2011), "Total phenolic content and antioxidant capaCityof extracts obtained from 6 important fruit residues", *Food Res. Int.*, **44(1)**, pp.391-396.

[20] G.H. Xu, H.S. Oberoi, D.S. Uppal, et al. (2008), "Minerals, phenolic compounds, and antioxidant capacity of citrus peel extract by hot water", *J. Food Chem.*, **73(1)**, pp.11-17, DOI: 10.1016/j.foodres.2010.10.001.

[21] H.D. Jang, K.S. Chang, T.C. Chang, et al. (2010), "Antioxidant potentials of buntan pumelo *(Citrus grandis* Osbeck.) and its ethanolic and acetified fermentation products", *Food Chem.*, **118(3)**, pp.554-558, DOI: 10.1016/j.foodchem.2009.05.020.

[22] I. Fidrianny, P.I. Sari, K.R. Wirasutisna (2015), "Antioxidant activities in various peel extracts of four varieties rambutan (*Nephelium lappaceum*) using DPPH, FRAP assays", *Int. J. Pharmacog. Phytochem. Res.*, **7(2)**, pp.280-285.

[23] W. Xi, B. Fang, Q. Zhao, et al. (2014), "Flavonoid composition and antioxidant activities of Chinese local pummelo (*Citrus grandis* Osbeck.) varieties", *Food Chem.*, **161**, pp.230-238, DOI: 10.1016/j.foodchem.2014.04.001.

[24] Y. Zu, H. Yu, L. Liang, et al. (2010), "Activities of ten essential oils towards propionibacterium acnes and PC-3, A-549 and MCF-7 cancer cells", *Molecules*, **15(5)**, pp.3200-3210, DOI: 10.3390/molecules15053200.

DOI: 10.31276/VJSTE.63(2).58-63

Determination of the appropriate level of manure fertilisation for *Moringa oleifera* grown for animal feed

Tran Thi Hoan[1], Tu Quang Hien[1*], Mai Anh Khoa[1], Tu Quang Trung[2]

[1]*Thai Nguyen University of Agriculture and Forestry, Quyet Thang Commune, Thai Nguyen City, Thai Nguyen Province, Vietnam*

[2]*Thai Nguyen University of Education, 20 Luong Ngoc Quyen Street, Quang Trung Ward, Thai Nguyen City, Thai Nguyen Province, Vietnam*

Received 29 October 2020; revised 14 January 2021; accepted 28 January 2021

Abstract:

The purpose of this study is to determine the appropriate level of chicken manure for the green fodder *M. oleifera* grown for leaf meal production as a supplement into poultry diet to improve poultry product quality (i.e., meat and egg). The experiment was conducted at Thai Nguyen University of Agriculture and Forestry, Vietnam, for two years from 2018 to 2019. The experiment consisted of four treatments (NT) represented by four different levels of chicken manure, namely, 0 tons (NT1), 10 tons (NT2), 20 tons (NT3) and 30 tons/ha/yr (NT4). Each treatment was carried out over an area of 24 m^2 with 5 replicates. The experiment was the complete randomised block design. Other factors such as plantation density, nitrogen, phosphate, potassium fertiliser levels, cutting height, and cutting intervals, etc., were similar among treatments. The results showed that the leaf dry matter yield of NT1 through NT4 was 6.919, 8.131, 8.975, and 9.494 tons/ha/yr, respectively. That of the leaf crude protein was 2.244, 2.694, 3.073, and 3.357 tons/ha/yr, respectively. Increasing manure levels from 0 to 30 tons/ha/yr decreased the dry matter content in the leaves by 1.43%, increased the crude protein in leaf dry matter basic by 2.93%, and decreased crude fibre in the leaf dry matter basic by 2.24%. Based on these results and data from statistical analysis, the most appropriate level of chicken manure application for *M. oleifera* was at 20 tons/ha/yr.

Keywords: **animal feed, level of manure fertilization, *Moringa oleifera*.**

Classification number: **3.1**

1. Introduction

The yield and quality of green fodders are influenced by several factors such as the varieties, seasons (rainy or dry seasons), soil fertility, and fertilisers, etc. Chemical fertilisers, especially nitrogen fertiliser, has a significant effect on green fodder yield. However, the prolonged utilization of chemical fertiliser will have negative effects on the soil such as soil acidification (decrease of pH), deficiency of organic matter in the soil, and decrease of soil microbial that leads to soil degeneration and solidification. The application of manure in combination with chemical fertilisers is believed to be the better solution to eliminate these negative effects. This is because, manure provides organic matter and other nutrients to the soil, improves soil chemo-physical characteristics, soil fertility, and fluff. Manure provides effective microbials as well as a suitable environment for the development of microbials, therefore, the decomposition of nutrients increases [1-3]. Several studies have reported that manure application improved green fodder yield and quality [4-6]. Therefore, the application of organic fertiliser, namely, manure, for green fodder plantation should be taken into account.

2. Materials and methods

The subject of this study, the green fodder *M. oleifera* was planted for leaf meal production for a more complete poultry diets in order to improve meat and egg quality. The experiment was conducted at Thai Nguyen University of Agriculture and Forestry, Thai Nguyen province, which is located in a mountainous area of Vietnam for a period of 2 years from 2018 to 2019.

The experiment consisted of four treatments (NT) corresponding to four different levels of chicken manure application, namely, NT1 for a 0 tons/ha/yr application, NT2 for 10 tons/ha/yr, NT3 for 20 tons/ha/yr, and NT4 for 30 tons/ha/yr. Each treatment was tested on an area of 24

[*]*Corresponding author: Email: tqhien.dhtn@moet.edu.vn*

m^2 with 5 replicates (each treatment consisted of 5 lots and, each lot was 24 m^2). The experiment was carried out under the complete randomised block design. Other factors such as plantation density, chemical (N, P, K) application levels, harvesting intervals, etc., were similar between treatments.

The monitoring parameters included productivities and yields of biomass, fresh leaves, dry matter, and chemical composition of the leaves. The productivities and yields were estimated following the method described by [7].

Productivities of biomass, fresh leaves, and dry matter were expressed as the weight of the biomass, fresh leaves, and dry matters obtained per ha per harvest, i.e. kg/ha/harvest. Biomass productivity was estimated by harvesting all five lots of a single treatment and, the average biomass productivity was calculated from the total biomass productivity of five lots. Fresh leaf productivity was estimated by randomly sampling 10 kg of biomass from each lot (10 kg×5 lots=50 kg) then the leaves and stems were separated and weighed to obtain the ratio of leaves per biomass. Fresh leaf productivity was defined to equal the biomass productivity multiplied by the fresh leaf and biomass ratio. Dry matter productivity was estimated by sampling five fresh leaf samples from five treatments, then oven drying the fresh leaves and calculating the dry matter per fresh leaf ratio. Dry matter productivity was defined to equal the fresh leaf productivity multiplied by the dry matter per fresh leaf ratio.

Yields of biomass, fresh leaves, and dry matter were calculated by adding productivities of harvests in a year or multiplying the average productivity per harvest by the number of harvests per year, which is expressed as ton/ha/yr. These two calculation methods differed by 0-5‰ due to rounding the average productivity of a harvest. Crude protein yield was obtained by multiplying dry matter yield with crude protein content in dry matter.

Chemical analysis was performed as described by [8] and the data obtained was statistically analysed following the method described by [9].

3. Results and discussion

3.1. Effect of different manure application levels on productivity of M. oleifera

3.1.1. Effect on biomass productivity

Biomass productivity data is the basic input data to calculate the fresh leaf and dry matter productivities and the biomass, fresh leaf, and dry matter yields. Thus, Table 1 provides the complete biomass productivity of every harvest. The total number of harvests over the 2 - year span was 11, of which five occurred in the first year and six in the second.

Table 1. Biomass productivity of treatments (kg/ha/harvest).

Harvest	NT1	NT2	NT3	NT4	SEM	p
	0 ton	*10 tons*	*20 tons*	*30 tons*		
1	26,870	32,583	37,629	40,323		
2	25,626	30,625	35,266	37,840		
3	20,100	24,470	27,612	29,748		
4	8,548	10,300	11,526	12,242		
5	6,116	7,536	8,414	8,952		
$\overline{X}_1$	17,452^c	21,103^b	24,089^a	25 821^a	1,079	0.000
6	9,800	11,290	13,358	15,246		
7	18,328	22,098	24,837	26,576		
8	19,854	22,386	25,040	26,342		
9	10,447	13,052	14,716	15,640		
10	6,554	8,019	9,139	9,796		
11	3,925	4,840	5,430	5,832		
$\overline{X}_2$	11,485^c	13,614^b	15,420^a	16,572^a	776	0.000
$\overline{X}$	14,197^c	17,018^b	19,361^a	20,776^a	913	0.000

$\overline{X}=[(\overline{X}_1 x5)+(\overline{X}_2 x6)]:11$; Duncan's multiple range test: similar character in the column (a, or b, c, d or e) means no significant difference among the average data.

The data in Table 1 showed that the development of biomass production for a period of two years was similar among treatments. Biomass productivity is illustrated in Fig. 1. The productivity of harvest during the first half of year one was high and gradually lowered during the second half of the year. This can be explained by the annual, application of manure, phosphate, and potassium occurring at the beginning of year, thus, during this period soil fertility is highly enriched and promotes productivity. After that, soil fertility gradually declined due to exploitation by the plants, which caused the productivity of later harvests to decrease. On the other hand, the first harvests were during the rainy season and thus the temperature and humidity were favourable for plant development. The other harvests were during the dry season, which is not favourable for plant development.

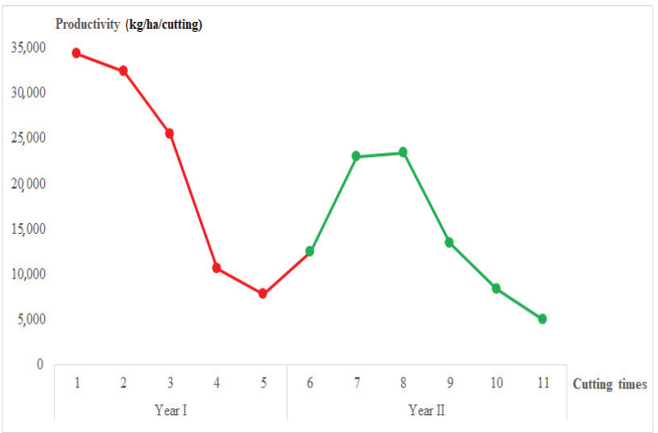

Fig. 1. Biomass productivity of harvests for 2 years.

Average productivity per harvest was higher during the first year and was lower during the second year. For example, if one considers the average productivity of biomass per harvest during the first year of NT1 as 100%, then the average productivity of harvests during the second year compared to the first would be 65%. This comparison was similar among the other treatments, which can be explained by the following two points. During the first year, plants were adequately provided with available nutrients from the soil and from supplied fertiliser; however, during the second year, soil fertility reduced gradually and nutrients were only supplied from fertiliser. Second as the age of the plants and number of cuttings increases, the regeneration capacity of the plants decrease.

The average biomass productivity per harvest for the first and second year and the average of 2 years increased when manure application levels increased. If one considers the average biomass productivity of the 2-year production of NT1 as 100%, then that of NT2 was 119.9%, NT3 was 136.4% and NT4 was 146.3%. Statistical analysis revealed that the average biomass productivity per harvest of the first year, second year, and the 2-year average of the treatments with manure application was significantly higher than that of the treatment without manure application ($p<0.001$). Among treatments with manure application, the NT3 and NT4 treatments showed significantly higher biomass productivity compared to that of NT2 ($p<0.001$), but not significant in NT3 and NT4 ($p>0.05$). These findings prove that the chicken manure application level for *M. oleifera* at 20 tons/ha/yr or above are suitable.

3.1.2. Effect on fresh leaf productivity

Fresh leaf productivity was affected by biomass productivity and the fresh leaves per biomass ratio. Based on the biomass productivity presented in Table 1 and the ratio of fresh leaves per biomass of 38.68%, one can easily determine the fresh leaf productivity of every harvest during the 2-year spans, therefore, Table 2 does not present fresh leaf productivity of every harvest, but illustrates the average fresh leaf productivity per harvest during the first year, second year, and the overall average of the 2-year treatments.

Table 2. Fresh leaf productivity of treatments (kg/ha/harvest).

Mean/year	NT1	NT2	NT3	NT4	SEM	p
$\overline{X}_1$	6,750^c	8,163^b	9,318^a	9,988^a	417	0.000
$\overline{X}_2$	4,442^c	5,266^b	5,964^a	6,410^a	300	0.000
$\overline{X}$	5,491^c	6,583^b	7,489^a	8,036^a	353	0.000

The data presented in Table 2 shows that average fresh leaf productivity per harvest increases accordingly with manure application levels. The average fresh leaf productivity per harvest for the first year increased from 6,750 kg (NT1) to 9,988 kg (NT4). That of the second year was lower, ranging from 4,442 kg to 6,410 kg, and the average over 2-year period ranged from 5,491 kg to 8,036 kg. If one considers the average fresh leaf productivity per harvest over 2-year period of NT1 as 100%, then that of NT2 was 119.9%, NT3 was 136.4%, and NT4 was 146.3%. Average fresh leaf productivity per harvest during the first year, second year, and over 2-year period for all treatments with manure application were significantly different compared to that without manure application ($p<0.001$). Among treatments with manure application, the average fresh leaf productivity per harvest of NT3 and NT4 were significantly higher than that of NT2 ($p<0.001$) but not between NT3 and NT4 ($p>0.05$).

3.1.3. Effect on dry matter productivity

*D*ry matter productivity is dependent on fresh leaf productivity and its dry matter content (i.e., dry matter productivity is equal to fresh leaf productivity multiplied by dry matter content in fresh leaves). Dry matter content in fresh leaves was different among treatments. It decreased with the increase of manure application levels as follows: NT1 was 22.91%, NT2 was 22.46%, NT3 was 21.79%, and NT4 was 21.48%. Based on the fresh leaf productivity data in Table 2 and the dry matter content in the fresh leaves, dry matter productivity is presented in Table 3.

Table 3. Dry matter productivity of treatments (kg/ha/harvest).

Mean/year	NT1	NT2	NT3	NT4	SEM	p
$\overline{X}_1$	1,546^b	1,833^b	2,030^a	2,145^a	92	0.000
$\overline{X}_2$	1,018^c	1,183^b	1,300^{ab}	1,377^a	66	0.000
$\overline{X}$	1,258^c	1,479^b	1,632^a	1,726^a	78	0.000

The data presented in Table 3 showed that dry matter productivity increased accordingly with the increase of manure application levels similar to the trends of biomass and fresh leaf productivities. However, the difference between the dry matter productivity of the treatments was not significant compared to the difference between biomass and fresh leaf productivity of the treatments. This is thought to occur because the increase in manure application resulted in the decrease of dry matter content in fresh leaves because dry matter productivity is equal to fresh leaf productivity multiplied by the dry matter content in fresh leaves. For example, the fresh leaf productivity of the overall average of 2 years of NT4 treatment was higher than that of NT1 by 46.3% but the average dry matter productivity of the overall of 2 years in NT4 was just higher than that of NT1 by 37.2%. Nevertheless, the average dry matter productivity/harvest over 2-year period in all treatments with manure application were significantly higher than that of the control ($p<0.001$). Among treatments with manure application, the dry matter productivity of NT3 and NT4 were significantly higher than that of NT2 ($p<0.001$), but was not significant between NT3 and NT4 ($p>0.05$).

Other studies on manure application for legumes [10, 11], *M. oleifera* [4], *Trifolium alexandrium* and *Lolium multiflorum* [5], and *Trichanthera gigantea* [6] had reported that manure application increased dry matter yield and our findings are supported by these studies.

3.2. Effect of different manure application levels on M. oleifera yield

Product yield was calculated by multiplying the average productivity/harvest by the number of harvests during the production year. There were five harvests during the first year and six harvests during second year. Based on data of mean productivity (biomass, fresh leaves, dry matter)/harvest of the first year and second year presented in Tables 1, 2, and 3, one can easily estimate the yields of biomass, fresh leaves, and dry matter from the first and second year. Therefore, Table 4 does not present yield data of the biomass, fresh leaves, and dry matter of each year but presents the mean of the overall yield of the 2 years. Crude protein yield was calculated by multiplying the dry matter yield by the crude protein content in the dry matter. This content for the NT1, NT2, NT3, and NT4 treatments was 32.43, 33.13, 34.24, and 35.36%, respectively.

Table 4. Average yields per year of treatments (ton/ha/year).

Categories	NT1	NT2	NT3	NT4	SEM	p
Biomass	78.084^{c}	93.599^{b}	106.485^{a}	114.268^{a}	5.020	0.000
Fresh leaves	30.203^{c}	36.204^{b}	41.188^{a}	44.199^{a}	1.942	0.000
Dry matter	6.919^{c}	8.131^{b}	8.975^{a}	9.494^{a}	0.429	0.000
Crude protein	2.244^{d}	2.694^{c}	3.073^{b}	3.357^{a}	0.145	0.000

The data presented in Table 4 shows that the biomass yield of *M. oleifera* increased from 78.084 tons/ha/yr (NT1) to 114.268 tons/ha/yr (NT4) and that of fresh leaves increased from 30.203 tons/ha/yr (NT1) to 44.199 tons/ha/yr (NT4). Biomass and fresh leaf yields in treatments with manure increased significantly compared to that of the control ($p<0.001$). Among treatments with manure, the yields of NT3 and NT4 were significantly different compared to NT2 ($p<0.001$) but this difference was not significant between NT3 and NT4 ($p>0.05$).

For the green fodders intended for leaf meal production, dry matter and crude protein yields are the most essential parameters to evaluate production capacity. Dry matter and crude protein yields were increased accordingly with the increase of manure application. The overall mean of the dry matter yield for the 2 years of *M. oleifera* harvest increased from 6.919 tons (NT1) to 9.494 tons/ha/yr (NT4). Crude protein yield increased from 2.244 to 3.357 tons/ha/yr. If one considers the dry matter yield of NT1 to be 100%, then that of NT2 was 117.5%, NT3 was 129.7%, and NT4 was 137.2%. Similarly, crude protein yield of all treatments was 100, 120.1, 136.9, and 149.6%, respectively. The overall mean of crude protein and dry matter yields of the 2 years of NT2, NT3, and NT4 treatments were higher than that of NT1. The yields of NT3 and NT4 were significantly higher than that of NT2 ($p<0.001$). However, the dry matter yields of NT3 and NT4 were not significantly different ($p>0.05$), therefore, the chicken manure application level for *M. oleifera* at 20 tons/ha/yr is the most suitable.

The average dry matter and crude protein yields of the first 2 years from several green fodders for leaf meal production such as cassava for foliage production were 7.0 tons/ha/yr and 1.7 tons/ha/yr [12], *Leucaena* were 6.0 tons and 1.7 tons/ha/yr [13], respectively; *Stylosanthes* were 7.8 tons/ha/yr and 1.4 tons/ha/yr [14], respectively; and *T. gigantea* were 10-12 tons/ha/yr and 2.4-3.2 tons/ha/yr [15], respectively. The average dry matter and crude protein yields of *M. oleifera* during the first two years in this experiment reached 6.919 to 9.494 tons/ha/yr and that of crude protein ranged between 2.244 tons to 3.357 tons/ha/yr. This proves that *M. oleifera* is a potential green fodder for leaf meal production.

3.3. The production efficiency of dry matter and crude protein from manure

The production efficiency production of dry matter and crude protein from manure can be estimated by subtracting dry matter and crude protein yields of treatments NT2, NT3, and NT4 by that of NT1, then divide by the total amount of manure applied for each ha in a year. The obtained data presented in Table 5.

Table 5. Production efficiency of manure for dry matter and crude protein.

Categories	Unit	NT2	NT3	NT4	SEM	p
DM increased	kg/ha/year	1,212[c]	2,056[b]	2,575[a]	43.3	0.000
CP increased	kg CP/ha/year	450[c]	829[b]	1,113[a]	21.6	0.000
M	ton/ha/year	10	20	30		
DM/M	kg DM/ton M	121.2[c]	102.8[b]	85.8[a]	3.4	0.000
CP/M	kg CP/ton M	45.0[c]	41.4[b]	37.1[a]	1.4	0.000

DM: dry matter; CP: crude protein; M: manure.

The data in Table 5 shows that an increase in manure application levels increased dry matter weight compared to NT1 (without manure) from 1,212 kg (NT2) to 2,575 kg/ha/yr (NT4). Crude protein increased from 450 kg to 1,113 kg/ha/yr. The increase of dry matter and crude protein over all treatments were significant ($p<0.001$).

When the manure application level increased, the dry matter and crude protein also increased but the production efficiency of 1 ton of manure decreased. Specifically, dry matter decreased from 121.2 kg/ton (NT2) to 85.8 kg/ton of manure (NT4), equivalent to 571 kg fresh leaves (DM/fresh leaf ratio of NT2 was 22.46%) and 425 kg fresh leaves (DM/fresh leaf ratio of NT4 was 21.48%), respectively. Additionally, crude protein decreased from 45.0 kg to 37.1 kg/ton of manure. The production efficiency of 1 ton of manure for all treatments was significant ($p<0.001$). Therefore, when applying manure fertiliser, it is important to consider the production efficiency as it decreases with an increase in manure levels.

Table 6. Comparison of production cost of different treatments (%).

Expenditure	NT1	NT2	NT3	NT4
	0 ton	*10 tons*	*20 tons*	*30 tons*
Expenditure/ha/2 yr	100	114.7	128.5	142.3
Leaf meal yield/ha/2 yr	100	117.5	129.7	137.2
Production cost/1 kg leaf meal	100	97.6	99.1	103.7

The expenditure for the nursery plants and chemical fertiliser were similar among the four treatments. However, there is a difference in the expenditure for manure fertiliser when levels of manure application increased. Although this resulted in an increase of yield, production labour harvesting, processing increased as well as the costs of the labour itself. The data presented in Table 6 reveals that, compared to NT1 (without manure), the total expenditure for 1 ha over the 2-yr time for NT2, NT3, and NT4 increased by 14.7, 28.5, and 42.3%, respectively. The leaf meal yield of NT2, NT3, and NT4 also increased by 17.5, 29.7, and 37.2%, respectively, compared to NT1. The manure treatments had a larger increase of leaf meal yield compared to the increase of production cost, which means the cost of production per every kg leaf meal would be lower and vice versa. Therefore, the cost to produce 1 kg leaf meal under the NT2, NT3, and NT4 schemes compared to NT1 was 97.6, 99.1, and 103.7%, respectively. Thus, an appropriate level of manure application should be chosen to reduce production costs.

3.4. Effect of manure levels on M. oleifera leaf quality

The quality of green fodders is usually evaluated by their chemical composition, thus, several main components such as dry matter (DM), crude protein (CP), ether extract (EE), crude fibre (CF), and ash were analysed. Along with the nitrogen free extract (NFE)=DM-(CP+EE+CF+Ash), the main component of *M. oleifera* presented in Table 7.

Table 7. Chemical composition of *M. oleifera* leaves.

NT	DM (% FL)	% DM					GE (kcal)
		CP	*EE*	*CF*	*Ash*	*NFE*	
NT1 (0)	22.91[a]	32.43[c]	6.63[b]	9.78[a]	9.04[a]	42.12[a]	4,644[a]
NT2 (10)	22.46[ab]	33.13[c]	6.81[b]	9.08[b]	9.17[a]	41.81[a]	4,657[a]
NT3 (20)	21.79[ab]	34.24[b]	7.07[a]	7.94[c]	9.41[a]	41.34[a]	4,667[a]
NT4 (30)	21.48[b]	35.36[a]	7.17[a]	7.54[c]	9.45[a]	40.48[a]	4,679[a]
SEM	0.649	0.577	0.143	0.377	0.612	1.708	54.972
p	0.013	0.000	0.000	0.000	0.681	0.475	0.779

Leaf sample at 50 days of cutting; FL: fresh leaves; GE: gross energy.

The data presented in Table 7 showed that when manure application levels increased, a decrease in leaf dry matter (decreased 1.43% from NT1 to NT4) was observed and the water content in the leaves increased. Therefore, the leaves of the plants with manure application were softer than those without manure application. However, the dry matter content in fresh leaves was only significantly different between NT4 and NT1 ($p<0.05$). The crude protein content in the dry matter increased with an increase of manure application level (increase of 2.93% from NT1 to NT4). The crude protein content in the dry matter of NT3 and NT4 were significantly higher than that of NT1 and NT2. This can be explained by the large amount of nitrogen contained within chicken manure, which is a source for crude protein synthesis. In contrast with crude protein content, crude fibre content in dry matter decreased with an increase of manure level (decreased by 2.24% from NT1 to NT4). The crude fibre content in the dry matter of NT3 and NT4 was significantly lower compared to that in NT1 and NT2. Crude protein and crude fibre are the main criteria that determine

the quality of the green fodders; therefore, the application of manure significantly improved the quality of *M. oleifera*. The best improvement was seen at the level of 20 tons/ha/yr than at the level of 10 tons/ha/yr.

Results from studies on the application of manure fertiliser for *Stylo guianensis* [10, 11], *Trifolium alexandrium* and *Lolium multiflorum* [5], and *Trichanthere gigantea* [6] all showed that manure fertiliser improved green fodder qualities such as increased crude protein content and decreased crude fibre content in the leaf dry matter. The findings are also supported by the works mentioned above.

4. Conclusions

Increasing chicken manure from 0 to 30 tons/ha/yr increased the average leaf dry matter yield over 2 year from 6.919 to 9.494 tons/ha/yr, increased the crude protein yield of leaves from 2.244 to 3.357 tons/ha/yr, increased crude protein content in leaf dry matter by 2.93%, and decreased crude fibre content in leaf dry matter by 2.24%. Based on dry matter yield, crude protein yield, leaf chemical composition, and statistical analysis of these parameters, it was concluded that chicken manure should be applied to *M. oleifera* at 20 tons/ha/yr.

CRediT author statement

Tran Thi Hoan, Tu Quang Hien: Conceptualisation, Methodology, Software, Resources, Writing - Review and Editing; Mai Anh Khoa: Data curation, Software, Writing - Original draft preparation; Tu Quang Trung: Supervision, Software, Validation.

COMPETING INTERESTS

The authors declare that there is no conflict of interest regarding the publication of this article.

REFERENCES

[1] O. Dikinya, N. Mufwanzala (2010), "Chickens manure-enhanced soil fertility and productivity: effects of application rates", *Journal of Soil Science and Environmental Management*, **1(3)**, pp.46-54.

[2] V.T. Giang, D. Minh, N.H. Cung (2011), "Utilization of microbial organic fertilizer to improve soil chemo-physical characteristics and disease elimination on durian fruit trees", *Can Tho University Journal of Science*, **17a**, pp.146-154 (in Vietnamese).

[3] L.V Phuc, N.B. Ve (2016), "Effect of organic and chemical fertilizers on soil characteristic and groundnut productivity (*Arachis hypogaea* L.)", *Can Tho University Journal of Science*, **43b**, pp.8-17 (in Vietnamese).

[4] A.W.M. Imoro, I. Sackey, A.H. Abubakari (2012), "Preliminary study on the effects of two different sources of organic manure on the growth performance of *Moringa oleifera* seedlings", *Journal of Biology, Agriculture and Healthcare*, **2(10)**, pp.147-158.

[5] H.S.A. Salama (2015), "Interactive effect of forage mixing rates and organic fertilizers on the yield and nutritive value of Berseem clover (*Trifolium alexandrium* L.) and annual Ryegrass (*Lolium multiflorum* Lam.)", *Agricultural Sciences*, **6**, pp.415-425, DOI: 10.4236/as.2015.64041.

[6] T.T. Kien (2019), *Study on Cultivation and Nutrients Composition of Trichanthera Gigantea as Animal Feed*, Final Scientific Project Report, Thai Nguyen University.

[7] T.Q. Hien, N.K. Quac, T.T. Nhung (2002), *Textbook for Pasture and Green Forage Crops*, Agricultural Publishing House, Hanoi, 116pp (in Vietnamese).

[8] K. Helrich, Association of Official Analytical (1990), *Official Methods of Analysis ofthe Association ofOfficial Analytical Chemists,* 15th edition, Arlington, VA, 746pp.

[9] T.N.D. Oanh, H.V Phu (2012), *Textbook for Method of Field Experiment*, Agriculture Publishing House, Hanoi, 210pp (in Vietnamese).

[10] H.V. Tao, N.Q. Toan (2010), "Effect of fertilizer application regime on biomass production of *S. guianensis* CIAT 184 and *S. guianensis* plus at Nghia Dan, Nghe An", *Vietnam Journal of Agricultural Sciences*, **8(1)**, pp.54-58 (in Vietnamese).

[11] H.T.B. Ngoc (2012), *Study on Cultivar, Processing and Storage of Stylosanthes Guianensis CIAT 184 Meal in Broiler and Layer Parents Stocks,* Thai Nguyen University, 174pp (in Vietnamese).

[12] T.Q. Hien, T.Q. Trung (2016), "Study on green matter and leaf meal production performance of cassava KM 94 cultivated in Thai Nguyen province", *Journal of Animal Husbandry Sciences and Technics (JAHST)*, **214**, pp.52-56 (in Vietnamese).

[13] T.T. Hoan, T.Q. Hien, T.Q. Trung (2017), "Study on green matter and leaf meal production performance of *Leuceana leucocephala* cultivated in Thai Nguyen Province", *Proceedings of National Conference on Animal and Veterinary Sciences,* pp.290-296 (in Vietnamese).

[14] T.Q. Hien, T.T. Hoan, T.Q. Trung (2017), "A study on the green matter and grass meal production performance of *Stylosanthes guianensis* CIAT 184 cultivated in Thai Nguyen province", *Vietnam Journal of Science and Technology*, **19(8)**, pp.23-27 (in Vietnamese).

[15] T.T. Kien, M.A. Khoa, T.T. Hoan, et al. (2019), "Effect of different nitrogen fertilizer application levels on yield and quality of the green fodder *Trichanthera gigantea*", *Proceedings of X International Symposium on Agriculture and Forestry*, **3-6**, pp.1482-1487.

DOI: 10.31276/VJSTE.63(2).64-69

Contribution of ginsenosides Rg1, Rb1 to the neuroprotective effect of *Panax notoginseng* in mouse organotypic hippocampal slice cultures exposed to oxygen and glucose deprivation

Nguyen Thi Thanh Loan[1, 2], Le Thi Xoan[1*], Pham Thi Nguyet Hang[1], Nguyen Van Tai[3]

[1]*Department of Pharmacology and Biochemisty, National Institute of Medicinal Materials, 3B Quang Trung, Trang Tien Ward, Hoan Kiem District, Hanoi, Vietnam*
[2]*Department of Pharmacology, Hanoi Medical University, 1 Ton That Tung, Trung Liet Ward, Dong Da District, Hanoi, Vietnam*
[3]*Department of Phytochemistry, National Institute of Medicinal Materials, 3B Quang Trung, Trang Tien Ward, Hoan Kiem District, Hanoi, Vietnam*

Received 30 November 2020; revised 14 February 2021; accepted 26 February 2021

Abstract:

We previously demonstrated that *Panax notoginseng* (PNG) root extract treatments exerted neuroprotective effects on brain injuries using middle cerebral artery occlusion in mice. The present study aims to investigate the neuroprotective effects of PNG extract and its ginsenosides Rg1 and Rb1 on ischemic neuronal damage caused by oxygen and glucose deprivation (OGD) in mouse organotypic hippocampal slice cultures (OHSCs). Before the experiments, hippocampal slices collected from 7-day-old *Swiss* mice were cultured for 7 days. OGD was triggered in OHSCs for 30, 60, or 90 min with the aim of finding the optimal period of OGD for drug testing. PNG extract (10, 30 µg/ml), ginsenosides Rg1 and Rb1 (5, 25 µM), or MK-801 25 µM, a reference drug, was added to the culture medium 24 h before OGD and these treatments were continued for 24 h after the optimum 60-min period of OGD. After 24 h of OGD exposure, the measurement of propidium iodide uptake was analysed in OHSCs to evaluate neuronal cell damage. The results showed that OGD time-dependently increased PI uptake of the OHSCs. PNG 30 µg/ml treatment reduced the OGD-induced neuronal cell damage in OHSCs. Ginsenosides Rg1 25 µM, Rb1 (5, 25 µM), as well as MK-801 (25 µM) significantly inhibited PI uptake 24 h after OGD exposure. However, ginsenoside Rg1 5 µM did not show any significant effects on the OGD-induced neuronal cell damage. These findings indicated that ginsenosides Rg1 and Rb1 contributed to the neuroprotective effects of PNG against ischemic damage in OHSCs and the neuroprotective effect of ginsenoside Rb1 was stronger than that of ginsenoside Rg1.

Keywords: **ginsenoside *Rb1*, ginsenoside *Rg1*, organotypic hippocampal slice cultures, oxygen and glucose deprivation, *Panax notoginseng*.**

Classification number: **3.3**

1. Introduction

Stroke, an acute cerebrovascular disease, is the second largest cause of death [1]. This disease remains the leading cause of disabilities globally and has a rapidly increasing rate in developing countries. Because of an arterial occlusion, ischemic stroke is responsible for the majority of strokes. However, there are only a few effective remedies for this disease. Management of the disease focuses on reperfusion therapy using intravenous thrombolysis. In addition, an endovascular thrombectomy is commonly performed for ischemic stroke. While both therapies reduce disabilities, they are time-critical [1]. Therefore, seeking new natural products that have beneficial effects for the prevention/therapy of ischemic stroke without causing adverse reactions are greatly needed.

The roots of *Panax notoginseng* (PNG) are widely used in Vietnamese traditional medicine for the treatment of blood disorders including blood stasis, bleeding, and blood deficiency [2]. It is reported that PNG with an intraperitoneal route of administration displays strong neuroprotective effects in rats against global cerebral ischemia-reperfusion [3]. We previously demonstrated that the ethanolic extract of PNG root (150 mg/kg) with oral administration exerted neuroprotective effects on the brain following ischemic injury in middle cerebral artery

*Corresponding author: Email: xoanle@nimm.org.vn

occlusions (MCAO) of subjected mice by reducing the infarct volume and improving neurofunctional recovery [4]. However, in this article, the question of which components in PNG are responsible for producing these neuroprotective effects is answered.

More than 20 major active components in *P. notoginseng* root are ginsenosides, which are a group of saponins that are identified chemically [5]. Because of their steroidal structure, ginsenosides possess diverse pharmacological activities. They enable interaction with cell membranes, ion channels, as well as extra- or intra-cellular receptors resulting in altering the transcriptional level. Ginsenosides Rb1 and Rg1 (Fig. 1) are the most abundant ginsenosides presenting in PNG roots [5]. Xian-Si Zeng, et al. demonstrated that treatments with ginsenosides Rg1 and Rb1 show roles in protecting the brain from ischemic damage by significantly reducing infarction volume and alleviating neurological deficits caused by cerebral ischemia-reperfusion [6]. Together, these findings raise the possibility that ginsenosides Rg1 and Rb1 may play a role on the neuroprotective effect of *P. notoginseng* root against cerebral ischemia.

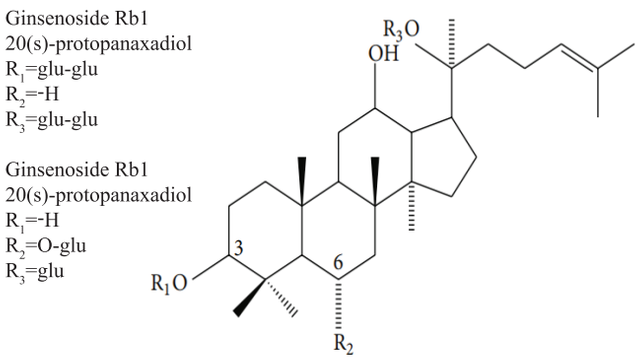

Fig. 1. Chemical structure of ginsenosides Rg1 and Rb1 [7].

Because of the important *in vivo*-like organization of nervous tissues in organotypic hippocampal slice cultures (OHSCs), they are commonly used as a model for screening neuroprotective agents for many neurodegenerative diseases and ischemia [8]. It is well known that neurons need oxygen and glucose to maintain survival function. Although brain tissues constitute only 2% of one's total body weight, their metabolic demands are extremely high. Moreover, the lack of anaerobic metabolism and glycogen storage can decrease the blood flow thus lowering oxygen and glucose levels. During an ischemic stroke, the interruption of blood flow and oxygen-glucose deprivation (OGD) can cause neuronal death [9]. Thus, oxygen-glucose deprivation (OGD) in OHSCs are widely used as an *in vitro* model of ischemia to evaluate the neuroprotective effects of potential drugs.

In ischemia, glutamate excitotoxicity occurs when too much glutamate has been released into the synapse. This excess glutamate overstimulates postsynaptic glutamate receptors, especially N-methyl-d-aspartate (NMDA) receptors. Consequently, calcium overloads and activated cytotoxic enzymes proceed to the injured neurons [10]. An NMDA antagonist can protect many neurons against glutamate neurotoxicity. Hence, in this model, MK-801, a specific NMDA receptor antagonist, was used as the positive control.

This study aimed to investigate the anti-ischemia effects of *Panax notoginseng* root extract and its ginsenosides Rg1 and Rb1 on ischemic neuronal damage caused by oxygen and glucose deprivation in mouse organotypic hippocampal slice cultures.

2. Materials and methods

2.1. Preparation of the Panax notoginseng root extract

The root of *Panax notoginseng* (PNG) was identified and provided by Dr. Pham Thanh Huyen (Department of Medicinal Plant Resources, National Institute of Medicinal Materials, Hanoi, Vietnam). The extraction procedure of *Panax notoginseng root* extract has been described in our previous report [4]. Briefly, the root of PNG was sliced and dried in a hot-air oven at 50°C and ground to a powder. The powder (256.6 g) was extracted with ethanol 70% (1:7 w/v) at reflux for 2 h. The extraction process was repeated 2 times. Then, the extracts were concentrated under reduced pressure at 50°C and dried in a vacuum oven at 50°C to obtain the dry PNG extract (71.9 g). The extract was stored at 4°C until use. Based on high performance liquid chromatography (HPLC) analysis, the PNG extract was estimated to contain 15.86% ginsenoside Rg1 and 12.04% ginsenoside Rb1.

2.2. Animals

Seven-day-old *Swiss* mice (National Institute of Hygiene and Epidemiology, Hanoi, Vietnam) were housed in the laboratory animal room (25±1°C, 65±5% humidity, 12 h light/dark cycle). The animals were given food and water *ad libitum*.

2.3. Ischemia caused by oxygen and glucose deprivation in mouse organotypic hippocampal slice cultures

Organotypic hippocampal slice cultures (OHSCs) were prepared and cultivated according to the method previously described in [8, 10]. Briefly, the 7-day-old pups were decapitated and the hippocampi were rapidly dissected in ice cold media. The hippocampus was cut transversely (450 µm thick) by using a McIlwain™ Tissue Chopper (Mickle Laboratory Engineering Co. Ltd., Surrey, UK) and

transferred onto a membrane filter (Omnipore™ Membrane Filters, JHWP02500; Merck Millipore, Bedford, MA). Organotypic hippocampal slices were laid on an O-shaped plastic doughnut plate in 6-well plates with a culture medium. The culture medium for the hippocampal slices included 50% minimum essential medium, 25% Hank's balanced salt solution, 23% heat-inactivated horse serum, and 2% B-27 (GIBCO, Rockville, MD, USA) supplemented with 6.5 g/l glucose, 50 units/ml penicillin-G, and 50 µg/ml streptomycin sulfate (GIBCO, Rockville, MD, USA). The slices were then kept in an incubator that maintained 37°C and 95% moist air/5% CO_2 for 7 d before the experiments. The culture medium was replaced by a fresh one two times a week.

Oxygen- and glucose-deprivation (OGD) of OHSCs: according to previous studies [8, 10], OGD was used as an *in vitro* model of ischemia-reperfusion injury with a slight modification. The culture medium was deprived of D-glucose and then equilibrated with 95% N_2-5% CO_2 for 90 min (OGD medium). The OHSCs were exposed to the OGD media and were then quickly placed in an airtight chamber with 95% N_2-5% CO_2 gas flow for 60 min, except in a specially stated case. After the exposure of OGD, the slices were returned to conventional media and maintained in the incubator for 24 h before imaging for cell death.

(+)-MK-801 hydrogen maleate (MK-801; Sigma Chemicals, St. Louis, MO, USA) and ginsenosides Rg1 and Rb1 (Chendu Biopurify Phytochemical Ltd., China) were dissolved in dimethyl sulfoxide (DMSO) to form a 10 mM test drug stock solution. The stock solutions were unopened and stored at -20°C until use. The OHSCs were incubated with the culture media supplemented with PNG extract (10 and 30 µg/ml), ginsenosides Rg1 and Rb1 (5 and 25 µM), or MK-801(25 µM) for 24 h before OGD exposure and these treatments were continued for 24 h after a period of OGD.

2.4. Evaluation of the neuronal cell damage in OHSCs

The neuronal cell damage in OHSCs was quantified 24 h after exposure to OGD by using propidium iodide (PI) staining as done in previous studies [8, 10]. OHSCs were stained with PI (2.5 µg/ml, Sigma Chemicals, St. Louis, MO, USA) for 30 min. Then, the hippocampal cell damage was evaluated using a microscope (Olympus IX73, Olympus Inc., Tokyo, Japan). Image-J software (ver. 1.41, NIH; Bethesda, MD, USA) was employed to analyse the average intensities of the slices. The value obtained from the control slices exposed to 100 µM N-methyl-D-aspartic acid (NMDA; ACROS Organics™, India) for 24 h was used as 100% PI-fluorescence.

2.5. Data analysis

SigmaPlot 12.0 (SYSTA Software Inc, Richmond, CA, USA) was used for statistical analysis. One-way analysis of variance (ANOVA) followed by the Student-Newman-Keuls post-test were assessed to compare the differences between groups. Statistically significant differences were considered when the p value was less than 0.05.

3. Results

3.1. Determination the optimum period of OGD

With the aim to find the optimal period of OGD, OHSCs were exposed to OGD for 30, 60, and 90 min. The results in Fig. 2 show that exposure of OHSCs to OGD for 30, 60, and 90 min significantly increased the percentage of total PI fluorescence. The measurement of % PI-fluorescence 24 h after OGD demonstrated that OGD caused hippocampal neuronal cell damage in a manner depending on the duration of OGD exposure. The most suitable OGD time is 60 min. Thus, in the following experiments, we applied the 60-min optimum duration of OGD to induce ischemia in OHSCs.

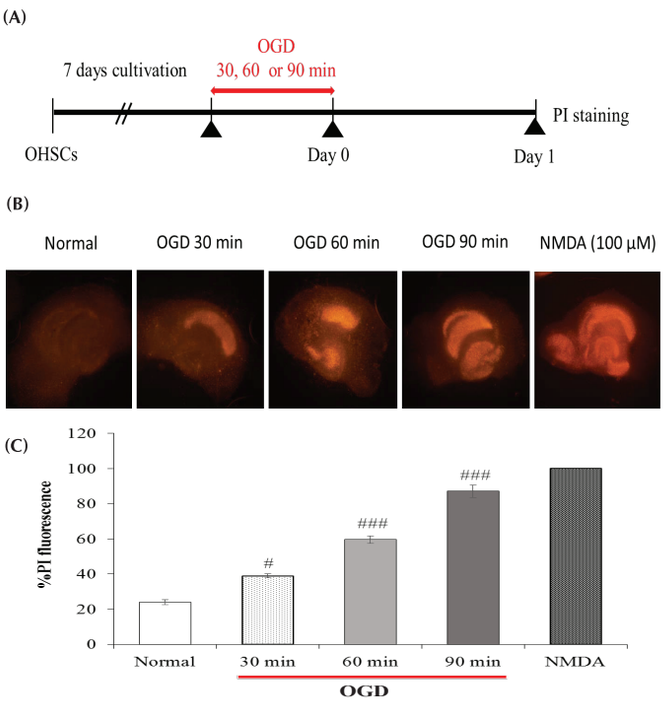

Fig. 2. Oxygen and glucose deprivation (OGD) induced neuronal cell damage in the organotypic hippocampal slice culture (OHSCs). (A) Experimental protocol: scheduling time of OGD. The neuronal cell damage was determined by measuring the PI uptake signal at 24 h after OGD treated; **(B)** Images of hippocampal neuronal damage caused by 30, 60, 90 min OGD treatment; **(C)** % of total PI fluorescence. Data represents Mean±S.E.M (n=4). #: p<0.05, ##: p<0.01, ###: p<0.001 compared to normal OHSCs.

3.2. Preventive effects of PNG against OGD-induced neuronal cell damage in OHSCs

Using OGD induced ischemia in the OHSC model, we evaluated the neuroprotective effect of PNG. The results in Fig. 3 show that the PI uptake signal of the vehicle-treated OHSC markedly increased. The treatment with 10-µg/ml PNG extract insignificantly reduced the percentage of PI fluorescence in the OGD-induced OHSCs. In contrast, 30 µg/ml PNG extract and MK-801 (25 µM) significantly attenuated OGD-induced neuronal cell damage.

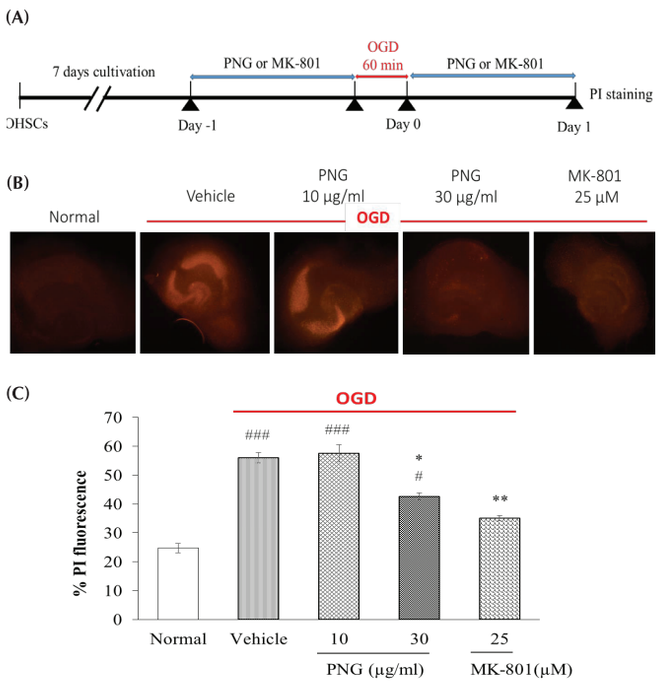

Fig. 3. Effects of PNG extract on OGD-induced neuronal cell damage in OHSCs. (A) Experimental protocol. OHSCs were treated with PNG extract for 24 h before OGD and 24 h after the 60-min period of OGD. Neuronal cell damage was determined by measuring the PI uptake signal at 24 h after OGD treated; **(B)** Images of hippocampal neuronal damage of OHSCs treated with 60-min OGD in the vehicle and presence of PNG extract (10, 30 µg/ml) and MK-801 (25 µM); **(C)** % of total PI fluorescence caused by 60-min OGD. Data represents Mean±S.E.M (n=4). ###: p<0.001 compared to normal OHSCs; *: p<0.05, **: p<0.01 vs. OHSCs treated with vehicle.

3.3. Preventive effects of ginsenosides Rg1 and Rb1 against OGD-induced neuronal cell damage in OHSCs

Ginsenosides Rb1 and Rg1 are the most abundant ginsenosides presenting in PNG root [5]. In this study, the PNG extract containing 15.86% ginsenoside Rg1 and 12.04% ginsenoside Rb1 raised the possibility that ginsenosides Rg1 and Rb1 may play a role on the neuroprotective effect of the PNG extract against OGD-induced ischemic neuronal cell damage. To test this possibility, we next employed OGD as an *in vitro* model of ischemia to evaluate the anti-ischemia effects of ginsenosides Rg1 and Rb1. The percentage of PI fluorescence of the vehicle-treated OGD group significantly increased compared to the signal of the normal control slices (shown in Fig. 4). Treatment with ginsenoside Rg1 (5 µM) insignificantly reduced the PI uptake signal in comparison with the vehicle-treated OGD group. However, the exposure of ginsenosides Rg1 (25 µM) and Rb1 (5, 25 µM) in OGD-treated OHSCs significantly decreased the percentage of total PI fluorescence signal. Treatment of MK-801 (25 µM) significantly attenuated OGD-induced neuronal cell damage. The protective activity observed with the ginsenoside Rb1 treatment was similar to that caused by MK-801.

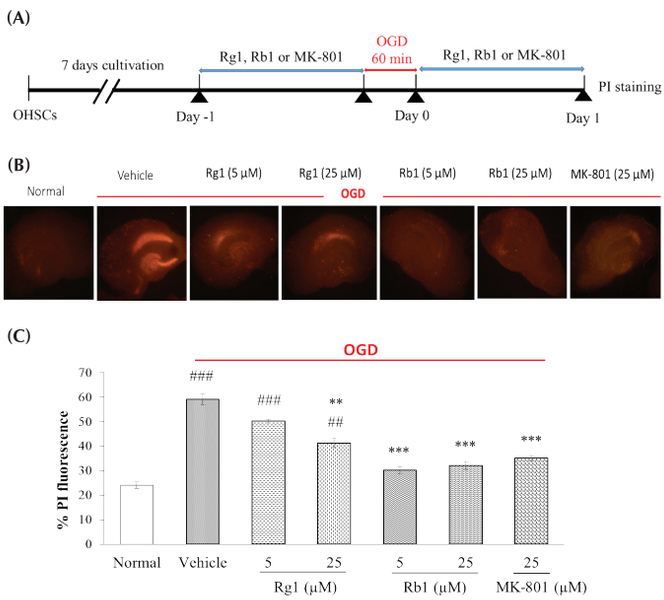

Fig. 4. Effects of ginsenosides Rg1 and Rb1 on OGD-induced neuronal cell damage in OHSCs. (A) Experimental protocol. OHSCs were treated with ginsenosides Rg1 and Rb1 for 24 h before OGD and 24 h after the 60-min period of OGD. Neuronal cell damage was determined by measuring the PI uptake signal at 24 h after OGD treated; **(B)** Images of hippocampal neuronal damage of OHSCs treated with 60-min OGD in the vehicle and presence of ginsenosides Rg1, Rb1 (5, 25 µM) and MK-801 (25 µM); **(C)** % of total PI fluorescence caused by 60-min OGD. Data represents Mean±S.E.M (n=4). ##: p<0.01, ###: p<0.001 compared to normal OHSCs; **: p<0.01, and ***: p<0.001 vs. OHSCs treated with vehicle.

4. Discussion

In this study, we employed mouse OHSCs to investigate the anti-ischemia effects of *Panax notoginseng* root extract and its ginsenosides Rg1 and Rb1 on neuronal damage

caused by OGD. Our finding strongly suggested that ginsenosides Rg1 and Rb1 play an important role in the neuroprotective action of PNG against ischemic damage and that the neuroprotective effect of ginsenoside Rb1 was stronger than that of ginsenoside Rg1.

The hippocampus is composed of the CA1, CA2, and CA3 pyramidal neurons and dentate gyrus (DG) granule cells. Interestingly, organotypic hippocampal cultures retain a complex three-dimensional organization of nervous tissues that are the same as that of *in vivo* brain tissues. Because of the important *in vivo*-like organization of nervous tissues of OHSCs, it is commonly used as an *in vitro* model for studying neuroprotective agents in neurodegenerative diseases [9]. In OHSCs, OGD is widely used as an *in vitro* model of ischemia. Thus, OHSCs exposed to OGD can provide a surrogate system to evaluate neuronal cell damage following an ischemic injury. In the ischemia models, the hippocampus is one of the most susceptible regions of the brain. Functionally, the excessive activation of glutamate and increase in intracellular calcium play an important role in the acute phase of neuronal damage. Recently, many studies have strongly suggested that apoptosis is considered to have a significant role in delayed neuronal death [9]. In addition, in many cases, it is very difficult to have a large number of substances to test in animal models. Thus, this is a suitable model for screening neuroprotective effects of pharmacological agents. In our study, we applied the 60-min optimum duration of OGD to induce ischemia in OHSCs. The exposure of OHSCs to OGD for 30, 60 and 90 min significantly increased the percentage of total PI fluorescence in a manner depending on the duration of OGD exposure. However, with 30 min OGD, neuronal cell death was not sufficient to evaluate the neuroprotective effects of the tested drugs. In contrast, within 90 min, the percentage of PI fluorescence of vehicle-treated OHSCs was almost equivalent to NMDA-treated OHSCs, which could lead to inaccuracies in the evaluation of the effects of tested drugs. Therefore, 60 min was the most suitable period for OGD for screening neuroprotective effects of pharmacological agents.

To our knowledge, this is the first study to investigate the neuroprotective effects of PNG on OGD-induced neuronal cell damage in OHSCs. The results showed that the treatment with 10-µg/ml PNG extract failed to reduce OGD-induced neuronal cell damage under our experimental conditions. In contrast, 30-µg/ml PNG extract significantly decreased ischemic neuronal cell damage. In our previous study, we demonstrated that 150 mg/kg of PNG root ethanol extract exerted neuroprotective effects on brain injury using middle cerebral artery occlusion for 60 min in mice [4]. Thus, the results of this study confirm the neuroprotective effects of PNG in ischemic-induced neuronal injury. Besides, *in vivo* studies do not answer the question of whether the test drug has a direct effect on the target organ or if it is converted to an active substance. In these *in vitro* experiments using OHSCs, our data suggests that the neuroprotective effects of PNG in ischemic-induced neuronal injury are at least partially involved in the direct effect of PNG on hippocampal neuronal cell under ischemic conditions.

In the present study, we investigated whether treatment of OHSCs with ginsenosides Rg1 and Rb1 was able to prevent neurotoxicity resulting from OGD. Because of their amphipathic property, ginsenosides have the ability to intercalate into the plasma membrane. Consequently, this leads to alterations of membrane fluidity and affects the function of the membrane [11]. Ginsenosides Rb1 and Rg1 are the most abundant ginsenosides present in PNG roots. Based on high performance liquid chromatography analysis, the PNG ethanolic extract was estimated to contain 15.86% ginsenoside Rg1 and 12.04% ginsenoside Rb1. The present study revealed ginsenosides Rg1 (25 µM) and Rb1 (5, 25 µM) reduced OGD-induced neuronal cell damage in the OHSCs. These results demonstrated that ginsenosides Rg1 and Rb1 play an important role on the neuroprotective effects of PNG against ischemic damage in OHSCs. Interestingly, the effect of Rb1 was comparable to that of MK-801, a specific NMDA receptor antagonist. Several recent studies have reported the mechanism of action of Rg1 and Rb1. Rg1 inhibits calcium influx through NMDA receptors and other voltage-dependent ion channels. Additionally, Rg1 modulates the production of intracellular nitric oxide synthase, so it promotes hippocampal neurogenesis. Rb1 helps to regulate homeostasis in the brain by regulating the expression of neuropeptide Y. Moreover, by enhancing the Nrf2/Ho-1 pathway, Rb1 can protect neuronal cells against oxidative injury in ischemia [5]. Besides, the present data highlights that, compared to ginsenoside Rb1, ginsenoside Rg1 had much less protective effect on cerebral ischemic injury. These findings are supported by a previous report that ginsenosides Rg1 and Rb1 exerted neuroprotective effects against ischemic injury with ginsenoside Rb1 having the strongest effect out of all the tested ginsenosides [12]. Ginsenosides are structurally divided into protopanaxadiol-type ginsenosides and protopanaxatriol-type ginsenosides. Ginsenoside Rb1 belongs to the protopanaxadiol type while ginsenoside Rg1 belongs to the protopanaxatriol type ginsenosides. This suggests the important role of the protopanaxatriol-type structure on the neuroprotective action of PNG. The difference between the two groups is

the attached position of sugar moieties. However, to the best of our knowledge, there is no research that explains the relationship between the different structures and the neuroprotective mechanism of the ginsenosides.

5. Conclusions

The present study demonstrated that ginsenosides Rg1 and Rb1 play an importance role on the neuroprotective action of PNG against ischemic damage and that the neuroprotective effect of ginsenoside Rb1 was stronger than that of ginsenoside Rg1.

CRediT author statement

Nguyen Thi Thanh Loan, Le Thi Xoan: Conceptualisation, Methodology, Software, Resources, Writing - Review and Editing; Pham Thi Nguyet Hang, Nguyen Van Tai: Data curation, Software, Writing - Original draft preparation.

ACKNOWLEDGEMENTS

This study was supported by a grant from National Institute of Medicinal Materials, Ministry of Health, Vietnam.

COMPETING INTERESTS

The authors declare that there is no conflict of interest regarding the publication of this article.

REFERENCES

[1] B.C.V. Campbell, D.A.D. Silva, M.R. Macleod, et al. (2019), "Ischaemic stroke", *Nature Reviews Disease Primers*, **5(1)**, DOI: 10.1038/s41572-019-0118-8.

[2] T.B. Nguyen (2006), "Pharmacological activity of sanchi ginseng (*Panax notoginseng*)", *J. Pharm. Pharmacol*, **58(8)**, pp.1007-1019, DOI: 10.1211/jpp.58.8.0001.

[3] H.Y. Son, H.S. Han, H.W. Jung, et al. (2009), "*Panax notoginseng* attenuates the infarct volume in rat ischemic brain and the inflammatory response of microglia", *J. Pharmacol. Sci.*, **109(3)**, pp.368-379, DOI: 10.1254/jphs.08197fp.

[4] X.T. Le, H.T.N. Pham, T.V. Nguyen, et al. (2016), "Neuroprotective effect of *Panax notogingseng* against ischemic neuronal injury in mice", *Journal of Medicinal Materials*, **21(3)**, pp.169-174.

[5] P. Mohanan, S. Subramaniyam, R. Mathiyalagan, et al. (2018), "Molecular signaling of ginsenosides Rb1, Rg1, and Rg3 and their mode of actions", *J. Ginseng Res.*, **42(2)**, pp.123-132, DOI: 10.1016/j.jgr.2017.01.008.

[6] X.S. Zeng, X.S. Zhou, F.C. Luo, et al. (2014), "Comparative analysis of the neuroprotective effects of ginsenosides Rg1 and Rb1 extracted from *Panax notoginseng* against cerebral ischemia", *Can. J. Physiol. Pharmacol.*, **92(2)**, pp.102-108, DOI: 10.1139/cjpp-2013-0274.

[7] N.T. Rokot, T.S. Kairupan, K.C. Cheng, et al. (2016), "A role of ginseng and its constituents in the treatment of central nervous system disorders", *Evidence-Based Complementary and Alternative Medicine*, **2016**, DOI: 10.1155/2016/2614742.

[8] H.S. Cui, K. Matsumoto, Y. Murakami, et al. (2009), "Berberine exerts neuroprotective actions against *in vitro* ischemia induced neuronal cell damage in organotypic hippocampal slice cultures: Involvement of B-cell lymphoma 2 phosphorylation suppression", *Biol. Pharm. Bull*., **32(1)**, pp.79-85, DOI: 10.1248/bpb.32.79.

[9] K.E. Sandoval, K.A. Witt (2008), "Blood-brain barrier tight junction permeability and ischemic stroke", *Neurobiol. Dis.*, **32(2)**, pp.200-219, DOI: 10.1016/j.nbd.2008.08.005.

[10] C. Xing, K. Arai, E.H. Lo, et al. (2012), "Pathophysiologic cascades in ischemic stroke", *Int. J. Stroke*, **7(5)**, pp.378-385, DOI: 10.1111/j.1747-4949.2012.00839.x.

[11] X.T. Le, H.T.N. Pham, T.V. Nguyen, et al. (2015), "Protective effects of *Bacopa monnieri* on ischemia-induced cognitive deficits in mice: The possible contribution of bacopaside I and underlying mechanism", *J. Ethnopharmacol*., **164**, pp.37-45, DOI: 10.1016/j.jep.2015.01.041.

[12] D.C. Chung, K.S. Hong, J. Kang, et al. (2008), "Injury of neurons by oxygen-glucose deprivation in organotypic hippocampal slice culture", *Korean Journal of Pediatrics*, **51(10)**, pp.1112-1117, DOI : 10.3345/kjp.2008.51.10.1112.

DOI: 10.31276/VJSTE.63(2).70-73

Chemical constituents and antimicrobial activity of *Lisotrigona cacciae* propolis collected in Hoa Binh province

Le Nguyen Thanh[1, 2*], Nguyen Phuong Thao[3], Nguyen Tu Minh[3], Trinh Khanh Huyen[3], Vu Thi Kim Oanh[1, 2], Dinh Ngoc Thuc[4], Tran Thi Ngat[5], Nguyen Thi Phuong Lien[5]

[1]*Institute of Marine Biochemistry, Vietnam Academy of Science and Technology (VAST), 18 Hoang Quoc Viet Street, Nghia Do Ward, Cau Giay Districy, Hanoi, Vietnam*

[2]*Graduate Unversity of Science and Technology, VAST, 18 Hoang Quoc Viet Street, Nghia Do Ward, Cau Giay Districy, Hanoi, Vietnam*

[3]*GATE Center, Vinschool, 208 Nguyen Huu Canh Street, Ward 22, Binh Thanh District, Ho Chi Minh City, Vietnam*

[4]*Department of Scientific Management, Hong Duc University, 565 Quang Trung Street, Dong Ve Ward, Thanh Hoa City, Thanh Hoa Province, Vietnam*

[5]*Institute of Ecological and Biological Resouces, VAST, 18 Hoang Quoc Viet Street, Nghia Do Ward, Cau Giay Districy, Hanoi, Vietnam*

Received 21 February 2020; revised 29 April 2020; accepted 15 May 2020

Abstract:

Propolis is a bee product that originates from plant resin and exhibits various biological activities and phytochemical compositions. Propolis products have been used as medicinal agents for centuries. Propolis has numerous health benefits stemming from its many pharmacological activities due to its antioxidant, antimicrobial, antiviral, anti-inflammatory, and anticancer properties. The chemical study on the propolis of the stingless bee Lisotrigona cacciae collected from Hoa Binh province led to the isolation of four compounds including cycloartenol (1), cochinchinone A (2), α-mangostin (3), and isomangiferolic acid (4). *Mangifera indica* (Xoài) and *Cratoxylum cochinchinense* (Thành Ngạnh Nam) were suggested to be the resin sources of the propolis. The propolis EtOH extract showed good antimicrobial activity against the Gram (+) strains *B. cereus* with an MIC value of 8 µg/ml. Among the isolated compounds, α-mangostin (3) was the most active and displayed strong activity against the five strains *B. cereus*, *E. feacalis*, *S. aureus*, *P. aeruginosa*, and the fungus *C. albicans* with MIC values of 1-2 µg/ml.

Keywords: **antimicrobial activity, *Lisotrigona cacciae*, propolis, stingless bee, α-mangostin.**

Classification number: **3.4**

1. Introduction

Propolis is a bee product that originates from plant resin and exhibits various biological activities and phytochemical compositions. Propolis products have been used as medicinal agents for centuries. Propolis has numerous health benefits stemming from its many pharmacological activities due to its antioxidant, antimicrobial, antiviral, anti-inflammatory, and anticancer properties. Previous chemical studies of propolis has led to the isolation of flavonoids, terpenoids, phenolic acids and their esters, lignans and coumarins [1]. However, information regarding the chemical composition of Vietnamese bee propolis remains limited. Cycloartane-type triterpenes and alkyl phenols were isolated from the propolis of the stingless bees *Trigona minor* and *Lisotrigona cacciae* [2-4] while xanthones and homoisoflavonoids were found from the *Lisotrigona sp.* propolis [4, 5]. Herein, four compounds were isolated from the propolis of the stingless bee *Lisotrigona cacciae* in the Hoa Binh province and were identified as cycloartenol (**1**), cochinchinone A (**2**), *α*-mangostin (**3**), and isomangiferolic acid (**4**). The activity of these compounds and EtOH extract against several microbial strains are also described.

2. Experimental

2.1. Propolis sample

Stingless bee propolis was collected from beehives in the Tan Lac district, Hoa Binh province, in November of 2018. The stingless bee species was determined to be *Lisotrigona cacciae* by Ms. Tran Thi Ngat and Dr. Nguyen Thi Phuong Lien of the Institute of Ecology and Biological Resources (VAST).

2.2. General procedures

The NMR spectra were taken using a Bruker AM500 FT-NMR spectrometer with TMS as an internal standard. The electrospray ionization mass spectra (ESI-MS) were obtained using Agilent 1260 series single quadrupole LC/MS system. Column chromatography (CC) was performed on silica gel (Kieselgel 60, 40-63 µm, Merck). Analytical and preparative thin layer chromatography were performed using precoated silica gel plates (Merck $60F_{254}$).

*Corresponding author: Email: lethanh7676@gmail.com

2.3. Extraction and isolation

The propolis of *Lisotrigona cacciae* (158 g) was extracted with EtOH (1 l x 4 times, 1 day/time) at room temperature. The EtOH solvent was evaporated *in vacuo*. The residue (126 g) was suspended in H_2O and was then extracted with ethyl acetate (3 times x 500 ml/time). The organic solvents were removed *in vacuo* to obtain ethyl acetate residue (108 g). The ethyl acetate residue was subjected to a silica gel column chromatography (CC) and was eluted with a gradient solvent of *n*-hexane-EtOAc (100:0-0:100) to afford 12 fractions (F1-F12). Fraction F2 (600 mg) was fractionated by silica gel CC and eluted with *n*-hexane/EtOAc (9/1, v/v) to yield compound **1** (15 mg). Fraction F7 (1 g) was purified by silica gel CC and was eluted with *n*-hexane/acetone (98/2, v/v) to afford compound **2** (63 mg). Fraction F10 (1.28 g) was chromatographed on silica gel CC and eluted with *n*-hexane/EtOAc (8/2, v/v) to yield 5 fractions (F10.1-F10.5). The F10.4 (50 mg) was purified by preparative TLC using *n*-hexane/EtOAc (9/1, v/v) as the eluant to afford compound **3** (4 mg) and compound **4** (21 mg).

Cycloartenol (**1**): White solid, ESI-MS *m/z* 427 $[M+H]^+$. ^{1}H-NMR (500 MHz, $CDCl_3$) δ: 5.10 (1 H, t, *J*=7.0 Hz, H-24), 3.28 (1 H, m, H-3), 1.68 (3 H, s, H-27), 1.60 (3 H, s, H-26), 0.97 (3 H, s, H-28), 0.87 (3 H, s, H-18), 0.88 (3 H, d, *J*=7.0 Hz, H-21), 0.81 (3 H, s, H-30), 0.56 (1 H, d, *J*=4.5 Hz, H-19), 0.57 (1 H, d, *J*=4.5 Hz, H-19). ^{13}C NMR (125 MHz, $CDCl_3$) δ: 130.9 (C-25), 125.3 (C-24), 78.9 (C-3), 52.3 (C-17), 48.8 (C-14), 48.0 (C-8), 47.1 (C-5), 45.3 (C-13), 40.5 (C-4), 36.3 (C-22), 35.9 (C-20), 35.6 (C-15), 32.9 (C-12), 32.0 (C-1), 30.4 (C-2), 29.9 (C-19), 28.1 (C-16), 26.5 (C-11), 26.1 (C-10), 26.0 (C-7), 25.7 (C-27), 25.4 (C-28), 24.9 (C-23), 21.1 (C-6), 20.0 (C-9), 19.3 (C-30), 18.2 (C-21), 18.0 (C-19), 17.6 (C-26), 14.0 (C-29).

Cochinchinone A (**2**): Yellow solid, ESI-MS *m/z* 449 $[M+H]^+$. ^{1}H-NMR (500 MHz, $CDCl_3$) δ: 13.06 (s,1-OH), 7.61 (1 H, d, *J*=3 Hz, H-8), 7.33 (1 H, d, *J*=9 Hz, H-5), 7.24 (1 H, dd, *J*=3 Hz, 9 Hz, H-6), 6.46 (1 H, s, OH), 6.19 (1 H, s, OH), 5.27 (2 H, m, H-2', H-2''), 5.05 (1 H, t, *J*=7 Hz, H-6''), 3.55 (2 H, d, *J*=7.5 Hz, H-1''), 3.45 (2 H, d, *J*=7 Hz, H-1'), 2.09 (2 H, m, H-5''), 2.05 (2 H, m, H-4''), 1.87 (3 H, s, H-9''), 1.84 (3 H, s, H-4'), 1.76 (3 H, s, H-5'), 1.63 (3 H, s, H-10''), 1.57 (3 H, s, H-8''). ^{13}C NMR (125 MHz, $CDCl_3$) δ: 180.9 (C-9), 161.1 (C-3), 158.3 (C-1), 153.0 (C-4a), 152.4 (C-7), 150.5 (C-4b), 137.8 (C-3''), 135.0 (C-3'), 131.8 (C-7''), 123.9 (C-6''), 123.9 (C-6), 121.6 (C-2'), 121.6 (C-2''), 120.7 (C-8a), 119.0 (C-5), 109.1 (C-8), 109.1 (C-2), 105.1 (C-4), 103.2 (C-9a), 39.7 (C-4''), 26.4 (C-5''), 25.8 (C-5'), 25.6 (C-10''), 21.8 (C-1''), 21.6 (C-1'), 17.9 (C-4'), 17.7 (C-8''), 16.3 (C-9'').

α-Mangostin (**3**): Yellow solid, ESI-MS *m/z* 411 $[M+H]^+$. ^{1}H-NMR (500 MHz, CD_3OD) δ: 6.70 (1 H, s, H-5), 6.25 (1 H, s, *J*=9Hz, H-4), 5.25 (2 H, m, H-2', H-2''), 4.09 (2 H, d, *J*=6.5 Hz, H-1''), 3.77 (3 H, s, 7-OMe), 3.30 (2 H, d, *J*=7.5 Hz, H-1'), 1.84 (3 H, s, H-5''), 1.79 (3 H, s, H-4''), 1.69 (3 H, s, H-4'), 1.67 (3 H, s, H-5'). ^{13}C NMR (125 MHz, CD_3OD) δ: 183.1 (C-9), 163.6 (C-3), 161.6 (C-1), 157.9 (C-4b), 156.7 (C-4a), 156.2 (C-6), 144.8 (C-7), 138.5 (C-8), 131.8 (C-3'), 131.7 (C-3''), 125.1 (C-2'), 123.8 (C-2''), 112.2 (C-8a), 111.4 (C-2), 103.8 (C-9a), 102.8 (C-5), 93.1 (C-4), 61.3 (7-OMe), 27.1 (C-1'), 26.0 (C-4'), 25.9 (C-4''), 22.2 (C-1''), 18.3 (C-5'), 17.9 (C-5'').

Isomangiferolic acid (**4**): White solid, ESI-MS *m/z* 457 $[M+H]^+$. ^{1}H-NMR (500 MHz, CD_3OD) δ: 6.79 (1 H, t, *J*=7 Hz, H-24), 3.33 (1 H, br s, H-3), 2.28 (1 H, m, H-23a), 2.18 (1 H, m, H-23), 1.83 (3 H, s, H-27), 1.04 (3 H, s, H-18), 0.98 (3 H, s, H-28), 0.96 (3 H, d, *J*=6.5 Hz, H-21), 0.95 (3 H, s, H-30), 0.89 (3 H, s, H-29), 0.55 (1 H, d, *J*=4 Hz, H-19), 0.38 (1 H, d, *J*=4 Hz, H-19). ^{13}C NMR (125 MHz, CD_3OD) δ: 173.6 (C-26), 145.9 (C-24), 126.8 (C-25), 77.7 (C-3), 53.5 (C-17), 50.1 (C-14), 48.5 (C-8), 46.4 (C-13), 42.2 (C-5), 40.6 (C-4), 37.2 (C-20), 36.6 (C-15), 36.1 (C-22), 34.1 (C-12), 30.7 (C-19), 29.5 (C-2), 29.1 (C-16), 28.6 (C-1), 27.8 (C-10), 27.3 (C-11), 26.9 (C-23), 26.5 (C-7), 26.5 (C-28), 22.2 (C-29), 21.8 (C-6), 21.9 (C-6), 19.8 (C-30), 18.6 (C-21), 18.5 (C-18), 12.4 (C-27).

2.4. Antimicrobial activity

The antimicrobial activity was determined by multi-concentration dilution method [6] and expressed as MIC (minimal inhibitory concentration) values. The isolated compounds were diluted in dimethylsulfoxide (DMSO) at the following concentrations: 256, 128, 64, 32, 16, 8, 4, 2, and 1 µg/ml, which were used for the antimicrobial test. The positive controls were streptomycin for bacterial strains and cyclohexamide for fungus. Three strains of Gram-positive (*Enterococcus faecalis ATCC299212*, *Staphylococcus aureus ATCC25923*, *Bacillus cereus ATCC13245)*; three strains of Gram-negative bacteria (*Escherichia coli ATCC25922*, *Pseudomonas aeruginosa ATCC27853*, *Salmonella enterica ATCC13076*), and the fungus *Candida albicans ATCC10231* were used for the test.

3. Results and discussion

Compound **1** was isolated as a white solid. The ESI-MS spectrum showed a protonated molecular ion peak *m/z* of 427 $[M+H]^+$, which corresponds to a molecular formula of $C_{30}H_{50}O$ (M=426). The ^{1}H-NMR spectrum displayed the characteristic signals of a cycloartane-type triterpene with

two H-19 proton signals at δ_H of 0.79 (1 H, d, *J*=4.0 Hz) and 0.57 (1 H, d, *J*=4.0 Hz) and seven methyl signals at δ_H values of 1.68 (s, H-27), 1.60 (s, H-26), 0.97 (s, H-28), 0.87 (s, H-18), 0.88 (d, *J*=7.0 Hz, H-21) and 0.81 (s, H-30) (Fig. 1). An oxymethine group signal was observed at δ_H 3.28 (1 H, m, H-3). The ^{13}C-NMR and DEPT spectra of **1** revealed 30 carbon signals including 7 methyl groups at δ_C of 25.4 (C-28), 19.3 (C-29), 18.1 (C-21), 18.0 (C-18), 13.9 (C-30), and 9.2 (C-27), with 2 olefinic carbons at δ_C of 130.9 (C-25) and 125.3 (C-24) and an oxymethine group at δ_C of 78.9 (C-3). Therefore, compound **1** was determined as cycloartenol. The NMR data of **1** were in accordance with published values [7].

Compound **2** was obtained as a yellow solid. The ESI-MS showed a *quasi*-molecular ion peak *m/z* of 449 $[M+H]^+$, which corresponds to a molecular formula of $C_{28}H_{32}O_5$ (M=448). The ^{1}H-NMR spectrum revealed a hydrogen-bonded OH proton at δ_H of 13.06 (s) and three aromatic protons in an ABX system at δ_H 7.61 (1 H, d, *J*=3 Hz, H-8), 7.33 (1 H, d, *J*=9 Hz, H-5) and 7.24 (1 H, dd, *J*=3 Hz; 9 Hz, H-6). The characteristic signals of protons in an isoprenyl group were displayed at δ_H 5.27 (m), 3.45 (2 H, d, H-1'), 1.84 (3 H, s, H-4'), and 1.76 (3 H, s, H-5'). In addition, the presence of a geranyl group was indicated from the signals at δ_H 5.27 (m), 5.05 (1 H, t, H-6''), 2.09 (2 H, m, H-5''), 2.05 (2 H, m, H-4''), 1.87 (3 H, s, H-9''), 1.63 (3 H, s, H-10'') and 1.57 (3 H, s, H-8''). In the ^{13}C-NMR spectrum of **2**, 28 carbon signals were observed including a signal of a carbonyl group at δ_C 180.9 (C-9), signals of prenyl group at δ_C 135.0 (C-3'), 121.6 (C-2'), 25.8 (C-5'), 21.6 (C-1'), and 17.9 (C-4'), and signals of a geranyl group at δ_C 137.8 (C-3''), 131.8 (C-7''), 123.9 (C-6''), 121.6 (C-2''), 39.7 (C-4''), 26.4 (C-5''), 25.6 (C-10''), 21.8 (C-1''), 17.7 (C-8''), and 16.3 (C-9''). Compound **2** was determined to be cochinchinone A. The NMR data of **2** agreed with reported literature [8].

Compound **3** was obtained as a yellow solid. The ESI-MS revealed a *quasi*-molecular ion peak *m/z* of 411 $[M+H]^+$ suggesting that the molecular formula of **3** is $C_{24}H_{26}O_6$ (M=410). The ^{1}H-NMR spectrum showed the presence of two aromatic singlet protons at δ_H values of 6.70 and 6.25. In addition, there was one methoxy group found at δ_H 3.77 (s). The presence of two olefinic protons were found at δ_H 5.25 (2 H, m), then 2 methylene groups at δ_H 4.09 (d) and 3.30 (d), and four methyl singlets at δ_H 1.84 (s, H-5''), 1.79 (s, H-4''), 1.69 (s, H-4') and 1.67 (s, H-5') confirmed the presence of two isoprenyl groups.

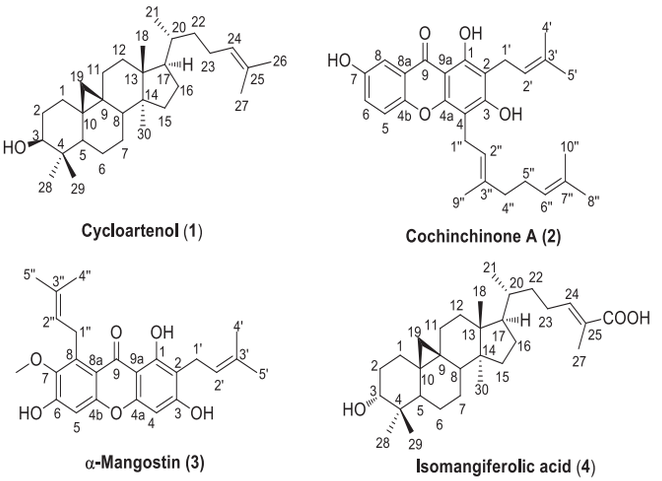

Fig. 1. Chemical structures of compounds 1-4.

The ^{13}C-NMR spectrum showed the presence of a carbonyl group at a δ_C of 183.1 (C-9), a methoxy group at a δ_C of 61.3 (7-OMe), and four methyl groups at δ_C values of 26.0 (C-4'), 25.9 (C-4''), 18.3 (C-5') and 17.9 (C-5''). Based on the spectral analysis, compound **3** was identified as α-mangostin. The analytical NMR data of **3** are identical with those previously published [9].

Compound **4** was isolated as a white solid. The ESI-MS showed a protonated molecular ion peak *m/z* of 457 $[M+H]^+$, which suggested the molecular formula of **4** is $C_{30}H_{48}O_3$ (M=456). The ^{1}H-NMR spectrum of **4** is similar to that of compound **1** and showed the signals of a cycloartane-type triterpene with 2 protons at δ_H of 0.55 (1 H, d, H-19) and 0.38 (1 H, d, H-19). However, in the NMR spectrum, only six methyl groups were displayed at δ_H 1.04 (3 H, s, H-18), 0.98 (3 H, s, H-28), 0.96 (3 H, d, *J*=6.5 Hz, H-21), 0.95 (3 H, s, H-30) and 0.89 (3 H, s, H-29). The ^{13}C-NMR and DEPT spectra of **4** showed 30 carbon signals including the signal of a carboxylic acid group at δ_C 173.0 (C-26), signals of 2 olefinic carbons at δ_C 145.7 (C-24) and 126.6 (C-25), a signal of an oxymethine group at δ_C 78.8 (C-3) and signals of 6 methyl groups at δ_C values of 25.4 (C-28), 19.3 (C-30), 18.1 (C-21), 18.0 (C-18), 14.0 (C-29), and 11.9 (C-27). Therefore, compound **4** was determined as isomangiferolic acid. The NMR data of **4** agreed with the values in the reported literature [10].

The cycloartan triterpenes and xanthones from the propolis of *Lisotrigona cacciae* collected in Hoa Binh were also found from the propolis in Binh Dinh province [4]. Cycloartenol and isomangiferolic acid were found in the *Mangifera indica* tree (Xoài), which is a common plant source of bee propolis [2, 4, 10, 11]. Cochinchinone A is only isolated from the plant *Cratoxylum cochinchinense* (Thành Ngạnh Nam) while α-mangostin is usually found

in *Cratoxylum cochinchinense* and the *Garcinia* species [8, 9, 12, 13]. Therefore, *Mangifera indica* and *Cratoxylum cochinchinense* trees are possibly the plant sources of this *Lisotrigona cacciae* propolis.

Table 1. Antimicrobial activity of EtOH extract and isolated compounds.

Samples	MIC (µg/ml)						
	E. faecalis	*S. aureus*	*B.cereus*	*E.coli*	*P. aeruginosa*	*S. enterica*	*C.albicans*
EtOH extract	32	32	8	na	64	na	128
Compound **1**	64	128	256	na	128	na	256
Compound **2**	16	32	16	na	64	na	128
Compound **3**	1	1	1	16	2	32	1
Compound **4**	1	64	128	na	2	na	16
Streptomycin	256	256	128	32	256	128	-
Cyclohexamide	-	-	-	-	-	-	32

na: not active; -: not tested.

The propolis EtOH extract and isolated compounds were tested for antimicrobial activity. As shown in Table 1, the EtOH extract displayed selective antimicrobial activity against Gram (+) strains over Gram (-) strains and the *C. albicans* fungus. The EtOH extract exhibited good activity on *B. cereus* with an MIC value of 8 µg/ml. Among the isolated compounds, *α*-mangostin **(3)** displayed the strongest activity against three Gram (+) strains, *P. aeruginosa,* and *C. albicans* with MIC values ranging between 1-2 µg/ml. *α*-Mangostin also had moderate activity on *E. coli* and *S. enterica*. Isomangiferolic acid (**4**) showed strong activity against *E. faecalis* and *P. aeruginosa* with MIC values of 1 and 2 µg/ml, respectively.

3. Conclusions

The phytochemical investigation on the propolis of the stingless bee *Lisotrigona cacciae* from the Hoa Binh province led to the isolation of four compounds including cycloartenol (**1**), cochinchinone A (**2**), *α*-mangostin (**3**), and isomangiferolic acid (**4**). The plants *Mangifera indica* and *Cratoxylum cochinchinense* were possible resin sources of the *L. cacciae* propolis. The EtOH extract showed good antimicrobial activity on Gram (+) strains *B. cereus* with an MIC value of 8 µg/ml. *α*-Mangostin (**3**) was the most active compound displaying strong activity against the five strains *B. cereus*, *E. feacalis, S. aureus*, *P. aeruginosa,* and the fungus *C. albicans* with MIC values ranging between 1-2 µg/ml. Isomangiferolic acid (**4**) also exhibited strong antimicrobial activity against *E. faecalis* and *P. aeruginosa.*

CRediT author statement

Le Nguyen Thanh, Nguyen Phuong Thao, Nguyen Tu Minh: Conceptualisation, Methodology, Software, Resources, Writing - Review and Editing; Trinh Khanh Huyen, Vu Thi Kim Oanh, Dinh Ngoc Thuc: Data curation, Software, Writing - Original draft preparation; Tran Thi Ngat, Nguyen Thi Phuong Lien: Supervision, Software, Validation.

ACKNOWLEDGEMENTS

This research is funded by GATE Center and Vietnam Academy of Science and Technology under grant number QTBG01.01/20-21.

COMPETING INTERESTS

The authors declare that there is no conflict of interest regarding the publication of this article.

REFERENCES

[1] M. Popova, B. Trusheva, V. Bankova (2019), "Propolis of stingless bees: A phytochemist's guide through the jungle of tropical biodiversity", *Phytomedicine*, DOI: 10.1016/j.phymed.2019.153098.

[2] H.X. Nguyen, M.T. Nguyen, N.T. Nguyen, et al. (2017), "Chemical constituents of propolis from Vietnamese *Trigona minor* and their antiausterity activity against the PANC-1 human pancreatic cancer cell line", *J. Nat. Prod.*, **80(8)**, pp.2345-2352, DOI: 10.1021/acs.jnatprod.7b00375.

[3] H.X. Nguyen, T.N.V. Do, M.T.T. Nguyen, et al. (2018), "A new alkenylphenol from the propolis of stingless bee *Trigona minor*", *Natural Product Communications*, **13(1)**, DOI: 10.1177/1934578X1801300121.

[4] K. Georgieva, M. Popova, L. Dimitrova, et al. (2019), "Phytochemical analysis of Vietnamese propolis produced by the stingless bee *Lisotrigona cacciae*", *PLOS ONE*, **14(4)**, DOI: 10.1371/journal.pone.0216074.

[5] H.T. Thoa, H.T. Van, V.T.K. Oanh, et al. (2018), "Isolated xanthones from the propolis of stingless bee (*Lisotrigona furva*)", *Pharmaceutical Journal*, **58(10)**, pp.22-24.

[6] F. Hadacek, H. Greger (2000), "Testing of antifungal natural products: Methodologies, comparability of results and assay choice", *Phytochemical Analysis*, **11(3)**, pp.137-147.

[7] T. Kato, B. Frei, M. Heinrich, et al. (1996), "Antibacterial hydroperoxysterols from *Xanthosoma robustum*", *Phytochemistry*, **41(4)**, pp.1191-1195, DOI: 10.1016/0031-9422(95)00765-2.

[8] W. Mahabusarakam, W. Nuangnaowarat, W.C. Taylor (2006), "Xanthone derivatives from *Cratoxylum cochinchinense* roots", *Phytochemistry*, **67(5)**, pp.470-474, DOI: 10.1016/j.phytochem.2005.10.008.

[9] Liandhajani, M.I. Iwo, Sukrasno, et al. (2013), "Sunscreen activity of *α*-mangostin from the pericarps of *Garcinia mangostana*", *Journal of Applied Pharmaceutical Science*, **3(6)**, pp.70-73, DOI: 10.7324/JAPS.2013.3610.

[10] C.E. Martinez, M.C. Lozada, S.H. Ortega, et al. (2012), "^{1}H and ^{13}C NMR characterization of new cycloartane triterpenes from *Mangifera indica*", *Magnetic Resonance in Chemistry*, **50(1)**, pp.52-57, DOI: 10.1002/mrc.2836.

[11] N. Pujirahayu, T. Suzuki, T. Katayama (2019), "Cycloartane-type triterpenes and botanical origin of propolis of stingless Indonesian bee *Tetragonula sapiens*", *Plants*, **8(3)**, DOI: 10.3390/plants8030057.

[12] S. Laphookhieo, J.K. Syers, R. Kiattansakul, et al. (2006), "Cytotoxic and antimalarial prenylated xanthones from *Cratoxylum cochinchinense*", *Chemical and Pharmaceutical Bulletin*, **54(5)**, pp.745-747, DOI: 10.1248/cpb.54.745.

[13] M. Taher, D. Susanti, M.F. Rezali, et al. (2012), "Apoptosis, antimicrobial and antioxidant activities of phytochemicals from *Garcinia malaccensis* Hk.f", *Asian Pacific Journal of Tropical Medicine*, **5(2)**, pp.136-141, DOI: 10.1016/S1995-7645(12)60012-1.

DOI: 10.31276/VJSTE.63(2).74-80

Herbicide resistant weeds: The case of resistance to glyphosate

The Duc Ngo*

Plant Resources Center, Vietnam Academy of Agricultural Sciences, An Khanh Commune, Hoai Duc District, Hanoi, Vietnam

Received 22 April 2020; revised 15 June 2020; accepted 29 June 2020

Abstract:

Glyphosate has become the most widely used herbicide worldwide since 1974 with a global use of 8.6 billion kg (glyphosate active ingredient) between 1974 and 2014. This study reports on glyphosate resistant (GR) weeds and their resistance mechanisms based on global scientifically reported cases. Forty-nine different weed species have evolved resistance to glyphosate in 29 countries with a total of 318 identified cases worldwide. Fifty percent of these resistance cases were found in glyphosate-resistant cropping systems. There were 255 identified cases (80.2%) of glyphosate resistance in the top five countries (in terms of number of cases and species), namely USA, Australia, Argentina, Brazil, and Canada. The five most popular weed species (in terms of number of cases) found to be resistant to glyphosate were *Conyza canadensis*, *Amaranthus palmeri*, *Amaranthus tuberculatus*, *Lolium perenne* ssp. *Multiflorum*, and *Ambrosia artemisiifolia* with 42, 42, 29, 26, and 21 reported cases, respectively. Out of 49 weed species, 19 GR weed species were found to not only be resistant to glyphosate but also to other herbicide sites of action (multiple herbicide resistance). Glyphosate resistance mechanisms in weeds include (1) target-site alterations: target-site mutation and target-site gene amplification; and (2) non-target-site mechanisms involving different modes of exclusion from the target site: reduced glyphosate uptake, reduced glyphosate translocation, and enhanced glyphosate metabolism. It is essential to have an integrated weed management program that includes not only smart herbicide mixtures and rotations, but also cultural, manual, mechanical, and crop-based weed management methods.

Keywords: **crop, glyphosate resistance, herbicide, mechanism, resistance, tolerance, weed.**

Classification number: **3.4**

1. Introduction

Glyphosate is the most widely used non-selective herbicide in the world [1]. There are several main attributes that make glyphosate a valuable herbicide. For example, it provides simple, inexpensive, flexible, and effective control of a broad spectrum of weeds in a wide variety of agronomic situations [2]. The use of this herbicide has continued to increase as its patent has expired and price declined. When the price of glyphosate declined, it was not only used in high-value crops [1] but also in many other crop or non-crop situations, such as weeds with burndown application, fallow situations, along roadsides, around structures, and in parks [3]. Importantly, when GR crops such as GR soybean (*Glycine max* (L.) Merr.), cotton (*Gossypium hirsutum* L.), and maize (*Zea mays* L.) became available for planting in the U.S in 1996, 1997, and 1998, respectively, and later in other countries, more glyphosate has been used in GR cropping systems. These GR cropping systems made it possible to use glyphosate as a broadcast, post-emergence herbicide by controlling all emerged weeds over a wide range of application timings.

Glyphosate (N-phosphonomethyl glycine) is a phosphonomethyl derivative of the amino acid glycine and has a unique mode of action. Glyphosate inhibits the enzyme 5-enolpyruvylshikimate-3-phosphate synthase (EPSPS) [4], which is present in plants, fungi, and bacteria, but not in animals [5]. EPSPS is the sixth enzyme of the shikimic acid pathway, in which phosphoenolpyruvate (PEP) and erythrose 4-phosphate are converted to chorismate, the precursor

* *Email: thengoduc@gmail.com*

of the aromatic amino acids (phenylalanine, tyrosine, and tryptophan) and many aromatic secondary metabolites (e.g., auxins, phytoalexins, anthocyanins, and lignin) [6]. EPSPS catalyses the transfer of the enolpyruvyl moiety from PEP to shikimate-3-phosphate (S3P) [7]. Glyphosate is a transition state analogue of PEP and inhibits EPSPS through the formation of an EPSPS-S3P-glyphosate ternary complex, only binding to the enzyme after the formation of EPSPS-S3P binary complex [8]. Therefore, glyphosate acts as a competitive inhibitor with PEP as it occupies its binding site [9]. EPSPS inhibition by glyphosate prevents the biosynthesis of aromatic amino acids [7]. Glyphosate is the only commercial herbicide that targets EPSPS in all higher plants [1].

Herbicide resistance is defined by the Weed Science Society of America [10] as the inherited ability of a plant to survive and reproduce following exposure to a dose of herbicide normally lethal to the wild type. In a plant, resistance may be naturally occurring or induced by techniques such as genetic engineering or selection of variants produced by tissue culture or mutagenesis. Similarly, S.B. Powles, et al. (1996) [11] defined herbicide resistance as "the inherited ability of a weed population to survive a herbicide application that is normally lethal to a vast majority of individuals of that species". To develop effective herbicide resistance management strategies, it is essential to understand the processes and means by which weeds withstand labelled herbicide treatments. Thus, this document reports GR weeds based on scientifically reported cases globally and their resistance mechanisms to glyphosate are discussed.

2. Occurrence of GR weeds

In 1996, the first evolved resistance to glyphosate in weed species was reported in rigid ryegrass (*Lolium rigidum* Gaudin) in Australia [12]. Since then, there has been a sharp increase in the number of GR weeds because of the decades long over-reliance on glyphosate for pre-sowing weed control and the introduction and rapid adoption of GR transgenic crops in the mid-1990s [13]. To date, 318 cases of glyphosate resistance have been identified in 49 different weed species in 29 countries worldwide [14, 15]. Among these cases, about 50% were found in GR cropping systems [3] such as GR cotton, maize, soybean, and canola (*Brassica* spp.). Between 1974 and 2014, the global use of glyphosate active ingredient was 8.6 billion kg and 19% (over 1.6 billion kg) of glyphosate used in USA. Glyphosate use in the GR cropping systems accounted for 56% of total global glyphosate usage in 2012 [16]. I. Heap, et al. (2018) [3] stated that both high rates (implying a high selection pressure) and low rates of glyphosate application (implying a low selection pressure) would result in more rapid evolution of herbicide resistance. Therefore, half of glyphosate resistance cases were found in these GR crop systems.

There were 255 identified cases (80.2%) of glyphosate resistance in the top five countries (in terms of number of cases and species). There were 169 cases in 17 species in the United States of America (USA), 36 cases in 19 species in Australia, 19 cases in 15 species in Argentina, 17 cases in 10 species in Brazil, 14 cases in 6 species Canada (Table 1). These four countries (except Australia) were also in the top five countries that planted more than 90% of genetically modified (GM) crops worldwide. In 2018, the top five GM crop-growing countries, namely USA, Brazil, Argentina, Canada and India, produced 75.0, 51.3, 23.9, 12.7, and 11.6 million ha of GM crops, respectively [17].

The number of GR cases in USA was 4.6 times that in Australia. However, Australia was on the top in the number of weed species evolved resistance to glyphosate with 19 weed species (Table 1). There were 125.3 million kg of glyphosate active ingredient used in USA in 2014 [16], while annual glyphosate use in Australia was 24.1 million kg of active ingredient [18]. In Southeast Asia, glyphosate resistance has been reported in Malaysia and Indonesia in goosegrass (*Eleusine indica* (L.) Gaertn.) and woody borreria (*Hedyotis verticillata* (L.) Lam.). There were no cases of GR weed reported in Vietnam (Table 1).

Table 1. GR weeds: number of cases and species by country.

No	Country	No. of cases	No. of species
1	United States	169	17
2	Australia	36	19
3	Argentina	19	15
4	Brazil	17	10
5	Canada	14	6
6	Spain	6	5
7	Colombia	5	4
8	South Africa	5	2
9	Chile	4	1
10	Greece	4	4
11	Italy	4	3
12	New Zealand	4	2
13	France	3	2
14	Japan	3	3
15	Malaysia	3	2
16	Paraguay	3	3
17	Portugal	3	3
18	China	2	2
19	Costa	2	2
20	Mexico	2	2
21	Israel	2	2
22	Bolivia	1	1
23	Czech Republic	1	1
24	Hungary	1	1
25	Indonesia	1	1
26	Poland	1	1
27	Switzerland	1	1
28	Turkey	1	1
29	Venezuela	1	1

Adapted from [14] (accessed 30 March 2020) and [15]

Among the 49 different weed species that have evolved resistance to glyphosate, the top five weed species (in terms of number of cases) contributed to 160 cases (50.3%). They were horseweed (*Conyza canadensis* (L.) Cronq.), palmer amaranth (*Amaranthus palmeri* S. Watson), tall waterhemp (*Amaranthus tuberculatus* (Moq.) J.D. Sauer), Italian ryegrass (*Lolium perenne* ssp. *multiflorum* (Lam.) Husnot), and common ragweed (*Ambrosia artemisiifolia* L.) with 42, 42, 29, 26, and 21 reported cases, respectively. *Conyza canadensis* was the most commonly found GR weed species with 42 cases in 13 countries (Table 2). *Lolium rigidum* was the first weed species to evolve resistance to glyphosate in Australia in 1996 [12] followed by 48 others weed species. In 2020, *Chloris distichophylla* (Lag.) from areas of soybean cultivation in Brazil was the 49th weed species that evolved resistance to glyphosate [15].

Unfortunately, 19 out of 49 GR weed species had evolved multiple herbicide resistance (Table 2), leaving growers with fewer herbicidal options for weed control. For example, *A. tuberculatus* in Ontario, Canada evolved multiple resistance (4 herbicide sites of action) to (1) EPSP synthase inhibitors (phosphanoglycine: glyphosate), (2) acetolactate synthase (ALS) inhibitors (imidazolinones), (3) Photosystem II inhibitors (triazines), and (4) protoporphyrinogen oxidase (PPO) inhibitors (diphenylether). *Amaranthus palmeri* in Arkansas, USA also evolved multiple resistance (5 herbicide sites of action) to (1) EPSP synthase inhibitors, (2) ALS inhibitors, (3) PPO inhibitors, (4) microtubule inhibitors (initroaniline), and (5) long chain fatty acid inhibitors (chloroacetamides).

In Vietnam, herbicides and mechanical and manual weeding are used for weed control. There were 104 glyphosate-based herbicides registered in Vietnam [19]. The annual glyphosate use in Vietnam was 3.22 million kg of active ingredient [18]. Glyphosate accounted for 36% of total herbicide use (in terms of active ingredient) and 35% of total spray area in Vietnam. Glyphosate use in rubber, coffee, rice, and sugarcane accounted for 57, 12, 6, and 5%, respectively, of total usage [18]. Fourteen genetically modified (GM) crop events for herbicide tolerance have been approved in Vietnam, include eight events (three events for glyphosate tolerance) of maize (*Zea mays* L.) and six events (three events for glyphosate tolerance) of soybean (*Glycine max* L.) [20]. Glyphosate-tolerant maize was grown on 55,000 ha in Vietnam [18]. GR weed has not been scientifically reported in Vietnam yet. This may be because there have been insufficient studies in weed science and herbicide resistance in Vietnam, and particularly, research in glyphosate resistance. I. Heap, et al. (2018) [3] also stated that herbicide resistant weeds were underreported in developing countries. Additional research needs to be conducted in weed science in order to improve weed management practices in these countries. However, populations of barnyard grass (*Echinochloa crus-galli* (L.) P. Beauv.) collected at several locations in the Mekong delta, Vietnam were confirmed to be resistant to two herbicide sites of action, namely synthetic auxins inhibitors (quinclorac) and ALS inhibitors (bispyribac, penoxsulam) [21].

Table 2. GR weeds: Number of cases and countries by species.

No	Species	No. of cases	No. of countries	Multiple resistance
1	*Conyza canadensis*	42	13	Yes
2	*Amaranthus palmeri*	42	3	Yes
3	*Amaranthus tuberculatus*	29	2	Yes
4	*Lolium perenne* ssp. *multiflorum*	26	9	Yes
5	*Ambrosia artemisiifolia*	21	2	Yes
6	*Lolium rigidum*	17	8	Yes
7	*Ambrosia trifida*	17	2	
8	*Kochia scoparia*	17	2	Yes
9	*Eleusine indica*	14	10	Yes
10	*Conyza bonariensis*	13	10	Yes
11	*Conyza sumatrensis*	11	7	Yes
12	*Poa annua*	7	2	Yes
13	*Echinochloa colona*	6	4	Yes
14	*Sorghum halepense*	5	2	Yes
15	*Lolium perenne*	4	3	Yes
16	*Amaranthus hybridus*	4	2	Yes
17	*Digitaria insularis*	3	3	
18	*Chloris virgata*	3	1	
19	*Salsola tragus*	3	1	
20	*Brassica rapa*	2	2	Yes
21	*Parthenium hysterophorus*	2	2	
22	*Urochloa panicoides*	2	2	
23	*Chloris truncata*	2	1	
24	*Amaranthus spinosus*	1	1	
25	*Avena fatua*	1	1	
26	*Avena sterilis* ssp. *ludoviciana*	1	1	
27	*Bidens pilosa*	1	1	
28	*Bidens subalternans*	1	1	
29	*Brachiaria eruciformis*	1	1	
30	*Bromus catharticus*	1	1	
31	*Bromus diandrus*	1	1	
32	*Bromus rubens*	1	1	
33	*Carduus acanthoides*	1	1	Yes
34	*Chloris elata*	1	1	
35	*Chloris radiata*	1	1	
36	*Cynodon hirsutus*	1	1	
37	*Echinochloa crus-galli var. crus-galli*	1	1	
38	*Hedyotis verticillata*	1	1	Yes
39	*Helianthus annuus*	1	1	
40	*Hordeum murinum* ssp. *glaucum*	1	1	
41	*Lactuca saligna*	1	1	
42	*Lactuca serriola*	1	1	
43	*Leptochloa virgata*	1	1	
44	*Paspalum paniculatum*	1	1	
45	*Plantago lanceolata*	1	1	
46	*Raphanus raphanistrum*	1	1	Yes
47	*Sonchus oleraceus*	1	1	
48	*Tridax procumbens*	1	1	
49	*Chloris distichophylla*	1	1	

Adapted from [14] (accessed 30 March 2020) and [15]

3. Glyphosate resistance mechanisms

Resistance mechanisms to glyphosate in weeds include (1) target-site alterations and (2) non-target-site mechanisms.

3.1. Target-site mechanisms

Target-site alterations include (1a) target-site mutation [22-24], represented by amino acid substitutions that affect herbicide interactions at the target enzyme; and (1b) target-site gene amplification [25-27], where sufficient EPSPS protein is produced so that the shikimate pathway can continue to operate despite the fact that glyphosate inhibits some of the enzyme.

Target-site mutations that change Pro106 of EPSPS to Ala, Leu, Ser, or Thr have been reported in GR populations of 6 different weed species [28, 29]. It was concluded that the Pro101 (position Pro106 in plant mature EPSPS consensus corresponds to position Pro101 in *E. coli*) is not directly involved in molecular interactions with either glyphosate or the substrate PEP, but any mutation at this site would shift other amino acids (Thr97 and Gly96) towards the inhibitor molecule resulting in a structural change to the glyphosate-binding site [30]. More recently, a double amino acid substitution in a single EPSPS allele (Thr102Ile+Pro106Ser) was found in glyphosate-resistant *E. indica* populations from Malaysia and China [23, 24]. This double amino acid substitution conferred high-level glyphosate resistance (more than 180-fold) [23] whereas the single Pro-106 mutations of the 6 weed species provided only moderate resistance (less than 10-fold) [29]. Another double TIPT mutation (Thr102Ile and Pro106Thr) was reported in a population of glyphosate-resistant greater beggarticks (*Bidens subalternans* DC.) from Paraguay [31]. Especially, a triple amino acid substitution from TAP to IVS was found in the EPSPS gene of a GR smooth pigweed population (*Amaranthus hybridus* L.) from Argentina. The nucleotide substitutions were Ile102 (ATA), Val103 (GTC), and Ser106 (TCA) in place of Thr102 (ACA), Ala103 (GCG), and Pro106 (CCA), respectively [32].

Glyphosate resistance due to extensive amplification of the EPSPS gene was first revealed in a population of *A. palmeri* in Georgia, USA in 2010 [27] and in Arkansas, USA in 2018 [33]. This mechanism has since been identified in 8 other weed species: *L. multiflorum* [26], spiny amaranth (*Amaranthus spinosus* L.) [34], *A. tuberculatus* [35, 36], *E. indica* [24], kochia (*Kochia scoparia* (L.) Schrad.) [37], ripgut brome (*Bromus diandrus Roth*) [25], windmillgrass (*Chloris truncata* R. Br) [38], and smooth barley (*Hordeum*

murinum ssp. *glaucum* (Steud.)) [39]. Individuals of the GR populations contained few to many more copies of the EPSPS gene than did the susceptible plants, with the number of EPSPS copies found to be variable both between and within populations. For example, *A. palmeri* from Georgia, the Carolinas, and New Mexico had, respectively, 5 to 160-fold [27], 22 to 36-fold [40], and 2 to 8-fold [41] more copies of the EPSPS gene and a 10 to 36-fold increase in *B. diandrus* [25] and a 10 to 25-fold increase in *L. multiflorum* [26]. It has been suggested that the effect of additional copies of the EPSPS is additive and additional copies confer higher levels of resistance to glyphosate [27]. This amplification of the EPSPS gene produces sufficient EPSPS protein to enable the shikimate pathway to continue to operate despite glyphosate inhibition of some of the enzymes [42].

3.2. Non-target-site mechanisms

Glyphosate is taken up through plant surfaces and leaf uptake rates vary considerably between species. Diffusion is the most likely mode of transport across the plant cuticle [1], which varies in composition and thickness among different plant species. Uptake is also dependent on several interdependent factors: droplet size and droplet spread, surfactant type and concentration, ionic strength and salt concentration, humidity, and, most importantly, glyphosate concentration [43]. After it is absorbed, the physicochemical properties of glyphosate enable it to be translocated from the leaf via phloem transport to meristematic growing points in the roots and shoots [1, 43]. The phloem movement of glyphosate and the efficiency of translocation are affected by the health and developmental stage of the plant, which is often related to environmental conditions [43] such as temperature.

Non-target-site mechanisms include (2a) reduced glyphosate uptake [44, 45], where less glyphosate is absorbed by resistant plants than susceptible plants; (2b) reduced glyphosate translocation [44, 46-48], where amounts of glyphosate absorbed by both resistant and susceptible plants are similar after glyphosate treatment; however, the absorbed herbicide mostly remains in the treated leaf in resistant biotypes and only a smaller amount of glyphosate was transported to the meristems of the treated plant; and (2c) enhanced glyphosate metabolism [49, 50].

Reduced glyphosate uptake has been reported in GR populations of sourgrass (*Digitaria insularis* (L.) Mez ex Ekman) and johnsongrass (*Sorghum halepense* (L.) Pers.) [44, 45]. L.B. Carvalho, et al. (2012) [45] stated that reduced glyphosate uptake is one of the glyphosate resistance mechanisms in *D. insularis* in Brazil. The susceptible plants absorbed at least 12% more glyphosate than resistant sourgrass plants up to 48 h after treatment. Reduced glyphosate translocation has been found in GR plants of *S. halepense, L. rigidum*, and perennial ryegrass (*Lolium perenne* L.) [44, 46-48]. It was reported that reduced glyphosate translocation to meristems is the main mechanism conferring glyphosate resistance in *S. halepense* in Argentina. The amount that translocated to the meristems of the resistant plants was threefold less than in the susceptible plants of johnsongrass [44]. Enhanced glyphosate metabolism has been reported in some weed species such as an Australian population of *E. colona* [49] and in the populations of 3 *Conyza* species from Greece [50]. It was revealed that glyphosate was metabolized to produce aminomethylphosphonic acid and glyoxylate [49, 50].

4. Conclusions

In conclusion, weeds that are resistant to glyphosate will continue to increase in terms of both number of species and cases. However, this increase can be slowed down by improved resistance management. For example, it may not be sustainable to use a single herbicide to manage weeds. Herbicides need to be exploited in a more sustainable way and additional methods must be used to control GR weeds. To have sustainable weed management practices, herbicides should not only involve smart herbicide mixtures and rotations, but also be part of a much more intensive integrated weed management program [51] that includes mechanical, cultural, and crop-based weed management strategies.

ACKNOWLEDGEMENTS

The author gratefully acknowledges all of the scientists that have contributed the data (weeds resistant to EPSP synthase inhibitors) to the international survey of herbicide resistant weeds. The author would like to thank anonymous reviewers for their useful suggestions and comments. Disclaimer: The views, opinions, or recommendations expressed in this document are those of the author and do not necessarily reflect or should not be reported as those of the organization he is affiliated to.

COMPETING INTERESTS

The author declares that there is no conflict of interest regarding the publication of this article.

REFERENCES

[1] S.O. Duke, S.B. Powles (2008), "Glyphosate: A once-in-a- century herbicide", *Pest Manage. Sci.*, **64(4)**, pp.319-325, DOI: 10.1002/ps.1518.

[2] A.D. Baylis (2000), "Why glyphosate is a global herbicide: Strengths, weaknesses and prospects", *Pest Manage. Sci.*, **56(4)**, pp.299-308, DOI: 10.1002/(SICI)1526-4998(200004)56:4<299::AID-PS144>3.0.CO;2-K.

[3] I. Heap, S.O. Duke (2018), "Overview of glyphosate-resistant weeds worldwide", *Pest Manage. Sci.*, **74(5)**, pp.1040-1049, DOI: 10.1002/ps.4760.

[4] N. Amrhein, B. Deus, P. Gehrke, et al. (1980), "The site of the inhibition of the shikimate pathway by glyphosate: II. Interference of glyphosate with chorismate formation *in vivo* and *in vitro*", *Plant Physiol.*, **66(5)**, pp.830-834, DOI: 10.1104/pp.66.5.830.

[5] G.M. Kishore, D.M. Shah (1988), "Amino-acid biosynthesis inhibitors as herbicides", *Annu. Rev. Biochem.*, **57**, pp.627-663, DOI: 10.1146/annurev.bi.57.070188.003211.

[6] K.M. Herrmann, L.M. Weaver (1999), "The shikimate pathway", *Annu. Rev. Plant Biol.*, **50(1)**, pp.473-503, DOI: 10.1146/annurev.arplant.50.1.473.

[7] A.P. Jones, C.M. Smith (2010), "Biochemical mechanisms and molecular basis of evolved glyphosate resistance in weed species", *Glyphosate Resistance in Crops and Weeds*, pp.119-140, DOI: 10.1002/9780470634394.ch6.

[8] M.F. Alibhai, W.C. Stallings (2001), "Closing down on glyphosate inhibition - with a new structure for drug discovery", *Proceedings of The National Academy of Sciences of The United States of America*, **98(6)**, pp.2944-2946, DOI: 10.1073/pnas.061025898.

[9] E. Schönbrunn, S. Eschenburg, W.A. Shuttleworth, et al. (2001), "Interaction of the herbicide glyphosate with its target enzyme 5-enolpyvuvylshikimate 3-phosphate synthase in atomic detail", *Proceedings of The National Academy of Sciences of The United States of America*, **98(4)**, pp.1376-1380, DOI: 10.1073/pnas.98.4.1376.

[10] Weed Science Society of America (1998), "Technology notes: herbicide resistance and herbicide tolerance defined", *Weed Technol.*, **12(4)**, pp.789-790.

[11] S.B. Powles, C. Preston, I.B. Bryan, et al. (1996), "Herbicide resistance: Impact and management", *Advances in Agronomy*, **58**, pp.57-93, DOI: 10.1016/S0065-2113(08)60253-9.

[12] J. Pratley, P. Baines, P. Eberbach, et al. (1996), "Glyphosate resistance in annual ryegrass", *Proc. Eleventh Ann. Conf. Grassld. Soc. NSW*, pp.121-122.

[13] S.B. Powles (2008), "Evolved glyphosate-resistant weeds around the world: Lessons to be learnt", *Pest Manage. Sci.*, **64(4)**, pp.360-365, DOI: 10.1002/ps.1525.

[14] I.M. Heap (2020), "Weeds resistant to EPSP synthase inhibitors (G/9)", *The International Survey of Herbicide-Resistant Weeds*, http://weedscience.org/summary/MOA. aspx?MOAID=12, accessed 14 January 2020.

[15] J.G.V. Garcia, S. Golmohammadzadeh, C.P. Bautista, et al. (2020), "New case of false-star-grass (*Chloris distichophylla*) population evolving glyphosate resistance", *Agronomy*, **10(3)**, DOI: 10.3390/agronomy10030377.

[16] C.M. Benbrook (2016), "Trends in glyphosate herbicide use in the United States and globally", *Environmental Sciences Europe*, **28(3)**, DOI: 10.1186/s12302-016-0070-0, accessed 14 January 2020.

[17] International Service for the Acquisition of Agri-biotech Applications (ISAAA) (2020), *Biotech Country Facts and Trends*, available at: http://www.isaaa.org/resources/publications/biotech_country_facts_and_trends/default.asp, accessed 14 January 2020.

[18] G. Brookes (2019), "Glyphosate use in Asia and implications of possible restrictions on its use", *AgBioForum, Online Advanced Publication*, **21(1)**, pp.1-26.

[19] Ministry of Agriculture and Rural Development (2019), *No: 10/2019/TT-BNNPTNT on 20 Sept 2019, Lists of Pesticides Permitted for Use or Banned from Use in Vietnam* (in Vietnamese).

[20] International Service for the Acquisition of Agri-biotech Applications (2020), *The GM Crop Events Approved in Vietnam, GM Approval Database*, http://www.isaaa.org/ gmapprovaldatabase/, accessed 14 January 2020.

[21] D. Le, N.M. Chon, R.K. Mann, et al. (2018), "Efficacy of Rinskor™ (florpyrauxifen-benzyl ester) on herbicide resistant barnyardgrass (*Echinochloa crus-galli*) in rice fields of Mekong delta, Vietnam", *Journal of Crop Science and Biotechnology*, **21(1)**, pp.75-81, DOI: 10.1007/s12892-017-0142-0.

[22] S.R. Baerson, D.J. Rodriguez, M. Tran, et al. (2002), "Glyphosate-resistant goosegrass. Identification of a mutation in the target enzyme 5-enolpyruvylshikimate-3-phosphate synthase", *Plant Physiol.*, **129(3)**, pp.1265-1275, DOI: 10.1104/pp.001560.

[23] Q. Yu, A. Jalaludin, H. Han, et al. (2015), "Evolution of a double amino acid substitution in the 5-enolpyruvylshikimate-3-phosphate synthase in *Eleusine indica* conferring high-level glyphosate resistance", *Plant Physiol.*, **167(4)**, pp.1440-1447, DOI: 10.1104/pp.15.00146.

[24] J.C. Chen, H.J. Huang, C.X. Zhang, et al. (2015), "Mutations and amplification of *EPSPS* gene confer resistance to glyphosate in goosegrass (*Eleusine indica*)", *Planta*, **242(4)**, pp.859-868, DOI: 10.1007/s00425-015-2324-2.

[25] J.M. Malone, S. Morran, N. Shirley, et al. (2016), "*EPSPS* gene amplification in glyphosate-resistant *Bromus diandrus*", *Pest Manage. Sci.*, **72(1)**, pp.81-88, DOI: 10.1002/ps.4019.

[26] R.A. Salas, F.E. Dayan, Z. Pan, et al. (2012), "*EPSPS* gene amplification in glyphosate-resistant Italian ryegrass (*Loliumperenne ssp. multiflorum*) from Arkansas", *Pest Manage. Sci.*, **68(9)**, pp.1223-1230, DOI: 10.1002/ps.3342.

[27] T.A. Gaines, W. Zhang, D. Wang, et al. (2010), "Gene amplification confers glyphosate resistance in *Amaranthus palmeri*", *PNAS*, **107(3)**, pp.1029-1034, DOI: 10.1073/pnas.0906649107.

[28] R.D. Sammons, T.A. Gaines (2014), "Glyphosate resistance: State of knowledge", *Pest Manage. Sci.*, **70(9)**, pp.1367-1377, DOI: 10.1002/ps.3743.

[29] T.A. Gaines, I.M. Heap (2016), "Mutations in herbicideresistant weeds to EPSP synthase inhibitors", *International Service for The Acquisition of Agri-Biotech Applications (ISAAA)*, http://www.weedscience.org/Mutations/MutationDisplayAll.aspx?MOAID=12, accessed 14 January 2020.

[30] M.L.H. Fried, T. Funke, M.A. Priestman, et al. (2007), "Structural basis of glyphosate tolerance resulting from mutations of Pro101 in *Escherichia coli* 5-enolpyruvylshikimate-3-phosphate synthase", *J. Biol. Chem.*, **282(45)**, pp.32949-32955, DOI: 10.1074/jbc.M705624200.

[31] H.K. Takano, V.N. Fernandes, F.S. Adegas, et al. (2020), "A novel TIPT double mutation in EPSPS conferring glyphosate resistance in tetraploid *Bidens subahernans*", *Pest Manage. Sci.*, **76(1)**, pp.95-102, DOI: 10.1002/ps.5535.

[32] M.J. Garcia, C. Palma-Bautista, A.M. Rojano-Delgado, et al. (2019), "The triple amino acid substitution TAP-IVS in the EPSPS gene confers high glyphosate resistance to the superweed *Amaranthus hybridus*", *International Journal of Molecular Sciences*, **20(10)**, DOI: 10.3390/ijms20102396.

[33] D.A. Giacomini, P Westra, S.M. Ward (2018), "Variable inheritance of amplified EPSPS gene copies in glyphosate-resistant palmer amaranth (*Amaranthus palmeri*)", *Weed Sci.*, **67(2)**, pp.176-182, DOI: 10.1017/wsc.2018.65.

[34] V.K. Nandula, A.A. Wright, J.A. Bond, et al. (2014), "*EPSPS* amplification in glyphosateresistant spiny amaranth (*Amaranthus spinosus*): A case of gene transfer via interspecific hybridization from glyphosate-resistant palmer amaranth (*Amaranthus palmeri*)", *Pest Manage. Sci.*, **70(12)**, pp.1902-1909, DOI: 10.1002/ps.3754.

[35] L. Lorentz, T.A. Gaines, S.J. Nissen, et al. (2014), "Characterization of glyphosate resistance in *Amaranthus tuberculatus* populations", *J. Agric. Food Chem.*, **62(32)**, pp.8134-8142, DOI: 10.1021/jf501040x.

[36] L.A. Chatham, C. Wu, C.W. Riggins, et al. (2015), "*EPSPS* gene amplification is present in the majority of glyphosate-resistant Illinois waterhemp (*Amaranthus tuberculatus*) populations", *Weed Technol.*, **29(1)**, pp.48-55.

[37] A.T. Wiersma, T.A. Gaines, C. Preston, et al. (2015), "Gene amplification of 5-enol-pyruvylshikimate-3-phosphate synthase in glyphosate-resistant *Kochia scoparia*", *Planta*, **241(2)**, pp.463-474, DOI: 10.1007/s00425-014-2197-9.

[38] T.D. Ngo, J.M. Malone, P. Boutsalis, et al. (2018), "EPSPS gene amplification conferring resistance to glyphosate in windmill grass (*Chloris truncata*) in Australia", *Pest Manage. Sci.*, **74(5)**, pp.1101-1108, DOI: 10.1002/ps.4573.

[39] P. Adu-Yeboah, J.M. Malone, B. Fleet, et al. (2019), "EPSPS gene amplification confers resistance to glyphosate resistant populations of *Hordeum glaucum* Stued (northern barley grass) in South Australia", *Pest Manage. Sci.*, **76(4)**, pp.1214-1221, DOI: 10.1002/ps.5671.

[40] A. Chandi, S.R. Milla-Lewis, D. Giacomini, et al. (2012), "Inheritance of evolved glyphosate resistance in a North Carolina Palmer amaranth (*Amaranthus palmeri*) biotype", *International Journal of Agronomy*, **2012**, DOI: 10.1155/2012/176108.

[41] M.M. Moghadam, J. Schroeder, J. Ashigh (2013), "Mechanism of resistance and inheritance in glyphosate resistant Palmer amaranth (*Amaranthus palmeri*) populations from New Mexico, USA", *WeedSci.*, **61(4)**, pp.517-525, DOI: 10.1614/WS-D-13-00028.1.

[42] S.B. Powles (2010), "Gene amplification delivers glyphosateresistant weed evolution", *PNAS*, **107(3)**, pp.955-956, DOI: 10.1073/pnas.0913433107.

[43] G.M. Dill, R.D. Sammons, P.C.C. Feng, et al. (2010), "Glyphosate: Discovery, development, applications, and properties", *Glyphosate Resistance in Crops and Weeds*, DOI: 10.1002/9780470634394.ch1.

[44] M.M.V. Aiub, M.C. Balbi, A.J. Distefano, et al. (2012), "Glyphosate resistance in perennial *Sorghum halepense* (Johnsongrass), endowed by reduced glyphosate translocation and leaf uptake", *Pest Manage. Sci.*, **68(3)**, pp.430-436, DOI: 10.1002/ps.2286.

[45] L.B.D. Carvalho, P.L. Alves, F.G. Torralva, et al. (2012), "Pool of resistance mechanisms to glyphosate in *Digitaria insularis*", *J. Agric. Food Chem.*, **60(2)**, pp.615-622, DOI: 10.1021/jf204089d.

[46] Y. Bostamam, J.M. Malone, F.C. Dolman, et al. (2012), "Rigid ryegrass (*Lolium rigidum*) populations containing a target site mutation in EPSPS and reduced glyphosate translocation are more resistant to glyphosate", *Weed Sci.*, **60(3)**, pp.474-479, DOI: 10.1614/WS-D-11-00154.1.

[47] H. Ghanizadeh, K.C. Harrington, T.K. James, et al. (2015), "Mechanisms of glyphosate resistance in two perennial ryegrass (*Lolium perenne*) populations", *Pest Manage. Sci.*, **71(12)**, pp.1617-1622, DOI: 10.1002/ps.3968.

[48] D.L. Colwill, S. Powles, T. Hawkes, et al. (2002), "Investigations into the mechanism of glyphosate resistance in *Lolium rigidum*", *Pestic. Biochem. Physiol.*, **74(2)**, pp.62-72, DOI: 10.1016/S0048-3575(03)00007-5.

[49] L. Pan, Q. Yu, H. Han, et al. (2019), "Aldo-keto reductase metabolizes glyphosate and confers glyphosate resistance in *Echinochloa colona*", *Plant Physiol.*, **181(4)**, pp.1519-1534, DOI: 10.1104/pp.19.00979.

[50] C. Anagnostopoulos, P. Stasinopoulou, P. Kanatas, et al. (2020), "Differences in metabolism of three *Conyza* species to herbicides glyphosate and triclopyr revealed by LC-MS/MS", *Chilean Journal of Agricultural Research*, **80(1)**, pp.100-107, DOI: 10.4067/S0718-58392020000100100.

[51] J.M. Green (2014), "Current state of herbicides in herbicideresistant crops", *Pest Manage. Sci.*, **70(9)**, pp.1351-1357, DOI: 10.1002/ps.3727.

DOI: 10.31276/VJSTE.63(2).81-88

Effects of red and blue light emitting diodes on biomass and astaxanthin of *Haematococcus pluvialis* in pilot scale angled twin-layer porous substrate photobioreactors

Thanh-Tri Do[1, 2], Bich-Huy Tran-Thi[3], Binh-Nguyen Ong[3], Tuan-Loc Le[3], Thanh-Cong Nguyen[3], Quoc-Dang Quan[4], Thuong-Chi Le[5], Dai-Long Tran[5], Michael Melkonian[6], Hoang-Dung Tran[7*]

[1]University of Science, Vietnam National University - Ho Chi Minh City, 227 Nguyen Van Cu Street, Ward 4, District 5, Ho Chi Minh City, Vietnam
[2]Faculty of Biology, Ho Chi Minh city University of Education, 280 An Duong Vuong Street, Ward 4, District 5, Ho Chi Minh City, Vietnam
[3]Faculty of Biotechnology, Nguyen Tat Thanh University, 300A Nguyen Tat Thanh Street, Ward 13, District 4, Ho Chi Minh City, Vietnam
[4]Agency for Southern Affairs of Ministry of Science and Technology, 31 Han Thuyen Street, Ben Nghe Ward, District 1, Ho Chi Minh City, Vietnam
[5]Van Lang University, 45 Nguyen Khac Nhu Street, Co Giang Ward, District 1, Ho Chi Minh City, Vietnam
[6]Max Planck Institute for Plant Breeding Research, Carl-von-Linne-Weg, Koeln City, Germany
[7]Ho Chi Minh City University of Food Industry, 140 Le Trong Tan Street, Tay Thanh Ward, Tan Phu District, Ho Chi Minh City, Vietnam

Received 23 December 2020; revised 28 February 2021; accepted 15 March 2021

Abstract:

Astaxanthin has been shown to be one of the most powerful antioxidants out of many other carotenoids. Astaxanthin can be found in the shells of crustaceans, seafood, the yeast Phaffia rhodozyma, and in some bacteria at low concentrations. However, the green alga *Haematococcus pluvialis* is able to synthesize and accumulate astaxanthin in high and is thus used to produce astaxanthin on an industrial scale. The production of natural astaxanthin is usually accomplished by suspended cultivation of the microalgae Haematococcus pluvialis (open or closed systems). In this study, for the purpose of cost reduction, *H. pluvialis* is grown in pilot scale angled twin-layer porous substrate photobioreactors with light energy from red/blue LEDs that can produce red light, blue light, or a combination of blue-red light. The total dry biomass of the microalgae reached a maximum of 40.74 g.m-2 under blue-red LEDs. The early initiation of blue-red LED illumination (on day 2) after algae immobilization in the biofilm resulted in the highest accumulation of astaxanthin in the dry biomass, which reached a maximum of 1.3% (w/w) after 10 d of culture.

Keywords: **angled, astaxanthin, biofilm, *Haematococcus pluvialis*, photobioreactor, porous substrate, twin-layer.**

Classification number: **3.5**

1. Introduction

Astaxanthin has been shown to be one of the most powerful antioxidants out of many other carotenoids [1-3]. Astaxanthin can be found in the shells of crustaceans, seafood, the yeast *Phaffia rhodozyma*, and in some bacteria at low concentrations. However, the green alga *Haematococcus pluvialis* is able to synthesize and accumulate astaxanthin in high concentrations (possibly up to 5-6% [w/w] in the dry biomass) and is thus used to produce astaxanthin on an industrial scale [4-7].

Astaxanthin production from *H. pluvialis* is almost exclusively performed with suspended cultivation (open or closed systems). Outdoor open systems can be large shallow ponds, reservoirs, circular ponds or raceways, and the algal suspension is stirred by paddle wheels under sunlight. The amount of astaxanthin can reach 1.5-3.0% of dry biomass. The advantage of this culture system is its simple construction and operation. However, limitations like low light efficiency, loss of culture medium due to evaporation, large space requirements, and high risk of contamination inhibiting the growth of the target alga can occur in these systems [8]. Closed culture systems can limit the risk of contamination, for example, photobioreactors (PBRs) in the form of flat panel, tubular or columnar bioreactors. Environmental conditions (pH, light intensity, temperature, and CO_2 concentration) are better controlled and water evaporation and CO_2 loss are minimized in closed PBRs. However, some significant disadvantages of closed PBRs are difficulty controlling the cumulative oxygen concentration and costs of setting up and maintaining them in comparison to open ponds [9-11].

*Corresponding author: Email: dungth@hufi.edu.vn

The immobilized algal culture model in a twin-layer porous substrate photobioreactor (TL-PSBR) has been shown to have several advantages over traditional suspension cultivation systems [12-15]. The TL-PSBR was originally placed vertically and had many advantages such as less water consumption, less restricted gas exchange surface, and easy separation of water from algal biomass when harvested. Additionally, the final cell density (standing crop) can be up to 100 times higher than in suspended cultivation [13, 14].

Recently in Vietnam, studies on culturing *H. pluvialis* in pilot-scale TL-PSBRs have been carried out with high capacity illuminations using a system of 10 high pressure sodium lamps (250 W/lamp) or 8 high-pressure sodium lamps (400 W/lamp). These illuminations stimulate the growth and accumulation of astaxanthin in *H. pluvialis* to achieve high yields [16, 17]. However, these lighting systems consume large amounts of energy that reduce production efficiency and emit considerable heat, which brings difficulty to the control of temperature in the culture environment [17].

Monochromatic illumination from light emitting diodes (LED) has been used in plant culture as well as in microalgae. The LEDs show many advantages such as high efficiency of converting electricity to light (less heat, more energy saving), creating light with a wavelength that matches the absorption spectrum of the pigments in microalgae, and a long service life [18-21]. However, the number of studies on the application of LEDs for the production of astaxanthin from *H. pluvialis* is limited, especially those in immobilized microalgal cultivation such as PSBR systems.

In this study, the effect of the light spectrum from LEDs (red LED, blue LED, and blue-red LED) on biomass growth and astaxanthin accumulation of *H. pluvialis* in angled TL-PSBR was evaluated. From there, the type of LED light most suitable for culturing *H. pluvialis* to produce astaxanthin in TL-PSBRs will be selected for further studies.

2. Materials and methods

2.1. Algal strain and suspended cultivation to prepare microalgae for fixation to biofilm

The microalga *H. pluvialis* CCAC 0125 (Central Collection of Algal Cultures; https://www.uni-due.de/biology/ccac/) was maintained and cultured in the Biotechnology Laboratory, Nguyen Tat Thanh University, Vietnam. Algae were suspended with BG-11H medium [22] in flasks of 500 ml (for 14 d), 2 l (14 d) and 10 l (20 d) at 23±2°C while illuminated by fluorescent lamps with a light intensity of 30-40 µmol photon $m^{-2}s^{-1}$ and a light/dark cycle of 14 h/10 h.

2.2. Experimental designs

The experiments were carried out on pilot-scale angled TL-PSBRs [16]. Each chamber was illuminated by a separate set of LEDs. Each LED luminaire was composed of 16 Bridgelux LED chips (Bridgelux, Inc., China) (Fig. 1). The LED chips selected for use were red LEDs, blue LEDs, and blue-red LEDs (1 blue:3 red). The LEDs were installed in a steel frame and automatically controlled to turn on and off by timers. The distance from the LEDs to the biofilms was adjusted to ensure the light intensity on the algal surface was 100-120 µmol photons $m^{-2}s^{-1}$. The light intensity was measured with a photometer Lutron LX-1108 (Taiwan).

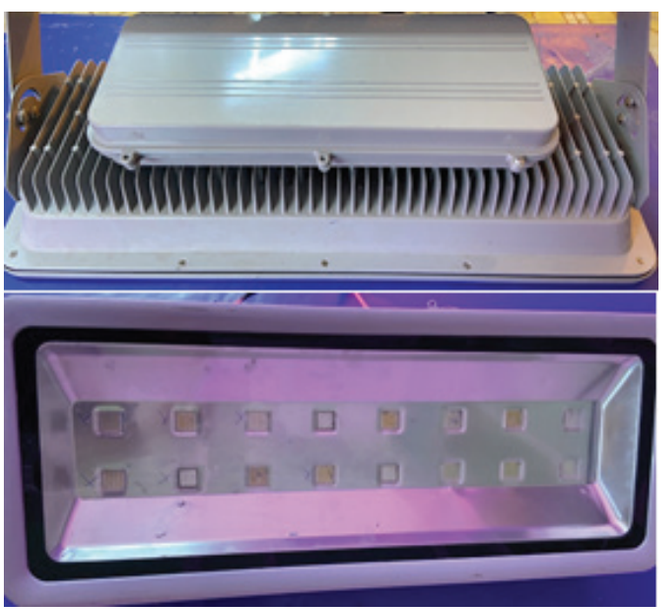

Fig. 1. The LED luminaires have 16 LED chips used in the experiments.

2.2.1. Effects of monochromatic light on growth and astaxanthin accumulation

Experiments were conducted with blue light (wavelength 430-480 nm), red light (wavelength 620-650 nm), simultaneous combinations of red and blue light with a ratio of 3 red:1 blue (Fig. 2). The intensity of the light was 100-120 µmol photon $m^{-2}s^{-1}$.

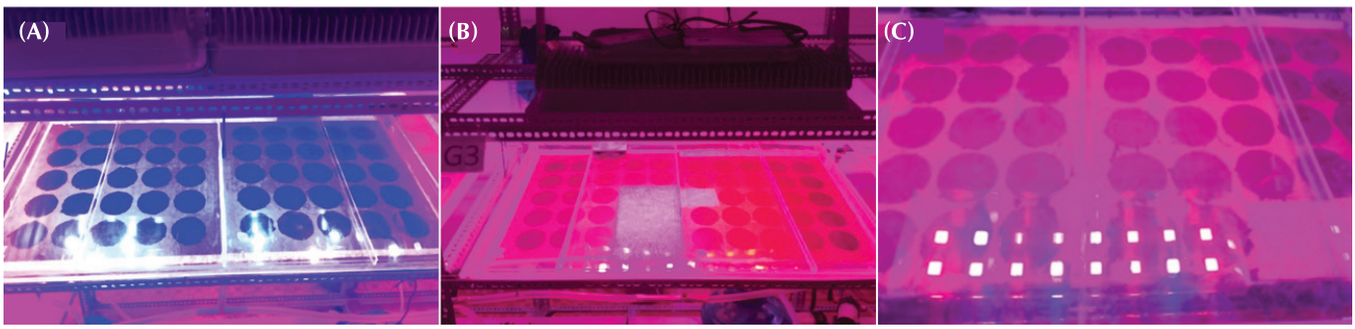

Fig. 2. The monochromatic LED luminaires used in the experiments: (A) blue light, (B) red light and (C) combinations of red with blue light.

2.2.2. Effects of combinations of red LED and blue-red LED illuminations over the culture period

With the aim of increasing algal biomass in the early days of cultivation (with red light) and stimulating astaxanthin accumulation in the last days of cultivation (with red and blue light), the combination formulas in this experiment were: (1) 10 d with blue and red LEDs, (2) 2 d with red LEDs followed by 8 d with blue and red LEDs, (3) 4 d with red LEDs followed by 6 d with blue and red LEDs, (4) 6 d with red LEDs followed by 4 d with blue and red LEDs, (5) 8 d with red LEDs followed by 2 d with blue and red LEDs, and finally (6) 10 d with red LEDs. The intensity of light was always maintained at 100-120 µmol photon $m^{-2}s^{-1}$.

2.3. Centrifugation to concentrate algae in suspension and immobilization of algae to biofilm in angled TL-PSBRs

2.3.1. Centrifugation to collect concentrated algae

Green stage microalgae were concentrated from suspended cultivation (cell density is about 5×10^5 cells ml^{-1}) by centrifugation at 800 *g* for 5 min with a ROTANTA 460 RC high volume centrifuge (Hettich, Germany). The concentrated algal suspension at the bottom of the centrifuge tube was collected and the dry biomass was determined. To determine the dry biomass, 1 ml of concentrated suspension was added to filter paper (dried and weighed, m_b (g)) and dried at 105°C for *2* h. Dry algae and paper were cooled in the desiccator for 30 min, weighed, and the drying process was repeated until the mass was constant (m_a (g)). The dry biomass of *H. pluvialis* in 1 ml of concentrated algae suspension was calculated as m_x (g/ml)=m_a-m_b and repeated 3 times to calculate the mean weight (m_A). Total algal biomass obtained was m(g)=$V_A\times m_A$, where V_A is the volume of concentrated algae solution. An initial algal density of 7.5 $g.m^{-2}$ was applied to establish the biofilm.

2.3.2. Algae immobilization on angled TL-PSBRs

In order to immobilize the microalgae to create a biofilm, the algal suspension was painted onto the substrate layers with a soft brush. The algae were painted in circles with a radius of 4 cm (each plot had an area of about 50.24 cm^2) (Fig. 3) to facilitate sampling at the time of 4, 6, 8, 10 d after immobilization. The volume of concentrated algal suspension needed to immobilize each plot was calculated as:

$$V\ (ml) = \frac{7.5}{m_A} \times 0.005024$$

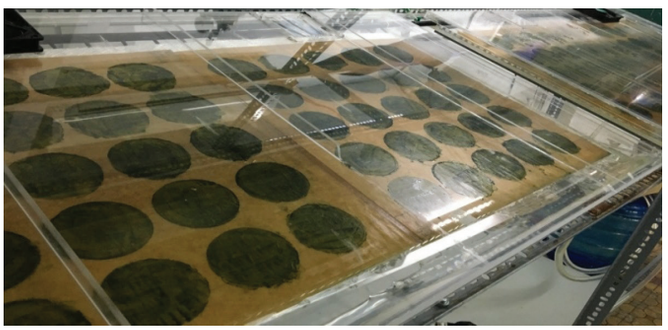

Fig. 3. Algae were immobilized into circular plots in angled TL-PSBRs.

2.4. Culture conditions after algal immobilization

Algal biofilms in TL-PSBRs were cultivated for 10 d. Nutrition for growth of microalgae was provided with 40 l of BG-11H medium from day 1 to day 7, the medium was replaced after 2 or 3 d. After 7 d of culture, the BG-11H medium was replaced with 40 l of N- and P-free medium (stress medium). The culture medium was aerated with 1% CO_2 (v/v) added to keep the pH between 6.5-8. Filtered water was added to the culture medium every day to compensate for evaporation, which ensured that the electrical conductivity of the medium was only about 1800-2000 µS/cm. The room temperature during experiments was maintained at 23-26°C.

2.5. The following variables were monitored

2.5.1. Environmental factors

Temperature, pH, and electrical conductivity of the BG-11H medium were measured daily during culture in the TL-PSBRs.

2.5.2. The growth of microalgae

Microalgae growth was monitored by the dry biomass of microalgae obtained per m^2 at 4, 6, 8, 10 d after inoculation of algae onto the substrate layer. The fresh algal biomass in a circular area with a radius of 4 cm was scraped with a plastic piece (3×5 cm) and placed in a 10 ml centrifuge tube (pre-weighed, m_1). The sample was then dried at 105°C for 2 h. The dry algae and tube were cooled in a desiccator for 30 min, weighed, and the process was repeated the dry weight was constant (m_2). The dry weight of microalgae per m^2 was calculated as $m(g.m^{-2})=(m_2-m_1)/0.005024$. Three biological samples (n=3) were collected for each treatment at each time for statistical analysis.

2.5.3. Astaxanthin content in the dry biomass (A%)

To determine the astaxanthin content in *H. pluvialis*, 0.001 g of dry biomass was weighed with a high precision balance and placed in a 2 ml centrifuge tube with cap. Then, 0.5 ml 90% acetone (v/v) was added and shaken vigorously with stainless steel balls (0.5 cm in diameter) for 3 h to allow all cells to rupture (as evaluated by microscopic examination) and release astaxanthin. Then, 1 ml of 90% acetone was added and the sample centrifuged at 6000 *g* for 30 sec. The supernatant was collected and 90% acetone was added to obtain a final volume of 2.0 ml. The procedure was performed in the dark or under weak diffused light to minimize the breakdown of astaxanthin.

The pigment extracts were measured for optical density at a wavelength of 530 nm [22]. The astaxanthin concentration was determined using a standard curve equation constructed with standard astaxanthin (Sigma-Aldrich) dissolved in acetone 90%. (Fig. 4). The standard curve equation is y=0.0577x+0.0131, where y is the OD value and x is the concentration of astaxanthin ($\mu g\ ml^{-1}$). Astaxanthin concentration was determined according to the equation (x) ($\mu g\ ml^{-1}$) = (OD_{530nm} (y)-0.0131)/0.0577.

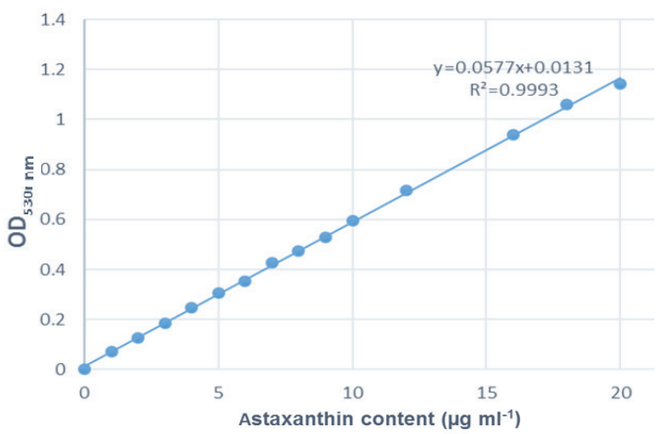

Fig. 4. Calibration curve for astaxanthin concentration.

2.5.4. Ratio of astaxanthin in dry biomass

(A%)=[x($\mu g\ ml^{-1}$)x2 (ml)x100%]/[0.001(g)x1,000,000]

Astaxanthin productivity ($mg.m^{-2}d^{-1}$)=[m(mg)xA%]/10

2.5.5. Morphological criteria of microalgae under optical microscope

Algal cell morphology was observed with an Olympus CX21 optical microscope (Japan).

2.6. Data analysis

Statistical analyses were made by using R (version 3.4.2). Tukey's HSD (honestly significant difference) test was use for analysis of difference in experiments. The data were analysed by using Microsoft Excel 365. The presented values were average value (Mean) ±SD (standard deviation) of three replicates (n=3).

3. Results

3.1. Effect of monochromatic light on growth and astaxanthin accumulation of H. pluvialis in TL-PSBRs

3.1.1. Results of monitoring environmental factors

Monitoring results show that the pH was maintained at 6.6-7.57 throughout the culture period, which was still within the optimal range for the growth of *H. pluvialis*. The temperature of the BG-11H medium was maintained at 21-24°C during experiments (Table 1).

Table 1. Results of monitoring the pH and temperature of the culture medium. The same nutrient medium was used for all treatments in an experiment.

Day	1	2	3	4	5	6	7	8	9	10
pH	6.60	6.96	6.89	7.06	7.21	7.31	7.57	7.40	7.20	7.28
Temperature (°C)	24.2	23.6	23.8	23.3	22.0	22.0	21.2	21.4	21.3	21.2

3.1.2. Effect of monochromatic light on the growth of H. pluvialis

The dry biomass for all three treatments increased during the first 6 d (initial dry biomass was 7.5 $g.m^{-2}$) under the same culture conditions and light intensity (range from 100-120 µmol photon m^{-2}/s) but different types of monochromatic LED (red, blue or the combination blue and red) (Fig. 5). There was almost no significant change in the dry biomass when illuminated by the blue LED from day 6 to day 10 ($p>0.05$, n=3).

For algae illuminated by the red LED, an increase in dry biomass was observed until day 6, which then decreased after day 8 (Fig. 5). The dry biomass of microalgae illuminated by the combination of blue and red LED, however, increased continuously over the culture period of 10 d and the growth was linear with a rate of 3.06 $g.m^{-2}d^{-1}$.

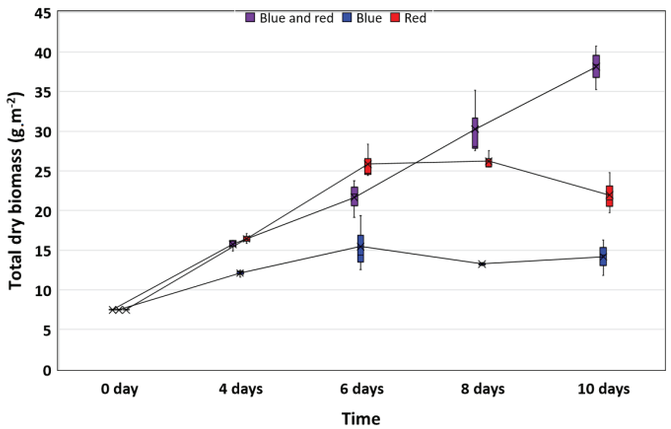

Fig. 5. Total dry biomass of *H. pluvialis* over time when illuminated with different types of monochromatic light.

After 10 d of culture, the total dry biomass of microalgae with the red and blue LEDs combination was the highest, in fact, much higher than the blue LED or red LED alone ($p<0.05$, n=3). The dry biomass yield was highest at around 3.06 $g.m^{-2}d^{-1}$ when illuminated with a combination of blue and red LEDs.

3.1.3. Effect of monochromatic light on astaxanthin accumulation of H. pluvialis

The percentage of astaxanthin accumulated in the dry biomass of *H. pluvialis* over the culture period is shown in Fig. 6. At day 4, the astaxanthin content in the biomass was highest with LEDs containing blue light (up to 1.7% in the blue and red LED lighting) and then decreased until day 8. This was likely because during the first days of cultivation, the algal cells in the thin biofilm were exposed to relatively high light intensities favouring astaxanthin accumulation. When the biofilm became thicker (i.e., >20 g dry weight/m^2, Fig. 7), the percentage of cells in the lower cell layers increased, which are shaded by the upper layers, thus lowering the overall astaxanthin content of the biofilm.

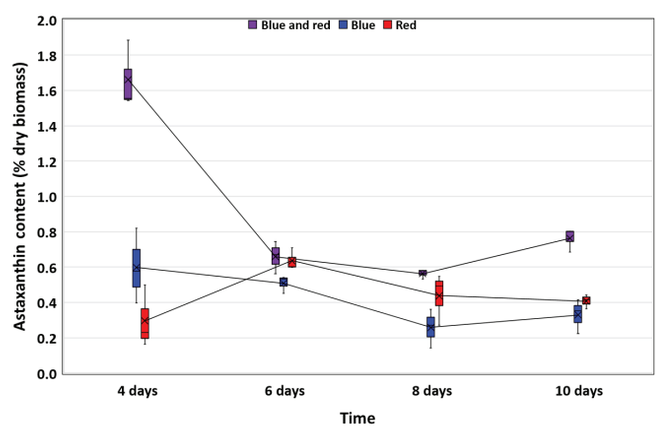

Fig. 6. Percentage of astaxanthin in dry biomass of *H. pluvialis* over time when illuminated with different types of monochromatic light.

Under red LED illumination, astaxanthin accumulation was highest at day 6 (Fig. 6) and then gradually decreased. After 10 days, the percentage of astaxanthin in the dry biomass was highest in the blue and red LED combination treatment (average 0.76%, Fig. 6), which is significantly higher than that of using only red or blue LEDs ($p<0.05$, n=3).

Therefore, the total dry biomass and the percentage of astaxanthin in the dry biomass after 10 days of culture were highest in the treatment with the combination of blue and red LEDs, thus the astaxanthin amount ($mg.m^{-2}$) was also highest in this treatment (Table 2) and the difference was statistically significant compared with the other two treatments ($p<0.05$, n=3).

Table 2. Astaxanthin standing crop per square meter ($mg.m^{-2}$) after 10 days when illuminated with different types of monochromatic light.

Blue and red LEDs	Blue LED	Red LED
291.99±44.73[a]	46.99±18.37[b]	89.75±15.85[c]

[a, b, c]: letters in the same row indicate statistically significant difference ($p<0.05$).

3.1.4. Effect of monochromatic light on biofilm surface and microscopic morphology of H. pluvialis

The macroscopic appearance of the algal biofilm surface over the culture period at different LED exposures is shown in Fig. 7. In general, the thickness of the biofilms increased

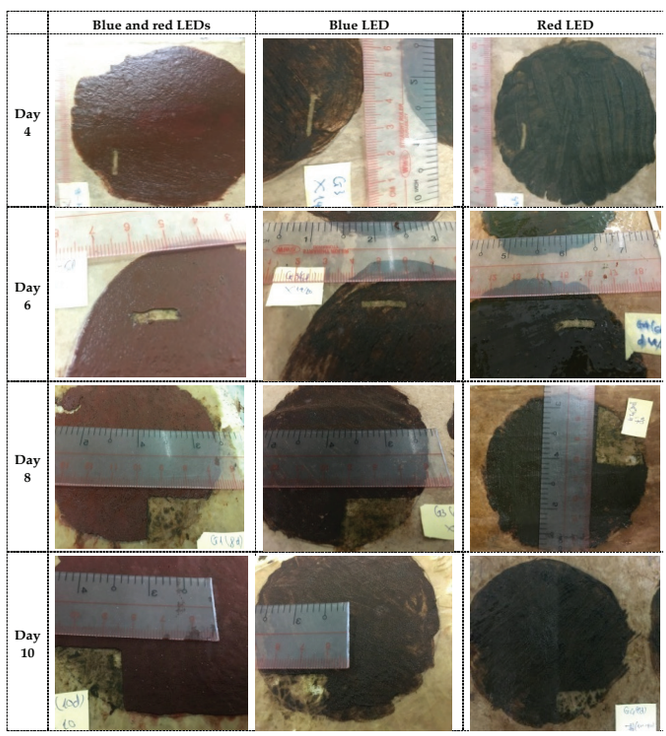

Fig. 7. Biofilm surface of *H. pluvialis* when illuminated with different types of monochromatic light.

over time in accordance with the determinations of the total dry biomass, of which the thickest was that of the blue and red LED treatment.

The biofilm surface colour was also markedly different between the 3 treatments. After 10 d, the algal surface under red LED was still green in accordance with the very low level astaxanthin content while the biofilm surface from the combined blue and red LED illumination had a red colour.

3.2. Effects of the combinations of red LED and blue-red LED illuminations over the culture period on H. pluvialis in TL-PSBRs

Previous studies have shown that red light stimulates the growth of *H. pluvialis* while blue light stimulates astaxanthin accumulation [23-25]. Therefore, this experiment investigated the effect of combining red LED illumination in the early days and blue-red LED illumination in the following days to investigate the ability to stimulate both algal growth and accumulation of astaxanthin.

3.2.1. Effects of the combinations of red LED and blue-red LED illuminations over the culture period on growth

Under the same culture conditions and light intensity (100-120 µmol photon m^{-2}/s), the total biomass of microalgae generally increased with culture time for all 6 treatments (initial dry biomass was 7.5 $g.m^{-2}$) (Fig. 8). The total dry biomass and biomass productivity were highest in the treatment with the the greatest number of days of blue-red LED (0 day of red +10 days of blue-red). After 10 days of culture, the total dry biomass in this treatment (0 day of red +10 days of blue-red) was the highest at 38.1 $g.m^{-2}$, which is much higher than the other treatments and the difference was statistically significant ($p<0.05$, $n=3$). The lowest total dry biomass occurred in treatment (5) (8 days with red LEDs +2 days with blue and red LEDs) and treatment (6) (10 days with red LEDs +0 day with blue and red LEDs), which was 25.1 and 26.28 $g.m^{-2}$, respectively. Thus, the combination of blue and red lighting from the beginning still showed the highest dry biomass increase after 10 d of culture.

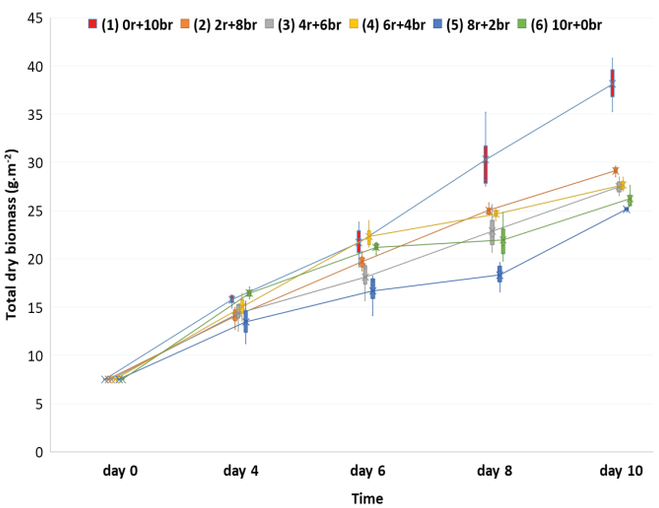

Fig. 8. Total dry biomass of *H. pluvialis* over time when illuminated by LEDs. r: red LED, br: blue-red LED.

3.2.2. *Effects of the combinations of red LED and blue-red LED illuminations over the culture period on the astaxanthin accumulation of H. pluvialis*

The percentage of astaxanthin accumulated in the dry algal biomass over the culture time is shown in Fig. 9. The percentage of astaxanthin in the dry biomass reached its highest value of 1.2% after 10 d in treatment (2:2 days red LEDs followed by 8-d blue-red LEDs) and the difference was statistically significant compared with treatments (1), (4), (5) and (6) ($p<0.05$, $n=3$).

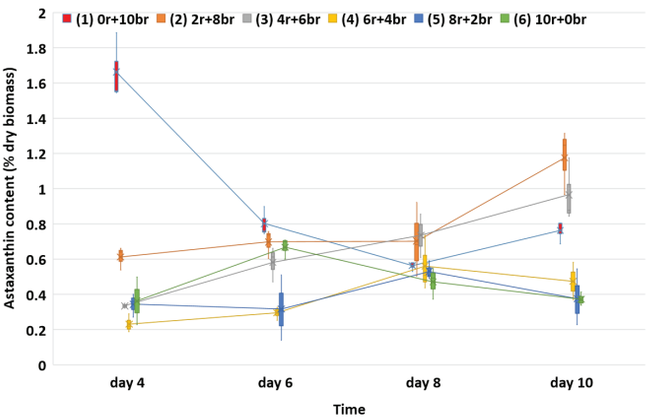

Fig. 9. Content of astaxanthin in the dry biomass of *H. pluvialis* over time when illuminated by LEDs. r: red LED, br: blue-red LED.

These results occurred because in treatments with more blue-red light, the microalgal layers in the biofilm were stimulated to accumulate more astaxanthin upon transition to the red phase. Conversely, the more days of red LED illumination, the greater the number of cells in the green phase in the biofilm layers, which results in a low percentage of astaxanthin in the dry biomass. On day 10, the astaxanthin contents in the dry biomass of the six treatments were distributed into two distinct groups: one with a higher astaxanthin content (1, 2, and 3) and one with a significantly lower percentage of astaxanthin in the biomass (4, 5, and 6) (Fig. 9). This suggests that a minimum of 6-d exposure to blue LEDs is required to attain higher astaxanthin values.

The results of determining the ratio of astaxanthin in dry biomass also showed that the percentage of astaxanthin when fully illuminated with blue-red LEDs reached the highest value at day 4 but then decreased gradually. In the early days of blue-red LED illumination, cells had

mainly accumulated astaxanthin and changed into the red phase but the dry biomass of microalgae did not increase as significantly. Thus, the content of astaxanthin in dry biomass would be high.

Table 3 summarizes the amount of astaxanthin ($mg.m^{-2}$) obtained in 6 treatments with combination LED illumination. The results show that treatments (1), (2), and (3) gave the highest astaxanthin productivity and the difference between these treatments was not statistically significant ($p>0.05$, n=3), but was much higher than the rest of the treatments ($p<0.05$, n=3).

Table 3. Astaxanthin standing crop per square meter ($mg.m^{-2}$) after 10 d.

(1) 0 r+10 br	(2) 2 r+8 br	(3) 4 r+6 br	(4) 6 r+4 br	(5) 8 r+2 br	(6) 10 r+0 br
292.0±44.7[a]	342.9±60.3[a]	264.1±42.1[a]	130.8±27.5[b]	94.6±40.1[c]	97.5±10.1[c]

[a, b, c]: letters in the same row indicate statistically significant difference. $p<0.05$, r: red LED, br: blue-red LED.

4. Discussion

H. pluvialis and other green algae do not use all wavelengths of visible light spectrum (wavelengths between 400 and 700 nm) for photosynthesis, but only absorb mainly blue, purple, and red light. Fluorescent lamps contain 60% of the light that is suitable for photosynthesis. When using a combination of red and blue light, this ratio was up to 84%, increasing the amount of red light, the amount of light received by the photosynthetic chain was increased by 91% [26]. Red light provides a higher number of photons than white light for enhanced algal growth [26]. The use of blue light stimulated more algae proliferation and astaxanthin accumulation [24-27].

The two types of monochromatic LED light used in this study were red light (wavelength about 620-650 nm) and blue light (wavelength about 430-480 nm). In two-step suspension cultivations, previous studies using monochromatic light from LEDs have shown an energy efficiency in stimulating growth and accumulation of astaxanthin in the green microalga *H. pluvialis*. In particular, the red LED light played a major role in stimulating growth to increase the dry biomass but did not stimulate astaxanthin accumulation, so the astaxanthin productivity was usually quite low and similar to the results of this study. Meanwhile, blue LED light stimulated the microalgae to accumulate astaxanthin but was not effective in increasing the total dry biomass [21, 24, 25]. Consequently, the combination of these two monochromatic light sources had the effect of both stimulating biomass growth and the accumulation of astaxanthin in suspension cultivations [18-20, 27].

The results of this study are consistent with previous research, although immobilized microalgal cultivation displays many differences compared to suspended cultivation. This study showed that LEDs have great potential for the cultivation of *H. pluvialis* in a TL-PSBR both by increasing biomass and stimulating astaxanthin accumulation. The simultaneous use of blue and red LEDs produced the highest dry biomass productivity that reached 4.74 $g.m^{-2}d^{-1}$ under the experimental conditions used in this study and a culture period of 10 d. Previous research on immobilized *H. pluvialis* cultivation showed dry biomass productivities between 3.7-11.25 $g.m^{-2}d^{-1}$ after 7 to 15 d using fluorescence lamps [28, 29] or high power and high pressure sodium lamps as the light source [17, 30]. Recently, the use of monochromatic LEDs to cultivate immobilized algae in biofilms has been applied on *Chlorella* [31]. Our initial research using LED light to grow *H. pluvialis* in pilot scale angled TL-PSBRs resulted in a relatively low astaxanthin yield. For the application of LEDs in angled TL-PSBRs, further studies need to be performed to increase productivity of astaxanthin accumulation by variation of environmental parameters and the use of other strains or mutants [7, 32, 33].

5. Conclusions

The combination of blue and red LEDs with an intensity of 100-120 µmol photons $m^{-2}s^{-1}$ in immobilized *H. pluvialis* cultivation resulted in the highest dry biomass and astaxanthin accumulation compared to using only blue or red LEDs.

CRediT author statement

Thanh-Tri Do, Bich-Huy Tran-Thi, Binh-Nguyen Ong: Conceptualisation, Methodology, Software, Resources, Writing - Review and Editing; Tuan-Loc Le, Thanh-Cong Nguyen, Quoc-Dang Quan, Thuong-Chi Le: Data curation, Software, Writing - Original draft preparation; Dai-Long Tran, Michael Melkonian, Hoang-Dung Tran: Supervision, Software, Validation.

COMPETING INTERESTS

The authors declare that there is no conflict of interest regarding the publication of this article.

REFERENCES

[1] Y.M. Naguib (2000), "Antioxidant activities of astaxanthin and related carotenoids", *J. Agric. Food Chem.*, **48(4)**, pp.1150-1154, DOI: 10.1021/jf991106k.

[2] M. Guerin, M.E. Huntley, M. Olaizola (2003), "Haematococcus astaxanthin: Applications for human health and nutrition", *Trends Biotechnol.*, **21(5)**, pp.210-216, DOI: 10.1016/S0167-7799(03)00078-7.

[3] I. Faraone, C. Sinisgalli, A. Ostuni, et al. (2020), "Astaxanthin anticancer effects are mediated through multiple molecular mechanisms: A systematic review", *Pharmacol. Res.*, **155**, DOI: 10.1016/j.phrs.2020.104689.

[4] G. Panis, J.R. Carreon (2016), "Commercial astaxanthin production derived by green alga *Haematococcus pluvialis*: A microalgae process model and a techno-economic assessment all through production line", *Algal Research*, **18**, pp.175-190, DOI: 10.1016/j.algal.2016.06.007.

[5] M.M. Shah, Y. Liang, J.J. Cheng, et al. (2016), "Astaxanthin-producing green microalga *Haematococcus pluvialis:* From single cell to high value commercial products", *Front. Plant. Sci.*, **7**, DOI: 10.3389/ fpls.2016.00531.

[6] K.S. Khoo, S.Y. Lee, C.W. Ooi, et al. (2019), "Recent advances in biorefinery of astaxanthin from *Haematococcus pluvialis*", *Bioresource Technol.*, **288**, DOI: 10.1016/j.biortech.2019.121606.

[7] X. Li, X. Wang, C. Duan, et al. (2020), "Biotechnological production of astaxanthin from the microalga *Haematococcus pluvialis*", *Biotechnol. Adv.*, **43**, DOI: 10.1016/j.biotechadv.2020.107602.

[8] M. Olaizola, M. Huntley (2003), "Recent advances in commercial production of astaxanthin from microalgae", *Recent Advances in Marine Biotechnology*, Science Publishers, **9**, pp.143-164.

[9] L. Brennan, P. Owende (2010), "Biofuels from microalgae - A review of technologies for production, processing, and extractions of biofuels and co-products", *Renewable and Sustainable Energy Reviews*, **14(2)**, pp.557-577, DOI: 10.1016/j.rser.2009.10.009.

[10] O. Giuseppe, S. Piero, M. Antonio (2014), "Advances in photobioreactors for intensive microalgal production: configurations, operating strategies and applications", *J. Chem. Technol. Biotechnol.*, **89(2)**, pp.178-195, DOI: 10.1002/jctb.4218.

[11] F.G. Acien, E.M. Grima, A. Reis, et al. (2017), "Photobioreactors for the production of microalgae, in microalgae-based biofuels and bioproducts", *Microalgae-Based Biofuels and Bioproducts*, Woodhead Publishing, pp.1-44, DOI: 10.1016/B978-0-08-101023-5.00001-7.

[12] R.M. Benstein, Z. Cebi, B. Podola, et al. (2014), "Immobilized growth of the peridinin-producing marine dinoflagellate *Symbiodinium* in a simple biofilm photobioreactor", *Mar. Biotechnol.*, **16(6)**, pp.621-628, DOI: 10.1007/s10126-014-9581-0.

[13] T. Li, B. Podola, M. Melkonian (2016), "Investigating dynamic processes in a porous substrate biofilm photobioreactor - A modeling approach", *Algal Research*, **13**, pp.30-40, DOI: 10.1016/j.algal.2015.11.006.

[14] T. Naumann, Z. Çebi, B. Podola, et al. (2013), "Growing microalgae as aquaculture feeds on twin-layers: A novel solid-state photobioreactor", *Journal of Applied Phycology*, **25(5)**, pp.1413-1420, DOI: 10.1007/s10811-012-9962-6.

[15] E.C.M. Nowack, B. Podola, M. Melkonian (2005), "The 96-well twin-layer system: a novel approach in the cultivation of microalgae", *Protist*, **156(2)**, pp.239-251, DOI: 10.1016/j.protis.2005.04.003.

[16] H.D. Tran, T.T. Do, T.L. Le, et al. (2019), "Cultivation of *Haematococcus pluvialis* for astaxanthin production on angled bench-scale and large-scale biofilm-based photobioreactors", *Vietnam Journal of Science, Technology and Engineering*, **61(3)**, pp.61-70, DOI: 10.31276/VJSTE.61(3).61-70.

[17] T.T. Do, B.N. Ong, M.L.N. Tran, et al. (2019), "Biomass and Astaxanthin productivities of *Haematococcus pluvialis* in an angled twin-layer porous substrate photobioreactor: Effect of inoculum density and storage time", *Biology (Basel)*, **8(3)**, DOI: 10.3390/biology8030068.

[18] T. Xi, D.G. Kim, S.W. Roh, et al. (2016), "Enhancement of astaxanthin production using *Haematococcus pluvialis* with novel LED wavelength shift strategy", *Appl. Microbiol. Biotechnol.*, **100(14)**, pp.6231-6238, DOI: 10.1007/s00253-016-7301-6.

[19] S. Pereira, A. Otero (2020), "*Haematococcus pluvialis* bioprocess optimization: Effect of light quality, temperature and irradiance on growth, pigment content and photosynthetic response", *Algal Research*, **51**, DOI: 10.1016/j.algal.2020.102027.

[20] S. Cui, X. Li, Y. Zhang, et al. (2020), "Design of automatic illumination culture system for *Haematococcus pluvialis* based on LED", *Proceedings of 2019 Chinese Intelligent Automation Conference*, **586**, pp.393-400, DOI: 10.1007/978-981-32-9050-1_45.

[21] R. Ma, S.R. Thomas-Hall, E.T. Chua, et al. (2018), "Blue light enhances astaxanthin biosynthesis metabolism and extraction efficiency in *Haematococcus pluvialis* by inducing haematocyst germination", *Algal Research*, **35**, pp.215-222, DOI: 10.1016/j.algal.2018.08.023.

[22] A.C. Kiperstok (2016), *Optimizing Immobilized Cultivation of Haematococcus Pluvialis for Astaxanthin Production*, PhD thesis, University of Cologne, 128pp.

[23] Y. Li, F. Miao, Y. Geng, et al. (2012), "Accurate quantification of astaxanthin from *Haematococcus crude* extract spectrophotometrically", *Chinese Journal of Oceanology and Limnology*, **30(4)**, pp.627-637, DOI: 10.1007/s00343-012-1217-5.

[24] Y.H. Ho, H.M. Leung, S.Y. Yuen, et al. (2018), "Maximization of astaxanthin production from green microalga *Haematococcus pluvialis* using internally-illuminated photobioreactor", *Advances in Bioscience and Bioengineering*, **6(2)**, pp.10-22, DOI: 10.11648/j.abb.20180602.11.

[25] K.T. Pham, T.C. Nguyen, T.H.Luong, et al. (2018), "Influence of inoculum size, CO_2 concentration and LEDs on the growth of green microalgae *Haematococcus pluvialis* flotow", *Vietnam Journal of Science and Technology*, **60(4)**, pp.59-65, DOI: 10.31276/VJSTE.60(4).59-65.

[26] J.H. Jou, C.C. Lin, T.H. Li, et al. (2015), "Plant growth absorption spectrum mimicking light sources", *Materials (Basel)*, **8(8)**, pp.5265-5275, DOI: 10.3390/ma8085240.

[27] H.L. Tran, K.H. Lee, C.H. Hong (2015), "Effects of LED irradiation on the growth and Astaxanthin production of *Haematococcus lacustris*", *Biosciences Biotechnology Research Asia*, **12(2)**, pp.1167-1173, DOI: 10.13005/bbra/1769.

[28] W. Zhang, J. Wang, J. Wang, et al. (2014), "Attached cultivation of *Haematococcus pluvialis* for astaxanthin production", *Bioresource Technol.*, **158**, pp.329-335, DOI: 10.1016/j.biortech.2014.02.044.

[29] M. Wan, D. Hou, Y. Li, et al. (2014), "The effective photoinduction of *Haematococcus pluvialis* for accumulating astaxanthin with attached cultivation", *Bioresource Technol.*, **163**, pp.26-32, DOI: 10.1016/j.biortech.2014.04.017.

[30] A.C. Kiperstok, P. Sebestyén, B. Podola, et al. (2017), "Biofilm cultivation of *Haematococcus pluvialis* enables a highly productive one-phase process for astaxanthin production using high light intensities", *Algal Research*, **21**, pp.213-222, DOI: 10.1016/j.algal.2016.10.025.

[31] H. Yuan, Y. Wang, Y. Xi, et al. (2020), "Light-emitting diode power conversion capability and CO_2 fixation rate of microalgae biofilm cultured under different light spectra", *Energies*, **13(7)**, DOI: 10.3390/en13071536.

[32] P.I. Gomez, P. Haro, P. Lagos, et al. (2016), "Intraspecific variability among Chilean strains of the astaxanthin-producing microalga *Haematococcus pluvialis* (Chlorophyta): An opportunity for its genetic improvement by simple selection", *Journal of Applied Phycology*, **28(4)**, pp.2115-2122, DOI: 10.1007/s10811-015-0777-0.

[33] N. Wang, B. Guan, Q. Kong, et al. (2016), "Enhancement of astaxanthin production from *Haematococcus pluvialis* mutants by three-stage mutagenesis breeding", *J. Biotechnol.*, **236**, pp.71-77, DOI: 10.1016/j.jbiotec.2016.08.009.

Analysis of production, consumption and environmental burden of plastic industry in Vietnam by input-output table

Thi Yen Ta[1, 2*], Thi Anh Tuyet Nguyen[1], Hoang Thi Hong Van[3]

[1]*School of Environmental Science and Technology, Hanoi University of Science and Technology, 1 Dai Co Viet Street, Bach Khoa Ward, Hai Ba Trung, Hanoi, Vietnam*

[2]*Faculty of Environmental, Hanoi University of Natural Resources and Environment, 41A Phu Dien Road, Phu Dien Ward, Bac Tu Liem District, Hanoi, Vietnam*

[3]*College of Urban Works Construction, Yen Thuong Street, Yen Thuong Ward, Gia Lam District, Hanoi, Vietnam*

Received 12 December 2020; revised 21 March 2021; accepted 5 April 2021

Abstract:

The plastic industry is an economic sector that plays an important role in promoting a circular economy in Vietnam. This study used the updated 2018 input-output (IO) table to identify and analyse the production and consumption of seven different plastics including: HDPE, PS, PE, PET, PVC, PP, and others. The study also integrated the IO model to unveil the environmental burden of these plastics through the plastic demand of 40 economic sectors and households. As a result, in 2018, the amount of direct solid waste from the plastic industry was 58,147 tons and the amount of indirect solid waste from the plastic industry to other economic sectors and the household sector were 214,258 tons and 6,262 tons, respectively. Agriculture and its services, food processing, fashion manufacturing, basic chemical production, electrical and electronic equipment production, and transport production embodied the highest indirect burdens due to their use of plastic products. This study contributes to MFA research and developing strategies for sustainable production and consumption of plastics and the management of plastic waste in Vietnam.

Keywords: **consumption, economic, IO table, plastic, production.**

Classification number: **5.3**

1. Introduction

The plastic industry is an important sector to the Vietnamese economy. Over the period of 2010-2015, the industry reached an annual growth rate of 16-18% in which there were items with growth rates of nearly 100% [1]. The plastic industry is one of ten industries that the Vietnamese government prioritizes for development planning due to its stable growth rate and reasonable export efficiency. Vietnam's consumption demand for plastic products has also increased significantly from 35 kg/person/year in 2007 to 108 kg/person/year in 2018 [2].

The plastic industry is divided into four main segments, which include packaging plastic (41%), construction plastic (24%), civil plastic (20%), and engineering plastics (15%) [1]. Plastic materials are categorized by two main types:

- (i) Thermoplastics (PE, HDPE, LDPE, LLDPE, PP, PS, PVC): these plastics can be recycled many times and the main outputs are plastic packaging, construction materials, consumer products, electrical/electronic equipment, and furniture/appliances, etc. Consumer demand for PE and PP are the most common, which accounts for about 48.5% of these plastics.

- (ii) Thermosetting plastic (epoxy, melamine, phenolic, polyurethane, and urea): these plastic materials are not recyclable. The plastics are mainly used in construction, furniture, transportation, adhesives, electronics, printing inks, and coatings [1].

The increase in plastic consumption leads to higher volumes of plastic waste and the accumulation of plastic across all economic sectors. Internationally, many studies

*Corresponding author: Email: ttyen@hunre.edu.vn.

have been conducted such as a material flow analysis of plastic waste to promote a circular economy [3], the role of stakeholders in the plastic industry value chain in implementing solutions to achieve a transition to a circular economy in the European plastic packaging industry [4], the analysis of plastic tax benefits and disadvantages within a circular economy [5], proposing plastic waste management scenarios [6], assessment and circularity potential of recovery systems for household plastic waste [7], and the characterization and evaluation of plastic recyclability [8]. In Vietnam, there have been several studies on the effects of plastic production and consumption on the environment, the impact of plastic recycling in craft villages, green-house gas emissions from plastic production, the environmental burden of PET plastic, effects of plastic waste on the sea environment, and the reality of plastic waste in Vietnam [2, 9-13]. These studies mainly focus on analysis of the green-house gas (GHG) emissions of plastic recycling on the household scale of craft villages or the analysis of the GHG burden on economic sectors by the plastic industry. To the best of our knowledge, there have been no studies on analysing the burdens of plastic waste from economic sectors and households. Therefore, it is essential to unveil these environmental burdens through plastic demand and consumption. This study is expected to be a valuable reference for policymakers in proposing a resource-efficient plastic waste management solution and specifically targets the management of plastic materials and waste by consumers.

There are different approaches to the investigation of material flow. One approach is material flow analysis (MFA) [3, 14] and another is using an IO table [15, 16]. An IO table is a mathematical economic model simulating the relationship between the manufacturing industries and the products of the economy. A number of studies have used the IO model to analyse the relationship of emissions and/or waste between economic sectors [17, 18].

This study used the IO model to determine the current state of production and consumption of plastics in Vietnam's economic sectors and households combined with LCI techniques to determine the environmental burdens of the plastic industry through demand from other economic sectors and households.

2. Methods

The IO model was proposed by W. Leontief and is useful in the analysis of economic activity [15]. The model can be described by

$$(x_1)_i = \sum_{j=1}^{N} (z_{11})_{ij} (x_1)_j + (y_1)_i \qquad (i = 1, 2\ldots, N) \quad (1)$$

where $(x_1)_i$ is the total output of goods i, $(z_{11})_{ij}$ is the technical coefficient that represents the intermediate input of goods j required to produce a unit of goods i, and $(y_1)_i$ is the final demand of goods i.

Based on the 2018 IO table updated by RAS method [19, 20], this research identified current plastic productions, the plastic consumption of economic sectors (ICONS), and the plastic consumption of households (DCONS). Through an inventory of the life cycle of plastic products, this research determined the coefficient of the plastic waste generation of production activities (WF_i). By integrating the life cycle inventory (LCI) and the 2018 IO table, this study estimated the environmental burden from consumption by households (W-DCONS) and consumption by economic sectors (W-ICONS). However, this study did not consider imported and domestically produced plastic (DoProd) of virgin plastic and the amount of plastic waste recycled and disposed of after consumption.

Figure 1 shows the connection flow from the production and consumption of plastic products. Plastic consumption is determined by the formula:

$$CONS = DCONS + ICONS + IM \quad (2)$$

To obtain the consumption demand of plastic products (DCONS and ICONS) of economic sectors and households, the plastic industry's 2018 IO table is converted to physical units.

This study conducted surveys at factories that manufacture plastic products and determined the coefficient of plastic waste emissions at these factories (WF_i). Based on the consumption demand of plastic products by economic sectors and households, the study estimated the environmental burdens using the following formula:

$$W\text{-}DCONS = DCONS * WF_i \quad (3)$$

$$W\text{-}ICONS = ICONS * WF_i \quad (4)$$

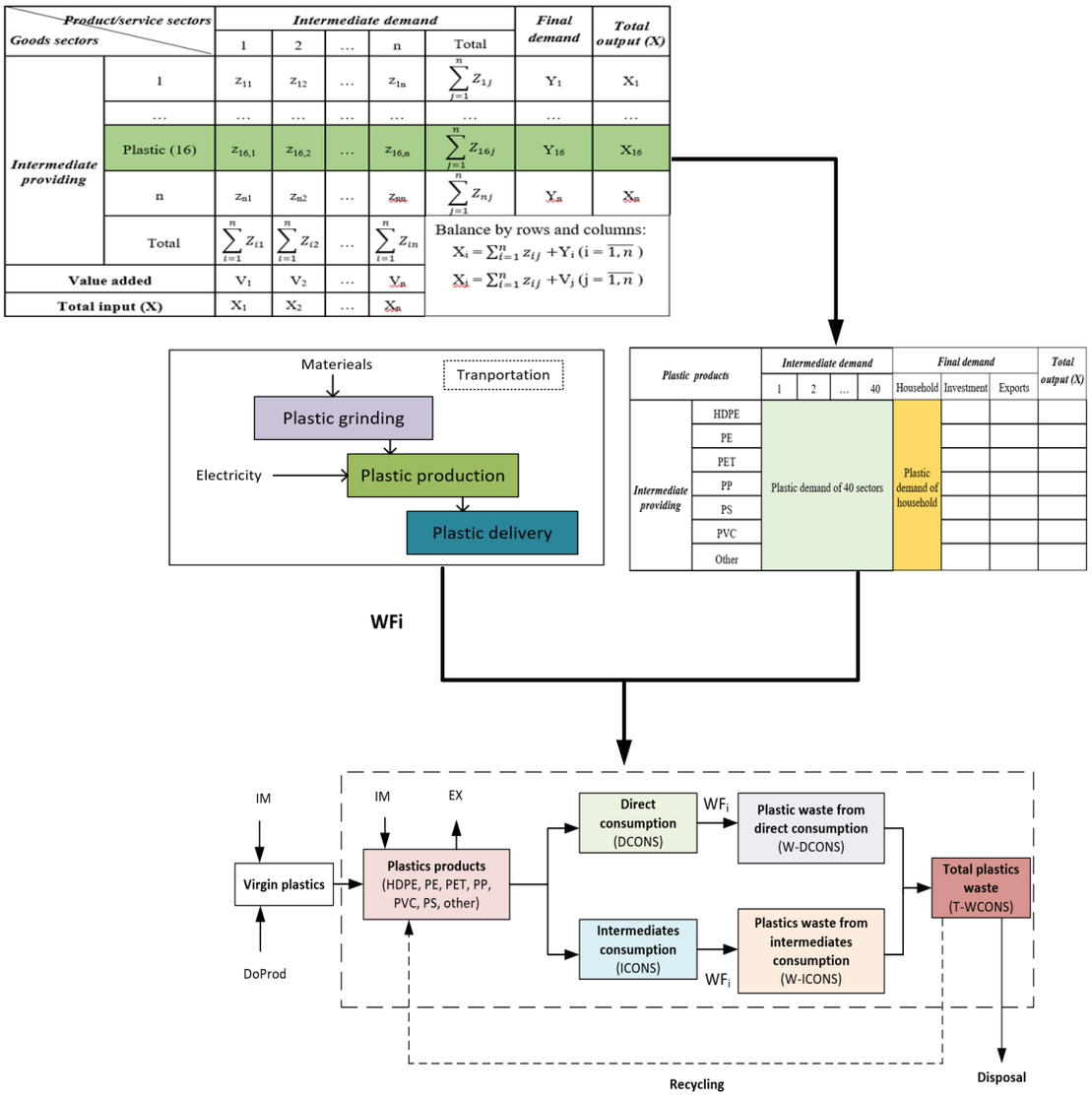

Fig. 1. Research method.

Total plastic waste emissions were determined based on the following formula:

$$T\text{-}WCONS = W\text{-}DCONS + W\text{-}ICONS \quad (5)$$

Based on statistics from the General Statistics Office, this study identified the consumption structure of plastics and classified plastic products into 7 main plastic groups (i = HDPE, PE, PET, PP, PVC, PS, other).

Plastic wastes can be categorized into two types: (1) plastic waste from final consumption (post-consumer plastic waste) and (2) industrial plastic waste consisting of plastic losses from the production such as plastic packaging waste arising from packing, processing, and assembly of plastic products. This study identified plastic as the second type to determine the coefficient of plastic waste generation in the factories. A survey of 10 factories and 10 households producing plastic products in two plastic craft villages (Minh Khai, Hung Yen Province and Trieu Khuc - craft village of Hanoi) were conducted. As a result, the plastic waste coefficient (WF_i) of the 7 types of plastic HDPE, PE, PET, PP, PVC, PS, and other were 0.03291; 0.03480; 0.02594; 0.04303; 0.02911; 0.02848; and 0.03670 tons/ton of plastic, respectively.

3. Results and discussion

3.1. Plastic production and consumption

The plastic industry has four main segments: packaging plastic, household plastic, construction plastic, and engineering plastic. Fig. 2 shows that there have been structural changes to these segments over different periods. In the first stage, household plastic accounted for nearly 60% of the production value, then gradually decreased over time because household plastic was imported more to Vietnam.

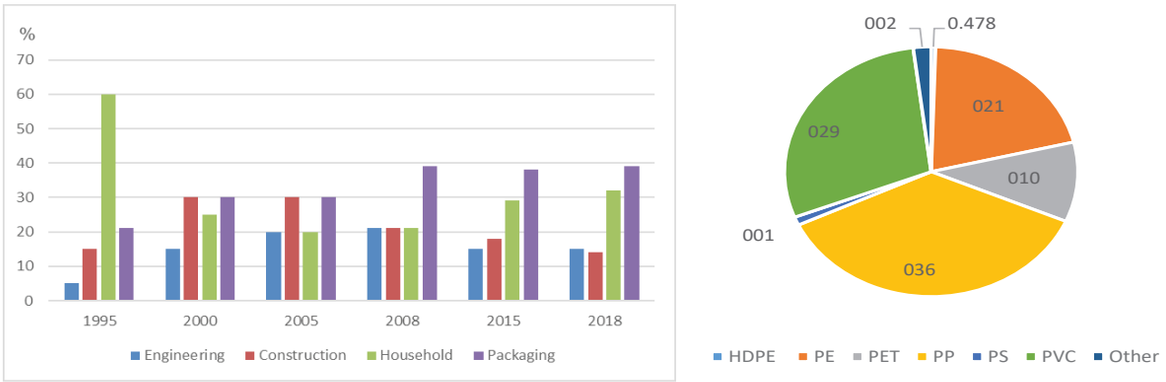

(A) (B)

Fig. 2. Structure of plastic industry in Vietnam. (A) Structure of plastic industry by year; **(B)** Structure of plastics consumption in 2018.

Since 2008, the plastic packaging industry increased to nearly 40% and remained stable until 2018. This could be a potential plastic segment because the consumer demand in households and industries for this plastic is very large. In addition, this segment had one of the largest export volumes of plastic over all segments of the plastic industry.

This study uses an updated 2018 IO table to identify the current state of production and consumption in the plastics industry and estimated that the output of plastic in 2018 was 10.2 million tons, of which the amount of plastic for intermediate consumption for other economic sectors was 7.7 million tons, while that for household consumption was 178.9 thousand tons, for exports was 3.8 million tons, and imports were 1.5 million tons (Fig. 3). On average, consumer demand for PP, PE, and PVC plastic products was higher than that of other plastics (Fig. 2B and Fig. 3). Due to their many preeminent features, these thermoplastics have the ability to produce a wide range of plastic products for industries and household consumption. In 2018, the output of exported plastic products was twice larger than that of imported plastic products. Exported plastic products, which were mainly plastic packaging products, accounted for 40% (PE, PP, and PET).

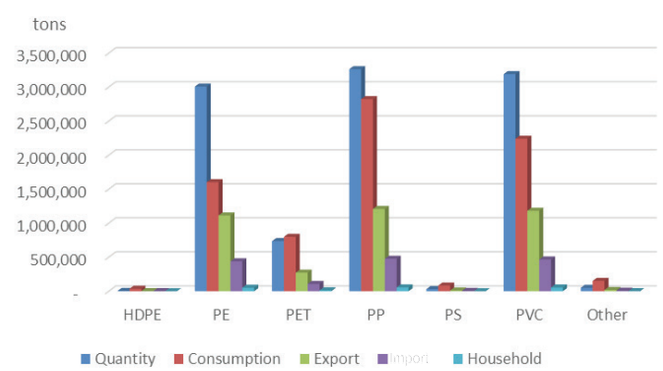

Fig. 3. Plastic quantity and consumption in Vietnam in 2018.

3.2. Plastic products demand of the economic sectors in 2018

The plastic consumption demand (PDs) of 40 economic sectors of Vietnam in 2018 is shown in Fig. 4, in which the 2018 IO table was converted to physical units. The total plastic demand of the economy in 2018 was 7,739 thousand tons in which 7 plastic types were included, namely, PP (2,823 thousand tons), PVC (2,242 thousand tons), PE (1,602 thousand tons), PET (799 thousand tons), HDPE (36.9 thousand tons), PS (83.5 thousand tons), and other (152.05 thousand tons).

Plastic products supply most of the economic sectors and there is a difference between the plastic consumption of each economic sector. PP and PE plastics provide for many economic industries like *Agriculture and its services* (S1), *Fashion manufacturing* (S9), *Paper and its services* (S11), *Basic chemicals* (S15), and *Trading* (S31). PP and PE are two preeminent materials that produce many products. In contrast, HDPE, PVC, PET, and other plastics only supply to some specific industries. Specifically, HDPE plastic has good bearing capacity, moisture resistance, and heat resistance so it is used for plastic packaging capable of holding dangerous materials, which are mainly supplied to the *Gasoline and lubricants* (S13), *Basic chemicals* (S15), and *building materials* (S17) sectors. PVC plastic is mainly used for manufacturing *building materials* (S17), *Electronic, electronic equipment* (S19), and for *Civil construction* (S29). PET plastic has low release ability and produces thin and light products in all three types of blow, suction, and molding technologies so it is often used to manufacture *food packaging for the food industry* (S8), and packaging of *Electronic, electronic equipment* (S19). A part of PET plastic is used for fabric production in the *Fashion manufacturing* (S9) sector. Other plastics are thermoplastics that are capable of producing some typical plastic products in the engineering industry so they are widely used for the engineering groups of *building materials* (S17), *Equipment and tool production* (S20), and *Transport production* (S21). The consumption demand for plastic in the *trade and service industries* sectors (S30-S40) are mainly plastic packaging products and household plastics produced from PE and PP plastic.

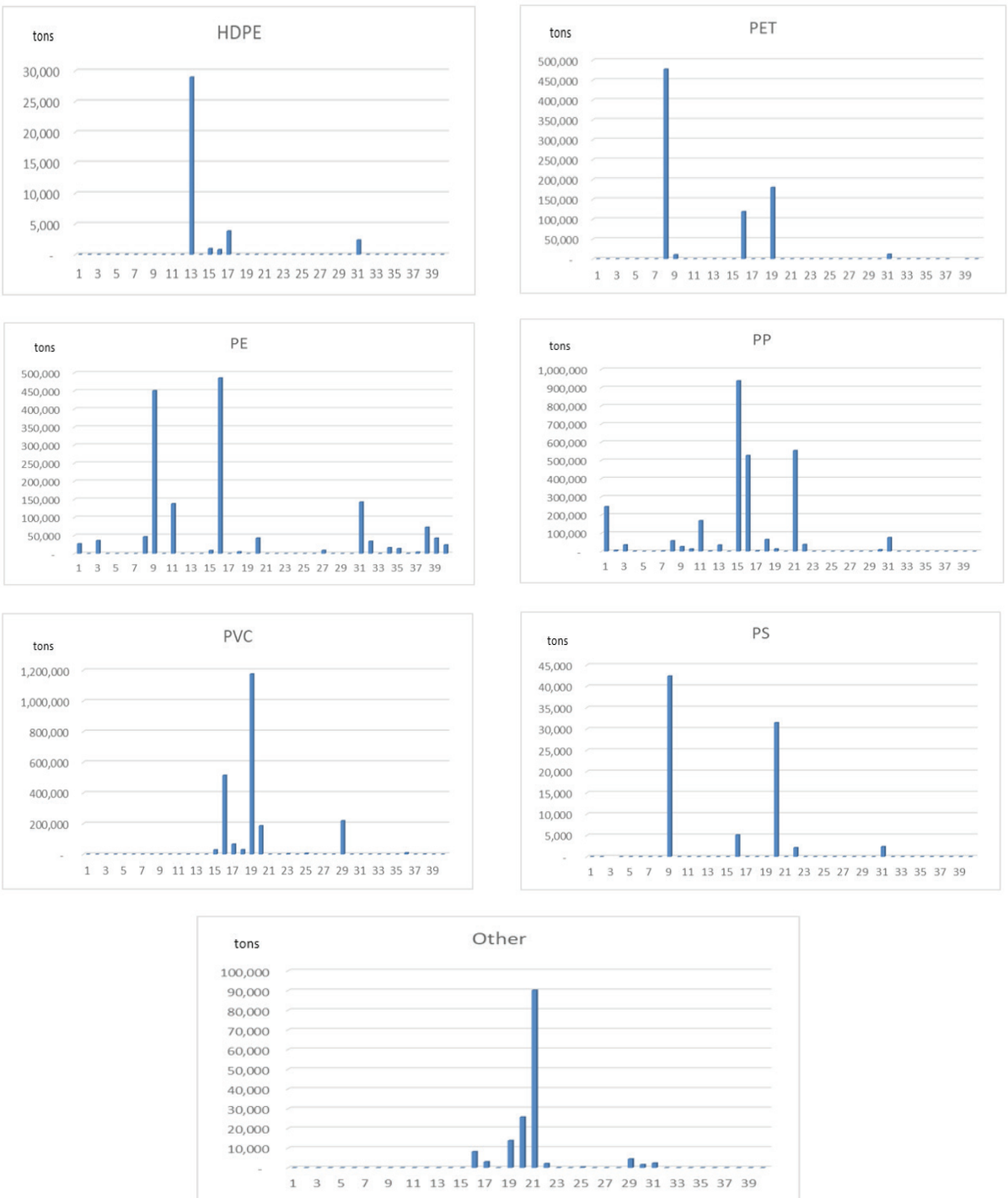

Fig. 4. Plastics demand of 40 sectors in 2018 (tons).
S1: agriculture and its services; S2: forestry and its services; S3: fishery and aquaculture; S4: hard coal and lignite; S5: crude oil; S6: natural gas or LPG; S7: extractive; S8: food processing; S9: fashion manufacturing; S10: wood products; S11: paper and its service; S12: coke; S13: gasoline and lubricants; S14: other oil mining; S15: basic chemicals; S16: plastics; S17: building materials; S18: metal production; S19: electronic, electronic equipment; S20: equipment and tool production; S21: transport production; S22: medical equipment; S23: electricity and production and delivery; S24: gas and services; S25: water; S26: sewerage and wastewater treatment services; S27: solid waste collection, treatment and disposal services; S28: other waste treatment; S29: civil construction; S30: repairing services; S31: trading; S32: transport; S33: post services; S34: hotels and catering; S35: editing and communication services; S36: financial intermediation and insurance services; S37: real estate activities; S38: other business activities; S39: administrative and education; S40: other community, social, and personal services.

3.3. Environmental burdens from plastic production and uses

Based on the coefficient of solid waste generated from the production of plastic products, this study integrated the 2018 IO table to determine the amount of solid waste in the plastic industry contributing to other economic sectors. It was estimated that the total solid waste emissions of the plastic industry were 278,667 tons of which the amount of direct solid waste from the plastic industry was 58,147 tons (Fig. 5), the indirect emissions of the plastic industry from other economic sectors were 214,258 tons (Fig. 6), and from household consumption was 6,262 tons (Fig. 7).

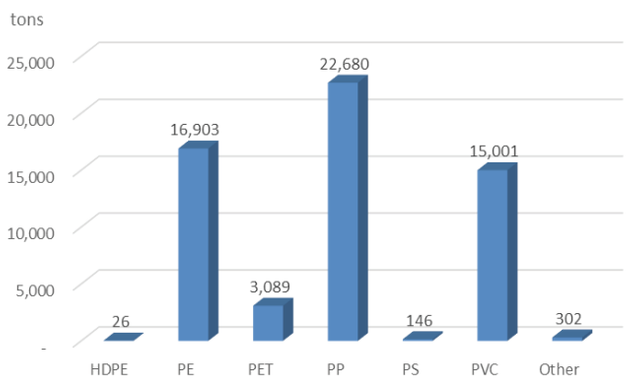

Fig. 5. Waste from plastic sector in 2018.

PP, PE, and PVC plastics were three types of plastics with a higher emission contribution to the plastics industry than the rest of the plastics.

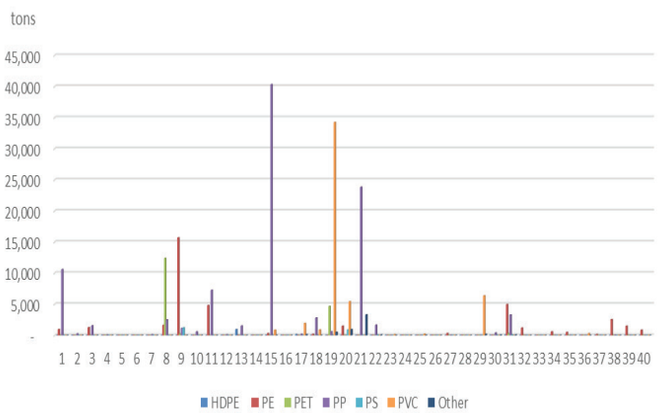

Fig. 6. Indirect plastic waste from sectors in 2018.

The emission contribution of PP was the highest among the plastics (98,786 tons). PP is a group of plastics with high consumption demand. The production of this type of plastic can be easily burned, so the wastage rate of this plastic is higher than that of other types. However, this type of plastic is easy to recover, reuse, and recycle and the recycling process does not require high quality plastic input waste. Thus, the environmental burden of this plastic is negligible.

PVC and PE are two types of plastic with large emissions at 50,268 tons and PE 38,862 tons, respectively. However, PVC plastic is mostly supplied to industries for direct use such as construction while PE plastic often produces packaging products such as plastic bags, bottles, jars, and disposable cups. These types of plastic products are difficult to be collected for recycling, so the impacts of PE plastics are of great concern.

In general, the contribution of emissions from the plastic industry mainly comes from economic groups with high demand for plastic products such as *basic chemical industry* (S15), *food processing* (S8), *Fashion manufacturing* (S9), *Electronic, electronic equipment* (S19), and *Transport production* (S21).

This study also estimated indirect emissions due to plastic use from households (Fig. 7). Plastic products directly consumed by households are packaging (plastic bags, bottles, jars, box trays, etc.) and household plastic (buckets, dishes, cups, water pipes, etc.). Therefore, PE, PP, PET, and PVC resins are the groups of plastics that contribute more indirectly than other plastics in household consumption. Moreover, the statistics of plastic products consumed by household groups are often more difficult to collect because most of them are disposable plastic packaging and the collection efficiency depends greatly on the environmental consciousness of the user. Therefore, to improve the efficiency of collection and recycling, it is necessary to pay attention to this consumer group.

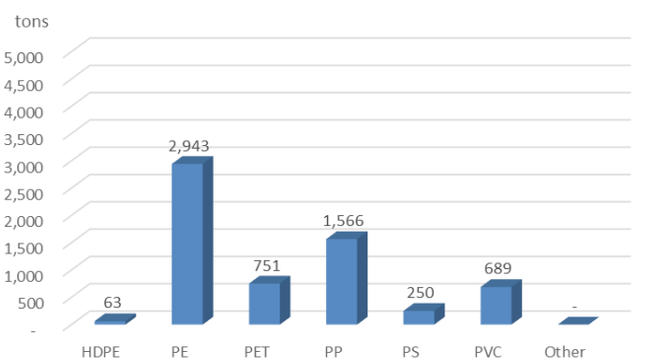

Fig. 7. Waste plastic of household consumption in 2018.

The results of this study are the basis for the development of the plastic industry and the basis for developing a strategy of collection, reuse, and recycling of various plastic products to improve plastic waste management and treatment efficiency. Indeed, while the plastic industry contributes to most economic sectors, the use of plastic products is creating great pressure on the environment and the government is in a place to encourage the reduction of plastic generation. Therefore, to ensure the stable development of the plastic industry in the coming time, plastic manufacturers need to gradually change production materials to increase product life cycle (for example, converting products plastic bags to non-woven PET bags) or the manufacture of biodegradable plastic products. The government is expected to support enterprises in converting production technology from conventional plastic to biodegradable plastic materials.

Different plastic types have different contributions to economic industries and each plastic has different functions and consumption characteristics. Therefore, it is necessary to have policies for the collection and management of plastic waste for each plastic type to ensure that it does not affect the development of the plastic industry. For single-use plastic groups that are often difficult to collect for recycling, it is necessary to have policies that encourage consumers to change their usage habits. On the side of the economic sectors that use this packaging group, it is necessary to have changes in product design to limit the use of single-use plastic packaging or to improve or develop longer lifecycle packaging.

Plastic supply to economic industries accounts for a larger proportion than its supply to households, but the collection of plastic products from economic sectors is easier because it is tied to inter-legal regulations related to waste management of businesses. Meanwhile, plastic generated from households is more difficult to manage because it depends much on the habits and awareness of consumers. Therefore, policies on plastic waste management need to focus their impact on consumers (households) instead of economic sectors as well as offer better collection measures for the household consumption of plastic.

4. Conclusions

Using the IO method, the flows of different types of plastics between production and consumption sectors in 2018 and their environmental burdens were identified in this study. PP, PVC, and PE were the three types of plastic with the largest plastic waste. PP and PE plastics contributed mainly to agriculture services, fashion manufacturing, paper production, basic chemical, and trading sectors. PET is the major contributor to solid waste generation in food processing, fashion manufacturing, and electronic equipment sectors. PVC contributes to building materials, electronic equipment, and civil construction sectors. The burdens of production to the environment from household consumption mainly came from four plastic types including PE (2,943 tons), PP (1,566 tons), PVC (689 tons), and PET (751 tons). It is necessary to develop policies to manage plastic waste for each plastic type to ensure that it does not affect the development of the plastic industry and promote sustainable consumption towards a circular economy.

CRediT author statement

Thi Yen Ta: Conceptualisation, Methodology, Software, Resources, Writing - Review and Editing; Thi Anh Tuyet Nguyen: Data curation, Software, Writing - Original draft preparation; Hoang Thi Hong Van: Supervision, Software, Validation.

COMPETING INTERESTS

The authors declare that there are no conflicts of interest regarding the publication of this paper.

REFERENCES

[1] Vietnam Plastic Association (2018), *Plastic Industry Report* (Vietnamese).

[2] T.T. Yen, N.T.A. Tuyet (2020), "Using IO table in analysing the environmental burden of PET plastic packaging industry in Vietnam", *VNU Journal of Science: Earth and Environmental Sciences*, **36(2)**, pp.90-98, DOI: 10.25073/2588-1094/vnuees.4570 (Vietnamese).

[3] S. Millette, E. Williams, C.E. Hull (2019), "Materials flow analysis in support of circular economy development: plastics in Trinidad and Tobago", *Resources, Conservation and Recycling*, **150**, DOI: 10.1016/j.resconrec.2019.104436.

[4] E. Foschi, A. Bonoli (2019), "The commitment of packaging industry in the framework of the European strategy for plastics in a circular economy", *Administrative Sciences*, **9(1)**, DOI: 10.3390/admsci9010018.

[5] T. Walker, D. Gramlich, A.D. Bergeron (2020), "The case for a plastic tax: A review of its benefits and disadvantages within a circular economy", *Sustainability*, **4**, pp.185-211, DOI: 10.1108/S2514-175920200000004010.

[6] C. Bureecam, T. Chaisomphob, P.Y. Sungsomboon (2018), "Material flows analysis of plastic in Thailand", *Thermal Science*, **22(6A)**, pp.2379-2388, DOI: 10.2298/TSCI160525005B.

[7] M.K. Eriksen, A. Damgaard, A. Boldrin, et al. (2019), "Quality assessment and circularity potential of recovery systems for household plastic waste", *Journal of Industrial Ecology*, **23(1)**, pp.156-168, DOI: 10.1111/jiec.12822.

[8] G. Faraca, T. Astrup (2019), "Plastic waste from recycling centres: Characterisation and evaluation of plastic recyclability", *Waste Management*, **95**, pp.388-398, DOI: 10.1016/j.wasman.2019.06.038

[9] D.K. Chi (2018), "White pollution problem", *Journal of Science and Technology of Vietnam*, **7**, pp.40-42 (Vietnamese).

[10] N.T.K. Thai, L.T.M. Huong (2011), "Evaluate the current situation of solid waste management in scrap recycling craft villages and propose management solutions", *Journal of Construction Science and Technology*, **9**, pp.114-120 (in Vietnamese).

[11] T.T. Yen, N.T.A. Tuyet (2018), "Life cycle inventory for PET packages in the intergration with IO table of Vietnam", *Vietnam Journal of Science and Technology*, **56(2C)**, pp.111-117, DOI: 10.15625/2525-2518/56/2C/13037.

[12] N.T. Danh, H.T. Hoi (2019), "Effects of plastic waste to sea environment in Vietnam", *IOP Conference Series: Earth and Environmental Science*, **351**, DOI: 10.1088/1755-1315/351/1/012023.

[13] M.Q. Chau, A.T. Hoang, T.T. Truong, et al. (2020), "Endless story about the alarming reality of plastic waste in Vietnam", *Energy Sources - Part A: Recovery, Utilization, and Environmental Effects*, pp.1-9, DOI: 10.1080/15567036.2020.1802535.

[14] D. Kawecki, L. Goldberg, B. Nowack (2020), "Material flow analysis of plastic in organic waste in Switzerland", *Soil Use and Management*, **37(2)**, DOI: 10.1111/sum.12634.

[15] S. Nakamura, Y. Kondo (2009), *Waste Input-output Analysis: Concepts and Application to Industrial Ecology*, Springer, DOI: 10.1007/978-1-4020-9902-1.

[16] R.J. Myers, T. Fishman, B.K. Reck, et al. (2019), "Unified materials information system (UMIS): An integrated material stocks and flows data structure", *Journal of Industrial Ecology*, **23(1)**, pp.222-240, DOI: 10.1111/jiec.12730.

[17] C. Guo, J. Xu, L. Yang, et al. (2019), "Life cycle evaluation of greenhouse gas emissions of a highway tunnel: A case study in China", *Journal of Cleaner Production*, **211**, pp.972-980, DOI: 10.1016/j.jclepro.2018.11.249.

[18] K. Nakajima, K. Nansai, K. Matsubae, et al. (2011), "Identifying the substance flow of metals embedded in Japanese international trade by use of waste input-output material flow analysis (WIO-MFA) model", *ISIJ International*, **51(11)**, pp.1934-1939, DOI: 10.2355/isijinternational.51.1934.

[19] R.E. Miller, P.D. Blair (2009), *Input-output Analysis Foundations and Extensions*, Cambridge University Press, 784pp.

[20] B. Trinh, N.V. Phong (2013), "A short note on RAS method", *Advances in Management and Applied Economics*, **3(4)**, pp.133-137.

Vietnam Journal of Science, Technology and Engineering (VJSTE): Manuscript Template

General Instructions on using this template and submitting a manuscript to VJSTE: Thank you for preparing a manuscript for submission to VJSTE. Using this template, or following the guidelines below, will help us in processing your article.

The structure of different types of articles may vary according to the type of study, and the content of the article.

The following are the detailed main components of the original research and review articles submitted to the journal.

Original research

The original research should have three following parts:

Preliminary section: It includes title, list of all contributing authors with their institutional affiliation, and abstract (160-250 words) with at least 3 keywords.

Title: How to format a science article (replace with your real title)

Author(s): List the author name(s) separated by commas. Use superscript numbers to link affiliations, and symbols *†‡ for author notes. For example, Y. Obsie[1*], S.A. Adem[1, 2]

**Corresponding author(s):* Include the email addresses or telephone numbers of the corresponding author(s). Please use the asterisk (*) symbol for the corresponding author information. This information is at the bottom of the manuscript's first page.

Author's affiliation addresses:

[1]Affiliations should be preceded by superscript numbers corresponding to the author list

[2]For any institutions, please provide the institution name, street, district, city, country

Received ; revised ; accepted

Abstract:
Start your abstract here…
Keywords: **keyword 1, keyword 2, keyword 3…**
Classification number(s): **1.1, 3.4, 5.3, etc.**

Abstract: The abstract should range between 160 and 250 words and be structured in a single paragraph following keywords in a separate line. The abstract should represent the main part of the research manuscript. It should reflect a brief and comprehensive background following the aim of the study (main questions to be addressed), methods used for investigating the problem, a summary of significant findings, main conclusions, and implications of the results.

Keywords: They should come immediately after the abstract and contain 3-7 specific and relevant keywords. They should reflect the research study and the relevant field of research.

Classification numbers: Depend on the Journal's Classification Scheme.

Author(s) are encouraged to write a "Highlights" that summarises the most exciting, interesting points from your manuscript.

Manuscript section: It is the main body of the scientific manuscript including: 1) Introduction; 2) Material(s) and method(s); 3) Results and discussion (separation of these two sections is acceptable); 4) Conclusions; 5) Recommendations/Suggestions/ Implications/Study limitations...(if any). These sections may slightly vary depending on the type of research approach and design used in the research. Each section should be numbered.

All of the Figures, Tables, and Equations should be cited in numerical order.

Figures

Fig. #: (Begin each figure caption with a label, "**Fig. 1.**" for example, as a new paragraph).

Fig. 1. The figure caption should begin with an overall descriptive statement of the figure followed by additional text. They should be immediately after each figure. Figure parts are indicated with capital letters **(A)**. If you prefer, you can place both the actual figures and captions logically through the text near where they are cited rather than at the end of the file (but not both). If a paragraph in the main text begins with the name of a figure, write out "Figure" in full (e.g., <para> "Figure 1 shows...").

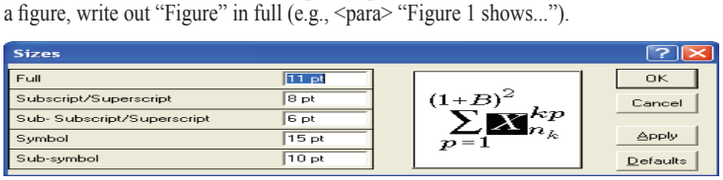

Fig. 1. The figure caption.

Tables

Table #: (Begin each table caption with a label "**Table 1.**", etc. as a new paragraph).

Table 1. Start this caption with a short description of your table. Format tables using the Word Table commands and structures. Do not create tables using spaces or tabs characters.

Table 1. Caption.

a	b	c	d	e
f				
g				
h				

Equations

$$\int_a^b x dx \tag{1}$$

Equations can be included. We do not recommend using the native Word 2007, 2008, 2010 or 2011 equation editor. This can in some cases produce less reliable MathML, the online markup language we use, which may result in display errors. Instead, use the legacy equation editor in Word (Insert menu; select insert object; select word equation) or use MathType (recommended). If you enter equations in simple LaTeX, check that they will convert accurately (Word 2007 and higher can convert simple LaTeX equations).

Closing section: It includes appendices/supplementary materials/data availability statement (if applicable), CRediT author statement (for multiple authors), acknowledgements (if applicable), competing interests, ethics (if any) and a complete list of references corresponding to all the citations given in the text of the manuscript. The appendices/supplementary materials may include data files and other material relevant to the research that should be submitted in separate files if required.

APPENDICES (if any)

The appendices should ideally be under 1000 words (approximately 2 A4 pages) for printing version. With longer appendices, they are only accepted for online publication.

CRediT author statement (for multiple authors)

CRediT offers authors the opportunity to share an accurate and detailed description of their diverse contributions to the published work.

ACKNOWLEDGEMENTS (if applicable)

This section is for the researchers who were funded for the research projects, and it should enclose all sources of financial support.

COMPETING INTERESTS

The author(s) declare(s) that there is no conflict of interest regarding the publication of this article.

REFERENCES

For in-text citation: References should be cited in the bracket with a number [1]. Multiple reference citations are separated by commas [2, 3] or if a series, dashes [4-6]. When citing sources with the author(s) and the year, they should be shortened to the first author's name, followed by et al. (with more than one author) and the year.

For reference list: With less than or equal to three authors, list all the author(s). With more than three authors, the first three should be listed and followed by et al.

References are listed in numerical order, and in the same order in which they are cited in text. The reference list should include all and only those references you have cited in the text. The reference list appears at the end of the article.

The reference consists of: Initial(s) and first/last name of the author(s), author' names separated by commas (Year of publication), "Titles of journal articles or chapter of book", *Title of Journal, Book or Other Publication*, **Volume(Number)** (if any), page numbers (if any), DOI (if any), URL and accessed date (if any) (in its original language if not English).

To cite a website and online/electronic resources, please include the accessed date (day month year).

Example of a reference list:

[1] T. Binzoni, T.S. Leung, D. Boggett, et al. (2003), "Non-invasive laser Doppler perfusion measurements of large tissue volumes and human skeletal muscle blood RMS velocity", *Phys. Med. Biol.*, **48(1)**, pp.2527-2549, DOI: 10.1088/0031-9155-48-15-318.

[2] H.W. Bischoff, H.C. Bold (1963), *Some Soil Algae from Enchanted Rock and Related Algal Species*, University of Texas Publications, 95pp.

[3] R. Busi (2016), "Weedy rice in the Philippines and Vietnam", https://www.aciar.gov.au/publication/technical-publications/weedy-rice-philippines-and-vietnam-final-report, accessed 15 July 2018.

Review articles

They should be different from the original research as they would contain different sections on the literature review. Authors may structure this part as per nature, background, and available literature on the issue argued in the manuscript.

For more detailed instructions, please visit our website: vietnamscience.vn or vietnamscience.vjst.vn

This manuscript template has been used from 2021 onwards.

P-ISSN 2525-2461 • E-ISSN 2615-9937

Vietnam Journal of Science, Technology and Engineering

JUNE 2021 • VOLUME 63 NUMBER 2

EDITORIAL BOARD

EDITORIAL OFFICE

113 Tran Duy Hung Str., Cau Giay Dist., Hanoi, Vietnam

Tel: (84.24) 39436793; Fax: (84.24) 39436794

Email: vjste@most.gov.vn

Website: vietnamscience.vn or vietnamscience.vjst.vn

PUBLICATION LICENCE

No.1153/GP-BTTTT 26th July 2011

No.2528/GP-BTTTT 26th December 2012

No.592/GP-BTTTT 28th December 2016